Bifurcations of attractors in 3D diffeomorphisms

A study in experimental mathematics

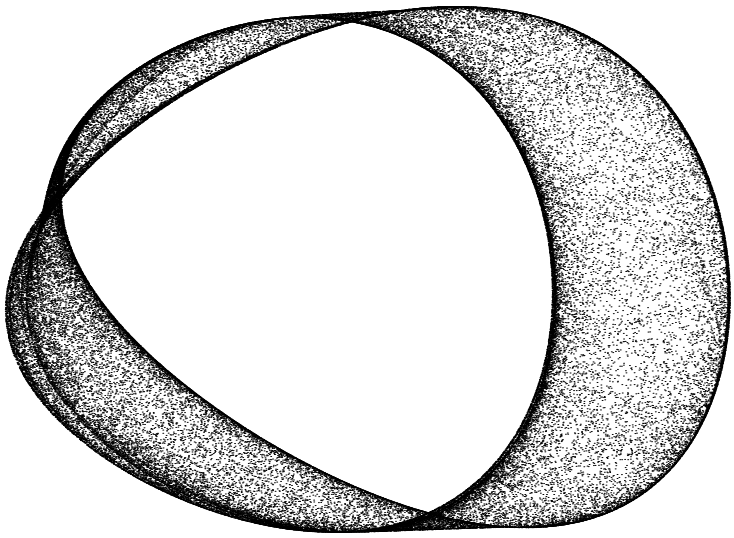

Renato Vitolo

Rijksuniversiteit Groningen

Bifurcations of attractors in 3D diffeomorphisms

A study in experimental mathematics

Proefschrift

ter verkrijging van het doctoraat in de
Wiskunde en Natuurwetenschappen
aan de Rijksuniversiteit Groningen
op gezag van de
Rector Magnificus, dr. F. Zwarts,
in het openbaar te verdedigen op
maandag 20 oktober 2003
om 16.00 uur

door

Renato Vitolo

geboren op 27 juli 1971
te Perugia (Italia)

Promotores:	Prof.dr. H. W. Broer
	Prof.dr. C. Simó
	Prof.dr. F. Takens
Beoordelingscommissie:	Prof.dr. B. Krauskopf
	Prof.dr. F. Verhulst
	Prof.dr. M. Viana

ISBN 90-367-1888-0

Preface and acknowledgements

Starting point of this thesis is the investigation of the Lorenz-84 climate model with seasonal forcing. Two students at Groningen University, Rutger Kock and Krista Homan, had written their master thesis on the subject. Supervisors were Henk Broer and Igor Hoveijn, in cooperation with Ferdinand Verhulst of Utrecht University and Theo Opsteegh of the Royal Dutch Meteorological Institute (KNMI).

The challenging problems found in these studies fitted well in the ongoing collaboration between the Dynamical Systems groups of Groningen University and of Universitat de Barcelona. Therefore, Henk Broer and Carles Simó set up a project aiming at the examination of the Lorenz-84 system in greater mathematical detail. In particular, the focus was on characterising various types of three-dimensional chaotic attractors and their transitions (bifurcations).

The first Chapter of the thesis contains a dynamical study of the Lorenz-84 climate model with seasonal forcing. Chapters three and four are devoted to mathematically analysing a class of chaotic attractors and a bifurcation observed in the Lorenz-84 system. During the research we maintained contact with the group of Yuri Kuznetsov, Lennaert van Veen, and Ferdinand Verhulst of Utrecht University, and Theo Opsteegh (KNMI), through seminars and feedback exchange.

My first words of thanks are directed to my advisors Henk Broer, Carles Simó, and Floris Takens.

I am indebted to Henk for teaching me how to set up and carry out an investigation, from the choice of the problem to the writing of the results. Henk, you were always there to talk mathematics and to support me. Without your continuous and solid support this thesis would not have been written.

Carles, I have learned a lot working at your side. Often, a conversation of an hour with you provided me with ideas and work for a few weeks. I am touched and inspired by your enthusiasm and sincere commitment to science, the art and desire of understanding.

Floris, many of the ideas for this research came out of discussions with you. Thanks for the help and the suggestions.

The jury of my PhD thesis consists of professors Bernd Krauskopf, Ferdinand Verhulst, and Marcelo Viana. I thank them for the time and care they have spent on reading the manuscript. Their remarks helped me improving the thesis.

During my stay in Groningen, I have had many interesting conversations with my colleagues of the Dynamical System group: Henk Bruin, Hans de Jong, Jun Hoo, Igor Hoveijn, Gerton Lunter, Marco Martens, Vincent Naudot, Martijn van Noort, Khairul Saleh, and Evgeny Verbitskiy. I thank Boele Braaksma, Wim Oudshoorn,

Nikolai Petkov, Henk de Snoo, Gert Vegter, Doeke de Vries, and Freddy Wubs for instructive conversations. Gert-Jan, I have enjoyed being your office-mate so much, that I consider it as a privilege. Thanks to Gerald, Madhu, Ricardo, and Robert for laughing with me. My warm thanks to Annemieke, Desiree, Eke, Esmee, Hanny, Harm, Helga, Ineke, Janieta, Jurjen, and Mariette for their sympathy and their kind help. I am grateful to all members of the faculty staff for their contribution to the working atmosphere, which has always been both pleasant and professional.

I am indebted to the Universitat de Barcelona for the kind hospitality during my several visits at MAIA. There I frequently had conversations with and help from many persons, including Enric Castellà, Amadeu Delshams, Joaquim Font, Ernest Fontich, Frederic Gabern, Gerard Gómez, Àlex Haro, Àngel Jorba, Manuel Marcote, Pau Martín, Josep Maria Mondelo, Estrella Olmedo, Joaquim Puig, Joan Carles Tatjer, and Jordi Villanueva. The atmosphere of enthusiasm for the research at that department has always impressed me.

A special thank you to Rafael de la Llave for his invitation to Austin and the interesting conversations. I thank the following persons for their interest in my research: Sylvain Crovisier, Sandro Frigio, Yuri Kuznetsov, Daan Lenstra, Franz Naselli, Riccardo Piergallini, Andrey Shil′nikov, Jorge Sotomayor, Sebastian Wieczorek, and Lennaert van Veen.

Thanks to my friends for being there: Enric, Franz, Rico, Sante. Thanks to the Dutch people for giving me the opportunity to work in the Netherlands and improve myself. This work is dedicated to my family: my parents Francesco and Giulia, my brother and sister Raffaele and Rosella, and the joy of my life, Alejandra.

Contents

Chapter 1

Introduction

The present work fits within the study of nonlinear deterministic dynamical systems depending on parameters. These systems are used for modelling in many disciplines, such as biology, mechanics, meteorology, physics and economy. The general goal is to understand the qualitative behaviour of these systems, and in particular:

1. The asymptotic, long term dynamics, where the system has settled down on an attractor.

2. The transitions between attractors due to variations of certain parameters (bifurcations).

We focus on discrete dynamical systems, generated by iteration of smooth invertible maps (diffeomorphisms). The orderly asymptotic dynamics takes place on attractors that have a simple geometry, like fixed points, periodic orbits, and invariant circles or tori. Usually the chaotic dynamics lives on strange attractors with a fractal structure. The purpose of this work is to understand the geometry of certain types of strange attractors, as well as the bifurcations leading to their formation.

1.1 The structure of three-dimensional strange attractors

The research presented in this thesis has been motivated by the following question:

> What is the structure of strange attractors for three-dimensional diffeomorphisms?

The term 'strange attractor' first appeared in the work of Ruelle and Takens [NRT, RT]. Evolutions starting near a strange attractor rapidly converge towards it, and are characterised by chaotic behaviour: two evolutions starting from nearby points typically separate exponentially fast [BC, ER, GH, MV]. Strange attractors carrying chaotic dynamics have been described in many experimental and numerical investigations, in models coming from various fields of research: biology [Kuz], economics [Hom], mathematics [ASFK, BST, Tat], mechanics [GH], meteorology [Lor, SNN, Vee, VOV], laser physics [WKL].

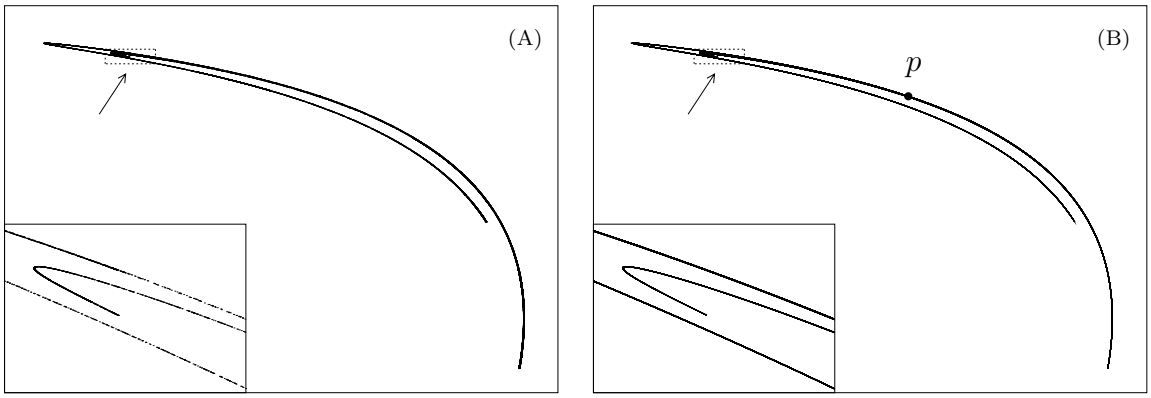

Figure 1.1: Structure of Hénon-like strange attractors. (A) Two-dimensional projection of an attractor occurring in a three-dimensional diffeomorphism P. The small box pointed by an arrow is magnified in the lower left corner. (B) A saddle fixed point p of P, plotted with its one-dimensional unstable manifold. The same windows are used in the two plots; the same holds for the magnifications. Notice the striking similarity.

The structure of strange attractors of two-dimensional diffeomorphisms is fairly well understood [BC, DRV, MV, Sim, Via1, LSY]. In particular, Hénon-like strange attractors [MV, Via1] are characterised by the property that there exists a periodic point p of saddle type such that the strange attractor coincides with the closure of the unstable manifold $\operatorname{clos} W^u(\mathrm{Orb}(p))$, where $\mathrm{Orb}(p)$ denotes the orbit of p. For an illustration of this, see Figure 1.1. In Figure 1.1 (A) an attractor of a three-dimensional diffeomorphism P is plotted, and in (B) a saddle fixed point p of P, with its one-dimensional unstable manifold. The occurrence of this type of strange attractors has been proved for a class of diffeomorphisms called Hénon-like [MV, Via1]. The first numerical example of this type of attractors was given in [Hen].

A periodic point is the simplest invariant set for a diffeomorphism P. The 'next' object in terms of geometrical and dynamical complexity is an invariant circle, *i.e.*, a closed smooth curve which is mapped onto itself by P. The diffeomorphism P generically has two types of dynamics on an invariant circle $\mathscr{C}$: quasi-periodic or Morse-Smale [Arn, BHS, GH, Kuz]. In the first case, repeated application of P on a point of $\mathscr{C}$ is equivalent to rotating the point along $\mathscr{C}$ in a rigid fashion. In the second case, the circle $\mathscr{C}$ contains a finite number of attracting periodic orbits, and the same number of repelling periodic orbits. Under iteration of P, any point of $\mathscr{C}$ not belonging to the repelling periodic orbits converges to one of the attracting periodic orbits.

This leads us to the central question:

> Given a diffeomorphism P and an invariant circle $\mathscr{C}$ of saddle type, are there strange attractors contained in the closure $\operatorname{clos} W^u(\mathscr{C})$?

This problem forms the basis of the third Chapter. There we consider a diffeomorphism T of the solid torus $\mathbb{R}^2 \times \mathbb{S}^1$ into itself. The diffeomorphism is obtained by the weak coupling of a planar Hénon-like map [MV] with a diffeomorphism of the circle $\mathbb{S}^1$ which is a perturbation of a rigid rotation. When the dynamics on $\mathbb{S}^1$ is

of Morse-Smale type, by using a theorem of Díaz-Rocha-Viana [DRV], we prove that Hénon-like strange attractor occur for the diffeomorphism T. In Figure 1.2 (A) we display one of the attractors of the diffeomorphism T in the period three case, where the picture is obtained by numerical simulation.

For a subset of parameter values, a different result is obtained for T. In this case, T is a perturbation of the product map given by a planar diffeomorphism K with a rigid rotation on $\mathbb{S}^1$, where K satisfies the properties:

1. K is dissipative, *i.e.*, it contracts area;

2. K has a saddle fixed point with a transversal homoclinic point [PT].

Under these hypotheses, we prove that the coupled diffeomorphism T has an invariant circle $\mathscr{C}$ of saddle type, such that the following property holds: the stable and unstable manifolds of $\mathscr{C}$ bound an open region U such that the orbits of all points in U are attracted to the closure of the unstable manifold $W^u(\mathscr{C})$. This shows the occurrence of an attractor inside $\operatorname{clos} W^u(\mathscr{C})$. When the dynamics on $\mathscr{C}$ is quasi-periodic, numerical evidence suggests that this attractor is strange; compare Figure 1.2 (B). The latter property remains conjectural and is topic of future research.

Remark 1.1. When speaking about numerical evidence for strange attractors in a concrete system, one should be aware of the following:

1. Most theoretical results concerning Hénon-like strange attractors are of a perturbative nature, meaning that these only hold in settings which are sufficiently close to a one-dimensional situation [BC, MV, LSY]. Furthermore, no explicit bounds are given for the size of the allowed perturbation.

2. The above theoretical results yield the occurrence of strange attractors for a nowhere dense parameter set $\mathcal{S}$ of positive Lebesgue measure. Given a specific, numerical parameter value, there is no algorithm to check whether this parameter value belongs to the set $\mathcal{S}$ or not.

This implies that, in general, the above theory does not guarantee that a numerically observed strange attractor actually exists in the examined system. For example, despite many efforts it still remains unproven whether the attractor numerically studied by Hénon a quarter of a century ago [Hen] is a Hénon-like strange attractor. Therefore, the structure and the properties expressed in [BC, MV, Via1, LSY] are considered as a general paradigm for the interpretation of numerical results which suggest the existence of strange attractors. In other words, Hénon-like strange attractors are conjectured to occur in a large class of dynamical systems. Throughout the thesis, when describing our numerical results, we will tacitly assume this conjecture.

The above discussion forms the mathematical core of the thesis, and is mainly reported in Chapter three. We now describe the remaining Chapters (two and four).

1.2 The Lorenz-84 climate model with seasonal forcing

Chapter two contains the basic examples which motivated the research presented in Chapters three and four. These examples are found in a model which is a perturbation

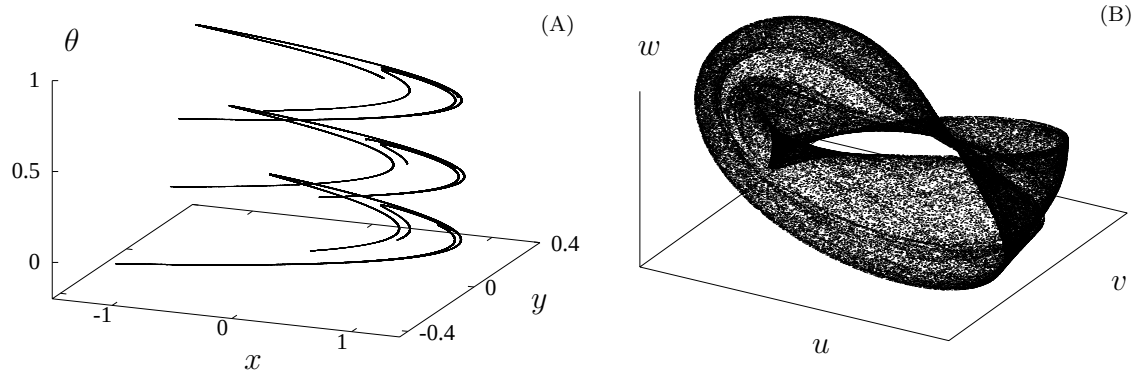

Figure 1.2: (A) Two-dimensional projection of a Hénon-like strange attractor of the diffeomorphism T studied in the third Chapter (see text for details). (B) Two-dimensional projection of a quasi-periodic Hénon-like strange attractor of T.

of a three-dimensional autonomous system of ordinary differential equations coming from meteorology, the Lorenz-84 model [Lor]. The Lorenz-84 model is the simplest approximation of the general atmospheric circulation at mid-latitude, on a scale of a few thousand kilometres in space and about a week in time.

In meteorology, low-dimensional models such as the Lorenz-84 system have drawn the attention of investigators over the last decades [Vee, VOV]. The reason is that both the equation of Fluid Dynamics for the atmospheric flow and the computer models used for weather prediction are hard to analyse mathematically. Low-dimensional models have the advantage that they can be studied by the qualitative methods of Dynamical Systems theory, such as bifurcation theory [Arn, GH, Kuz]. On the one hand, low-dimensional systems are not suitable to produce quantitatively correct predictions about the climate. Indeed, strong simplifications imposed to obtain such models. See [Vee] for a discussion about this aspect. On the other hand, the mathematical understanding of low-dimensional models helps clarify the qualitative, large scale dynamics of more complicated systems. Moreover, low-dimensional models have always played a central role as motivating examples for the development of the theory of Dynamical Systems [GH].

The model we study in the second Chapter is a non-autonomous perturbation of the Lorenz-84 model, constructed by introducing a periodic forcing, which simulates seasonal changes in north-south and ocean-land temperature contrasts. The non-autonomous model is analysed in terms of the Poincaré map [Arn, GH, Kuz], which is a diffeomorphism $P_{F,G,\varepsilon} : \mathbb{R}^3 \to \mathbb{R}^3$ depending on three control parameters (F, G, ε). The parameter ε is the relative amplitude of the periodic perturbation. The study focuses on the Dynamical Systems aspects of the model, and in particular on the question, posed at the beginning of this introduction, concerning the structure of strange attractors for three-dimensional diffeomorphisms. Various types of strange attractors are detected in the model; see Figure 1.3 and compare Remark 1.1. We conjecture that the attractors in Figure 1.3 are Hénon-like (A) and quasi-periodic Hénon-like (B), see the previous section. To be precise:

(A) There exists a saddle periodic point p of the map $P_{F,G,\varepsilon}$ such that the attractor in Figure 1.3 (A) coincides with the closure $\operatorname{clos} W^u(\mathrm{Orb}(p))$.

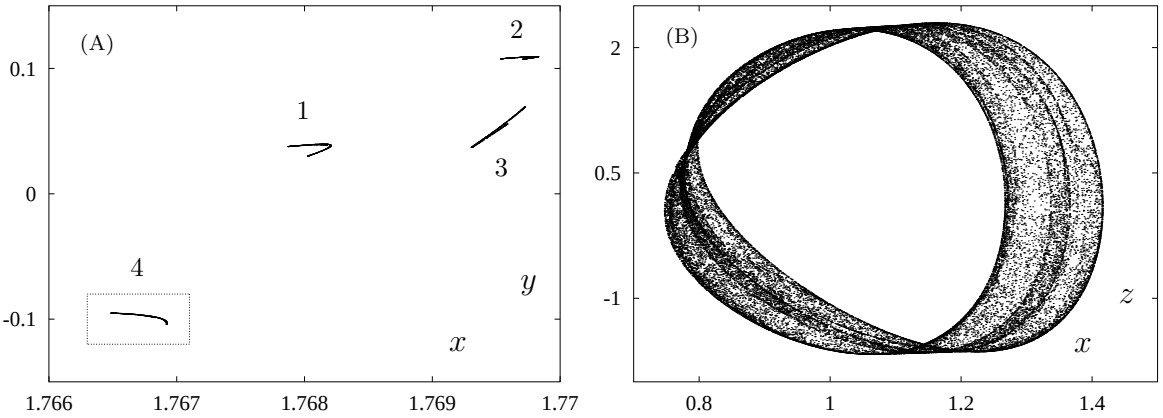

Figure 1.3: (A) Two-dimensional projection of a Hénon-like strange attractor of the diffeomorphism $P_{F,G,\varepsilon}$. The four components are mapped onto each other by $P_{F,G,\varepsilon}$ in the order given by the labels 1 to 4. The component in the box is magnified in Figure 1.1 (A). This attractor coexists with the period four saddle point p in Figure 1.1 (B). (B) Two-dimensional projection of a quasi-periodic Hénon-like strange attractor of $P_{F,G,\varepsilon}$.

(B) There exists a quasi-periodic invariant circle of saddle type such that this attractor coincides with the closure $\operatorname{clos} W^u(\mathscr{C})$.

One of the four components of the attractor in Figure 1.3 (A) is magnified in Figure 1.1 (A). In Figure 1.1 (B) we display a period four saddle point p together with its one-dimensional unstable manifold. This empirical observation suggests that the attractor in Figure 1.3 (A) coincides with $\operatorname{clos} W^u(\operatorname{Orb}(p))$.

The formation of strange attractors is often understood in terms of bifurcation scenarios, also called routes to chaos upon variation of parameters. In this respect, the numerical results are interpreted in the light of bifurcation theory, *i.e.*, the theory of quasi-periodic bifurcations [BHS, BHTB] and of hetero- and homoclinic tangency bifurcations [PT]. The attractor in Figure 1.3 (B) is created after two consecutive quasi-periodic period doublings of an invariant circle, followed by a homoclinic tangency of a saddle periodic point on the circle, occurring inside a resonance tongue [Arn, BST, GH]. The attractor in Figure 1.3 (B) is created after a period doubling cascade of periodic points.

Several papers on the autonomous Lorenz-84 system (see [BSV1] and references therein) are the starting point for the analysis of the map $P_{F,G,\varepsilon}$. The bifurcation diagram of the autonomous system is organised by a codimension two Hopf-saddle-node bifurcation of equilibria [SNN]. This dynamically rich bifurcation has been intensively studied in the general vector field case [BV, GH, Kuz]. In particular, under appropriate hypotheses, near a Hopf-saddle-node of equilibria the following bifurcations occur:

1. Shil′nikov bifurcations of equilibria of saddle-focus type.
2. Hopf–Neĭmark–Sacker bifurcations of a limit cycle, where a two-dimensional invariant torus is created.
3. Heteroclinic bifurcations, by which the torus is destroyed.

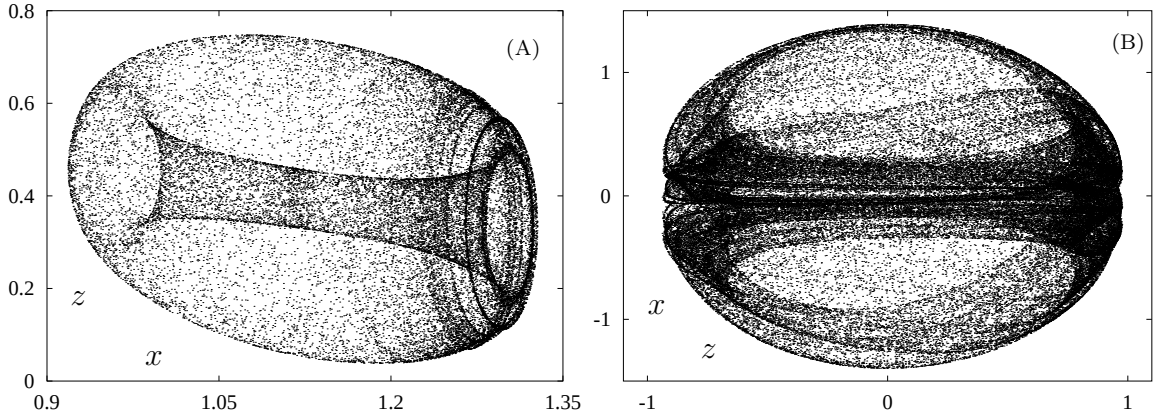

Figure 1.4: (A) Two-dimensional projection of a quasi-periodic Hénon-like strange attractor of the Poincaré map $P_{F,G,\varepsilon}$ of the forced Lorenz-84 system. (B) Two-dimensional projection of a quasi-periodic Hénon-like strange attractor of the model G studied in Chapter four.

See [BV, GH, Kuz] for the terminology. On the basis of perturbation theory, the Poincaré map $P_{F,G,\varepsilon}$ is expected to display many related phenomena. Indeed, for small ε we find that the map $P_{F,G,\varepsilon}$ has a Hopf-saddle-node bifurcation of a fixed point. Near this bifurcation point, the map $P_{F,G,\varepsilon}$ exhibits quasi-periodic Hopf bifurcations of an invariant circle [BHTB], where an invariant torus is created. Near these Hopf bifurcations, quasi-periodic Hénon-like attractors are numerically detected, see Figure 1.4 (A).

As far as we know, no systematic investigations of the Hopf-saddle-node bifurcation of fixed points of diffeomorphisms are known. This led to the research in the fourth Chapter.

1.3 Hopf-saddle-node bifurcation for fixed points of diffeomorphisms

In the fourth Chapter we analyse the Hopf-saddle-node bifurcation for diffeomorphisms in two model maps G and Q, constructed 'as generic as possible' when restricting to the unfolding class they belong to.

Quasi-periodic Hopf bifurcations [BHS, BHTB] of an invariant circle $\mathscr{C}$ occur for G and Q, at which a two-dimensional torus $\mathscr{T}$ branches off from $\mathscr{C}$. Bifurcations of an invariant circle $\mathscr{C}$ are well understood only in the case that the dynamics on $\mathscr{C}$ is quasi-periodic. To be more precise, at least two parameters are required for a generic, theoretical analysis of bifurcations of an invariant circle. In two-parameter families of maps having an invariant circle $\mathscr{C}$, Hopf bifurcations of $\mathscr{C}$ do not occur along continuous curves inside the parameter plane. They can only be described in a Cantor-like boundary in the parameter plane, formed by the intersection of a Cantor set of lines with a continuous curve. The resonance gaps in this Cantor-like boundary are called bubbles [BHS, Che]. Not much is known about the behaviour of the bifurcating circle $\mathscr{C}$ for parameter values inside the bubbles.

Quasi-periodic Hénon-like attractors are observed in G and Q (Figure 1.4 left),

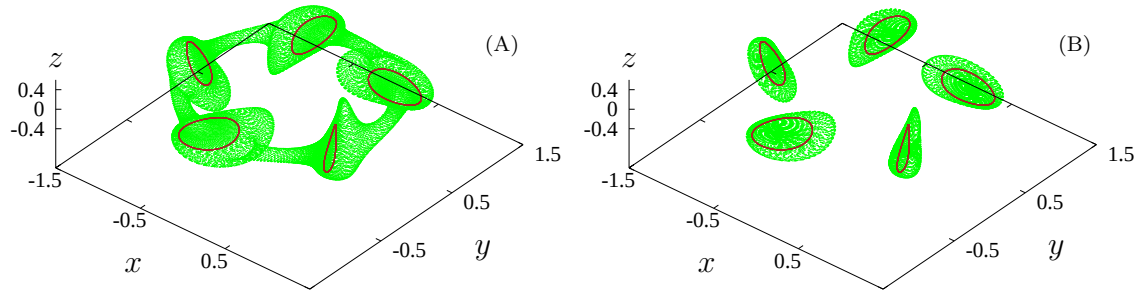

Figure 1.5: (A) An invariant 2-torus of the model G studied in Chapter four, coexisting with a period five attracting invariant circle. (B) A period five 2-torus of G coexisting with the period five circle. Both coexist with the 2torus in the left picture.

near the breakdown of the invariant torus $\mathscr{T}$. The same kind of attractor is found in the Poincaré map $P_{F,G,\varepsilon}$ of the forced Lorenz-84 model, compare Figure 1.4 right. In both cases, homoclinic and heteroclinic tangency bifurcations [PT] are involved in the destruction of the torus.

The model G is explicitly constructed for the study of a 1:5 bubble on the Hopf boundary H, where $\mathscr{C}$ has a weak resonance of order 1:5 [Arn, Tak]. It turns out that the 1:5 bubble on H is bounded by two secondary Hopf-saddle-node bifurcations of period five points of the map G. Both bifurcations take place on the invariant circle $\mathscr{C}$. The bifurcation diagram of G in the neighbourhood of the two secondary Hopf-saddle-node points is quite rich. It involves at least two families of period five invariant circles, two families of invariant tori, and one family of period five invariant tori. For example, in certain regions of the parameter plane a torus $\mathscr{T}$ coexists with a period five circle $\mathscr{C}^5$ (Figure 1.5 left), where both are attractors. Their basins of attraction are separated by a period five repelling invariant torus $\mathscr{T}^5$ (Figure 1.5 right). By varying the parameters, the torus $\mathscr{T}^5$ collides with the circle $\mathscr{C}^5$ through a quasi-periodic Hopf bifurcation. Again, this occurs on a 'Cantor-like' bifurcation boundary, interspersed by resonance bubbles. Therefore it seems that near a Hopf-saddle-node bifurcation for diffeomorphisms infinitely many subordinate resonant Hopf-saddle-node bifurcations take place, of various orders and at arbitrarily small scales.

1.4 Overview

Many mathematical problems arise in Dynamical Systems theory from the study of concrete models, such as the Lorenz-84 system with seasonal forcing. Chapter two is an inventory of the dynamics observed in the periodically forced Lorenz-84 model. This material provides the basic examples for the investigations pursued in Chapters three and four.

In Chapter three, two simplified settings are considered for the occurrence of a strange attractor inside $\operatorname{clos} W^u(\mathscr{C})$, the closure of the unstable manifold of an invariant circle $\mathscr{C}$ of saddle type. In the first scenario, Hénon-like strange attractors are proved to occur for a diffeomorphism T of the solid torus $\mathbb{R}^2 \times \mathbb{S}^1$. For certain parameter values, there exists an invariant circle $\mathscr{C}$ with rational rotation number such that the above strange attractors are contained in $\operatorname{clos} W^u(\mathscr{C})$. In a slightly dif-

ferent setting it is proved that $\operatorname{clos} W^u(\mathscr{C})$ contains an attractor, where the dynamics on $\mathscr{C}$ is quasi-periodic. The precise characterisation of the quasi-periodic Hénon-like attractors remains conjectural.

In Chapter four the Hopf-saddle-node bifurcation for fixed points of diffeomorphisms is studied in two model maps. These maps are constructed in such a way that they are likely to be representative of a large class of Hopf-saddle-node diffeomorphisms. The main point of interest is the rich bifurcation diagram near a 1:5 resonance bubble on a Hopf bifurcation boundary.

Throughout the thesis, particular emphasis is put on the study of strange attractors that are typical for three-dimensional diffeomorphisms. The theory of strange attractors for three-dimensional vector fields and for two-dimensional maps is quite developed. See *e.g.* the results on the Lorenz attractor [GH, Tuc] and on Hénon-like attractors [BC, DRV, MV, Via2, LSY]. On the other hand, attractors of diffeomorphisms having a genuine three-dimensional nature lie at the verge of the theory developed so far [Tat, Via1, Via2]. In this respect, the phenomena discussed in Chapters three and four display many similarities with those encountered in the forced Lorenz-84 model. In particular, quasi-periodic Hénon-like strange attractors seem to occur in a persistent and abundant way.

Many questions remain open for future research. We just mention a few:

1. The study of the Shil′nikov homoclinic tangency bifurcation for fixed points of diffeomorphisms of saddle-focus type; in particular, the analysis of the related attractors.

2. A rigorous theoretical analysis concerning the existence and structure of quasi-periodic Hénon-like strange attractors, in the spirit of [BC, MV, Via2, LSY].

3. A discussion of the Hopf-saddle-node bifurcation for fixed points of diffeomorphisms in a more general setting. Analysis of the global bifurcations occurring near the secondary Hopf-saddle-node points.

The three Chapters of this thesis are based on the papers [BSV1, BSV2, BSV3] respectively.

Bibliography for Chapter one

[ASFK] V.S. Anishchenko, M.A. Safonova, U. Feudel, J. Kurths: Bifurcations and transition to chaos through three-dimensional tori, *Int. J. of Bif. and Chaos* **4(3)** (1994), 595–607.

[Arn] V.I. Arnol′d: *Geometrical Methods in the Theory of Ordinary Differential Equations*, Springer–Verlag (1983).

[BC] M. Benedicks, L. Carleson: The dynamics of the Hénon map, *Ann. Math.* **133** (1991), 73–169.

[BHS] H.W. Broer, G.B. Huitema, M.B. Sevryuk: *Quasi-periodic Motions in Families of Dynamical Systems*, Springer LNM **1645** (1996).

[BHTB] H.W. Broer, G.B. Huitema, F. Takens, B.L.J. Braaksma: Unfoldings and bifurcations of quasi-periodic tori, *Mem. AMS* **83** (1990), 421.

[BST] H.W. Broer, C. Simó, J.C. Tatjer: Towards global models near homoclinic tangencies of dissipative diffeomorphisms, *Nonlinearity* **11** (1998), 667–770.

[BSV1] H.W. Broer, C. Simó, R. Vitolo: Bifurcations and strange attractors in the Lorenz-84 climate model with seasonal forcing, *Nonlinearity* **15(4)** (2002), 1205–1267.

[BSV2] H.W. Broer, C. Simó, R. Vitolo: Hénon-like strange attractors in a family of maps of the solid torus, *preprint University of Groningen*, submitted (2002).

[BSV3] H.W. Broer, C. Simó, R. Vitolo: The Hopf-saddle-node bifurcation for fixed points of diffeomorphisms, in preparation.

[BV] H.W. Broer, G. Vegter: Subordinate Shil′nikov bifurcations near some singularities of vector fields having low codimension, *ETDS* **4** (1984), 509–525.

[Che] A. Chenciner: Bifurcations de points fixes elliptiques. II. Orbites périodiques et ensembles de Cantor invariants, *Invent. Math.* **80** (1985), 81–106.

[DRV] L. Díaz, J. Rocha, M. Viana: Strange attractors in saddle cycles: prevalence and globality, *Inv. Math.* **125** (1996), 37–74.

[ER] J.-P Eckmann, D. Ruelle: Ergodic theory of chaos and strange attractors, *Rev. Mod. Phys.* **57** (1985), 617–655.

[GH] J. Guckenheimer, P. Holmes: *Nonlinear Oscillations, Dynamical Systems, and Bifurcations of Vector Fields*, Springer–Verlag (1983).

[Hen] M. Hénon: A two dimensional mapping with a strange attractor, *Comm. Math. Phys.* **50** (1976), 69–77.

[Hom] W.A. Brock, C. Hommes: Heterogeneous beliefs and routes to chaos in a simple asset pricing model. Algorithms and economic dynamics (Geneva, 1996). *J. Econom. Dynam. Control* **22(8-9)** (1998), 1235–1274.

[Kuz] Yu. Kuznetsov: *Elements of Applied Bifurcation Theory*, Springer–Verlag (1995).

[Lor] E.N. Lorenz: Irregularity: a fundamental property of the atmosphere, *Tellus* **36A** (1984), 98–110 .

[MV] L. Mora, M. Viana: Abundance of strange attractors, *Acta Math* **171** (1993), 1–71.

[NRT] S. Newhouse, D. Ruelle, F. Takens: Occurrence of strange Axiom A attractors near quasiperiodic flows on $\mathbb{T}^m$, $m \geq 3$, *Commun. Math. Phys.* **64** (1978), 35–40.

[PT] J. Palis, F. Takens: *Hyperbolicity & Sensitive Chaotic Dynamics at Homoclinic Bifurcations*, Cambridge Studies in Advanced Mathematics **35**, Cambridge University Press (1993).

[RT] D. Ruelle, F. Takens: On the nature of turbulence, *Comm. Math. Phys.* **20** (1971), 167–192.

[SNN] A. Shil′nikov, G. Nicolis, C. Nicolis: Bifurcation and predictability analysis of a low-order atmospheric circulation model, *Int. J. of Bif. and Chaos* **5(6)** (1995), 1701–1711.

[Sim] C. Simó: On the Hénon–Pomeau attractor, *J. Stat. Phys.* **21** (1979), 465–494.

[Tak] F. Takens: Forced oscillations and bifurcations, in *Applications of Global Analysis* **1** (1974), Communications of the Mathematical Institute Rijksuniversiteit Utrecht **3**. Reprinted in: *Global analysis of dynamical systems: Festschrift dedicated to Floris Takens for his 60th birthday* (H.W. Broer, B. Krauskopf, and G. Vegter Eds.), Institute of Physics Publishing, Bristol (2001).

[Tat] J.C. Tatjer: Three dimensional dissipative diffeomorphisms with homoclinic tangencies, *ETDS* **21(1)** (2001), 249–302.

[Tuc] W. Tucker: A rigorous ODE solver and Smale's 14th problem, *Found. Comput. Math.* **2(1)** (2002), 53–117.

[Vee] L. van Veen: *Time scale interaction in low-order climate models*, PhD thesis, University of Utrecht (2002).

[VOV] L. van Veen, T. Opsteegh, F. Verhulst: Active and passive ocean regimes in a low-order climate model, *Tellus* **53A** (2001), 616–628.

[Via1] M. Viana: Strange attractors in higher dimensions, *Bull. Braz. Math. Soc.* **24** (1993), 13–62.

[Via2] M. Viana: Multidimensional nonhyperbolic attractors, *Inst. Hautes Études Sci. Publ. Math.* **85** (1997), 63–96.

[LSY] Q. Wang, L.-S. Young: Strange Attractors with One Direction of Instability, *Comm. Math. Phys.* **218** (2001), 1–97.

[WKL] S. Wieczorek, B. Krauskopf, D. Lenstra: A unifying view of bifurcations in a semiconductor laser subject to optical injection, *Optics Communications* **172** (1999), 279–295.

Chapter 2

The Lorenz-84 climate model with seasonal forcing

2.1 Introduction

2.1.1 The periodically driven Lorenz-84 system

Weather and climate prediction are difficult tasks, because of the complexity of the atmospheric evolution. Computer models used for these predictions usually contain a high number of variables and parameters. Therefore, it is practically impossible to perform detailed studies of their dynamical properties. On the other hand, there is experimental evidence [109] that low-dimensional attractors appear in some hydrodynamical flows just after the onset of turbulence. As a consequence, low-dimensional models have attracted the attention of meteorologists, mathematicians and physicists over the last decades. Low-dimensional models are easier to study than the infinite-dimensional Navier–Stokes equations or large computer models. In particular, geometrical and qualitative methods from bifurcation theory [6, 56, 78] can be applied to clarify the transitions from regular to complicated dynamical behaviour.

In this Chapter we examine a model for the long term atmospheric circulation, proposed by Lorenz [80] in 1984, obtained by a Galerkin projection of an infinite dimensional model. This is a three-dimensional system given by

$$\begin{aligned} \dot{x} &= -ax - y^2 - z^2 + aF, \\ \dot{y} &= -y + xy - bxz + G, \\ \dot{z} &= -z + bxy + xz, \end{aligned} \tag{2.1}$$

where the dot represents differentiation with respect to the time t. System (2.1) has been used in climatological studies, for example by coupling it with a low-dimensional model for ocean dynamics. For related work, see [118] and references therein. On the other hand, the bifurcation diagram of (2.1) has been analysed in [102]. For other dynamical studies of this system, that we shall refer to as the *(autonomous) Lorenz-84* model, see [61, 82].

We briefly summarise the meaning of variables, parameters and constants in the Lorenz-84 model. The time unit of t is estimated to be five days. The variable x stands for the strength of the symmetric, globally averaged westerly wind current. The

variables y and z are the strength of cosine and sine phases of a chain of superposed waves transporting heat poleward. The terms in b represent displacement of the waves due to interaction with the westerly wind. The coefficient a, if less than one, allows the westerly wind current to damp less rapidly than the waves. The terms in F and G are thermal forcings: F represents the *symmetric* cross-latitude heating contrast and G accounts for the *asymmetric* heating contrast between oceans and continents. In a later paper [81], Lorenz pointed out that F and G should be allowed to vary periodically during a year. In particular, F should be larger in winter than in summer. However, in his numerical study he kept G fixed, identifying $(F, G) = (6, 1)$ and $(F, G) = (8, 1)$ with summer respectively winter conditions. He introduced a periodical variation of the parameter F between summer and winter conditions, by setting $F = 7 + 2\cos(2\pi t/T)$ with T of the order of magnitude of 1 year, *i.e.*, $T = 73$.

We use a slightly different approach, in order to study seasonal effects. Here F and G are both taken T periodic in time, by using

$$F(1 + \varepsilon\cos\omega t) \quad \text{and} \quad G(1 + \varepsilon\cos\omega t), \quad \omega = 2\pi/T\ .$$

The Lorenz-84 model thereby turns into a parametrically forced system:

$$\begin{aligned} \dot{x} &= -ax - y^2 - z^2 + aF(1 + \varepsilon\cos(\omega t)), \\ \dot{y} &= -y + xy - bxz + G(1 + \varepsilon\cos(\omega t)), \\ \dot{z} &= -z + bxy + xz. \end{aligned} \tag{2.2}$$

We refer to this three-dimensional T-periodic system as the *driven Lorenz-84* model. As in [61, 80, 81, 82, 102], the parameters a and b from now on are set to $a = 1/4$ and $b = 4$, while T is fixed at 73. The value of ε used in most of the numerical simulations is 0.5. However, smaller values are used when investigating the relation between the dynamics of systems (2.2) and (2.1). For this reason ε is used as a control parameter together with F and G. We indicate the three-dimensional parameter space by $\mathfrak{M} = \{F, G, \varepsilon\}$. Fixing a value $\varepsilon = \varepsilon^*$ means selecting a plane $\mathfrak{M}_{\varepsilon^*} = \{F, G\}$ inside $\mathfrak{M}$. Only positive values of G have to be considered, since solutions of (2.2) for $G = -G_0$ correspond to solutions for $G = G_0$ by changing the sign of y and z. For numerical experiments, we mainly focus on the parameter window

$$(F, G, \varepsilon) \in [0, 12] \times [0, 9] \times [0, 0.5],$$

for which (F, G) are centred around summer and winter conditions. However, we are also concerned with asymptotical properties of (2.2) for $G \to 0$ and $G \to \infty$. The driven system is studied in terms of its Poincaré map[1]

$$P_{F,G,\varepsilon} : \mathbb{R}^3 \to \mathbb{R}^3$$

which is a diffeomorphism depending on the parameters[2] (F, G, ε).

Remark 2.1. By 'periodic point' we mean a point $q \in \mathbb{R}^3$ such that $P^m(q) = q$ for some integer $m \neq 0$. A period m point and an invariant circle of P correspond to a period $|m|\,T$ limit cycle and an invariant two-torus, respectively, of the flow of (2.2), see Table 2.2 in Sec. 2.3.

[1] Also called stroboscopic, first return or period mapping.

[2] We often suppress some or all parameters in the notation, writing $P_{F,G}$ or P

The dynamics of the family $P_{F,G,\varepsilon}$ is first explored by iteration to an attractor for several values of (F, G), for $\varepsilon = 0.5$ fixed. In fact, P has an attracting bounded subset of $\mathbb{R}^3$ for all values of F, G and ε (see Sec. 2.2.1). The map P is computed by numerical integration of equation (2.2) over a period T. The length of the period causes P to be quite sensitive to initial conditions. To achieve sufficient numerical precision we chose a method of integration based on the Taylor expansion of the solution (see Sec. 2.A). Some preliminary results are examined in the next section.

2.1.2 Overview of the attractors of the Poincaré map

In Figure 2.1 we plotted one-dimensional projections of sequences of attractors of P. In each bifurcation diagram, G varies in a grid with spacing 0.01 on the line $F = F_0$, where F_0 is kept fixed. For each G on the grid, the y-projection of one attractor is plotted. We achieved a sort of continuity in the evolution of the attractors by using the following algorithm. Values $F = F_0$ and $G = 0$ are fixed initially. Starting from the point $q = (x, y, z) = (1, 2, 3)$, a loop of 2000 iterations of $P_{F_0,0}$ is carried out, of which the last 100 points are plotted. Then the parameter G is increased by 0.01 and the last point is used to start a new loop. Note that no coexistence of attractors (multistability) can be detected in this way.

The attractors plotted in Figure 2.1 belong to three classes: fixed (or periodic) points, invariant circles and strange attractors [89, 95, 100, 99]. A fixed point $\mathscr{A}$ is the unique attractor occurring for small F, compare Figure 2.1 (a) and (b). As G increases, its y-coordinate evolves continuously in the first case and has a jump at $G \simeq 0.5$ in the second. The fixed point $\mathscr{A}$ is also detected for all G larger than a value $G_{\mathscr{A}}$ depending on F. In Figure 2.1 (c)–(f) one has respectively[3] $G_{\mathscr{A}} \simeq 0.84$, 1.48, 3.9, 7.54.

At $F = 1.2$ (Figure 2.1 (c)) an invariant circle $\mathscr{C}$ occurs for G small, instead of $\mathscr{A}$. In the G-interval $(0.34, 0.37)$, pointed by a solid arrow, $\mathscr{C}$ is phase-locked to a fixed point attractor.[4] The circle shrinks down as G increases and at $G \simeq 0.78$ (marked by a dashed arrow) the fixed point $\mathscr{A}$ reappears. For G larger, the evolution of $\mathscr{A}$ is similar to Figure 2.1 (b): a discontinuity occurs at $G \simeq 0.84$, but $\mathscr{A}$ persists for all larger G.

The circle attractor $\mathscr{C}$ also exists for $F = 5$, 7, and 11, for G smaller than a threshold $G_{\mathscr{C}}$ depending on F. One has respectively $G_{\mathscr{C}} \simeq 0.64$, 0.33, and 0.48, marked by arrows in Figure 2.1 (d), (e) and (f). A 'doubled' circle $2\mathscr{C}$ occurs for $F = 7$ and $0.34 \lessdot G \lessdot 0.5$ (see Sec. 2.4.9). A strange attractor is found for most G values in the intervals $0.65 \lessdot G \lessdot 1.29$, $0.59 \lessdot G \lessdot 1.7$ and $0.5 \lessdot G \lessdot 2.04$ respectively, but for G larger the fixed point $\mathscr{A}$ reappears. For $F = 7$ and $F = 11$, $\mathscr{A}$ is again replaced by a circle attractor $\mathscr{C}_2$ in the intervals $2.15 \lessdot G \lessdot 3.89$ and $2.36 \lessdot G \lessdot 7.53$ respectively. This corresponds to the 'cigar'-like sequences $\mathscr{C}_2(7, G)$ in Figure 2.1 (e) and $\mathscr{C}_2(11, G)$ in (f).

Several transitions of the attractors are detected by this procedure. Then the following questions arise: what is the exact subdivision of the parameter plane $\mathfrak{M}_{0.5}$?

[3] When giving approximate numerical values we shall use the symbols $\lessdot$, $\gtrdot$ and $\simeq$ instead of $<$, $>$, and $=$.

[4] This corresponds to an Arnol′d tongue $\mathfrak{A}^0$ of rotation number zero [4, 41, 99].

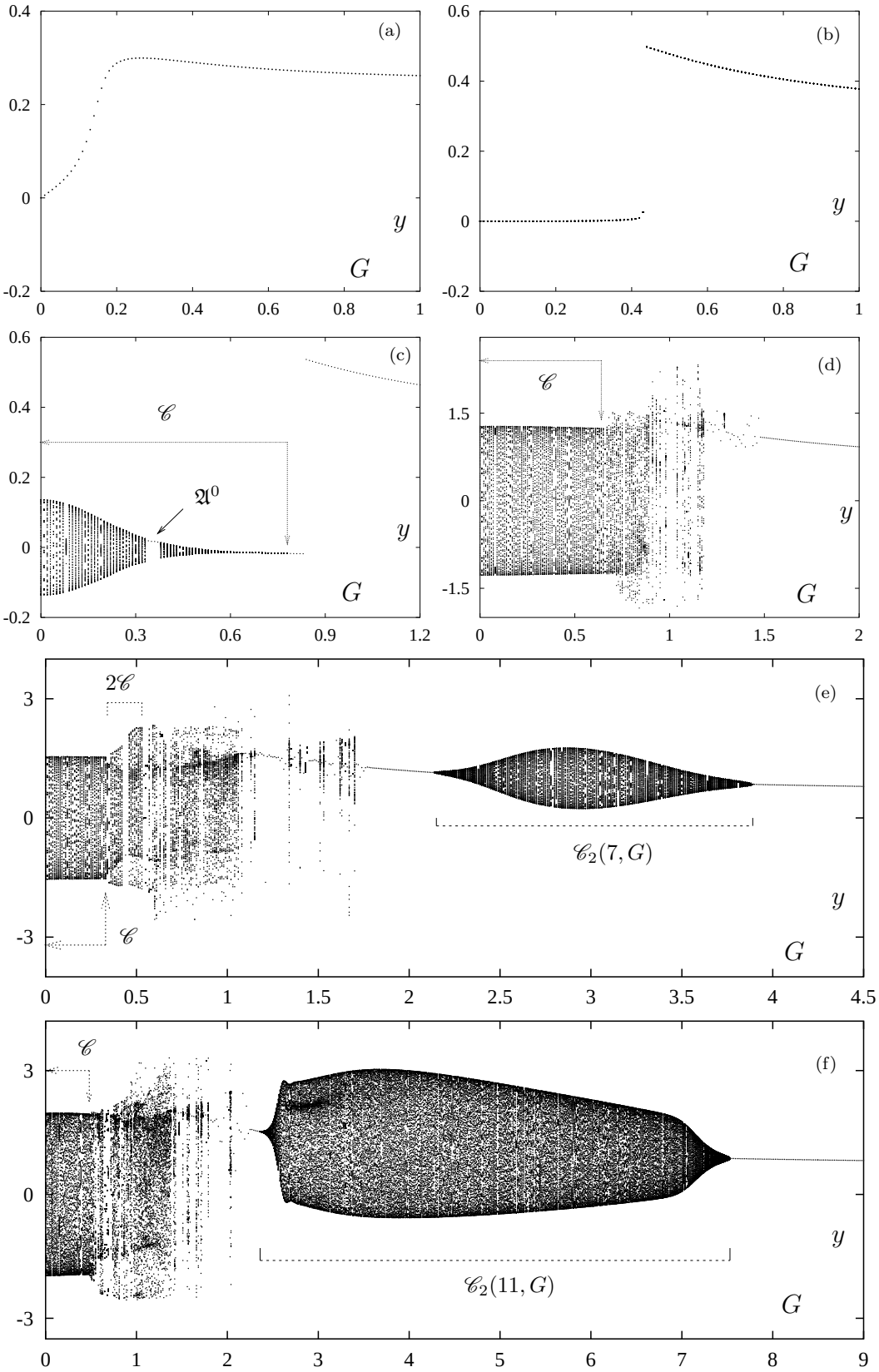

Figure 2.1: Projections on y of sequences of P-attractors as a function of G, for $\varepsilon = 0.5$. In each picture F is fixed: (a) $F = 0.2$ (b) $F = 0.7$ (c) $F = 1.2$ (d) $F = 5$ (e) $F = 7$ (f) $F = 11$. The last 100 points of each iteration loop are plotted, see text.

Can we characterise the transitions in terms of bifurcations? Which bifurcations lead to strange attractors? What are the dynamical properties of these strange attractors and the implications for the (un)predictability of the driven model? This Chapter is intended to provide a coherent inventory of the phenomenology and to give answers, whenever possible, to the above questions.

2.1.3 Setting of the problem and sketch of results

A first sketch of the organisation of $\mathfrak{M}_{0.5}$ again is obtained by brute force iteration. In Figure 2.2 we plotted a black dot for all (F, G)-values such that a fixed or periodic point attractor occurs.[5] Therefore, white points correspond either to a quasi-periodic invariant circle or to a strange attractor. A grid with spacing 1/200 is fixed inside $\mathfrak{M}_{0.5}$. For all (F, G) on the grid, N iterations of the map P are computed, starting each time from the point $q = (x, y, z) = (1, 2, 3)$. The condition checked in the algorithm for a period k point is that the maximum of

$$\text{dist}\left(P^n(q), P^{n-k}(q)\right), \text{dist}\left(P^n(q), P^{n-2k}(q)\right), \text{dist}\left(P^n(q), P^{n-3k}(q)\right)$$

be less than 10^{-12}. Usually, N is set to 200, but for a few parameter values it was necessary to take up to $N = 10^5$ iterates to get convergence to an attractor.

It turns out that a fixed point $\mathscr{A}$ is the unique attractor for G large (see Sec. 2.2.2 for a proof). A circle attractor $\mathscr{C}_2$ exists in region $\mathfrak{Q}_2$. The cigar-like sequences of attractors $\mathscr{C}_2(7, G)$ and $\mathscr{C}_2(11, G)$ in Figure 2.1 (e) and (f) correspond to sections of $\mathfrak{Q}_2$ by a vertical line $F = 7$ and $F = 11$ respectively. The dashed lines in Figure 2.2 are Arnol′d tongues with zero rotation number. These tongues are rather narrow and open up only at the lower boundary of $\mathfrak{Q}_2$, at some small black spikes visible in Figure 2.2 (b) (see Sec. 2.4.1). Quasi-periodicity appears thus to be prevalent in $\mathfrak{Q}_2$, in the sense that it occurs with large relative measure in the parameter space (see *e.g.* [95]). A circle attractor $\mathscr{C}$ occurs for $F > 1$ and G smaller than a certain value $G_{\mathscr{C}}(F)$, compare again Figure 2.1 (c)-(f). We guess that $\mathscr{C}$ persists for all parameter values inside the strip $\mathfrak{Q}_1$ in Figure 2.2 (b), bounded above by the line $G = 0.28$. As G increases, $\mathscr{C}$ may undergo different fates, depending on the value of F. For $1.25 \lessdot F \lessdot 1.7$, $\mathscr{C}$ crosses a period one Arnol′d tongue $\mathfrak{A}^0$ (compare Figure 2.2 (b)) and then breaks up (Sec. 2.4.8). Indeed, a chaotic range $\mathfrak{L}_1$ occurs just above $\mathfrak{A}^0$ (Figure 2.5). Several windows of periodicity occur and outside them, strange attractors occur like in Figure 2.6 (B).

For $F \gtrsim 5$ there is a different, wide region inside $\mathfrak{M}_{0.5}$ where strange attractors are found. In Figure 2.2 (b) one can see that this chaotic range becomes wider as F increases and is roughly divided into two parts, labelled by $\mathfrak{U}$ and $\mathfrak{L}_2$. In the latter, strange attractors are prevalent: periodic points occur only in small windows. Inside $\mathfrak{U}$, fixed point attractors seem to be prevalent, (compare the large wave-like black regions in Figure 2.2 (b)) and strange attractors now and then appear (also see Figure 2.12). Region $\mathfrak{Q}_2$ is separated from $\mathfrak{U}$ by a thin solid black strip where a unique fixed point attractor is detected.

Most of the above transitions of the attractors are explained in terms of bifurcation theory (see [38, 56, 78, 99] for a general presentation). The simplest bifurcation of $P_{F,G}$ is the loss of stability of a fixed point when one of the eigenvalues of $DP_{F,G}$

[5] To simplify the picture, no dots are plotted above the straight line $G = 3/4\,F$.

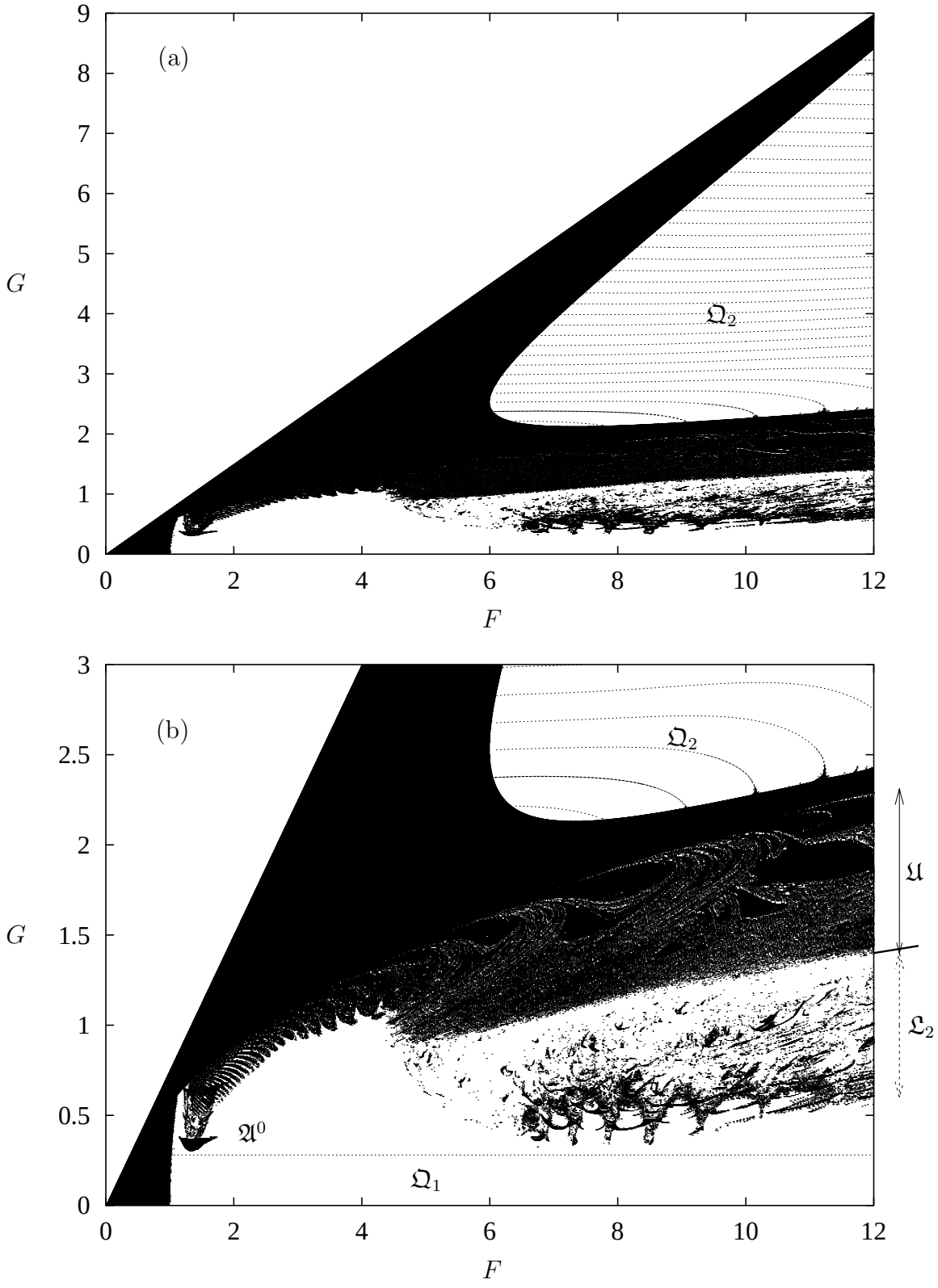

Figure 2.2: (a) Points in the parameter plane $\mathfrak{M}_{0.5}$ with a fixed or periodic point attractor are indicated by a black dot. (b) Magnification of part of Figure 2.2 (a). The dashed line $G = 0.28$ bounds strip $\mathfrak{Q}_1$. Two chaotic ranges $\mathfrak{L}_2$ and $\mathfrak{U}$ are labelled at the margin of Figure 2.2 (b), see text for explanation.

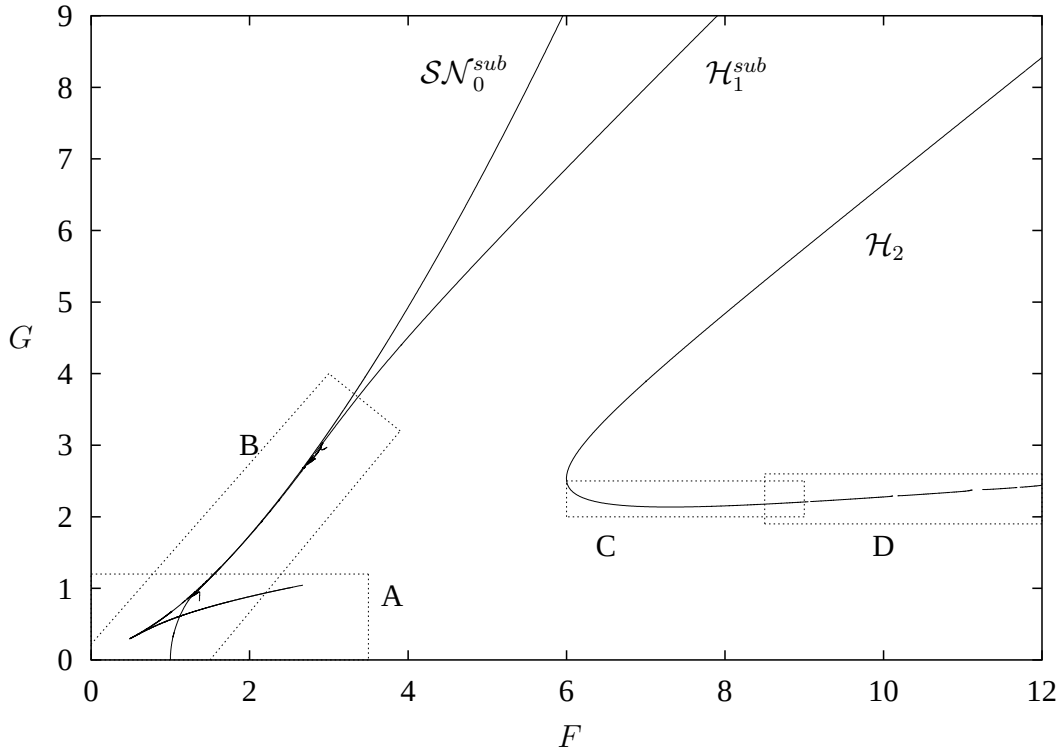

Figure 2.3: Bifurcation diagram of fixed points of the map $P_{F,G}$ for $\varepsilon = 0.5$. Boxes labelled by A, B, C, D are enlarged respectively in Figure 2.5 (left), Figure 2.18, Figure 2.22 (a) and (b).

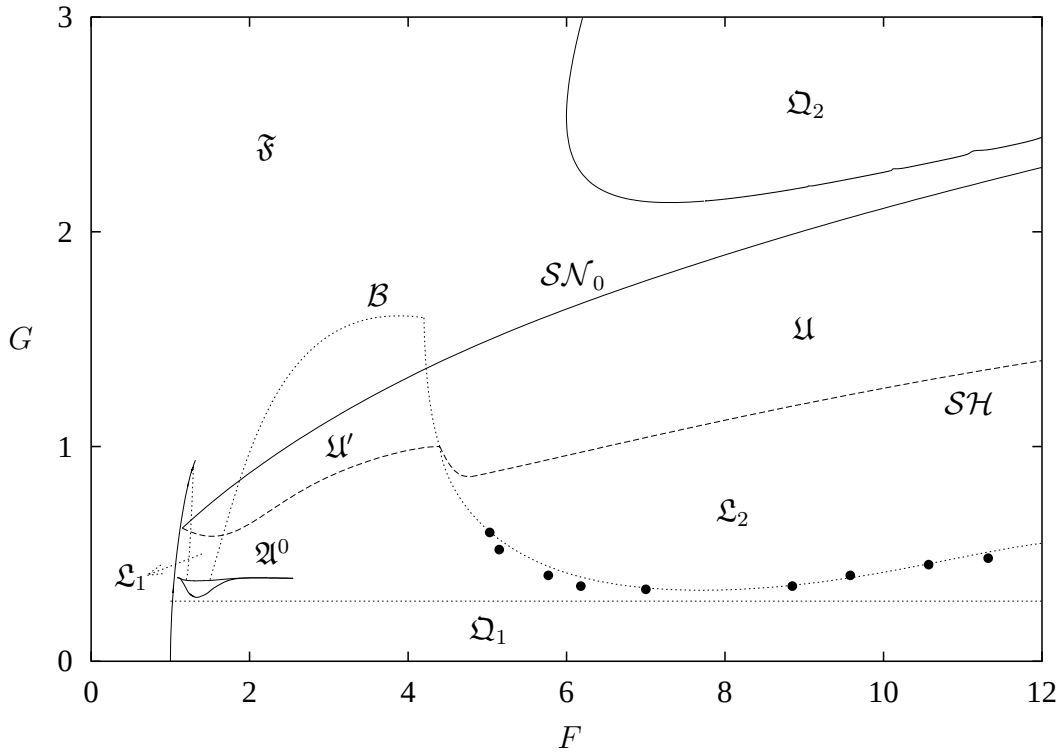

Figure 2.4: Sketch of the regions with same kind of dynamics in the window $[0, 12] \times [0, 3]$ in the parameter plane $\mathfrak{M}_{0.5}$. Thick dots indicate the occurrence of a quasi-periodic period doubling, where a doubled circle attractor $2\mathscr{C}$ appears (see Sec. 2.4.9).

crosses the unit circle. To this group belong the saddle-node, period doubling and the Hopf bifurcation [41, 89], all of which are found in the family $P_{F,G}$. A framework of bifurcation curves of fixed points is shown in Figure 2.3 and Figure 2.5 (left). Saddle-node bifurcations occur on the curves $\mathcal{SN}_0$, $\mathcal{SN}_0^{sub}$ and $\mathcal{SN}_1$. The two branches $\mathcal{SN}_0$ and $\mathcal{SN}_1$ of supercritical saddle-node bifurcations meet tangentially at a cusp $\mathcal{C}$. The Arnol′d tongue $\mathfrak{A}^0$ is bounded by two curves of supercritical saddle-node bifurcations.

Supercritical Hopf bifurcations of fixed points[6] occur on curves $\mathcal{H}_1$, $\mathcal{H}_1^{sub}$ and $\mathcal{H}_2$. The attracting invariant circle $\mathscr{C}$ is born from the attracting fixed point $\mathscr{A}$ as (F, G) cross $\mathcal{H}_1$ from left to right. This explains the change from the fixed point $\mathscr{A}$ in Figure 2.1 (b) to the circle $\mathscr{C}$ in Figure 2.1 (c). So the curve $\mathcal{H}_1$ is the boundary at the left of strip $\mathfrak{Q}_1$ in Figure 2.2 (b). Similarly, the circle attractor $\mathscr{C}_2$ is born from the attracting fixed point $\mathscr{A}$ for (F, G) crossing $\mathcal{H}_2$ and entering region $\mathfrak{Q}_2$.

Remark 2.2. To see the quadratic behaviour in the evolution of the radius of the invariant circles near the Hopf bifurcations, a much smaller scale is required in the parameter. See Remark 2.9 in Sec. 2.4.2 for examples.

A good part of the phenomena in Figures 2.1 and 2.2 can be explained by the previous results. This yields a subdivision of the parameter plane in regions with the same dynamics, Figure 2.4. There we also sketch the four chaotic ranges $\mathfrak{L}_1$, $\mathfrak{L}_2$, $\mathfrak{U}$, $\mathfrak{U}'$ (see below). The dashed curves $\mathcal{B}$ and $\mathcal{SH}$, as well as the boundary of $\mathfrak{L}_1$, are not bifurcation curves of $P_{F,G}$. $\mathcal{B}$ roughly indicates the breakdown of the circle $\mathscr{C}$ and $\mathcal{SH}$ denotes the boundary between $\mathfrak{L}_2$ and $\mathfrak{U}$. For details, see Secs. 2.4 and 2.5.

One of the main points of interest is the relation between the dynamics of systems (2.1) and (2.2). This is at first analysed as a perturbation problem from $\varepsilon = 0$ (see Sec. 2.3). Assuming that both the perturbative *Ansatz* [5, 56] and genericity [99] hold, bifurcations of the autonomous system persist inside $\mathfrak{M}_\varepsilon$, at least for ε sufficiently small. It turns out that the bifurcations sketched in Figure 2.3 for $\varepsilon = 0.5$ are indeed 'inherited' from the autonomous system $\varepsilon = 0$. Moreover, other bifurcations are found to persist for $\varepsilon = 0.01$ (Secs. 2.3.2 and 15). An important case is a codimension two Hopf-saddle-node bifurcation of a fixed point, which is an organising centre of the bifurcation diagram of the autonomous case [102].

However, in spite of all similarities, even for ε positive and small the planes $\mathfrak{M}_\varepsilon$ and $\mathfrak{M}_0$ present a number of differences. Arnol′d resonance tongues [6, 4, 23], attached to curves of Hopf bifurcations, appear in $\mathfrak{M}_\varepsilon$ (this is the case of $\mathfrak{A}^0$, Figure 2.5). Homoclinic connections[7] of the flow of system (2.1) generically are broken and replaced by homoclinic intersections and bifurcations for the map P (see Sec. 2.3.2). In this sense, $\varepsilon = 0$ already is a bifurcation value.[8] Apart from this, codimension three bifurcations may occur in the parameter space $\mathfrak{M}$, changing the global organisation of $\mathfrak{M}_\varepsilon$. Indeed, a codimension three bifurcation causes the disappearance of the Hopf-saddle-node point at ε smaller than 0.5. These differences between $\mathfrak{M}_{0.5}$ and $\mathfrak{M}_0$ are further discussed in Secs. 2.4 and 2.5.1.

[6] We recall that a Hopf bifurcation [41] of a fixed point of P corresponds to a Neĭmark–Sacker [56, 78] bifurcation of a limit cycle of the flow of system (2.2).

[7] Also called saddle connections [56, 99].

[8] Of infinite codimension, in the sense that adding time dependence can require infinitely many parameters for the unfolding.

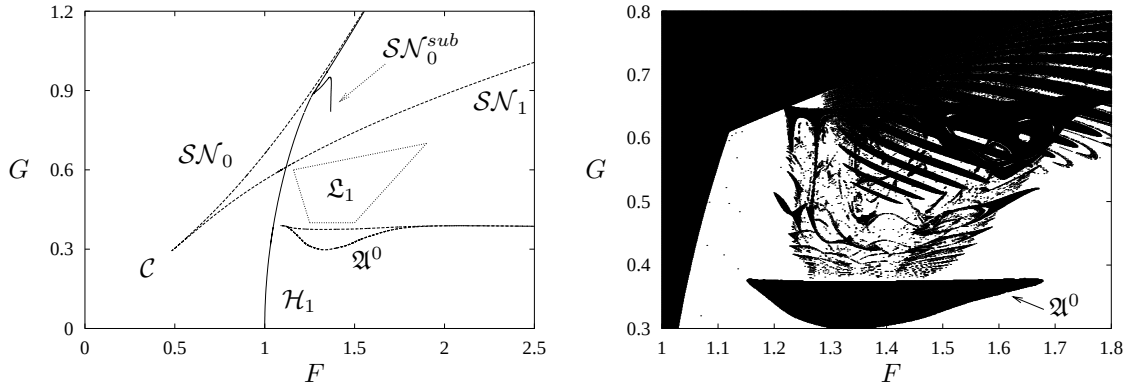

Figure 2.5: Left: magnification of box A in Figure 2.3. The cusp $\mathcal{C}$ terminates two curves of saddle-node bifurcations. Right: magnification of a part of Figure 2.2. The grid on the right figure is 10^{-3} in both F and G.

It is of special interest to determine which routes lead from simple to complicated dynamical behaviour, both for ε fixed or not. Two scenario's for the birth of strange attractors are theoretically understood: cascades of period doubling bifurcations [23, 41, 45, 99] and homoclinic tangency bifurcations [23, 95, 99]. The former is a gradual process where the complexity of the attractor increases stepwise as the parameter varies. Well-known model maps displaying strange attractors originating from cascades of period doubling are the logistic map [41, 45] and the Hénon map [11, 104]. On the other hand, homoclinic bifurcations may lead to a strange attractor *at once*. Unfoldings of homoclinic tangencies for one-parameter families of diffeomorphisms generically yield a large variety of dynamical phenomena. Hénon-like strange attractors or repellors occur with positive Lebesgue measure in the parameter space [42, 86, 120] (we recall that Hénon-like strange attractors coincide with the closure of the unstable manifold of some hyperbolic saddle point and their dimension is usually not much larger than one). Close to a homoclinic tangency, cascades of homoclinic tangencies accumulate, as well as cascades of period doubling bifurcations of periodic attractors [125]. Infinitely many periodic attractors can coexist close to a diffeomorphism with a homoclinic tangency. This is known as the Newhouse phenomenon [87, 96].

Several other phenomena are found close to homoclinic tangencies in concrete models. Cascades of cusps and accumulation of Arnol′d tongues on curves of homoclinic bifurcations have been reported in [23]. There it was conjectured that accumulation of Arnol′d tongues might be a mechanism for the creation of infinitely many sinks in the Newhouse phenomenon.

The basic dynamical property of a strange attractor is sensitive dependence with respect to initial conditions. Computation of the spectrum of the Lyapunov exponents [12] is one of the standard ways to detect chaotic behaviour, since a positive Lyapunov exponent implies sensitivity with respect to initial conditions [44, 99, 104, 109]. Moreover, knowledge of the Lyapunov spectrum of an attractor allows to compute its Lyapunov dimension [52, 67], considered to be an upper bound of the Hausdorff dimension under general assumptions. In what follows, the Lyapunov exponents are

denoted by λ_1, λ_2 and λ_3, with $\lambda_1 \geq \lambda_2 \geq \lambda_3$. The Lyapunov dimension is defined by

$$\mathrm{D_L} = k + \frac{\sum_{j=1}^{k} \lambda_j}{|\lambda_{k+1}|},$$

where k is the unique index such that $\sum_{j=1}^{k} \lambda_j \geq 0$ and $\sum_{j=1}^{k+1} \lambda_j < 0$. Another indicator of the dynamics is the power spectrum [30, 98]. In all power spectra we plot the square of the moduli of the Fourier coefficients against the frequency, where the latter is limited to the interval $[0, 1/2]$ (see Sec. 2.C for details).

The numerical results in Sec. 2.4 suggest that the strange attractors in the family $P_{F,G,\varepsilon}$ usually appear due to homoclinic tangencies. Period doubling cascades are sometimes observed and, in fact, the two scenario's are not independent, see *e.g.* [95, 104]. Strange attractors were found in the four regions $\mathfrak{L}_1$, $\mathfrak{L}_2$, $\mathfrak{U}$ and $\mathfrak{U}'$ in Figure 2.4. The birth of strange attractors in $\mathfrak{L}_k$ is caused by different phenomena than in $\mathfrak{U}$ and $\mathfrak{U}'$.

The strange attractor $\mathscr{L}_1$ in Figure 2.6 (B) occurs in $\mathfrak{L}_1$, right after the breakdown of an invariant circle.[9] For nearby parameter values, a period five attractor is found (Figure 2.7 (A)), inside an Arnol′d tongue $\mathfrak{A}^{1/5}$. The highest peak in its power spectrum (Figure 2.7 (a)) occurs—as it should—at frequency $f_1 = 0.2$, with one harmonic at $f_2 = 2f_1$. Note that the power spectrum of $\mathscr{L}_1$ (Figure 2.7 (b)) still has dominant frequency components at $\tilde{f}_1 = 0.1939$ and $\tilde{f}_2 = 0.3878 \simeq 2\tilde{f}_1$, respectively close to f_1 and f_2. This persistence of the peaks is due to intermittency of type I [97]. Indeed, a large number of iterates tends to stay close to the five regions inside $\mathscr{L}_1$ where the periodic attractor has just disappeared through a saddle-node bifurcation. The attractor $\mathscr{L}_1$ appears as a consequence of the destruction of the circle $\mathscr{C}$, caused by a homoclinic tangency inside $\mathfrak{A}^{1/5}$ (for more details on this route, see Sec. 2.4.7). As a result, $\mathscr{L}_1$ has the properties of a folded circle: its dimension is close to one ($\mathrm{D_L}(\mathscr{L}_1) \simeq 1.056$), its folded geometric structure is illustrated in Figure 2.8 (a).

Quasi-periodic bifurcations (Sec. 15) play an important role in the birth of strange attractors and repellors of dimension higher than two (Secs. 21 and 2.5.1). Attractors such as $4\mathscr{C}$ in Figure 2.7 (A) are created by two consecutive quasi-periodic period doublings, compare Sec. 2.4.9. The attractor $4\mathscr{C}$ is the union of two curves, each invariant under P^2. We call this type of invariant set a period two invariant curve, also see Secs. 2.4.9 and 2.5.1. For nearby parameter values, the strange attractor $\mathscr{Q}_1$ in Figure 2.7 (B) is found.[10]

However, a whole quasi-periodic period doubling cascade does not occur, since $4\mathscr{C}$ is destroyed by a homoclinic tangency inside an Arnol′d tongue (see Sec. 21). The fact that $\lambda_2 \simeq 0$ (Table 2.1) suggests that the dynamics on $\mathscr{Q}_1$ still preserves a quasi-periodic component, inherited from $4\mathscr{C}$. The power spectra of the two attractors, displayed in Figure 2.7 (a), (b), confirm this idea. The period two curve $4\mathscr{C}$ has two fundamental frequencies, one of which is of course 0.5. The other frequency $g_1 = 0.32839$ (labelled by 1 in Figure 2.7 (a)) is given by $j/2$, where j is the frequency of P^2 on any of the two invariant curves. All harmonics $g_k = kg_1$ up to order 35 are identified by crosses on the corresponding peak in Figure 2.7 (a). The remaining peaks occur on frequencies $h_k = 0.5 - g_k$, which are integer combinations of 0.5 and

[9] The notation $\mathscr{L}$ stands for large, see Sec. 2.4.11.

[10] The notation $\mathscr{Q}$ stands for quasi-periodic Hénon-like, see Sec. 21

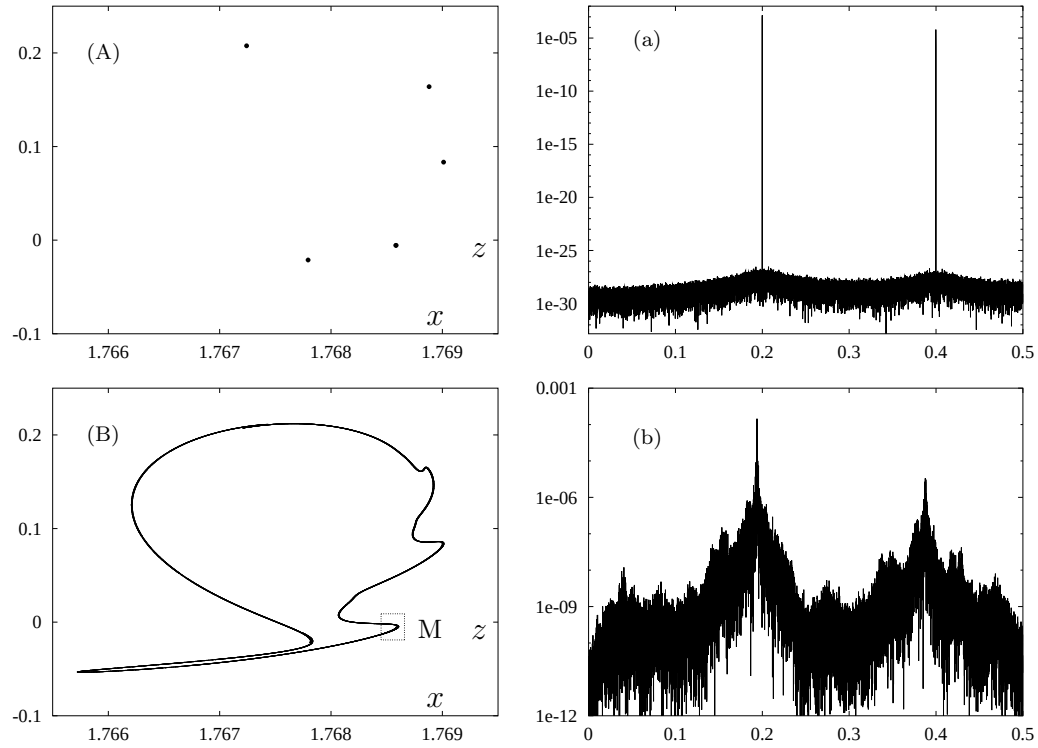

Figure 2.6: (A) Projection on (x, z) of a period five attractor of P, for $G = 0.4107$ and $F = 1.25$. (B) Same as (A) for the strange attractor $\mathscr{L}_1$, with $G = 0.4106$ (box M is magnified in Figure 2.8 left). (a), (b) Power spectra for (A), resp. (B).

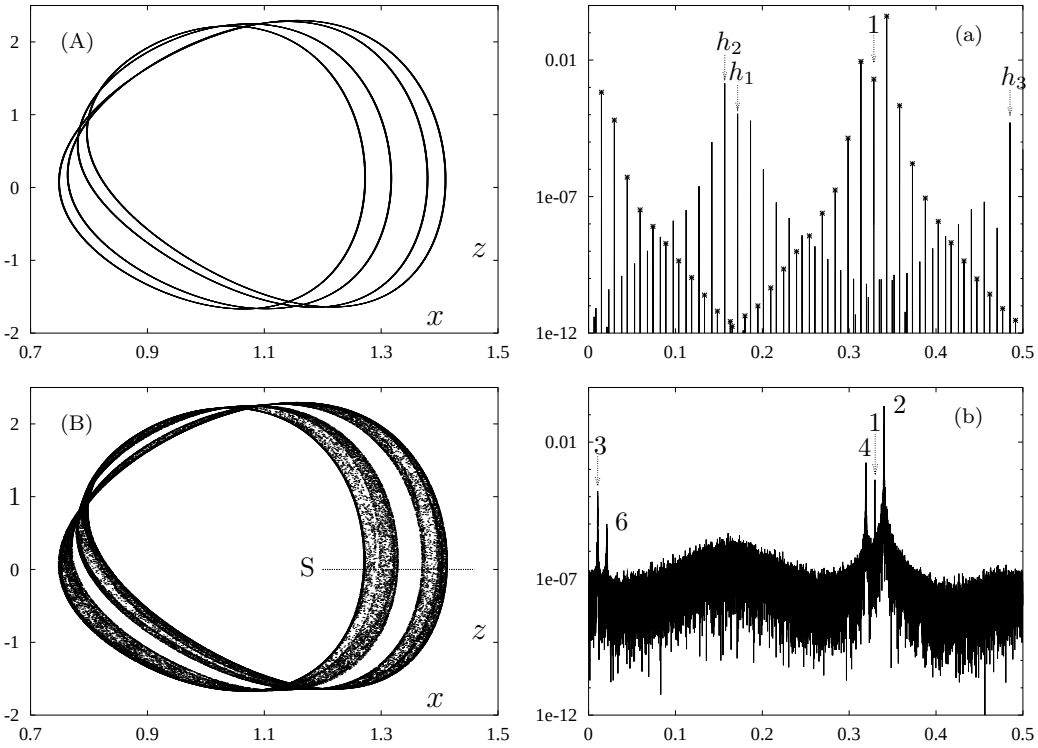

Figure 2.7: (A) Projection on (x, z) of the P-attractor $4\mathscr{C}$, occurring at $(F, G) = (11, 0.4969)$. (B) Same as (A) for the strange attractor $\mathscr{Q}_1$, with $G = 0.4972$. The section S is enlarged in Figure 2.8 right. (a), (b) Power spectra for (A) resp. (B).

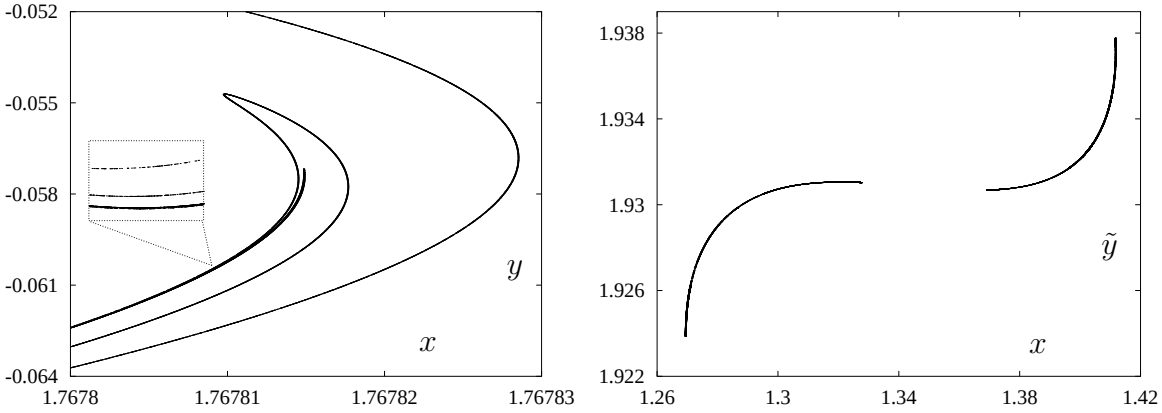

Figure 2.8: Left: magnification of box M in Figure 2.6 (B), projection on (x, y). A further magnification shows that the vertical line $x = 1.7678$ crosses the attractor in at least 5 layers. A new magnification (not displayed) reveals at least 9 layers. To go beyond that value requires higher accuracy in the integration. Right: a section of $\mathscr{Q}_1$ contained in a layer of thickness 2×10^{-3} around the plane $z = 0$, projected on $(x, \tilde{y})$, where $\tilde{y} = y - 0.135 \times z$.

g_k (the unique such combinations in the interval $[0, 0.5]$). For reference, h_1, h_2, and h_3 are labelled in Figure 2.7 (a).

The first four and the sixth harmonic of g_1 (labelled in Figure 2.7 (b)) persist in the spectrum of $\mathscr{Q}_1$, but all other harmonics have turned into broad band. This persistence of the harmonics can be again explained in terms of intermittency. Power spectra like in Figure 2.6 (b) or Figure 2.7 (b) are of mixed type [30]: they contain marked peaks (atoms of the spectral density) but also have a broad band component (locally continuous density).

The attractor $\mathscr{Q}_1$ is essentially three-dimensional, contained inside a 'fattened' Möbius strip. In reality, the fattening is rather thin, due to the size of the negative Lyapunov exponent λ_3 (Table 2.1). Indeed, this causes strong contraction in the normal direction and, therefore, the Lyapunov dimension is too close to 2. This is illustrated in Figure 2.8 right, where we plotted a section S of $\mathscr{Q}_1$ obtained by cutting it with a layer of thickness 2×10^{-3}, centred around the plane $z = 0$. For a better visualisation of the thinness in the normal direction, S is 'rotated' by using transformed coordinates. This projection is less than 2.5×10^{-6} wide in $\tilde{y}$, so that a Hénon-like structure in the normal direction cannot be distinguished. Values of x are limited in $(1.1, 1.5)$, corresponding to segment S in Figure 2.7 (B). We had to compute 10^8 iterates to achieve the 13005 points inside S plotted in the picture.

The above scenarios are quite common for the family $P_{F,G,0.5}$, close to the break-

	D_L	λ_1	λ_2	λ_3	e_1	e_2	e_3
A	1	1.1e-5	-0.18	-14.5	1.e-6	1.e-4	1.e-4
B	2.016	0.24	2.6.e-4	-14.9	1.e-4	1.e-4	2.e-4

Table 2.1: Lyapunov dimension and exponents of $4\mathscr{C}$ (A) and of the strange attractor $\mathscr{Q}_1$ (B) in Figure 2.7. The e_i's are estimates for the error in λ_i (see Sec. 2.B).

down of an invariant circle in $\mathfrak{L}_1$ or $\mathfrak{L}_2$. However, intermittency disappears as the parameters are shifted deeper inside $\mathfrak{L}_k$. The Lyapunov dimension increases, as well as the total power contained in the broad band component of the power spectra (Secs. 2.4.8 and 2.4.9).

strange attractors of a different type occur in $\mathfrak{U}$ (Figure 2.9 (A) and 2.10 (A)). The geometrical and dynamical structure of broken invariant circles is no longer present: the power spectra look like white noise, indicating that the iterates of P are uncorrelated (see Remark 2.12 in Sec. 2.C). We call these attractors 'Shil′nikov-like' because their shape is similar to that of Shil′nikov repellors found in the autonomous Lorenz-84 system $\varepsilon = 0$. In [102], the presence of such repellors was put in relationship with the occurrence of two curves of Shil′nikov bifurcations [56, 78], corresponding to homoclinic loops of a saddle-focus equilibrium. For nearby parameter values, limit cycles like in Figure 2.11 were detected. Because of oscillations followed by long excursions, such limit cycles are called spiral attractors [102]. In the driven Lorenz-84, spiral limit cycles occur for most parameter values in $\mathfrak{U}$ and $\mathfrak{U}'$. Only narrow Hénon-like attractors seem to occur in $\mathfrak{U}'$ (see Figure 2.38 (a) and 2.51 (a)). Similar attractors are found also in $\mathfrak{U}$.

The differences between $\mathfrak{U}$ and $\mathfrak{L}_2$ are illustrated by means of the Lyapunov dimension. In Figure 2.12 (a) we plotted a magnification of Figure 2.1(e). On the left of the picture, the circle $\mathscr{C}$ occurs: the Lyapunov dimension (Figure 2.12 (b)) is one, since the maximal Lyapunov exponent is zero. After crossing an Arnol′d tongue $\mathfrak{A}_0$ of rotation number zero, $\mathscr{C}$ locks again to a periodic point on a small interval and then breaks down. The Lyapunov dimension grows almost immediately up to ~ 2.1. Except for a few narrow Arnol′d tongues (where the dimension drops to zero), strange attractors are prevalent in the chaotic range $\mathfrak{L}_2$. Then, at $G \simeq 1.08$, some bifurcation occurs,[11] after which the evolution of the attractors changes significantly. For most parameter values in $\mathfrak{U}$ an attracting fixed point is found (in the intervals of zero Lyapunov dimension in Figure 2.12 (d))). The corresponding T-periodic limit cycles of system (2.2) are of spiral type. Shil′nikov–like strange attractors as in Figure 2.10 (A) occur for a few parameter values, singled out by the peaks in the Lyapunov dimension (Figure 2.12 (d)) and by some fuzzy vertical lines in Figure 2.12 (a). Further discussion on the classification of the strange attractors of P for $\varepsilon = 0.5$ is given in Sec. 2.4.11.

We now list some more points of interest of the family $P_{F,G,\varepsilon}$. Since the autonomous system (for $\varepsilon = 0$) exhibits Shil′nikov bifurcations, we may well expect three-dimensional homoclinic tangencies of a saddle-focus fixed point of a diffeomorphism. For analogy with the autonomous case, we shall call this multidimensional homoclinic bifurcation 'Shil′nikov tangency bifurcation' (Sec. 2.3.2).

A large variety of strange attractors can be found for $P_{F,G,\varepsilon}$ Some of these are essentially three-dimensional[12] and have dimension d with $2 < d \leq 3$. The theory for this class of attractors has not yet completely been developed: only partial results have been proven so far, see *e.g.* [113, 121]. Also the Newhouse–Ruelle–Takens scenario [89, 100] may occur, since for small ε the map $P_{F,G,\varepsilon}$ has a repelling invariant two-torus $\mathscr{T}$ inherited from the autonomous system (Sec. 15).

[11] This happens on the 'curve' labelled by $\mathcal{SH}$ in Figure 2.4

[12] By this we mean that they are not a suspension of a two-dimensional attractor.

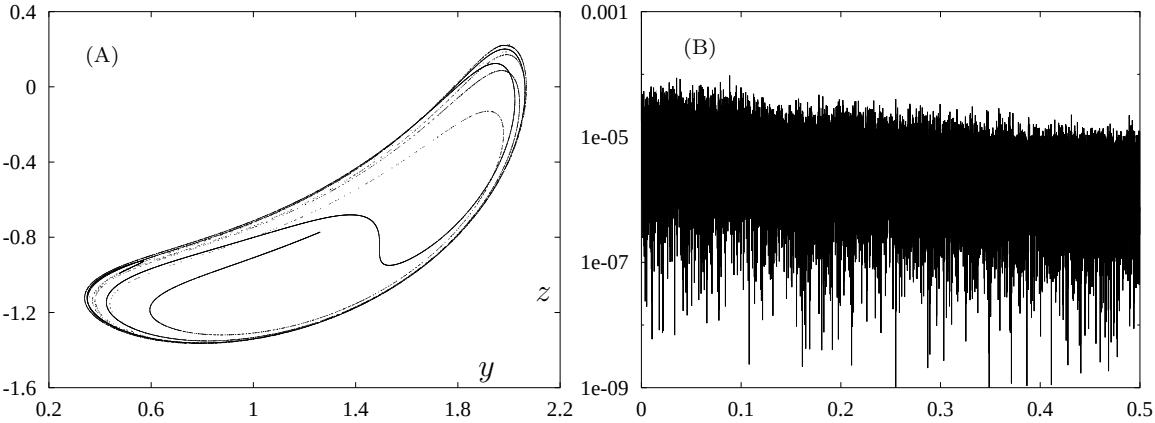

Figure 2.9: (A) Projection on (y, z) of the Shil′nikov-like strange P-attractor $\mathscr{S}_1$, occurring at $(F, G) = (7, 1.7545)$. (B) Power spectrum of $\mathscr{S}_1$.

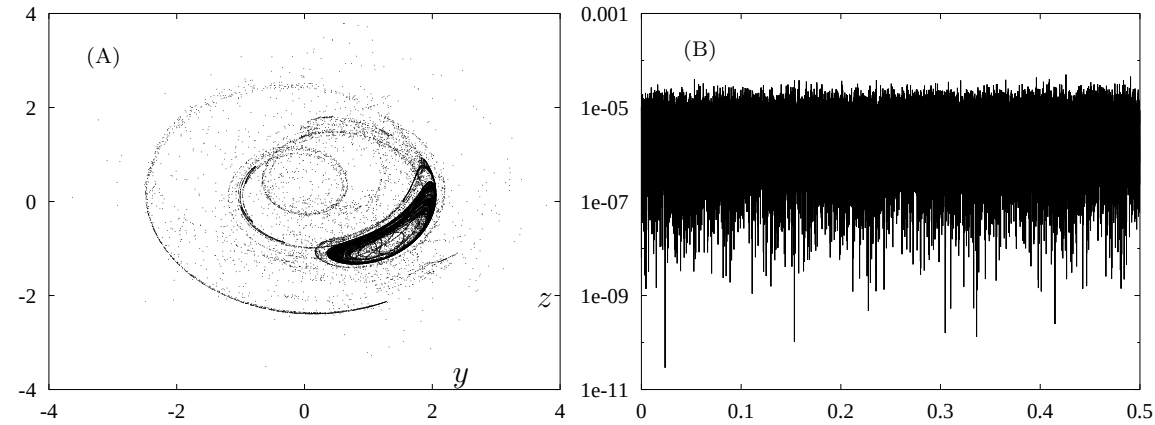

Figure 2.10: (A) Projection on (y, z) of the Shil′nikov-like strange P-attractor $\mathscr{S}_2$, occurring at $(F, G) = (7, 1.7)$. (B) Power spectrum of $\mathscr{S}_2$.

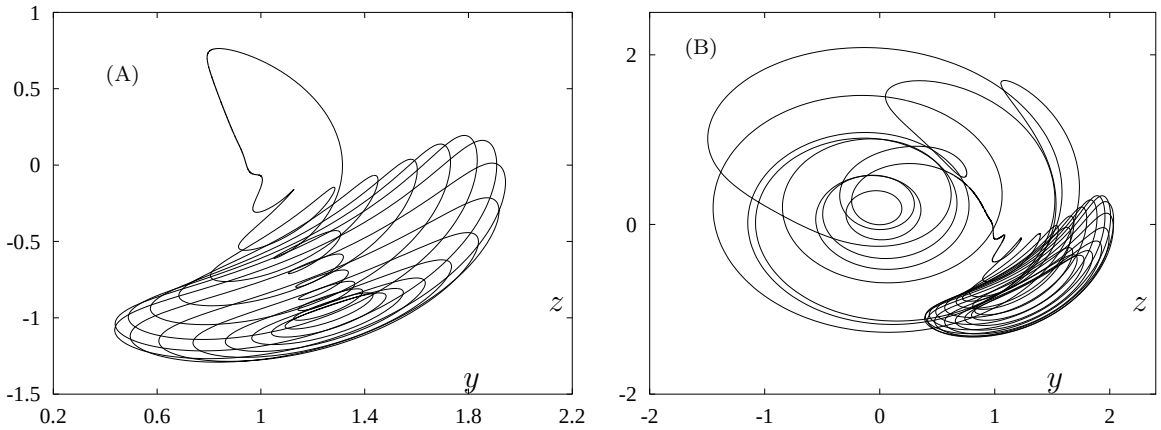

Figure 2.11: (A) Projection on (y, z) of 'spiral' limit cycle of (2.2), occurring at $(F, G) = (7, 1.75466)$. (B) Same as (A) for $G = 1.7015$.

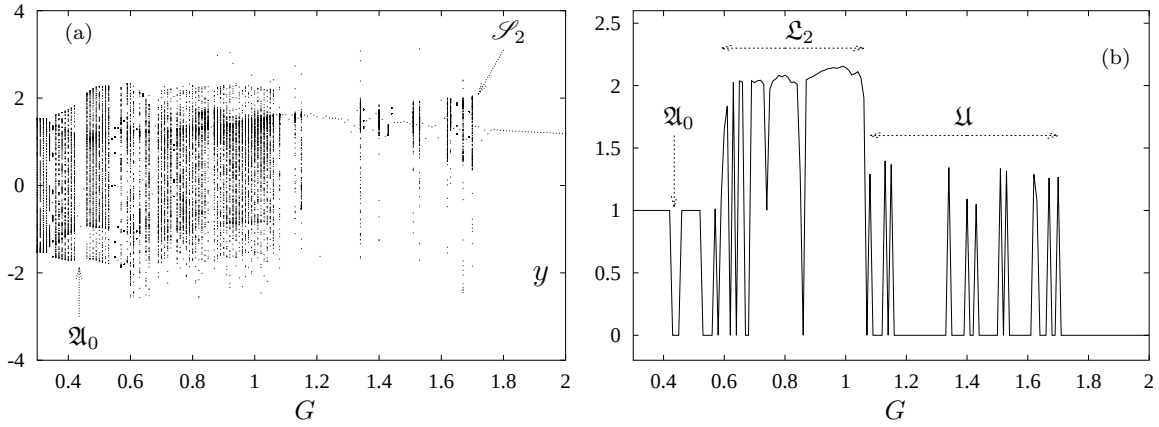

Figure 2.12: (a) Projection on y of sequences of P-attractors as a function of G for $F = 7$ fixed. The step in G is 0.01. An Arnol′d tongue $\mathfrak{A}_0$ of rotation number 0 is pointed by an arrow. The attractor pointed by an arrow is plotted in Figure 2.10 (A). (b) Lyapunov dimension of the attractors in (a).

As we have seen, the driven Lorenz-84 model displays a rich dynamics, with various bifurcations of the attractors. The chaotic ranges in the parameter plane are wide. It is a challenge to understand the corresponding bifurcation patterns of this model. The present Chapter aims at giving a rough inventory of the dynamics and an analysis of some of the bifurcations at hand.

2.2 Analytical results on the Poincaré map

In this section, we prove the following properties of the family $P_{F,G,\varepsilon}$.

1. For all F, G, ε the map $P_{F,G,\varepsilon}$ has an attractor (Sec. 2.2.1).
2. For G large, $P_{F,G,\varepsilon}$ has a unique attracting fixed point $\mathscr{A}$ (Sec. 2.2.2).
3. For $G = 0$ $P_{F,G,\varepsilon}$ has a unique fixed point, which is attracting for $F \leq 1$ and undergoes a supercritical Hopf bifurcation at $F = 1$.

The results are formulated in terms of the following system

$$\begin{aligned} \dot{x} &= -ax - y^2 - z^2 + aFf(t), \\ \dot{y} &= -y + xy - bxz + Gg(t), \\ \dot{z} &= -z + bxy + xz, \end{aligned} \tag{2.3}$$

with T-periodic continuous functions $f, g : \mathbb{R} \to \mathbb{R}$. System (2.2) is a particular case of (2.3), where $f(t) = g(t) = 1 + \varepsilon\cos(\omega t)$. At the end of each section, we describe the implications for the map $P_{F,G,\varepsilon}$.

2.2.1 Existence of attractors

For the autonomous Lorenz-84, there exists a bounded set in the phase space $\mathbb{R}^3 = \{x, y, z\}$, depending on the parameters F, G, which attracts all trajectories [81]. A similar property holds for system (2.3). Let $\|f\|_\infty \stackrel{\text{def}}{=} \sup_{t\in\mathbb{R}} |f(t)|$.

Proposition 2.1. *For $a > 0$ and every b, F, G, there exists a sphere $\mathscr{S} \subset \mathbb{R}^3$ centred at $(x, y, z) = (0, 0, 0)$ with radius r_0 depending on a, F, G, $\|f\|_\infty$, $\|g\|_\infty$, such that all integral curves of equation (2.3) ultimately penetrate $\mathscr{S}$ and then remain inside.*

Proof. We denote the Euclidean norm on $\mathbb{R}^2$ or $\mathbb{R}^3$ by $\|\ \|$. Consider a solution $(x, y, z)(t)$ of equation (2.3) and define $R(t) = \|(x, y, z)\|$. Using (2.3), we have

$$\frac{1}{2}\frac{d}{dt}(R^2) = -ax^2 - y^2 - z^2 + xaFf(t) + yGg(t) \leq$$
$$\leq -\tilde{a}R^2 + R\sqrt{a^2F^2\|f\|_\infty^2 + G^2\|g\|_\infty^2},$$

where $\tilde{a} \stackrel{\text{def}}{=} \min\{a, 1\}$. We have used the Schwartz inequality: $xaFf(t) + yGg(t) = \big(aFf(t), Gg(t)\big) \cdot (x, y) \leq \big\|\big(aFf(t), Gg(t)\big)\big\|\,\|(x, y)\|$. For R sufficiently large, namely

$$R > \tilde{a}^{-1}\sqrt{a^2F^2\|f\|_\infty^2 + G^2\|g\|_\infty^2} \stackrel{\text{def}}{=} r_0,$$

the function $R(t)$ is decreasing. Notice that it is sufficient to require that $f(t)$ and $g(t)$ be bounded on $\mathbb{R}$. □

Since $f(t) = g(t) = 1 + \varepsilon\cos(\omega t)$ and $a < 1$ in system (2.2), the radius of the attracting sphere $\mathscr{S}$ for the map $P_{F,G,\varepsilon}$ is $r_0 = (1 + \varepsilon)\sqrt{F^2 + G^2/a^2}$.

2.2.2 Occurrence of a unique fixed point attractor for large G

Proposition 2.2. *For all $a > 0$ and every b, F there exists a G_0 such that for all $G > G_0$, system (2.3) has a unique attracting periodic solution p^G.*

Proof. We scale the variables x, y, z of (2.3) as follows:

$$u = \delta^2 x, \quad v = \delta y, \quad w = \delta z, \qquad \text{with} \quad \delta = G^{-1/3},$$

so obtaining

$$\begin{aligned} \dot{u} &= -au - v^2 - w^2 + aF\delta^2 f(t), \\ \delta^2\dot{v} &= -\delta^2 v + uv - buw + g(t), \\ \delta^2\dot{w} &= -\delta^2 w + buv + uw. \end{aligned} \tag{2.4}$$

As G tends to infinity, δ approaches zero and (2.4) becomes a singularly perturbed system. For $\delta = 0$ we obtain the degenerate system

$$\dot{u} = -au - v^2 - w^2, \qquad u(v - bw) + g(t) = 0, \qquad u(bv + w) = 0.$$

The latter two equations yield

$$w = -bv, \qquad v = -\frac{g(t)}{(1 + b^2)u}. \tag{2.5}$$

Substituting (2.5) in (2.4), we get the one-dimensional equation

$$\dot{u} = -au - \frac{g^2(t)}{(1 + b^2)u^2}. \tag{2.6}$$

With the change of variables $p = u^3$, we obtain the linear differential equation

$$\frac{1}{3}\dot{p} = -ap - \frac{g^2(t)}{1+b^2}. \tag{2.7}$$

The solution of the Cauchy problem given by (2.7) with initial condition p_0 is

$$p(t) = e^{-3at}\left(p_0 - \frac{3}{1+b^2}\int_0^t e^{3as}g^2(s)ds\right).$$

The initial condition $p_0 = 3(1+b^2)^{-1}(1-e^{3aT})^{-1}\int_0^T e^{3as}g^2(s)ds$ belongs to a T-periodic solution $p_T(t)$, asymptotically stable and negative for all t. Given a solution $p(t)$ with initial condition $p_1 \in \mathbb{R}$, we have indeed $p(t) - p_T(t) = e^{-3at}(p_1 - p_0)$ which tends to zero as $t \to +\infty$, since $a > 0$.

Thus for $\delta = 0$, system (2.4) has a globally attracting periodic solution $s^0(t) = (u_T, v_T, w_T)$, where $u_T = (p_T)^{1/3}$ and v_T, w_T are obtained from u_T according to (2.5). We now prove that for δ small, that is, for G large, system (2.4) has a period T solution $s^\delta(t) = (u(t), v(t), w(t))$ such that $s^\delta(t) \to s^0(t)$ uniformly in $t \in [0, T]$ as $\delta \to 0$. The variational equation associated to (2.6) and to u_T is

$$\dot{V} = \left(-a + 2\frac{g^2(t)}{(1+b^2)u_T^3}\right)V, \qquad V(0) = 1, \qquad \text{where } V = \frac{\partial u_T}{\partial u_0}. \tag{2.8}$$

According to [47], it is sufficient to show that the unique T-periodic solution of (2.8) is identically zero. Since $p_T = u_T^3$ is solution of (2.7), we have

$$\frac{g^2(t)}{(1+b^2)u_T^3(t)} = \frac{g^2(t)}{(1+b^2)p_T(t)} = -a - \frac{1}{3}\frac{d}{dt}\log\left(p_T(t)\right).$$

Hence (2.8) becomes

$$\frac{d}{dt}\log\left(V(t)\right) = -3a - \frac{2}{3}\frac{d}{dt}\log\left(p_T(t)\right).$$

Therefore, the solution of (2.8) is

$$V(t) = e^{-3at}\left(\frac{p_T(t)}{p_0}\right)^{-2/3},$$

which tends to zero as $t \to +\infty$. In the original coordinates (x, y, z), s^δ corresponds to a unique attracting T-periodic solution p^G of (2.3), existing for G large. □

The occurrence of a unique attracting periodic orbit p^G was suggested by numerical experiments with system (2.2). In that case, p^G corresponds to the P-fixed point $\mathscr{A}$ occurring for G large (region $\mathfrak{F}$ in Figure 2.4).

2.2.3 Invariant circles for $G = 0$

Numerical experiments with the map $P_{F,G,\varepsilon}$ suggest that for $G = 0$, $F > 1$ and $0 \leq \varepsilon < 1$ (and possibly for a small range beyond $\varepsilon = 1$), the map has an invariant circle $\mathscr{C}$, born at $F = 1$ at a Hopf bifurcation of a fixed point. We here prove that for $G = 0$ and all F, the map $P_{F,\varepsilon} = P_{F,0,\varepsilon}$ has a fixed point undergoing a Hopf bifurcation at $F = 1$. Existence of the invariant circle for all $F > 1$ is proved for ε small.

We now consider the periodic orbits of system (2.3). Given a function $h : \mathbb{R} \to \mathbb{R}$, denote by $\overline{h}$ the average of h over the interval $[0, T]$, that is $\overline{h} \stackrel{\text{def}}{=} \frac{1}{T}\int_0^T h(s)ds$.

Proposition 2.3. *Suppose $\overline{f} \neq 0$. For $G = 0$ and for all F, system (2.3) has a unique T-periodic orbit $p^F(t)$, which is stable for $F \leq \overline{f}^{-1}$ and undergoes a Hopf bifurcation at $F = \overline{f}^{-1}$.*

Proof. For $G = 0$ system (2.3) has a symmetry and its dimension can be reduced. Indeed, the Cauchy problem given by (2.3) with initial condition (x_0, y_0, z_0) is equivalent to the reduced system

$$\begin{aligned} \dot{u} &= -au - r - a + aFf(t), & u(0) &= u_0, \\ \dot{r} &= 2ur, & r(0) &= r_0, \end{aligned} \tag{2.9}$$

where $r = y^2 + z^2$ and $u = x - 1$. The u-axis is invariant under the flow of (2.9). Putting $r = 0$, the first equation of (2.9) can be solved, giving

$$u(t) = e^{-at}\left(u_0 + 1 - e^{at} + aF\int_0^t e^{as}f(s)ds\right).$$

A unique periodic solution $u_T(t)$ exists, with initial condition

$$u_0 = \frac{1}{e^{aT} - 1}\left(1 - e^{aT} + aF\int_0^T e^{as}f(s)ds\right).$$

This implies that system (2.3) has a unique periodic solution $p^F(t) = (u_T(t) + 1, 0, 0)$ for $r_0 = 0$. We now prove that system (2.9) has no periodic solutions other than $p^F(t)$. Since we shall use the following fact again, we state it in a remark.

Remark 2.3. Consider a T-periodic solution $(u, r)(t)$ of (2.9). Then, either $r(t) = 0$ or $\overline{u} = 0$. Indeed, from the second equation in (2.9), one has

$$r(t) = r_0 \exp\left(2\int_0^t u(s)ds\right).$$

From $r(T) = r(0) = r_0$, it follows that either $r_0 = 0$, or $\int_0^T u(s)ds = 0$.

Continuing the proof, suppose that $(x, y, z)(t)$ is a T-periodic solution of (2.3) and take the corresponding solution $(u, r)(t)$ of (2.9). Averaging the first of the equations (2.9) over $[0, T]$ yields

$$\overline{u} = F\overline{f} - 1 - \overline{r}/a.$$

If $F\overline{f}-1\leq 0$, remark 2.3 implies that $r=y^2+z^2$ must be zero. Therefore $(x,y,z)(t)$ coincides with $p^F(t)$ (up to a time shift). If $F\overline{f}-1>0$, then the functions y and z have the form

$$y(t)=r(t)\cos(-bt+\theta_0),\qquad z(t)=r(t)\sin(-bt+\theta_0), \tag{2.10}$$

and they are not periodic[13] unless $r=0$.

To determine stability, we integrate the variational equation associated to (2.9) and $p^F(t)=(u_T(t)+1,0,0)$:

$$\dot{V}=\begin{pmatrix}-a & 0 & 0\\ 0 & u_T(t) & -b(u_T(t)+1)\\ 0 & b(u_T(t)+1) & u_T(t)\end{pmatrix}V,\quad V(0)=\begin{pmatrix}1&0&0\\0&1&0\\0&0&1\end{pmatrix}, \tag{2.11}$$

where V is the derivative of the flow of (2.9) with respect to initial conditions (x_0,y_0,z_0). Since $\dot{V}_{1k}=-aV_{1k}$, $k=1,2,3$, the first row of the monodromy matrix $V(T)$ is $(V_{11},V_{12},V_{13})(T)=(e^{-aT},0,0)$. Therefore, one eigenvalue of $V(T)$ is e^{-aT} and the other two do not depend on V_{21} and V_{31}. On the other hand, it is easy to see that

$$V_{32}=-V_{23}\qquad\text{and}\qquad V_{22}=V_{33}. \tag{2.12}$$

Indeed, define $W_1=V_{22}-V_{33}$ and $W_2=V_{23}+V_{32}$. Using (2.11), one obtains a linear homogeneous Cauchy problem for W_1 and W_2, with initial conditions $W_1^{(0)}=W_2^{(0)}=0$, which implies that $W_1(t)=W_2(t)=0$. So it is sufficient to solve the problem

$$\begin{aligned}\dot{V}_{22}&=u_TV_{22}+b(u_T+1)V_{23}, & V_{22}^{(0)}&=1,\\ \dot{V}_{23}&=-b(u_T+1)V_{22}+u_TV_{23}, & V_{23}^{(0)}&=0.\end{aligned} \tag{2.13}$$

We put (2.13) in complex form:

$$\dot{Z}=A(t)Z,\qquad\text{where}\quad Z=V_{22}+iV_{23},\quad A=u_T-ib(u_T+1).$$

Integration of the previous equation yields

$$(V_{22}+iV_{23})(T)=\exp\left(\int_0^T u_T(s)ds\right)\exp\left(-ib\int_0^T(u_T(s)+1))ds\right).$$

Using (2.12), one sees that the other two eigenvalues μ_2 and μ_3 of $V(T)$ are complex conjugated. Since their modulus is

$$\exp\left(\int_0^T u_T(s)ds\right)=\exp\left(T(F\overline{f}-1)\right),$$

then $p^F(t)$ is stable for $F\overline{f}-1<0$ and it loses stability as F increases through $1/\overline{f}$, because μ_2 and μ_3 cross the unit circle. Furthermore, we have

$$\arg(\mu_2)=-b\int_0^T(u_T(s)+1))ds=-bTF\overline{f},$$

which is equal to $-bT$ at the moment of the bifurcation. Since $-bT/2\pi$ is irrational[13], a Hopf bifurcation takes place. □

[13] This holds for the choice $b=4$ and $T=73$, for which $bT/2\pi=146/\pi$ is irrational.

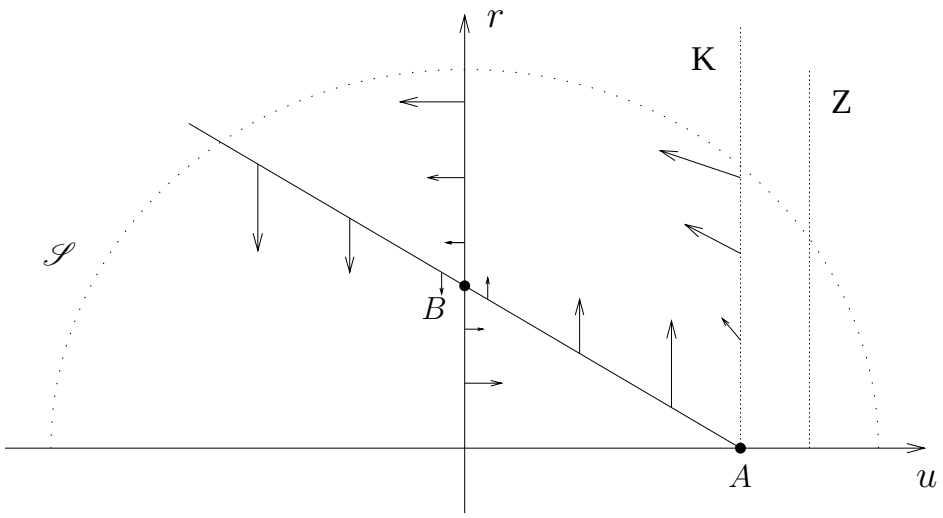

Figure 2.13: Phase portrait of the vector field W. The dashed half circle represents the attracting sphere $\mathscr{S}$ obtained in Sec. 2.2.1. The case $1 < F < 1 + a/2$ is sketched, for which the line Z ($u = a/2$) of zero divergence lies at the right of the saddle A.

We now show that in the autonomous case equation (2.9) has a unique global attractor for $F > 1$.

Proposition 2.4. *Consider system* (2.9)*, with* $F > 1$ *and* $f(t) = 1$ *for all* t*. The equilibrium* $B = (0, a(F-1))$ *is the unique global attractor of* (2.9)*.*

Proof. For $F > 1$, the vector field W (2.9) has two equilibria, B, which is stable, and the saddle $A = (F - 1, 0)$. By the Poincaré-Bendixson theorem, an attractor of the flow of (2.9) can be an equilibrium or a periodic orbit. We now show that the flow of (2.9) has no periodic orbits. The divergence $\operatorname{div} W = -a + 2u$ of W is negative for all (u, r) at the left of the line Z of zero divergence (Figure 2.13). We distinguish two cases. Suppose first that the saddle A lies at the left of line Z, that is, $1 < F < 1 + a/2$. Since the vector field W points leftward on all points of the vertical line K given by $(u = F - 1)$, any periodic orbit must lie at the left of K. But no periodic orbit can exist there, because the divergence is negative at the left of Z.

Take now an arbitrary value of F. If the vector field W (2.9) has a periodic orbit, this orbit must be born at a saddle-node bifurcation of periodic orbits. Indeed, no Hopf bifurcation of equilibria occurs for W, since the two equilibria never change stability type. Consider thus a saddle-node periodic orbit $\mathscr{O}$ of period S, parametrised by $\big(u(s), r(s)\big)$ for $s \in [0, S]$. Take a Poincaré map Q, defined in a suitable local section of $\mathscr{O}$. The eigenvalue μ of the derivative DQ at the fixed point of Q corresponding to $\mathscr{O}$ is one. On the other hand, $\overline{u} = 0$ by Remark 2.3 and, therefore,

$$\log(\mu) = \int_0^S \operatorname{div} W\big(u(s), r(s)\big) ds = \int_0^S (-a + 2u(s)) ds = -aS < 0,$$

which gives a contradiction. □

We now discuss the consequences of the above propositions for the family $P_{F,G,\varepsilon}$. Here we have $f(t) = 1 + \varepsilon\cos(\omega t)$, therefore $\overline{f} = 1$. The map $P_{F,G,\varepsilon}$ has a unique fixed point for $G = 0$ and all F, ε, which is stable for $F < 1$ and undergoes a Hopf bifurcation at $F = 1$. A circle attractor $\mathscr{C}$ is created there, but its persistence in F is guaranteed only for $F \approx 1$, by the theory of the Hopf bifurcation. On the other hand, hyperbolicity of the stable equilibrium B in Proposition 2.4 implies that system (2.9) has an attracting T-periodic orbit when applying a small T-periodic perturbation $f(t)$ (small in the sense that $\|f - 1\|_\infty$ is small). For the map $P_{F,G,\varepsilon}$, this implies the existence of the circle attractor $\mathscr{C}$ for all F and for small G and ε.

A remarkable consequence of (2.10) is that for *all* $F > 1$ the rotation number ρ is the constant on $\mathscr{C}$, namely $-bT/2\pi$. This situation is not generic in a family of circle mappings. Indeed, given the physical meaning of G (Sec. 2.1.1), the system for $G = 0$ seems to have too much symmetry and to be degenerate.

2.3 The driven system as a perturbation from the autonomous case

We now investigate the relations between the dynamics of the driven and the autonomous Lorenz-84, first introducing some notation. The flows of system (2.1) and (2.2) are denoted by $\Phi_{F,G}$ and $\Psi_{F,G,\varepsilon}$ respectively, where

$$\begin{aligned} \Phi_{F,G} &: \mathbb{R}^3 \times \mathbb{R} \to \mathbb{R}^3, && (x,y,z;s) \mapsto \Phi^s_{F,G}(x,y,z) \\ \Psi_{F,G,\varepsilon} &: \mathbb{R}^4 \times \mathbb{R} \to \mathbb{R}^4, && (x,y,z,t;s) \mapsto (\Psi^s_{F,G,\varepsilon}(x,y,z,t), t+s). \end{aligned}$$

The two flows are equivalent when $\varepsilon = 0$. More precisely, one has

$$\Psi^s_{F,G,0}(x,y,z,0) = \Phi^s_{F,G}(x,y,z) \quad \text{for every } (x,y,z,s) \in \mathbb{R}^4.$$

Therefore, $\Phi_{F,G}$-invariant dynamical objects are also $\Psi_{F,G,0}$-invariant. On the other hand, any dynamical property of $\Psi_{F,G,\varepsilon}$ can be expressed in terms of the Poincaré map $P_{F,G,\varepsilon}$, see Table 2.2. Notice that the flow $\Psi_{F,G,0}$ does not have equilibria, since $\dot{t} = 1$ in system (2.2). A hyperbolic equilibrium $q = (x,y,z)$ of Φ is said to be of type (m,n), with $m+n = 3$, if m eigenvalues of the linear part of the vector field (2.1) at q have negative real part, while n have positive real part. Similarly, a hyperbolic fixed point q of the map P is of type (m,n) if m eigenvalues of the derivative DP have modulus less than one and the remaining n lie outside the unit circle in the complex plane. At least one of the eigenvalues of $DP_{F,G,\varepsilon}$ at a fixed point is real.
We use the term Hopf bifurcation in each of the following cases.

1. Two complex conjugate eigenvalues of the linear part of the vector field (2.1) at an equilibrium cross the imaginary axis and a limit cycle of the three-dimensional flow Φ is born.

2. Two complex conjugate Floquet multipliers $\gamma\exp(\pm 2\pi i\rho)$ of a limit cycle of $\Phi_{F,G}$ or $\Psi_{F,G,\varepsilon}$ cross the unit circle[14] and an invariant two-torus is born.

[14] With $\rho \neq \pm 1/k$, for $k = 1,\dots,4$. These are codimension two bifurcations, called strong resonances [56, 78].

$\Phi_{F,G}$		$\Psi_{F,G,\varepsilon}$		$P_{F,G,\varepsilon}$
equilibrium	$\leftrightarrow$	period T limit cycle	$\leftrightarrow$	fixed point
limit cycle	$\leftrightarrow$	two-torus	$\leftrightarrow$	invariant circle
two-torus	$\leftrightarrow$	three-torus	$\leftrightarrow$	two-torus

Table 2.2: Equivalences for $\varepsilon = 0$ between invariant dynamical objects of the flow $\Phi_{F,G}$ of system (2.1) (left), of the flow $\Psi_{F,G,\varepsilon}$ of system (2.2) (centre), and of the Poincaré map $P_{F,G,\varepsilon}$. Centre and right column items are equivalent also for $\varepsilon > 0$.

3. Two complex conjugate eigenvalues $\gamma \exp(\pm 2\pi i\rho)$ of a fixed point of the map P cross the unit circle[14] and an invariant circle is born.

Notice that no limit cycle of the four-dimensional flow Ψ can be born in a standard Hopf bifurcation, since Ψ has no equilibria. Case 2 is often called Neĭmark–Sacker or torus bifurcation, also see footnote 6.

2.3.1 The autonomous system

We present some results on the autonomous Lorenz-84 system, mainly due to Shil′nikov, Nicolis and Nicolis [102]. The discussion begins with the bifurcation diagram of the flow $\Phi_{F,G}$ (Figure 2.14). For background on bifurcation theory and the relevant terminology see [23, 56, 78]. The organising centres are the following codimension two bifurcation points: a cusp $\mathcal{C}$, a Hopf-saddle-node point $\mathcal{HSN}$, both bifurcations of equilibria; a 1:1 and a 1:2 strong resonance point, and a cusp $\mathcal{CL}$, all bifurcations of limit cycles. Two branches of saddle-node curves of equilibria $\mathcal{SN}_0$ and $\mathcal{SN}_1$ meet tangentially at $\mathcal{C}$, forming a tongue-shaped region. In the neighbourhood of $\mathcal{C}$, three equilibria (two sinks and one saddle) coexist inside this tongue and only one sink $\mathscr{A}$ occurs outside.

A curve $\mathcal{H}_1$ of Hopf bifurcations of equilibria emanates from $(F, G) = (1, 0)$. The curves $\mathcal{SN}_0$ and $\mathcal{H}_1$ are tangent at the point $\mathcal{HSN}$. Above $\mathcal{HSN}$, both curves become subcritical and are denoted by $\mathcal{SN}_0^{sub}$ and $\mathcal{H}_1^{sub}$. A second curve $\mathcal{H}_2$ of supercritical Hopf bifurcations of equilibria (not reported in Figure 2.14) has been numerically computed in [102].

A curve of period doubling of limit cycles is marked by $\mathcal{PD}$. It is split by a 1:2 resonance point into a subcritical and a supercritical part, where the former lies above the 1:2 point. This point is connected to $\mathcal{HSN}$ by a curve $\mathcal{QH}_{sub}$ of subcritical Hopf bifurcations of limit cycles. The 1:1 and 1:2 resonance points are connected by a curve $\mathcal{QH}_{super}$ of supercritical Hopf bifurcations of limit cycles. The two curves indicated by $\mathcal{SL}$ (meeting at a cusp $\mathcal{CL}$) are saddle-node bifurcations of limit cycles.

We now explain how the dynamics varies with the parameters. A unique stable focus $\mathscr{A}$ exists for small F, to the left of curve $\mathcal{H}_1$ and outside the tongue with tip at $\mathcal{C}$. Following dashed segment A1 in Figure 2.14, from left to right: at the Hopf curve $\mathcal{H}_1$, below $\mathcal{HSN}$, $\mathscr{A}$ splits into an attracting limit cycle $\mathscr{M}$ and a saddle $\mathscr{B}_1$ of type $(1, 2)$. At $\mathcal{PD}$, below the 1:2 point, $\mathscr{M}$ loses stability and an attracting limit cycle $2\mathscr{M}$ is created. Crossing the curve $\mathcal{QH}_{super}$, $2\mathscr{M}$ loses stability and an attracting

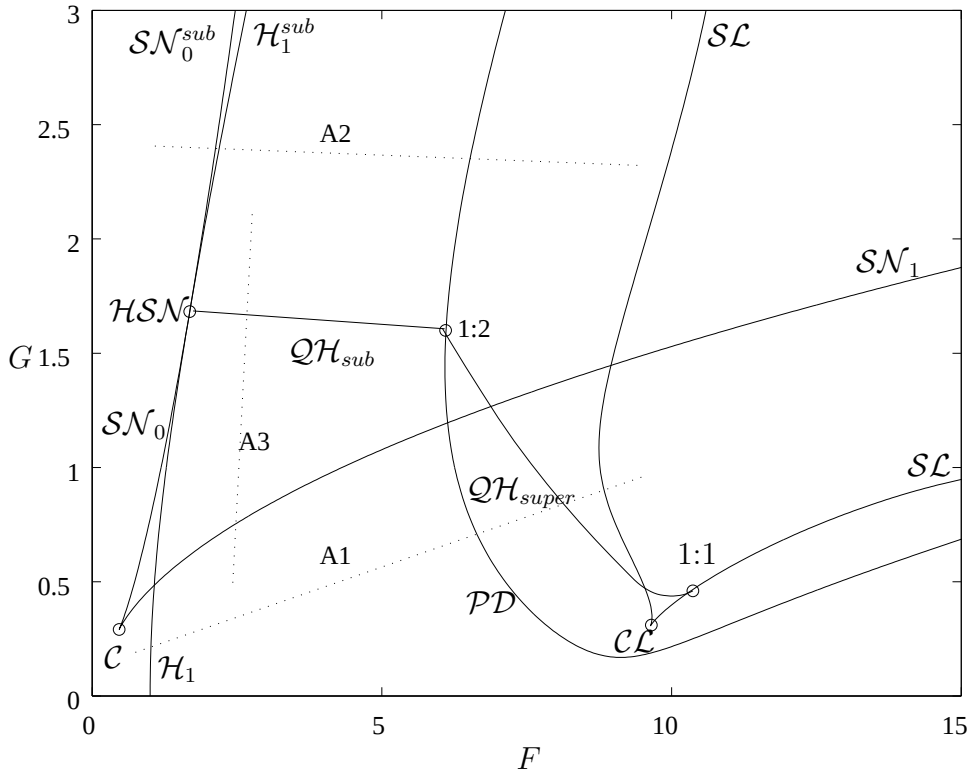

Figure 2.14: Bifurcation diagram of the autonomous system (2.1), from [61].

two-torus is created. Following segment A2 from left to right: the saddle-focus $\mathscr{B}_1$ and a repelling equilibrium are generated in a subcritical saddle-node bifurcation at the curve $\mathcal{SN}_0$. Crossing $\mathcal{H}$, the repellor turns into a saddle-focus $\mathscr{B}_2$ of type $(2,1)$ and a repelling limit cycle $\mathscr{M}$ is created. Then $\mathscr{M}$ undergoes a subcritical period doubling at the curve $\mathcal{PD}$. Following segment A3 from top to bottom: crossing the curve $\mathcal{QH}_{sub}$ downwards, $\mathscr{M}$ becomes attracting and a two-torus repellor is created. At $\mathcal{SN}_1$ the saddle $\mathscr{B}_2$ collides with the attractor $\mathscr{A}$.

It is known [31, 56, 78] that the bifurcation diagram near a Hopf-saddle-node point of three-dimensional vector field generically shows subordinate Shil′nikov bifurcations of equilibria. The latter is a complicated homoclinic phenomenon which may cause the birth of Shil′nikov strange attractors. Two curves of Shil′nikov homoclinic bifurcations (not reported in Figure 2.14) were computed numerically in [102]. Some other routes to chaos in Lorenz-84, such as cascades of period doublings, have been described in [82, 102].

Remark 2.4. It seems that some features of the above bifurcation diagram are rather common among low-dimensional systems with two parameters, compare *e.g.* [124]. The main ingredients are a Hopf-saddle-node point, a 1:1 and a 1:2 resonance point, connected by bifurcation curves of limit cycles. These global configurations are likely to be caused by a higher codimension bifurcation, 'hidden in the background' because of the lack of a sufficient number of active control parameters. A similar idea is expressed in the work of Carcassès *et al.* [33] (see also [23] and references therein),

who show that semi-global patterns formed by curves of period doubling and saddle-node bifurcation are confined to a certain number of configurations due to geometrical reasons.

One of the goals of the present work is to investigate which parts of the diagram in Figure 2.14 persist for the map $P_{F,G,\varepsilon}$ with $\varepsilon > 0$ and to find out which bifurcations play a role in the changes.

2.3.2 Persistent dynamical properties

We here summarise which dynamical properties of the autonomous Lorenz-84 system persist in the driven system for ε small.

Starting point is the bifurcation diagram in Figure 2.14. Assuming the correspondences in Table 2.2, all bifurcations of equilibria for $\Psi_{F,G}$ turn into bifurcations of fixed points for $P_{F,G,0}$. Similarly, bifurcations of limit cycles of $\Psi_{F,G}$ turn into bifurcations of invariant circles $P_{F,G,0}$. According to classical perturbation theory [5, 56, 38], hyperbolic [60, 99] fixed or periodic points, normally hyperbolic invariant circles and quasi-periodic tori of $P_{F,G,0}$ persist for $P_{F,G,\varepsilon}$, if the size ε of the perturbation is small. In the next section, we make a stronger statement, namely that for small ε the local bifurcation diagram of fixed points of $P_{F,G,\varepsilon}$ is a continuous deformation of that for $\varepsilon = 0$. The situation is more complicated for global (homoclinic) bifurcations, or for bifurcation of invariant circles (see Sec. 15 for the latter).

Bifurcations of fixed points

Consider a local bifurcation $\mathcal{B} \in \mathbb{R}^m$ of fixed points of a C^∞ map $P : \mathbb{R}^m \to \mathbb{R}^m$, where $\mathcal{B}$ has finite codimension. $\mathcal{B}$ is generic [56, 99] when the linear part and some higher order jet of P at the point $\mathcal{B}$ satisfy appropriate transversality conditions. If genericity holds, the Implicit Function Theorem implies that $\mathcal{B}$ persists under small perturbations of the map P.

Remark 2.5. Often, it is possible to formulate the above transversality conditions in terms of a normal form of P. One usually requires that a suitable combination C of the normal form coefficients of P be non-vanishing at $\mathcal{B}$. In this case, a small perturbation will not change the sign of C, nor the local bifurcation diagram around $\mathcal{B}$. Non-vanishing of C is usually checked by symbolic manipulation of the Taylor series, possibly in combination with numerical methods such as integration of differential equations.

The above conclusion can be applied to the family $P_{F,G,\varepsilon}$, assuming genericity of the bifurcations at $\varepsilon = 0$. In fact, genericity holds with the exceptions mentioned in Remark 2.6. All saddle-node curves are persistent in ε without changes and so is the cusp $\mathcal{C}$. As for the Hopf curves, an important modification introduced by the forcing is the creation of Arnol′d tongues and strong resonance points. Generic circle dynamics [4, 99] may be either quasi-periodic or phase locked, depending on the rotation number ρ. In particular, the dynamics is quasi-periodic if and only if ρ is irrational [41, 56]. Circle dynamics is degenerate for the map $P_{F,G,\varepsilon}$, at $\varepsilon = 0$, in the sense that it is a rigid rotation. We recall that a $P_{F,G,0}$-invariant circle $\mathscr{C}$ corresponds

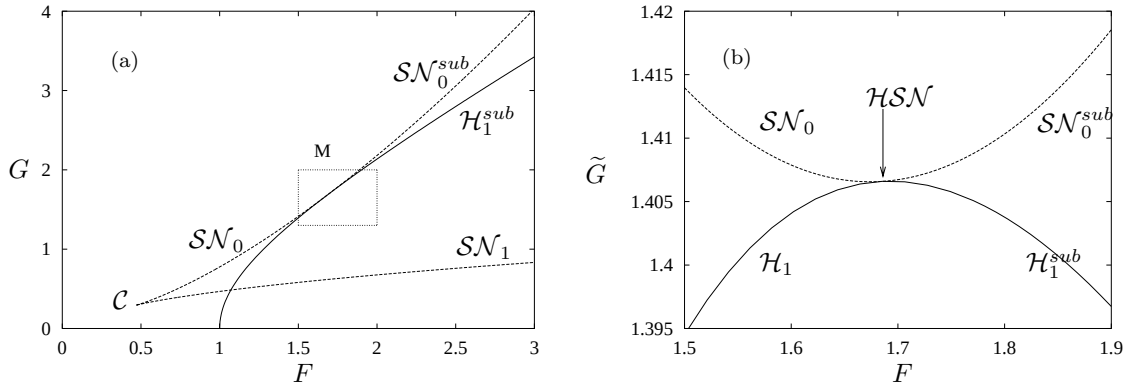

Figure 2.15: (a) Part of the bifurcation diagram of fixed points of $P_{F,G,0}$, for $\varepsilon = 0.01$. (b) Magnification of (a) of box M around the point $\mathcal{HSN}$. The latter graph has been deformed by an affinity, plotting couples $(F, \widetilde{G})$, where $\widetilde{G} = G - 1.5 \times (F - 1.5)$).

to the limit cycle $\mathscr{M}$ of the flow $\Phi_{F,G}$ (see Table 2.2). The rotation number on $\mathscr{C}$ is $\rho = T/T_L$, where T_L is the period of the limit cycle $\mathscr{M}$. Regions inside $\mathfrak{M}_0$ where an invariant circle occurs are foliated by lines (hairs) upon which the rotation number ρ is constant. Each hair $\mathfrak{A}^\rho$ is attached to a point belonging to the Hopf bifurcation curve where the circle has been created. At such a point, the two complex eigenvalues of the derivative $DP_{F,G,0}$ are equal to $\exp(\pm 2\pi i\rho)$. Points where $\rho = p/q$ with $q = 1, 2, 3, 4$ are called strong resonances. As ε increases from zero, hairs on which $\rho = p/q$ is rational split into resonance tongues $\mathfrak{A}^{p/q}$. The edges of the tongues have infinite order of contact as ε goes to zero [21, 29]. If $q \neq 1, \ldots, 4$, the two edges of $\mathfrak{A}^{p/q}$ meet at a tip attached to a Hopf point with rotation number p/q (also see Figure 2.40). In the case of a strong resonance, the local bifurcation diagram is richer, including also homoclinic bifurcations and chaos. Furthermore, a Hopf curve is interrupted by a generic strong resonance. Examples of some gaps produced on the Hopf curves for $\varepsilon = 0.5$ are presented in Sec. 2.4.2 and Sec. 2.4.1.

Remark 2.6. At $\varepsilon = 0$, all strong resonances introduced on the Hopf curves by the forcing are degenerate (non-generic). Consider a generic point $\mathcal{B} \in \mathcal{H}_1$ at $\varepsilon = 0$. Two eigenvalues of the linear part of the vector field (2.1) are purely imaginary, say, $\mu_\pm = \pm i\alpha$. Therefore, at $\varepsilon = 0$ two eigenvalues of DP at $\mathcal{B}$ are $\exp(\pm iT\alpha)$. If $T\alpha = p/q$ with $q = 1, \ldots, 4$, then $\mathcal{B}$ is a strong resonance for the map P. Since $\mathcal{B}$ is a generic Hopf bifurcation for the flow of the autonomous system, it does not interrupt the Hopf curve. Furthermore, a unique hair emanates from $\mathcal{B}$ and we conclude that $\mathcal{B}$, considered as a strong resonance of P, is degenerate.

Part of the bifurcation diagram of fixed points of $P_{F,G,\varepsilon}$ for $\varepsilon = 0.01$ is shown in Figure 2.15. The saddle-node curve, the Hopf curve, the cusp and the point $\mathcal{HSN}$ all persist for this value of ε. For concreteness the (F, G, x, y, z) values of this point are, approximately, (1.68390322, 1.68243988, 1.12474427, −0.01057355, 0.37742916). This can be compared with the corresponding values for $\varepsilon = 0$: (1.68405172, 1.68296855, 1.125, −0.01038068, 0.37370466) to see that the differences are quite small. However, for $\varepsilon = 0.5$ the point $\mathcal{HSN}$ does not persist, and the local bifurcation diagram is quite different (see Sec. 2.4.3).

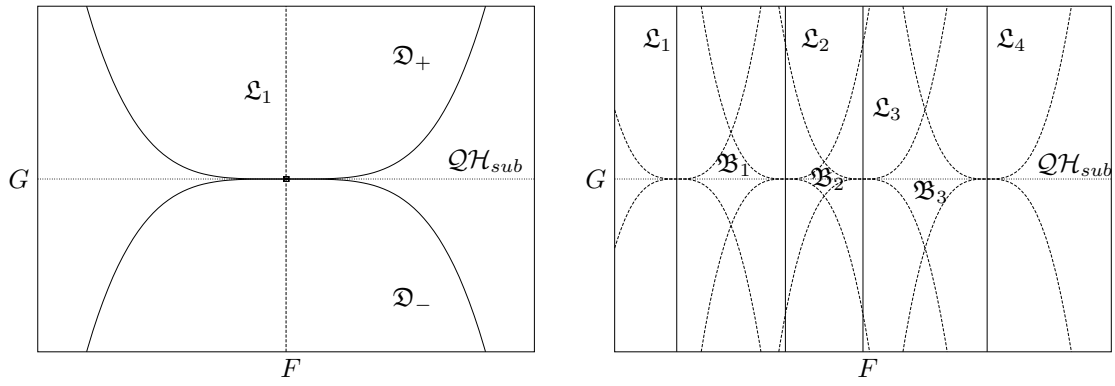

Figure 2.16: Left: two disks $\mathfrak{D}_+$ and $\mathfrak{D}_-$ are tangent to the curve $\mathcal{QH}_{sub}$ at the point D. Right: a Cantor subset of the curve $\mathcal{QH}_{sub}$ persists for $\varepsilon > 0$. In the complement of the disks, bubbles (or resonance holes) $\mathfrak{B}_1$, $\mathfrak{B}_2$ and $\mathfrak{B}_3$ appear.

We now turn to homoclinic bifurcations of fixed points. Homoclinic connections of the flow $\Phi_{F,G}$ of system (2.1) correspond to degenerate homoclinic tangencies for the map $P_{F,G,0}$. For $\varepsilon > 0$, the connections generically break, being replaced by transversal homoclinic intersections and nondegenerate homoclinic tangencies.[15] Special attention must also be payed to the accumulation of transversal homoclinic intersections. Depending on the geometry (*e.g.*, homoclinic orbits in a Shil′nikov-like case) it can be difficult to detect when the 'first' homoclinic tangency is produced. There may not even be a 'first' tangency.

Bifurcations of invariant circles

We discuss the influence of the forcing on the curves $\mathcal{PD}$, $\mathcal{QH}_{sub}$ and $\mathcal{QH}_{super}$ in Figure 2.14. Recall that the first is a curve of period doubling of the limit cycle $\mathscr{M}$, while the second and third are curves of sub- and super-critical Hopf bifurcations of $\mathscr{M}$, respectively. For a general presentation of all theory used in this section, see [17, 18] and references therein.

Limit cycles of the flow $\Phi_{F,G}$ of the system (2.1) turn into $P_{F,G,0}$-invariant circles, compare Table 2.2 and the previous section. For $\varepsilon > 0$, the circles have different bifurcation behaviour, depending on the rotation number ρ. In brief, the bifurcation diagram is locally persistent in ε only when restricting to Diophantine tori. For $\varepsilon = 0$ the sets in $\mathfrak{M}_\varepsilon$ where Diophantine circles occur locally have the product structure of a curve (of constant rotation number) times a Cantor set (of frequencies). Such local Cantor foliations of the parameter plane intersect the bifurcation curves at Cantor subsets, where the Diophantine circles are normally elliptic. To fix ideas, we briefly describe how the parameter plane $\mathfrak{M}_\varepsilon$ looks like for $\varepsilon > 0$ close to the curve $\mathcal{QH}_{sub}$. The circle $\mathscr{C}$ is Diophantine on all vertical lines labelled by $\mathfrak{L}_k$ in Figure 2.16 (right). Except at the intersections with $\mathcal{QH}_{sub}$, the circle $\mathscr{C}$ is normally hyperbolic. Then the theory implies that $\mathscr{C}$ persists also in two open regions on each side of line $\mathfrak{L}_k$. Two of these regions $\mathfrak{D}_+$ and $\mathfrak{D}_-$, called flat conic discs, are sketched in Figure 2.16 left. They have an infinite order of tangency with $\mathcal{QH}_{sub}$. Inside the conic discs $\mathscr{C}$ may be

[15] Also called (homoclinic) tangency bifurcations [56, 95].

	λ_1	λ_2	λ_3	e_1	e_2	e_3
A	-2.e-6	-0.01867	-0.0187	1.e-7	2.e-6	1.e-6
B	-2.e-6	-0.00269	-0.00271	3.e-7	2.e-6	1.e-6
C	5e-5	4.5e-7	-0.01	6.e-6	1.e-8	4.e-6

Table 2.3: Lyapunov exponents of the repellors in Figure 2.17, see footnote[16].

resonant and is repelling in $\mathfrak{D}_+$ and attracting in $\mathfrak{D}_-$. The torus repellor $\mathscr{T}$ occurs only in $\mathfrak{D}_-$. Note that the value of ε until which a given circle persists, depends strongly on the value of the Diophantine rotation number.

In this way, for $\varepsilon > 0$ each of the above curves turns into a frayed boundary as in Figure 2.16 (right). Outside all discs, small resonance regions remain in the parameter plane—the Chenciner 'bubbles', or resonance holes—where the behaviour of $\mathscr{C}$ under the perturbation is not predicted by the general theory. On the other hand, the resonance holes might as well be extremely small in size and, therefore, numerically hard to detect. Apart from these holes, strong resonances locally may destroy the curves.

Persistence of quasi-periodic Hopf bifurcations is now illustrated by a numerical example. A similar picture for quasi-periodic period doubling is presented in Sec. 2.4.9. For $(F, \varepsilon) = (1.8, 0.01)$ fixed, at $G = 1.683$ the circle repellor $\mathscr{C}$ occurs (Figure 2.17 (A)). The maximal Lyapunov exponent λ_1 is approximately zero, while λ_2 and λ_3 are negative,[16] indicating that $\mathscr{C}$ is both quasi-periodic and normally hyperbolic. Referring to Figure 2.16 (left), parameter values belong to $\mathfrak{L}_1 \cap \mathfrak{D}_+$.

At $G = 1.681$ (Figure 2.17 (B)), λ_2 and λ_3 are almost zero and $\mathscr{C}$ is normally elliptic. Parameter values are close to $\mathfrak{L}_1 \cap \mathcal{QH}_{sub}$ in Figure 2.16. The power spectrum contains six peaks labelled by k, corresponding to harmonics $f_k = kf_1$ of the fundamental frequency $f_1 = 0.4165$. At $G = 1.68$ the circle has become attracting and coexists with the torus repellor $\mathscr{T}$ (Figure 2.17 (C)). Parameters belong now to $\mathfrak{L}_1 \cap \mathfrak{D}_-$. Two Lyapunov exponents are zero on $\mathscr{T}$ and the power spectrum confirms the presence of two fundamental frequencies $f_1 = 0.4142$ and $g_1 = 0.19195$. Peaks occur at integer combinations of f_1 and g_1. In Figure 2.17 (c), we labelled peaks on frequencies f_1, $f_2 = 2f_1$, $f_1 - g_1$, $f_1 + g_1$ and $f_3 - g_1$ by 1, 2, h, j and l respectively. Notice that very small peaks g_1 and g_1 occur in Figure 2.17 (b), before the bifurcation. This is due to intermittency of type II [97].

Similar experiments for other values of F suggest that a large part of $\mathcal{QH}_{sub}$ survives for ε small. However, for $\varepsilon = 0.5$, no repelling torus is found and therefore the curve $\mathcal{QH}_{sub}$ does not seem to persist. See Secs. 2.4.5 and 2.5.1.

2.4 Dynamical inventory of the Poincaré map

The structure of the parameter plane $\mathfrak{M}_{0.5}$, sketched in Figure 2.4, is described in the next sections. The bifurcation diagram of fixed points (Figure 2.3) and the scanning

[16] Lyapunov exponents of repellors are computed using P^{-1}. All reported values hold for the inverted time.

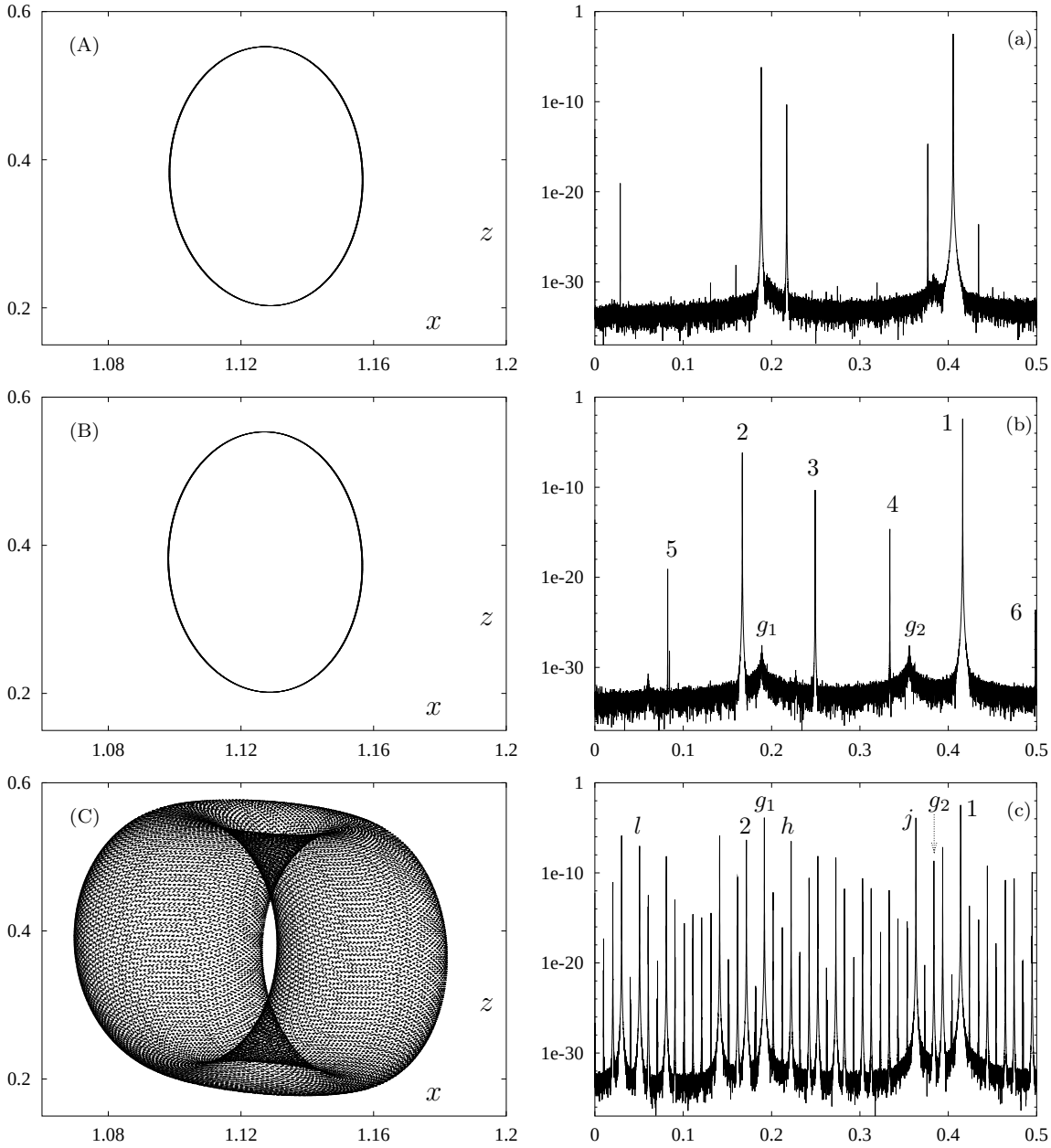

Figure 2.17: (A), (B), (C) Projections on (x, z) of repellors of $P_{1.8,G,0.01}$, for $G = 1.683$, $G = 1.681$, and $G = 1.68$ respectively. The initial point $(x, y, z) = (1.12, -0.17, 0.41)$ has been used in all cases. (a), (b), (c) Power spectra of the repellors.

for fixed points in Figure 2.2 (b) are repeatedly used in mapping out $\mathfrak{M}_{0.5}$. The reader is referred to all the above pictures for the labelling.

The dynamics of the autonomous case $\varepsilon = 0$ is preserved in a large part of $\mathfrak{M}_{0.5}$. In region $\mathfrak{F}$, that is either for G large or F small, a fixed point attractor $\mathscr{A}$ exists. Circle dynamics occurs in the two regions $\mathfrak{Q}_1$ and $\mathfrak{Q}_2$. So far, the only changes from the autonomous case are due to resonance phenomena in $\mathfrak{Q}_1$ and $\mathfrak{Q}_2$ and on the boundaries $\mathcal{H}_1$ and $\mathcal{H}_1^{sub}$ (see Sec. 2.3.2). The bifurcation diagram is unchanged also close to curves $\mathcal{SN}_0^{sub}$ and $\mathcal{SN}_0$ for F outside interval $\mathfrak{I} = \{F \mid 1.2 \lessdot F \lessdot 3\}$ (Figure 2.18). However, important modifications occur at $\varepsilon = 0.5$:

1. the disappearance of the Hopf-saddle-node point $\mathcal{HSN}$ and the destruction of the Hopf curves inside interval $\mathfrak{I}$ (Sec. 2.4.3).

2. The disappearance of the frayed curve of quasi-periodic Hopf bifurcations $\mathcal{QH}_{sub}$ (Sec. 2.4.5).

3. The creation of new families of fixed points close to $\mathcal{SN}_1$, away from the cusp $\mathcal{C}$ (Sec. 2.4.4). Part of this curve is the boundary between regions $\mathfrak{F}$ and $\mathfrak{U}$, $\mathfrak{U}'$.

4. The growth in size of the chaotic regions $\mathfrak{L}_2$ and $\mathfrak{U}$.

5. The creation of the chaotic regions $\mathfrak{L}_1$ and $\mathfrak{U}'$.

See Sec. 2.5.1 for comparisons with other values of ε. We proceed in order of increasing complexity of the phenomena, starting with region $\mathfrak{Q}_2$, where the situation is fairly well understood.

2.4.1 Circle dynamics inside region $\mathfrak{Q}_2$

A first indication of circle dynamics is given by the cigar-shaped sequences of attractors in Figure 2.1 (e) and (f). The cigars are projections on the plane (G, y) of one parameter families $\mathscr{C}_2(F_0, G)$ of circles, where F_0 is fixed to 7 and 11 respectively.

The circle $\mathscr{C}_2$ is born at supercritical Hopf bifurcations belonging to curve $\mathcal{H}_2$. To fix ideas, consider Figure 2.1 (e). The fixed point on the right (G large) is the attractor

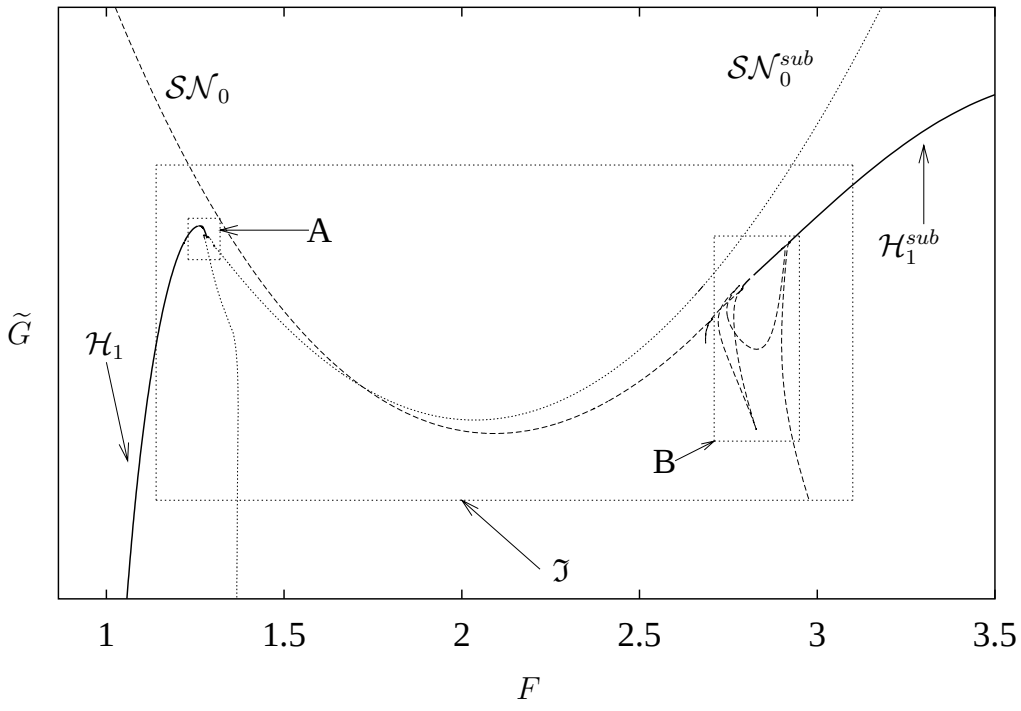

Figure 2.18: Bifurcation diagram of fixed points of $P_{F,G}$ for $\varepsilon = 0.5$, enlargement of box labelled by A in Figure 2.3. The graph has been affinely deformed, by plotting couples $(F, \widetilde{G})$, where $\widetilde{G} = (G - 1.3 \times (F - 1))$.

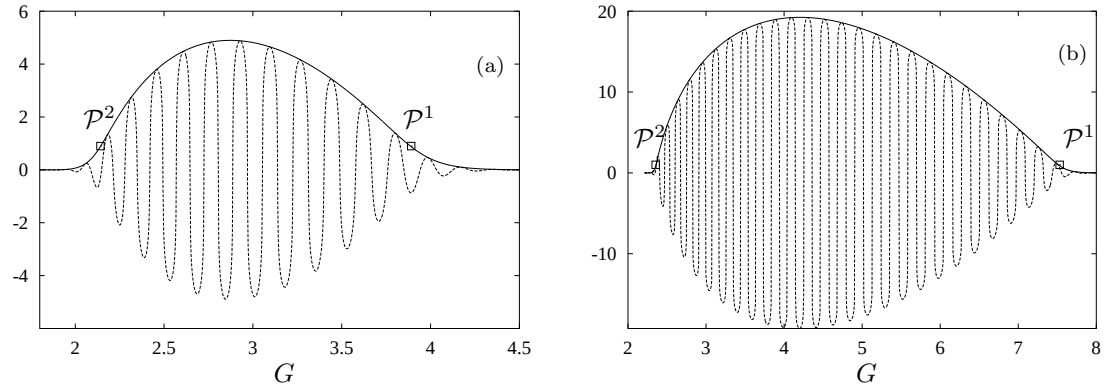

Figure 2.19: (a) Hyperbolic arcsine of the modulus (solid line) and real part (dashed line) of the eigenvalues of DP along a curve of continuation of fixed points, for $F = 7$. The two Hopf bifurcations $\mathcal{P}^1$ and $\mathcal{P}^2$ are marked by small boxes, see text for explanation. (b) Same as (a), for $F = 11$.

$\mathscr{A}$. As G decreases, $\mathscr{A}$ loses stability through a supercritical Hopf bifurcation, at a point $\mathcal{P}^1 \in \mathcal{H}_2$. This is illustrated in Figure 2.19 (a), where we plotted modulus and real part of the complex conjugate eigenvalues μ_1 and μ_2 of DP along a curve of fixed points. The curve is obtained by numerical continuation, starting from the attractor $\mathscr{A}$ and letting G decrease. The Hopf bifurcation $\mathcal{P}^1$ occurs at $G \simeq 3.89$, where $\mathscr{A}$ turns into a saddle-focus $\mathscr{B}$ of type $(1, 2)$. At that moment, $\mathscr{C}_2$ is created and starts expanding.[17] Then, at $G \simeq 2.14$ the circle $\mathscr{A}$ and the saddle $\mathscr{B}$ collide again, through a Hopf bifurcation $\mathcal{P}^2$, belonging to the lower branch of $\mathcal{H}_2$. Between $\mathcal{P}^1$ and $\mathcal{P}^2$ the real part of μ_1 on $\mathscr{B}$ changes sign several times, implying that μ_1 and μ_2 rotate around the origin inside the complex plane. The saddle $\mathscr{B}$ does not undergo other bifurcations between $\mathcal{P}^1$ and $\mathcal{P}^2$. For $F = 11$, the G-interval of existence of $\mathscr{C}_2$ and $\mathscr{B}$ is wider, since the two Hopf bifurcations occur at $G \simeq 7.53$ and $G \simeq 2.36$. Also notice that $\mathscr{B}$ becomes much more unstable than for $F = 7$, given the larger values of the modulus of the eigenvalues.

We investigated the dynamics on $\mathscr{C}_2$ by computing the Lyapunov exponents. The results for $F = 7$ and $F = 11$ are plotted in Figure 2.20. For all scanned G values between $\mathcal{P}^1$ and $\mathcal{P}^2$, the maximal Lyapunov exponent seems to be zero. Therefore, the dynamics on $\mathscr{C}_2$ is quasi-periodic for most parameter values in the cigars. This is also confirmed by the evolution of the rotation number on $\mathscr{C}_2$ for parameters on the above cigars, see Figure 2.21.

For definiteness, consider Figure 2.21 (a). Since $F = 7$ is fixed, parameter values belong to a vertical line $\mathfrak{V}$ in the plane $\mathfrak{M}_{0.5}$, intersecting many Arnol′d tongues in $\mathfrak{Q}_2$. The intersections are intervals on $\mathfrak{V}$ where the rotation number ρ of $\mathscr{C}_2$ is constant. Therefore, each segment of the broken line in Figure 2.21 (a) is a devil's staircase [41]. However, all horizontal plateaus, corresponding to intervals of constant rational rotation number, are extremely narrow. For example, intervals where $\rho = 0$ are intersections of $\mathfrak{V}$ with Arnol′d tongues where $\mathscr{C}_2$ is locked to a fixed point. The first such interval (pointed by an arrow in Figure 2.21 (a)) is less than 6×10^{-6} wide.

[17] A small scale on the parameter G is required to properly visualise this, see Remark 2.9 in Sec. 2.4.2.

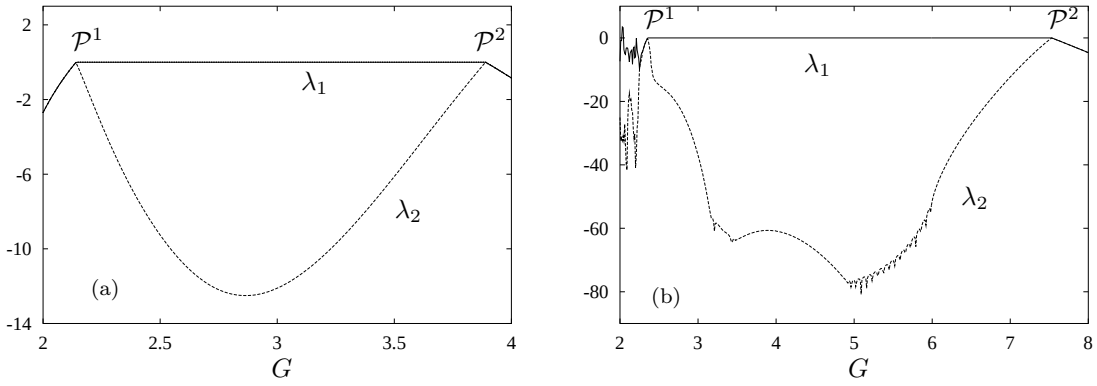

Figure 2.20: (a) Lyapunov exponents λ_1 and λ_2 in the G interval $[2, 4]$, with $F_0 = 7$. The step in G is 0.01. (b) Same for $G \in [2, 8]$, with $F_0 = 11$.

For concreteness, the values of G at the end points of the interval are 2.20340 30475 and 2.20340 89969, approximately. Similarly, all other Arnol′d tongues are very thin in $\mathfrak{Q}_2$, see below.

We now describe the global organisation of the Arnol′d tongues $\mathfrak{A}_k^0$ with zero rotation number inside $\mathfrak{Q}_2$. The first two tongues, $\mathfrak{A}_{30}^0$ and $\mathfrak{A}_{31}^0$, are shown in Figure 2.22 (a), together with $\mathcal{H}_2$.

Remark 2.7. The index k in $\mathfrak{A}_k^0$ is the number of windings of the T-periodic limit cycle of $\Phi_{F,G}$ corresponding to the fixed point occurring for parameter values inside $\mathfrak{A}_k^0$. This is illustrated in Figure 2.23 (a), where a limit cycle with initial condition inside $\mathfrak{A}_{35}^0$ is shown. An 'inner' and an 'outer' winding can be observed. The time evolution of the z-coordinate is plotted in Figure 2.23 (b) and the number of maxima in the interval $[0, T]$, which is also the number of windings, is 35. The number of windings increases by one unit from tongue $\mathfrak{A}_k^0$ to tongue $\mathfrak{A}_{k+1}^0$. Furthermore, the size of the inner windings inside tongue $\mathfrak{A}_k^0$ increases with k: in $\mathfrak{A}_{30}^0$ it is much smaller than in Figure 2.23 (a). Compare [123] for similar phenomena.

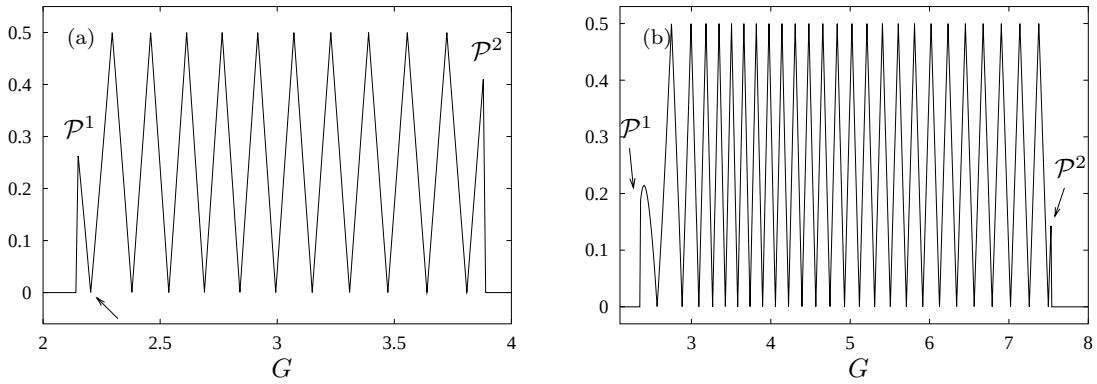

Figure 2.21: (a), (b) Rotation number ρ of $\mathscr{C}_2$ on the same G intervals as Figure 2.20 (a) and (b) respectively. When the fixed point attractor $\mathscr{A}$ occurs (outside the cigars, thus), we set $\rho = 0$. The step in G is 0.01.

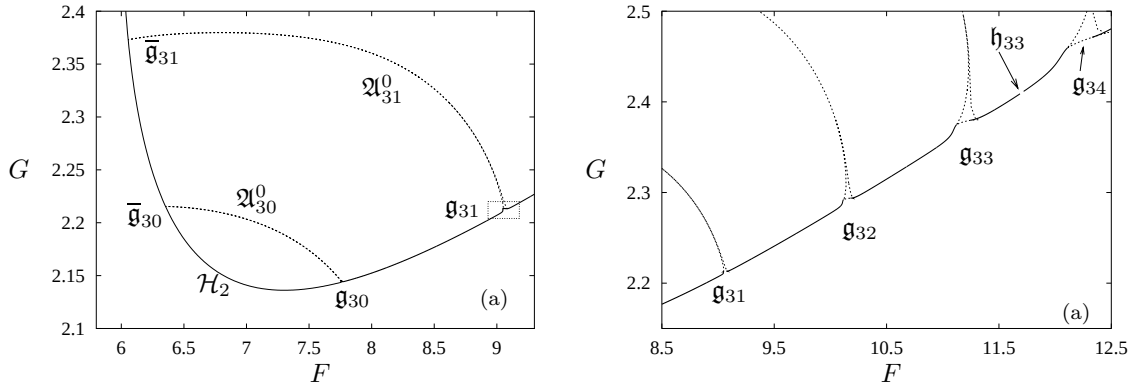

Figure 2.22: (a) Magnification of box C in Figure 2.3. The Hopf curve $\mathcal{H}_2$ is plotted with the first two Arnold tongues of zero rotation number. Magnifications of the boxes around the 1:1 resonance gaps $\overline{\mathfrak{g}}_{31}$ and $\mathfrak{g}_{31}$ are given in Figure 2.24 (a) respectively (b). (b) Portion of $\mathcal{H}_2$ contained inside box D in Figure 2.3, together with Arnol′d tongues with zero rotation number.

Each tongue $\mathfrak{A}^0_k$ intersects $\mathcal{H}_2$ two times, once at the lower and once at the upper branch. There, the Hopf curve $\mathcal{H}_2$ is interrupted by 1:1 resonance gaps, respectively $\mathfrak{g}_k$ and $\overline{\mathfrak{g}}_k$. To fix ideas, we consider the two gaps $\mathfrak{g}_{31}$ and $\overline{\mathfrak{g}}_{31}$ (Figure 2.24 (b) and (a) resp.). The gap $\mathfrak{g}_{31}$ is bounded by two 1:1 resonance points $\mathcal{BT}_{31,a}$ and $\mathcal{BT}_{31,b}$ (see Figure 2.24 (c) and (d)). Two saddle-node lines $\mathcal{SN}_{31,a}$ and $\mathcal{SN}_{31,b}$ are tangent to $\mathcal{H}_2$ at respectively $\mathcal{BT}_{31,a}$ and $\mathcal{BT}_{31,b}$. Furthermore, $\mathcal{SN}_{31,a}$ meets $\mathcal{SN}_{31}$ at a cusp $\mathcal{C}_{31,a}$ and $\mathcal{SN}_{31,b}$ meets $\mathcal{SN}_{31}$ at a cusp $\mathcal{C}_{31,b}$. The cusps $\mathcal{C}_{31,a}$ and $\mathcal{C}_{31,b}$ are connected by the saddle-node curve $\mathcal{SN}_{31,ab}$.

This structure is repeated at $\overline{\mathfrak{g}}_{31}$, at the other side of $\mathfrak{A}^0_{31}$, but the scale is much smaller (Figure 2.24 (a)). Two 1:1 resonance points and two cusps are connected by a fourth branch of saddle-node bifurcations, denoted by $\mathcal{SN}_{31,ba}$. The four saddle-node lines thus bound the tongue $\mathfrak{A}^0_{31}$. This type of semi-global organisation of resonance tongues has been described in other systems, see [92, 126].

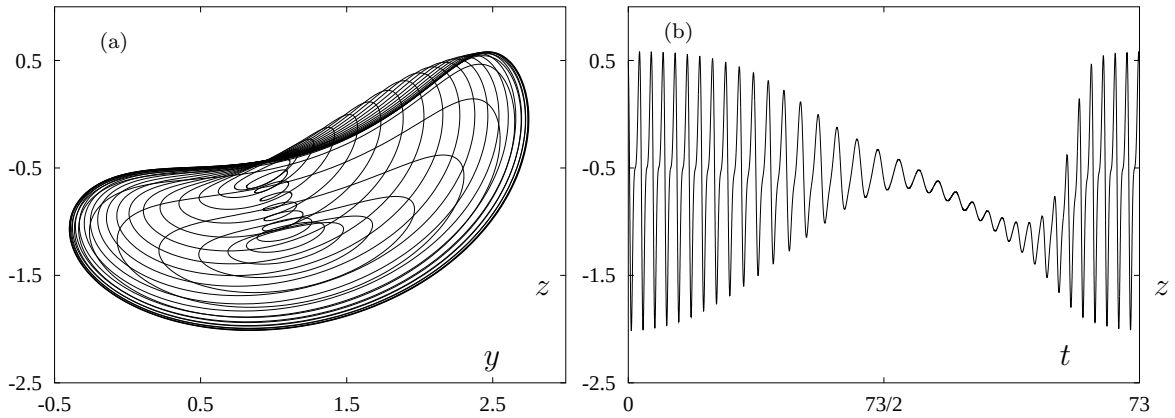

Figure 2.23: (a) Projection on (y, z) of a limit cycle corresponding to a period one phase-locked circle for parameter values $(F, G) = (9.3, 3.0472169822)$ inside $\mathfrak{A}^0_{35}$. (b) Same as (a), projection on the (t, z)-plane.

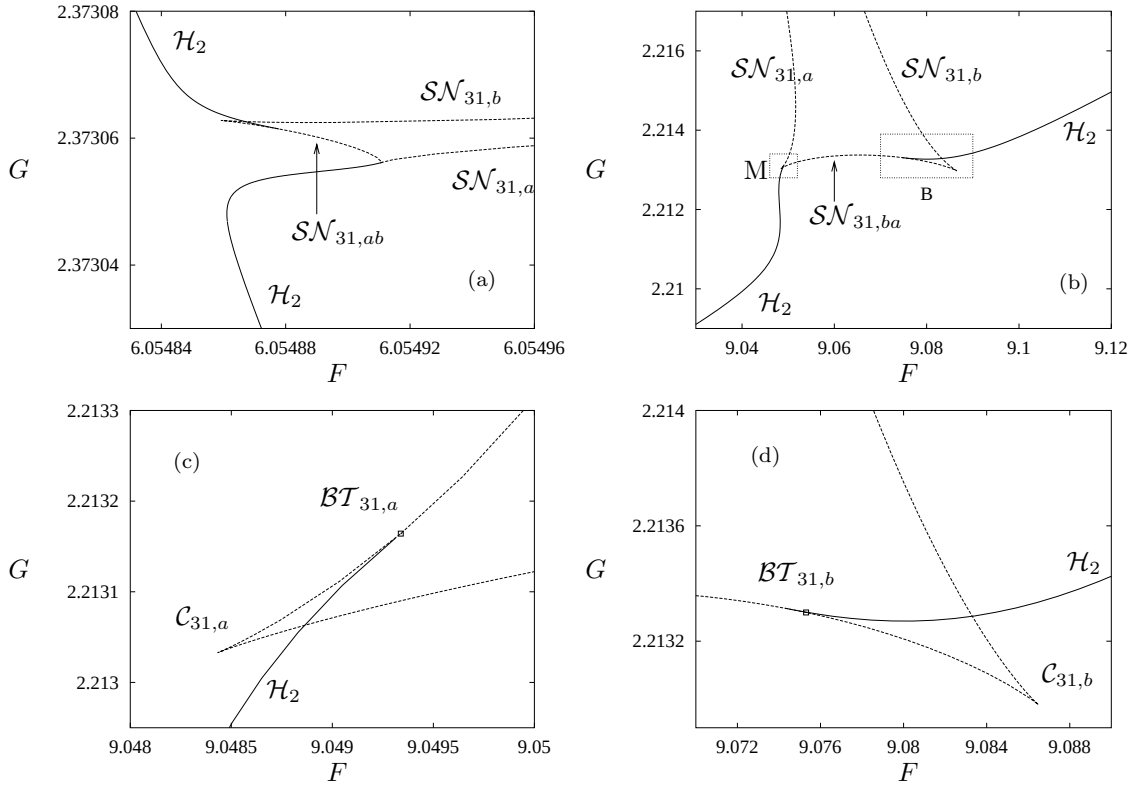

Figure 2.24: (a) Resonance gap $\overline{\mathfrak{g}}_{31}$ in the Hopf line $\mathcal{H}_2$. The dashed lines lines are saddle-node bifurcation curves. (b) Resonance gap $\mathfrak{g}_{31}$. (c), (d) Magnification of boxes L and M in (b), respectively, at the tangencies between $\mathcal{H}_2$ and the saddle-node curves

The same global structure seems to exist close to all other 1:1 resonance gaps in $\mathcal{H}_2$. Each gap $\mathfrak{g}_k$ on the lower branch of $\mathcal{H}_2$ is connected to a gap $\overline{\mathfrak{g}}_k$ on the upper branch by an Arnol′d tongue $\mathfrak{A}_k^0$ of rotation number zero. These tongues are plotted in Figure 2.2 (a), where they appear as lines crossing $\mathfrak{Q}_2$. Indeed, they are extremely narrow for most parameter values in $\mathfrak{Q}_2$. Arnol′d tongues of higher period are even narrower, so that the circle $\mathscr{C}_2$ is found quasi-periodic for most values inside $\mathfrak{Q}_2$. However, the tongues become wider close to the gaps $\mathfrak{g}_{31}$, at the lower branch of $\mathcal{H}_2$. Indeed, $\mathfrak{A}_{32}^0$ and $\mathfrak{A}_{33}^0$ form two small black spikes in Figure 2.2 (b), near the lower boundary of region $\mathfrak{Q}_2$. These spikes become even wider for larger ε, so that $\mathcal{H}_2$ is destroyed by strong resonance gaps, see Sec. 2.5.1.

More resonance gaps interrupting the continuity of $\mathcal{H}_2$ are shown in Figure 2.22 (b). The first three from the left and that at the right are 1:1 resonance gaps, while the second from right, labelled $\mathfrak{h}_{33}$, is due to a 1:2 resonance. The size of the gaps increases with F and on the lower branch of $\mathcal{H}_2$ it is much larger than on the upper one.

Remark 2.8. In the parameter space $\mathfrak{M}$ two curves of 1:1 resonance bifurcations pass through the two extremes of each gap. Both curves emanate from the same degenerate 1:1 resonance point on the curve $\mathcal{H}$ at $\varepsilon = 0$, compare Remark 2.6.

As we have shown, plenty of resonance gaps occur on $\mathcal{H}_2$ (the same holds for $\mathcal{H}_1$, see Sec. 2.4.3). It is known from the theory [56, 78] that the bifurcation diagram in

the neighbourhood of such codimension two points is rich, involving global homoclinic bifurcations, regions of chaoticity and homoclinic intersections. Such phenomena have been detected in [70], although using a smaller forcing period T. It is likely that they occur also in the family $P_{F,G}$, see Sec. 2.5.2.

2.4.2 Circle dynamics in $\mathfrak{Q}_1$

The circle $\mathscr{C}$ is born at Hopf points on the curve $\mathcal{H}_1$. This is illustrated in Figures 2.25 and 2.26, produced by a similar algorithm as Figure 2.1, with G fixed. The fixed point attractor $\mathscr{A}$ occurs for small F (left part of the figures). Crossing $\mathcal{H}_1$ from left to right, $\mathscr{A}$ undergoes a supercritical Hopf bifurcation at $F = 1.013$, where $\mathscr{C}$ appears.

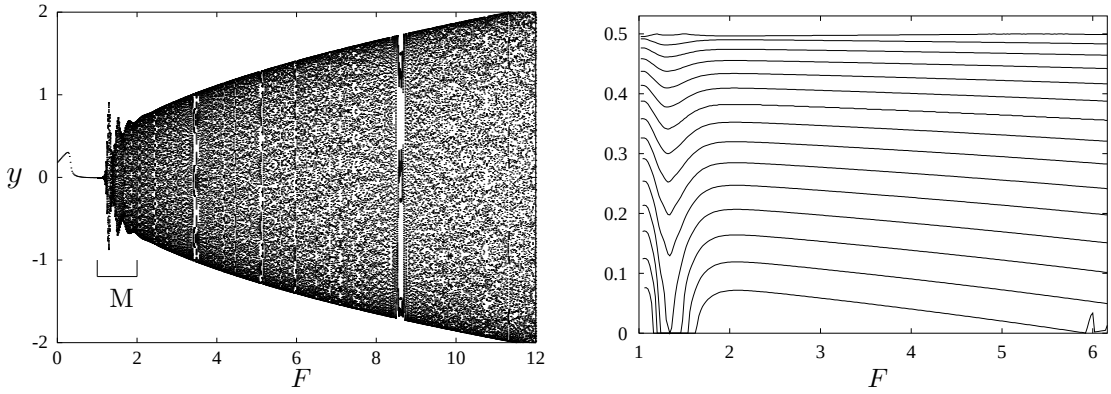

Figure 2.25: Left: projections on y of P-attractors as a function of F for $G = 0.2$ fixed. F is increased with a step of 0.02. The last 100 points of each loop are plotted. Interval M is enlarged in Figure 2.26. Right: rotation number (modulo 1/2, see Sec. 2.C) as a function of F. Each curve corresponds to a fixed value of G: $G = 0.36$ for the lowest and $G = 0.08$ for the upmost. Between two curves, G differs of 0.02.

Remark 2.9. If a Hopf bifurcation occurs at F_0 and the invariant circle exists for $F > F_0$, then the radius of the circle is $\mathcal{O}(\sqrt{F - F_0})$ as F tends to F_0 [56, 78]. In the family $P_{F,G}$, the interval of F usually has to be taken rather small to see this asymptotics, still visible in Figure 2.26 (b). On larger intervals, the expansion of the circle may look quite 'explosive', compare Figure 2.25 (left), Figure 2.26 (a) and Figure 2.43 later on. The same holds for Hopf bifurcations at the border of $\mathfrak{Q}_2$, compare the extremes of the 'cigars' $\mathscr{C}_2(7, G)$ and $\mathscr{C}_2(11, G)$ in Figure 2.1 (e) and (f).

In Figures 2.25 and 2.26, all attractors occurring for $F > 1.1$ are projections of $\mathscr{C}(F, G_0)$, with $G_0 = 0.2$. Also compare Figure 2.1 (c)–(f) for G small. Right after the Hopf bifurcation, for $1 \lessdot F \lessdot 2$, the size and form of $\mathscr{C}$ are quite sensitive to variations of G, also see Figure 2.26. For larger G, this phenomenon becomes more evident and, ultimately, inside region $\mathfrak{L}_1$ the circle $\mathscr{C}$ breaks (see Figure 2.43).

All Arnol′d tongues emanating from $\mathcal{H}_1$ are very thin and lie more or less parallel to the $G = 0$ axis. This is illustrated by a plot of the rotation number ρ as a function of F (Figure 2.25 right), computed on sequences of circles such as in Figure 2.25 (left) for a few fixed values of G. The lowest lines $G = 0.36$, 0.34 and 0.32 intersect the

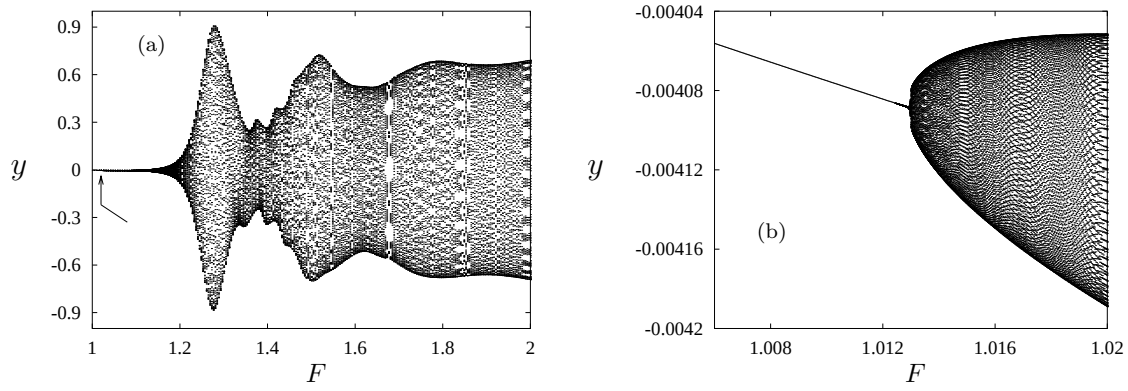

Figure 2.26: (a) Magnification of of interval M in Figure 2.25. Between consecutive loops of iterates, F is increased with a step of 0.004. (b) Magnification of a small interval pointed by an arrow in (a), where F is increased with a step of 3.5×10^{-5}. The last 100 points of each loop are plotted.

large period one tongue $\mathfrak{A}^0$ in Figure 2.2 (b). There ρ is zero and this also influences the other curves in Figure 2.25 (right). The small peak in ρ for $G = 0.36$ and F close to 6 is due to a quasi-periodic doubling of $\mathscr{C}_2$, followed by an undoubling. However, far from this peak and away from $\mathfrak{A}^0$ the rotation number changes quite slowly with F.

2.4.3 On the Hopf-saddle-node bifurcation point

For $\varepsilon = 0.01$, the curves $\mathcal{SN}_0$ and $\mathcal{SN}_0^{sub}$ in fact form one curve, split by the point $\mathcal{HSN}$ (Figure 2.15). On $\mathcal{SN}_0^{sub}$ a fixed point repellor $\mathscr{R}$ and a saddle $\mathscr{B}_1$ of type $(1, 2)$ are generated. Crossing $\mathcal{H}_1^{sub}$ from left to right, the fixed point repellor $\mathscr{R}$ turns into a saddle $\mathscr{B}_2$ of type $(2, 1)$, while a circle repellor $\mathscr{C}$ is born (also see Figures 2.36 and 2.35 later on).

For $\varepsilon = 0.5$, $\mathcal{SN}_0^{sub}$ and $\mathcal{SN}_0$ do not meet and the point $\mathcal{HSN}$ has disappeared (Figure 2.18). Most of the changes occur inside interval $\mathfrak{I}$ (this is where $\mathcal{HSN}$ occurs at $\varepsilon = 0.01$). The Hopf curves $\mathcal{H}_1$ and $\mathcal{H}_1^{sub}$ are broken to small fragments by many strong resonance points.

Three 1:2 resonance points and one 1:1 resonance on $\mathcal{H}_1$ are plotted in Figure 2.27 (a). Another 1:1 resonance point can be seen in Figure 2.27 (b). At these 1:1 resonance points, $\mathcal{SN}_0^{sub}$ is tangent to $\mathcal{H}_1$. For larger F, the resonance gaps increase even more in size and only minuscule segments of $\mathcal{H}_1$ survive inside $\mathfrak{I}$.

Remark 2.10. A Hopf curve in general can be continued across strong resonance gaps. Indeed, curves of fixed points emanate from such points, on which two eigenvalues μ_1 and μ_2 of DP are real, with $\mu_1\mu_2 = 1$. This is not a bifurcation condition, see [78]. For reference, such curves are plotted by dots in Figures 2.27 and 2.28.

We also want to stress that the curve $\mathcal{H}_1^{sub}$ is completely broken by strong resonances inside interval $\mathfrak{I}$. In Figure 2.28, $\mathcal{H}_1^{sub}$ is interrupted by two 1:2 resonance points and three 1:1 resonance points, two of which are shown in Figure 2.28 (b), the other

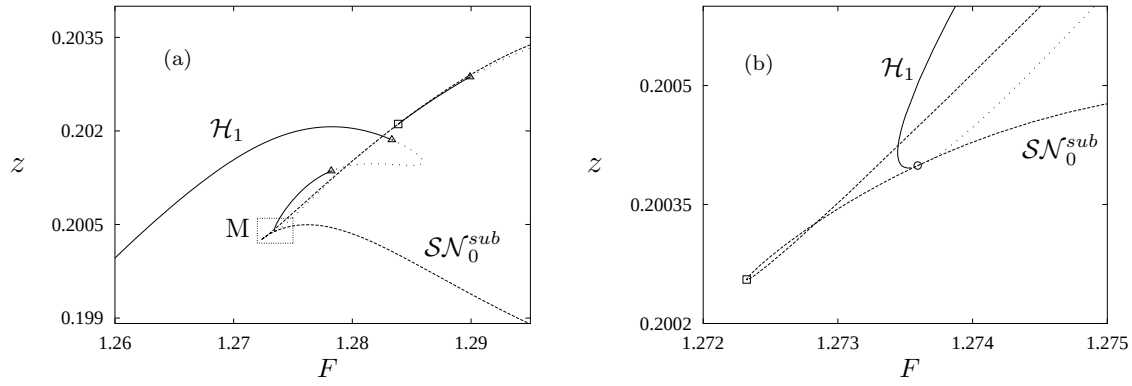

Figure 2.27: (a) Projection on (F, z) of portions of $\mathcal{H}_1$ (thick lines) and $\mathcal{SN}_0^{sub}$ (dashed lines), enlargement of box A in Figure 2.18. (b) Magnification of box M in (a). 1:1 resonance points are marked by small boxes, 1:2 resonance points by triangles and cusps by circles.

is not marked. The curve $\mathcal{SN}_0$ meets five cusps (two are shown in Figure 2.28 (b), one is not marked) and is tangent to $\mathcal{H}_1^{sub}$ at the 1:1 resonance points.

Since $\mathcal{HSN}$ persists at $\varepsilon = 0.01$ (Sec. 2.3.2), it must have disappeared through a sequence of higher codimension bifurcations at some intermediate ε before reaching $\varepsilon = 0.5$, see Sec. 2.5.1.

2.4.4 New families of fixed points in the chaotic range $\mathfrak{U}'$

It can be guessed from Figure 2.2 (b) and Figure 2.5 (right) that new families of fixed point attractors are created below curve $\mathcal{SN}_1$ in region $\mathfrak{U}'$. In this section we provide an explanation of how these families are connected to the fixed point attractor occurring in region $\mathfrak{F}$.

The curves $\mathcal{SN}_0$ and $\mathcal{SN}_1$ of saddle-node bifurcations meet tangentially at $\mathcal{C}$,

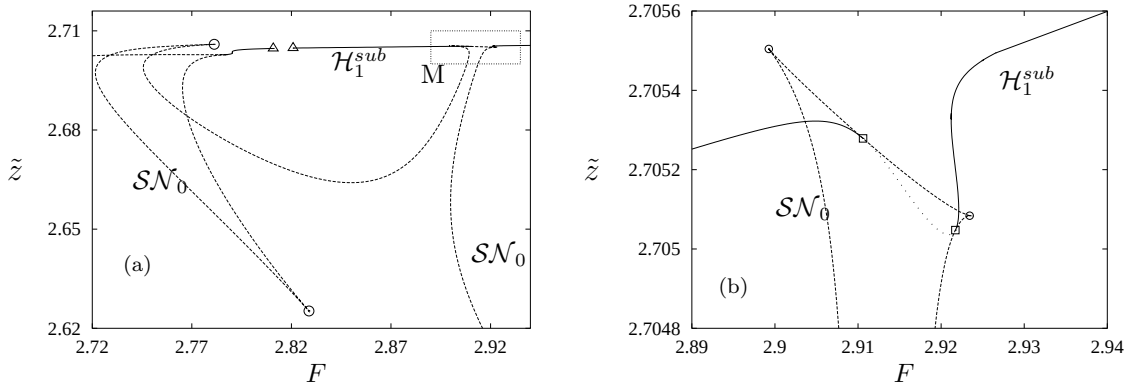

Figure 2.28: (a) Projection on $(F, \tilde{z})$ of portions of $\mathcal{H}_1^{sub}$ (thick lines) and $\mathcal{SN}_0$ (dashed lines), enlargement of box B in Figure 2.18. The graph has been affinely deformed by plotting $\tilde{z}(F, z) = (z - 1.46 \times (F - 2.7))$ on the vertical axis. (b) Magnification of box M in (a). Symbols mean the same as in Figure 2.27.

forming a tongue-shaped region (see Figure 2.5 (left)). Close to $\mathcal{C}$, the dynamics of P for $\varepsilon = 0.5$ is quite similar to that of the autonomous case $\varepsilon = 0$. A fixed point attractor and a saddle are generated on both curves when (F, G) enter the tongue. This is illustrated in Figure 2.29, where a curve K of fixed points is plotted. For G large, the fixed point attractor $\mathscr{A}_1$ is detected by iteration and continued for G decreasing. Arrows indicate the sense in which the curve is described. As G decreases, K becomes almost vertical (see Figure 2.29 (a), above box M). A magnification of box M (see Figure 2.29 (b)) shows that K meets a saddle-node point $\mathcal{T}_1$, belonging to $\mathcal{SN}_1$, where $\mathscr{A}_1$ turns into a saddle $\mathscr{B}_1$ of type $(2, 1)$. The branch of saddles makes an excursion at the right and meets a saddle-node point $\mathcal{T}_0$, belonging to $\mathcal{SN}_0$. Here, $\mathscr{B}_1$ collides with the attractor $\mathscr{A}_2$ and the branch of $\mathscr{A}_2$ extends down to $G = 0$. Notice that the latter saddle-node bifurcation clarifies the transition from Figure 2.1 (a) to Figure 2.1 (b). To visualise this, the points found in Figure 2.1 (b) are plotted together with the continuation curve in Figure 2.29 (a). In Figure 2.1 (b), G is increased by 0.01 at each step. When G is increased across $\mathcal{T}_0$, the attractor $\mathscr{A}_2$ disappears at $\mathcal{T}_0$, and the P-iterates are attracted to $\mathscr{A}_1$. So $\mathscr{A}_1$ and $\mathscr{A}_2$ coexist in the G-interval between $\mathcal{T}_0$ and $\mathcal{T}_1$. Consequently, a part of the tongue with tip at $\mathcal{C}$ is a region of bistability. For (F, G) at the left of curve $\mathcal{H}_1$, two fixed point attractors $\mathscr{A}_1$ and $\mathscr{A}_2$ coexist with the saddle $\mathscr{B}_2$ In fact, all of them belong to a unique surface of fixed points, partitioned by the saddle node curves $\mathcal{SN}_0$ and $\mathcal{SN}_1$. Outside the tongue or at the right of $\mathcal{H}_1$, only one fixed point attractor possibly occurs, denoted by $\mathscr{A}$. For example, $\mathscr{A}$ is detected for low values of F, see Figure 2.1 (a). At the right of $\mathcal{H}_1$, the fixed point $\mathscr{A}$ may coexist with the circle attractor $\mathscr{C}$, but also with a strange attractor, see Sec. 2.4.6.

For larger values of F the bifurcation diagram close to $\mathcal{SN}_1$ is more complicated than in the autonomous case. Many more fixed points appear here as F is increased. This is illustrated in Figure 2.30, similar to Figure 2.29 (b), but with $F = 0.8$. The point $\mathcal{T}_1$ again belongs to $\mathcal{SN}_1$. Two 'new' saddle-node bifurcation points $\mathcal{T}_2^a$ and $\mathcal{T}_2^b$ are detected close to $\mathcal{T}_1$. Denoting by G_a and G_b the values of G at which these two

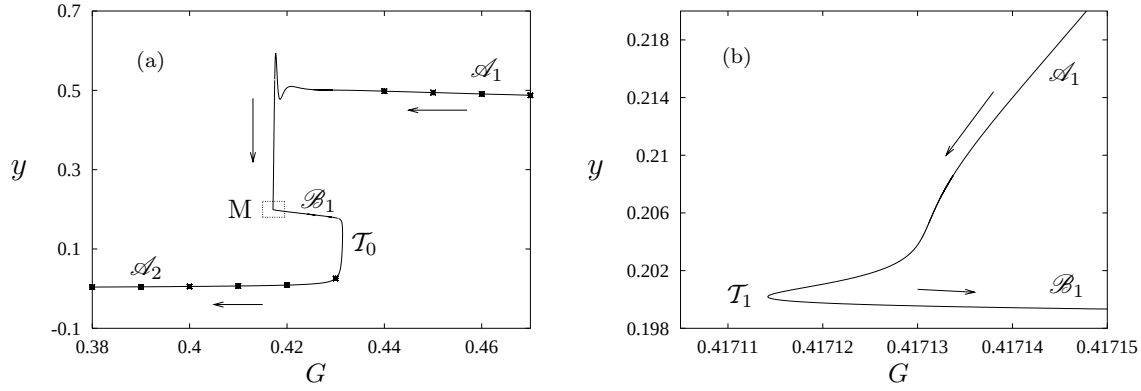

Figure 2.29: (a) Projection on (G, y) of curve of P-fixed points, joining the attractors $\mathscr{A}_1$ and $\mathscr{A}_2$, for $F = 0.7$. The curve is computed by numerical continuation. Crosses mark the fixed points found in Figure 2.1 (b). (b) Magnification of box marked by M in (a).

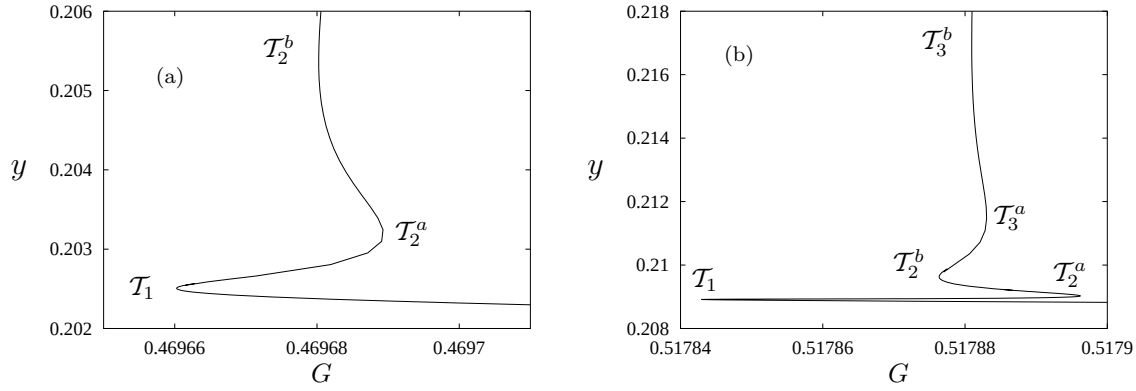

Figure 2.30: (a) Projection on (G, y) of a curve of fixed points of P obtained by continuation with respect to G, for $F = 0.8$. (b) Same as (a) for $F = 0.9$.

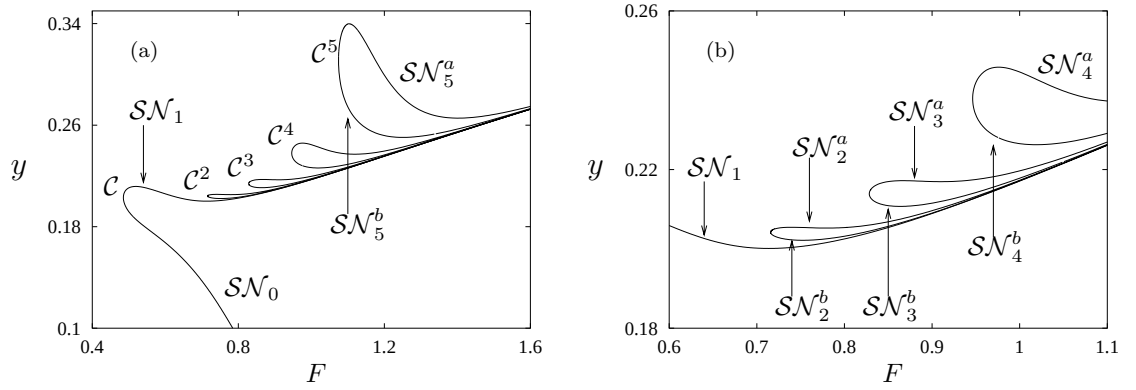

Figure 2.31: (a) Projection on (F, y) of curves of saddle-node bifurcation points. Four cusps are marked by $\mathcal{C}^k$, $k = 2, \ldots, 5$, while $\mathcal{C}$ is the same as in Figure 2.3. (b) Enlargement of the previous picture around the first three cusps $\mathcal{C}^k$.

points occur, four fixed points coexist[18] in the interval (G_a, G_b). For $F = 0.9$, four new saddle-node bifurcations occur, denoted by $\mathcal{T}_2^a$, $\mathcal{T}_2^b$, $\mathcal{T}_3^a$ and $\mathcal{T}_3^b$ (Figure 2.30 (b)). For G in a suitably small interval, P has up to six coexisting fixed points. The new bifurcations belong to curves emanating from a sequence of cusps, which possibly form a cascade, compare [23]. In Figure 2.31, we plotted the cusp $\mathcal{C}$ and the curves $\mathcal{SN}_0$ and $\mathcal{SN}_1$, together with eight curves $\mathcal{SN}_k^a$ and $\mathcal{SN}_k^b$, $k = 2, \ldots, 5$, of saddle-node bifurcations of fixed points. The points $\mathcal{T}_k^a$ and $\mathcal{T}_k^b$ belong to $\mathcal{SN}_k^a$ and $\mathcal{SN}_k^b$, which in turn emanate from a cusp $\mathcal{C}^k$. The projection on the (F, y) plane has been chosen to better distinguish the curves $\mathcal{SN}^k$. Indeed, in the (F, G) plane they all lie in a very narrow strip above the curve $\mathcal{SN}_1$.

We observe that a Shil′nikov tangency bifurcation might be related to the occurrence of the cusps and the coexistence of the several SN lines. A trace of this can be seen in the spiral-like form of the limit cycles of $\Psi_{F,G,0.5}$ (corresponding to periodic points of P). For the limit cycle in Figure 2.32 (a), the number of windings (see Sec. 2.4.1) is four (the fourth winding is quite narrow), while it is zero for the limit

[18] In fact, the vertical line $G = 0.469685$ intersects the curve in Figure 2.30 (a) at four points.

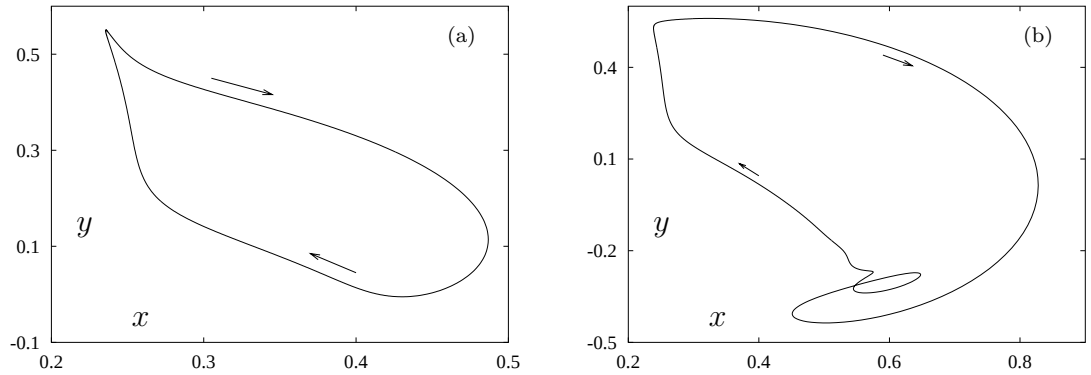

Figure 2.32: (a) Projection on (y, z) of a limit cycle of the flow $\Psi_{F,G,0.5}$ of system (2.2), for $(F, G) \simeq (1.2, 0.64)$. The corresponding fixed point belongs to curve $\mathcal{SN}^5$. (b) Same as (a), but the fixed point belongs to $\mathcal{SN}_1$.

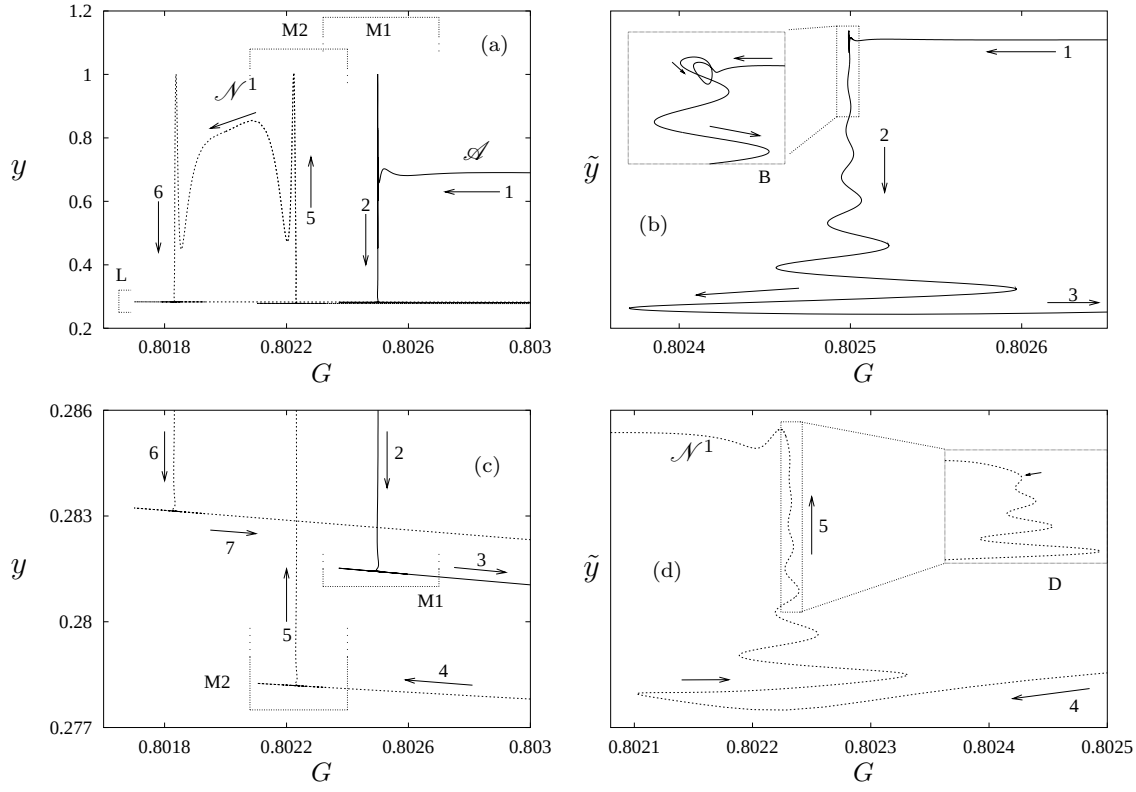

Figure 2.33: (a) A curve K of fixed points, obtained by continuation (see text). (c) Magnification of a horizontal layer L of (a). (b), (d) Magnifications of portions of K for G in the intervals M1 and M2 respectively. For better visualisation, only one part of K is plotted in each. A nonlinear transformation has been applied to distinguish the oscillations of K, which are not visible in (a) nor in (c).

cycle in Figure 2.32 (b). At each curve $\mathcal{SN}^{k+1,a}$ or $\mathcal{SN}^{k+1,b}$, a spiral limit cycle is created possessing one more revolution than on $\mathcal{SN}^{k,a}$ or $\mathcal{SN}^{k,b}$, thus with number of windings increased by one.

For F larger, inside regions $\mathfrak{U}'$ and $\mathfrak{U}$ one finds orbits with an 'inner' and an 'outer' spiralling (Figure 2.11 (a) in Sec. 2.1.3), or displaying even more complicated patterns (Figure 2.11 (b)). Compare with the winding orbits in [77]. Furthermore, new families of fixed point attractors appear in $\mathfrak{U}'$ and $\mathfrak{U}$. We illustrate this in Figure 2.33 (a), with a plot of a curve K of fixed points in $\mathfrak{U}'$. For better visualisation, two parts of K are plotted with different linestyles. A magnification of a horizontal layer marked by L is given in Figure 2.33 (c). The arrows indicate the direction we are following in the description. The curve K is obtained as Figure 2.29, by taking $\mathscr{A}_1$ and doing continuation for G decreasing (arrow 1 in Figure 2.33 (a) and (c)). The curve begins to oscillate inside a small G-interval M1, magnified in Figure 2.33 (b). Each turning point is a saddle node bifurcation (this holds for all pictures). At first the oscillations occur in a very narrow G-interval and can be seen only with a further magnification (box B in Figure 2.33 (b), where six SN bifurcations occur). Then, as y decreases (arrow 2 in Figure 2.33 (a), (b) and (c)), the oscillations tend to become wider in G and flatter in y, accumulating at the lowest branch of K. After 15 SN bifurcations, K makes a long excursion towards a saddle-node point[19] occurring for larger G, and then turns back (arrow 3 in Figure 2.33 (b) and (c)).

On the branch which is coming back (dashed curve under arrow 4 in Figure 2.33 (c) and (d)) the fixed points are saddles. Furthermore, this branch does not reach $G = 0$, but meets another turning point (in box M2 magnified in Figure 2.33 (d)) and begins to oscillate again. This time, after the first turning point, K goes upwards (arrow 5 in Figure 2.33 (a), (c) and (d)). After eleven SN bifurcations (the last is marked by an arrow in box D, Figure 2.33 (d)), the fixed points on K become attracting. These attractors occur in a small G interval, labelled by $\mathscr{N}^1$ in Figure 2.33 (a). This interval is roughly bounded by the two 'vertical barriers' close to arrows 5 and 6. As G decreases (arrows 6), the curve K again meets several SN bifurcations. After that, a branch of saddles again makes an excursion to a saddle-node point occurring for larger G (arrow 7 in Figure 2.33 (c)).

The whole process repeats itself for G smaller. By further continuation of K, we have found eight new branches $\mathscr{N}^k$ of attracting fixed points (Figure 2.34 (a)). Each of the new branches is bounded by two 'vertical barriers', where several saddle-node bifurcations occur. On each 'vertical barrier' the continuation curve oscillates as in Figure 2.33 (b) or (d). Therefore, for each G value in Figure 2.34 (b), many fixed points coexist, most of them being saddles. The corresponding T-periodic limit cycles of $\Psi_{F,G,0.5}$ are of spiral type.

It is natural to suspect that Shil′nikov tangency bifurcations may take place here. In fact, narrow Hénon-like strange attractors are found nearby in $\mathfrak{U}'$, see Sec. 2.4.6. In the autonomous system $\varepsilon = 0$ one curve of Shil′nikov bifurcations is tangent to the curve $\mathcal{SN}_1$ at several codimension two points. The organising centre for the phenomena described in this section could be one of such codimension two bifurcations of fixed points of $P_{F,G}$.

[19] For a clear visualisation we exclude the latter point from Figure 2.33 (a)-(d), just focusing on a small interval in G.

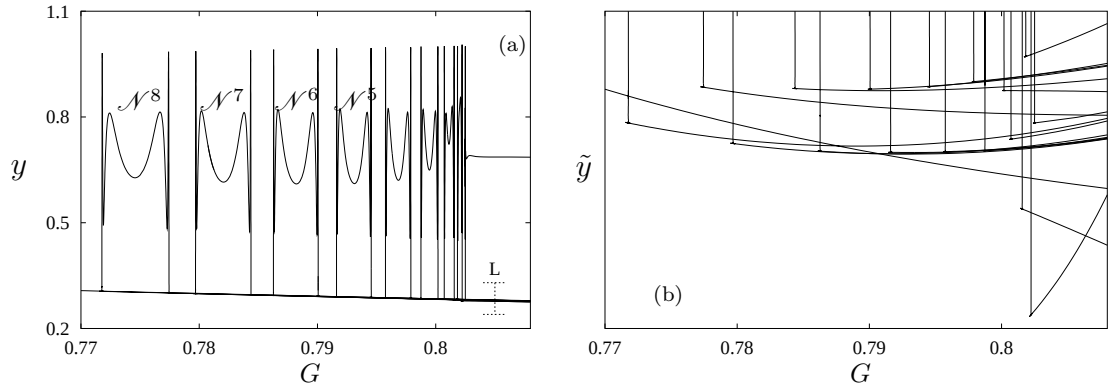

Figure 2.34: (a) A larger portion K (see text). (b) Magnification of a thin horizontal layer labelled by L in (a), showing coexistence of a lot of different branches of saddle fixed points.

2.4.5 On quasi-periodic Hopf bifurcations

For $\varepsilon = 0$ (Figure 2.3), the repelling circle $\mathscr{C}$ loses stability at quasi-periodic Hopf bifurcations belonging to the curve $\mathcal{QH}_{sub}$ (Sec. 15).

For $\varepsilon = 0.5$, numerical experiments reveal that $\mathscr{C}$ persists both for G small and for G large and is attracting in the former and repelling in the latter case. We recall that the attractor $\mathscr{C}$ is born at the Hopf curve $\mathcal{H}_1$, while the repellor $\mathscr{C}$ at the subcritical Hopf curve $\mathcal{H}_1^{sub}$ (Secs. 2.4.2 and 2.4.3). Thus at $\varepsilon = 0.5$ there appear gaps in the parameter plane where $\mathscr{C}$ does not persist, being replaced by strange attractors or repellors, or by nothing at all (in the latter case, by iteration only the fixed point $\mathscr{A}$ is detected). These gaps are roughly located around the position where the frayed curve $\mathcal{QH}_{sub}$ (Sec. 15) is expected to intersect the current line $F = const$ inside $\mathfrak{M}_\varepsilon$. We illustrate this by means of iteration to an attractor or repellor for $F = 5$ fixed, in Figure 2.35. The left part $G < 1.5$ is just a different projection of Figure 2.1 (d). The attracting fixed point $\mathscr{A}$, however, is represented also for larger G. In the right upper part ($G > 2$ and $z > -1$), P-repellors are plotted. The algorithm is the same as usual, but this time G is decreased and P^{-1} is iterated, to detect repellors. This way we perform a rough continuation scheme, for more accurate methods see Sec. 2.A.

To begin, the fixed point repellor $\mathscr{R}$ is found at $G = 6$. As G decreases, $\mathscr{R}$ undergoes a Hopf bifurcation at $G \simeq 5.71$, at a point belonging to curve $\mathcal{H}_1^{sub}$ in Figure 2.3. The circle repellor $\mathscr{C}$ persists down to $G \simeq 2.13$ (marked by an arrow in Figure 2.35), where it undergoes one quasi-periodic period doubling. A circle repellor $2\mathscr{C}$ is created, persisting down to $G \simeq 2.01$. At $G = 2$ one finds a strange repellor, but no repelling invariant set is found for smaller G. The precise scenario for the destruction of the strange repellor is not clear at the present moment.

At the other side of Figure 2.35, the circle attractor $\mathscr{C}$ is found at $G = 0$. Increasing G, the circle persists up to $G \simeq 0.65$ (marked by an arrow). strange attractors are detected for $0.66 \lessapprox G \lessapprox 1.3$, now and then replaced by windows of periodicity. For $G \gtrapprox 1.3$, the fixed point $\mathscr{A}$ is the unique attractor. No invariant circle (either attracting or repelling) is detected for $G \in (0.66, 2)$. However, an invariant circle of saddle type might persist in this gap (at least for most of the G values), thereby providing the

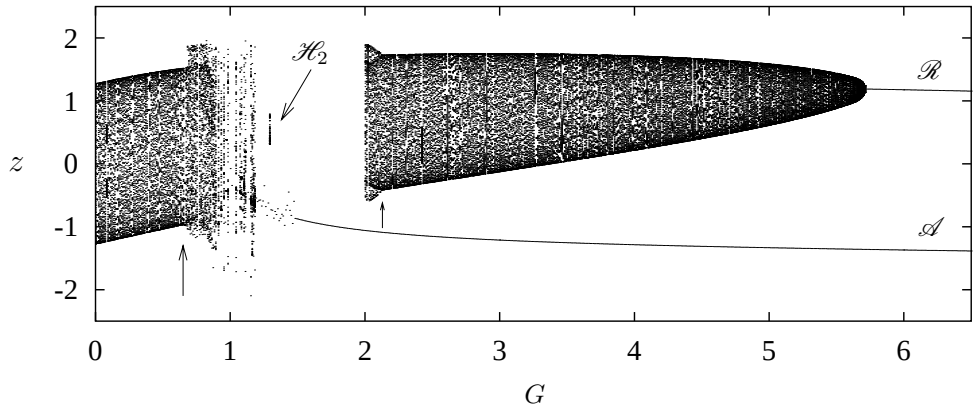

Figure 2.35: Projection on (G, z) of sequences of repellors and attractors of P for $F = 5$ and $\varepsilon = 0.5$. See text for explanation. The attractor $\mathscr{H}_2$ is plotted in Figure 2.51.

'link' between circle attractor and repellor.

The size of these gaps is not as large for other values of F. For $F = 4$, the circle $\mathscr{C}$ seems to exist for all values of G between 0 and 4.51, thus forming a one parameter family $\mathscr{C}(F_0, G)$ with $F_0 = 4$. This is illustrated in Figure 2.36 left, where we plotted attractors and repellors of P. The invariant set projected in the cigar-shaped region is the circle $\mathscr{C}$. For $G < 1.615$ (marked by an arrow), $\mathscr{C}$ is attracting and has been detected as for Figure 2.1. For $G > 1.615$, $\mathscr{C}$ is repelling and has been obtained as for Figure 2.35, using the inverse of P and letting G decrease. Although a quasi-periodic Hopf bifurcation might occur at $G > 1.615$ (where $\mathscr{C}$ changes stability), no invariant repelling torus could be detected. For all F-values in Figure 2.36 (left), the rotation number (modulo 1/2) of $\mathscr{C}$ is plotted on the right. It repeatedly takes on all values between zero and one, the number of complete oscillations tells how many times. This means that the Arnol′d tongues are crossed transversally, agreeing with the orientation as deduced from Figure 2.25 (right).

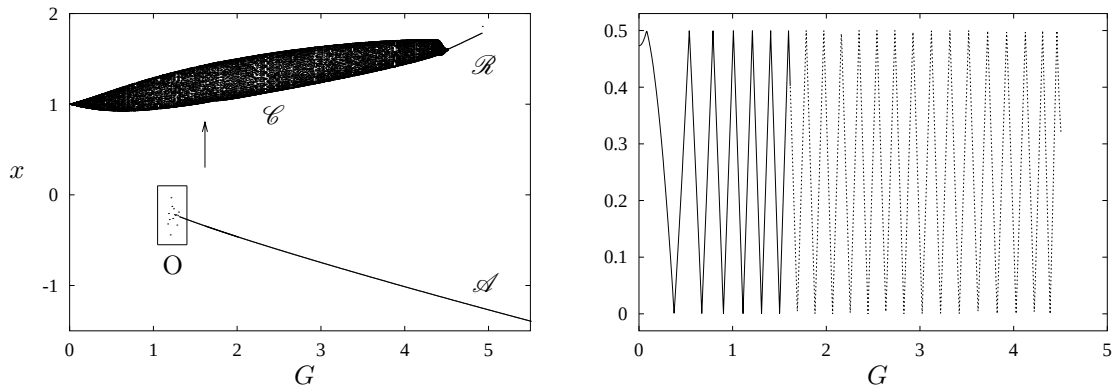

Figure 2.36: Left: projection on (G, x) of sequences of repellors and attractors for $F = 4$ and $\varepsilon = 0.5$. The picture has been obtained as Figure 2.35. Right: rotation number modulo 1/2 on $\mathscr{C}$, along the family plotted in the left picture.

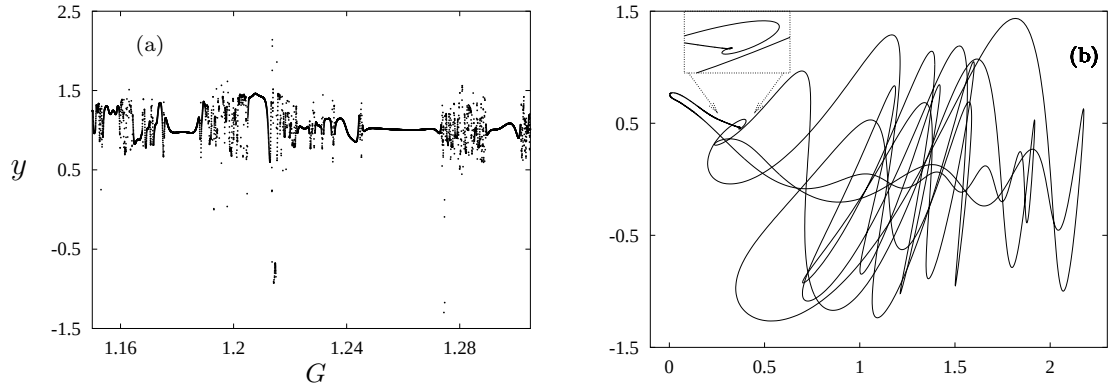

Figure 2.37: (a) Magnification of box labelled by O in Figure 2.36. Periodic points of P for $F = 4$ and G on a grid with spacing $2.e - 5$. For a few, sparse G-values, no periodic point is detected (see text). (b) Projection on (x, y) of a period T saddle limit cycle of $\Psi_{F,G,\varepsilon}$, corresponding to a saddle fixed point of P coexisting with the strange attractor in Figure 2.38 (a) at $G = 1.274585$.

2.4.6 Coexistence of attractors and saddles in $\mathfrak{U}'$

The projection in Figure 2.36 (left) has been chosen to illustrate coexistence of the attractors $\mathscr{C}$ and $\mathscr{A}$ in the G-interval $(1.17, 1.615)$. Close to $G = 1.17$ (box indicated by O), the coordinates of $\mathscr{A}$ are sensitive to changes in G. This is illustrated by a magnification of box O (Figure 2.37 (a)) obtained as follows. Parameter values are chosen on a vertical line intersecting region $\mathfrak{U}'$. In particular, F is fixed at 4 and G varies on a grid with spacing 2×10^{-5}. The map $P_{F,G}$ is iterated starting from the point $(x, y, z) = (-0.246612612, 1.006751225, -0.762249262)$. If there is convergence to a periodic point within 100 iterations, the (G, y) coordinates of the final point are plotted. We see relatively large G-intervals with an attracting fixed point, where the evolution of its y-coordinate is rather regular. At the extremes of such intervals, regions occur where the y-coordinate evolves wildly. The limit cycles of $\Psi_{F,G,\varepsilon}$ corresponding to these periodic points are of spiral type (Sec. 2.4.4).

In fact, the distribution of the fixed point attractors Figure 2.37 (a) is similar to Figure 2.34 (a). All branches of attracting fixed points are connected by branches of saddle fixed points. The limit cycles of $\Psi_{F,G,\varepsilon}$ corresponding to these saddles are also of spiral type (Figure 2.37 (b)). Several branches of saddle fixed points coexist in a G-interval; compare Figure 2.34 (b). For some parameter values no periodic attractor occurs. In this case, the P iterates converge either to the circle $\mathscr{C}$, or to some narrow Hénon-like attractor coexisting with $\mathscr{C}$, like $\mathscr{H}_3$ in Figure 2.38 (a). We stress that the statement about the Hénon-like character of numerically observed strange attractors is conjectural. See the discussion in Chapter one, and compare Remark 1.1. This explains the sparse white spots in $\mathfrak{U}'$, compare Figure 2.2 (b) and Figure 2.5 (right). Notice that the same type of Hénon-like attractor and the same structures of fixed point attractors/saddles occur in region $\mathfrak{U}$ (Sec. 2.4.10). In fact, the only difference is that no Shil′nikov-like attractors seem to occur in $\mathfrak{U}'$. Long chaotic transients are often observed (Figure 2.38 (b)), having the shape of Shil′nikov-like attractors. However they usually converge to the circle $\mathscr{C}$ or to a periodic or to a narrow Hénon-like

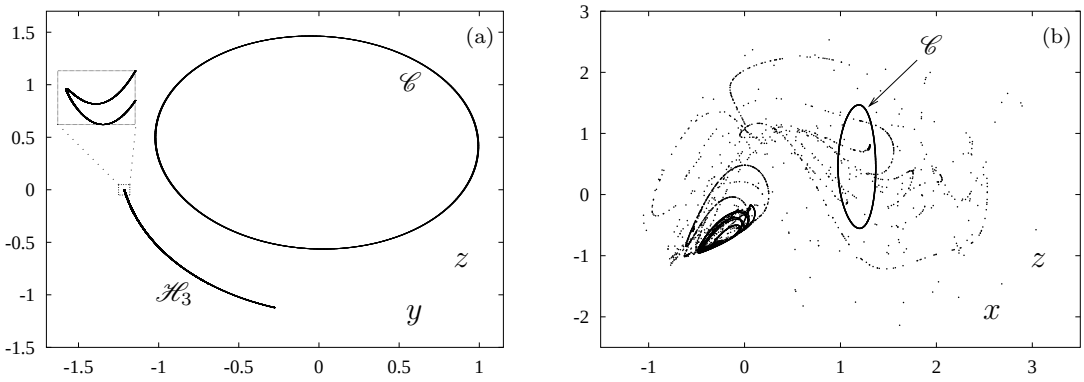

Figure 2.38: (a) Projection on (y, z) of the circle attractor $\mathscr{C}$ and of a Hénon-like attractor $\mathscr{H}_3$, coexisting at $(F, G) = (4, 1.274585)$. Initial conditions for $\mathscr{C}$ are $(x, y, z) = (1.14, -0.28, 1.4)$. (b) Projection on (x, z) of a chaotic transient of 69000 P-iterates at $(F, G) = (4, 1.30238)$, followed by convergence to the circle attractor $\mathscr{C}$. Initial point $(x, y, z) = (-0.367134395447287,\ 0.569918317744214,\ -0.883182668387643)$.

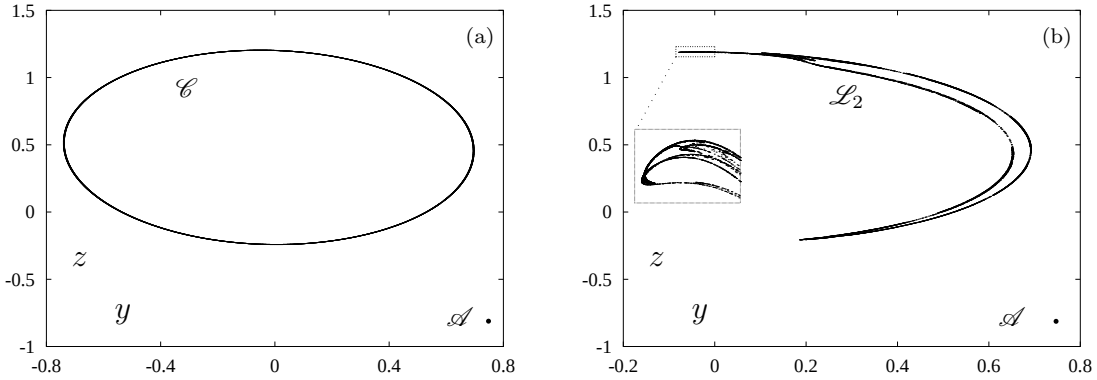

Figure 2.39: (a) Projection on (y, z) of the circle attractor $\mathscr{C}$, coexisting with the fixed point $\mathscr{A}$ at $(F, G) = (3, 1.4905)$. Initial conditions are $(x, y, z) = (1.3, 0.35, 1)$ for $\mathscr{C}$ and $(1, 2, 3)$ for $\mathscr{A}$. (b) Same as (a), with the strange attractor $\mathscr{L}_2$ at $G = 1.494$.

attractor. So, the disappearance of the invariant circle $\mathscr{C}$ seems to be a necessary condition for the occurrence of Shil′nikov-like attractors.

Above region $\mathfrak{U}'$, the fixed point $\mathscr{A}$ may coexist with $\mathscr{C}$ or with a strange attractor originating from the breakdown of $\mathscr{C}$. In both of the above regions, the fixed point $\mathscr{A}$ may coexist with a strange attractor as well. This is the case for the attractor $\mathscr{L}_2$ in Figure 2.39 (b), which is a folded circle (see Sec. 2.4.8), created in the following way. The circle $\mathscr{C}$ is locked to a fixed point in the G-interval $1.462 \lessdot G \lessdot 1.508$. The fixed point undergoes a Hopf bifurcation as G decreases through $G \simeq 1.4975$. At this point, $\mathscr{C}$ is broken and a new attracting circle $\widetilde{\mathscr{C}}$ appears. The latter circle enters an Arnol′d tongue of high period and breaks down inside it because of a homoclinic tangency and $\mathscr{L}_2$ is born.

This and other scenario's for the breakdown of a circle are described in the next section.

2.4.7 Mathematical intermezzo: breakdown of invariant circles and the creation of strange attractors

A large fraction of the strange attractors of $P_{F,G}$ at $\varepsilon = 0.5$ in regions $\mathfrak{L}_2$ and $\mathfrak{L}_1$ originates from the breakdown of an attracting invariant circle. (see Figure 2.6, 2.7 and 2.39 (b)). We devote this section to a summary of the known phenomenology for the destruction of an invariant circle in dissipative diffeomorphisms. For detailed studies, see [1, 7, 3, 8, 7, 23, 93].

Consider a two-parameter family of diffeomorphisms $Q_{F,G}$ of $\mathbb{R}^n$, having a curve $\mathcal{H}$ of Hopf bifurcations of fixed points. In Figure 2.40 we sketch the 'generic' semi-global structure of the parameter space close to an Arnol′d tongue. Two curves $\mathcal{SN}$ of saddle-node bifurcations emerge from a resonant point $\mathcal{R}$ on $\mathcal{H}$ and form the boundary of an Arnol′d tongue $\mathfrak{A}^{p/q}$ of period q. Outside $\mathfrak{A}^{p/q}$, and for (F, G) close to $\mathcal{H}$, the map $Q_{F,G}$ has a quasi-periodic attracting circle. We describe the routes occurring along the dashed paths starting at parameter values on the point $\mathcal{P}$, inside $\mathfrak{A}^{p/q}$. There, the circle $\mathscr{C}$ is phase-locked, meaning that $\mathscr{C}$ is formed by the union of an attracting periodic point $\mathscr{A} \cup W^u(\mathscr{B})$. Here $\mathscr{A}$ and $\mathscr{B}$ are periodic points born at the curve $\mathcal{SN}$, where $\mathscr{A}$ is an attractor and $\mathscr{B}$ is a saddle. For regularity properties of such resonant circle, see *e.g.* [23]. Moving along path A, at curve $\mathcal{D}$ the attractor $\mathscr{A}$ loses stability through a codimension one bifurcation. This might be a period doubling, but also a Hopf bifurcation, compare Figure 2.39. No strange attractors are created at this moment. This only occurs when crossing the critical curve $\mathcal{CR}_1$, which, for example, might be the boundary of a cascade of period doublings.

Along path B, at the curve $\mathcal{T}$ a tangency of the stable and unstable manifolds of the saddle $\mathscr{B}$ occurs. The circle is destroyed, but no strange attractor appears yet, since the point $\mathscr{A}$ is always stable between curves $\mathcal{SN}$ and $\mathcal{D}$. Strange attractors appear on path B1, when coming out of the tongue. Here, intermittency of type I is usually observed close to $\mathcal{SN}$ (this is what happens in Figure 2.6). The 'curve' $\mathcal{CR}_2$ corresponds to the creation of a non-smooth circle from $\mathscr{C}$ and has a complicated fractal structure [2, 23]. Along path C1, there is a sudden transition between a periodic attractor and a non-smooth circle strange attractor. Path C corresponds to the bifurcation from a locked to a quasi-periodic circle. Notice that all kinds of 'composite' routes can be observed. For example, there can be a finite number of period doublings, followed by a homoclinic tangency (path A1, see *e.g.* [23, 124]).

Remark 2.11. Our description only covers the main details in the most simple case. For example, along path B, the circle is usually destroyed before the homoclinic tangency on curve $\mathcal{T}$. Indeed, the latter may occur after a cubic and a quadratic tangency of the unstable manifold of the saddle periodic point with the strong stable foliation. For more details, see [23, 93].

We now list some other routes to chaos. In the Díaz–Rocha–Viana scenario [42], the unstable manifold of a saddle-node periodic point has a quadratic tangency with the strong stable foliation. Here, parameter values lie at the border of an Arnol′d tongue. Just outside the tongue, Hénon-like strange attractors occur, winding around the whole annulus containing the unstable manifold of the saddle-node. Such attractors are called 'large'. Large attractors were also studied in [13], in connection with a Shil′nikov-Hopf bifurcation.

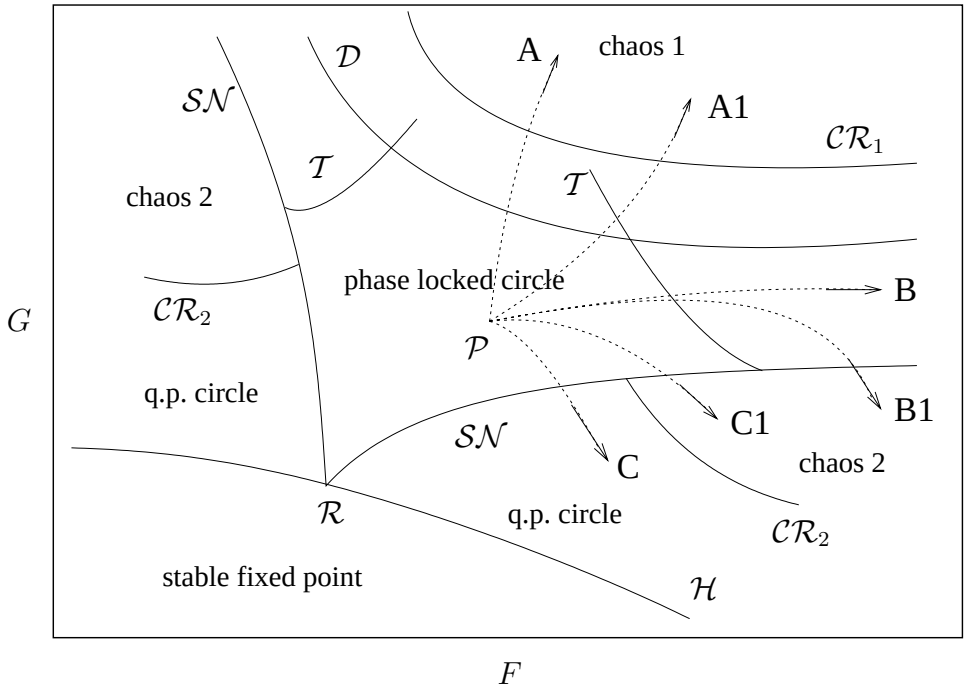

Figure 2.40: Dashed paths labelled by A, A1, B, B1, C1 indicate several routes to the breakdown of an invariant circle of $Q_{F,G}$, born from a fixed point at a curve $\mathcal{H}$ of Hopf bifurcations (see text for the notation). Figure taken from [2].

Finally, other dynamical objects could interact with the circle $\mathscr{C}$, for example through heteroclinic tangencies. This is the typical way in which the size of a strange attractor suddenly grows [104].

We have mainly distinguished four regions inside $\mathfrak{M}_{0.5}$ where strange attractors occur. In $\mathfrak{L}_1$ and $\mathfrak{L}_2$, the appearance of strange attractor is typically due to homoclinic tangencies inside an Arnol′d tongue (routes A1 and B1 in Figure 2.40) or period doubling (route A). Loss of smoothness (route C1) is more difficult to observe, given the ubiquitous occurrence of resonances of high order. In $\mathfrak{L}_2$, interaction with a quasi-periodic period doubling bifurcations leads to attractors of dimension higher than two. A different scenario leads to birth of strange attractors in $\mathfrak{U}$ and $\mathfrak{U}'$, probably due to a Shil′nikov tangency bifurcation. For a classification of the strange attractors of $P_{F,G}$, see Sec. 2.4.11.

2.4.8 The chaotic range $\mathfrak{L}_1$

We consider the region above the tongue $\mathfrak{A}^0$ of period one in Figure 2.5. There the parameter plane is crossed by several, relatively large Arnol′d tongues of higher periods. The circle $\mathscr{C}$ often breaks and strange attractors appear similar to $\mathscr{L}_1$ (Figure 2.6 (B)), with Lyapunov dimension slightly larger than one. Two views of this chaotic range are given in Figure 2.41 and Figure 2.43. The intervals where the maximal Lyapunov exponent λ_1 drops to negative values are Arnol′d tongues. In Figure 2.41 (b), a period k attractor occurs on intervals pointed by an arrow with label k. For small G (left of

the picture), $\mathscr{C}$ appears to persist, since λ_1 is approximately zero outside the tongues. A large Hénon-like attractor occurs at $G = 0.408$ (label $\mathscr{L}$ in Figure 2.41 (b)), a folded circle like $\mathscr{L}_1$ (Figure 2.6 (B)). Periodic points are detected for most parameter values near $G = 0.408$, with period ranging from 28 up to a few hundreds. For G larger, λ_1 increases and strange attractors are found more frequently. An arrow in Figure 2.41 (b) indicates the G-value at which $\mathscr{L}_1$ occurs, just outside an Arnol′d tongue $\mathfrak{A}_5$ of period five. A saddle-node bifurcation at the edge of $\mathfrak{A}_5$ destroys $\mathscr{L}_1$, locking it to a period five attractor. Notice that a period doubling occurs at $G = 0.4116$, followed by a period halving at $G = 0.4128$. The two bifurcations, where $\lambda_1 = 0$, bound a period 10 tongue $\mathfrak{A}_{10}$ inside $\mathfrak{A}_5$ (Figure 2.41 (a)).

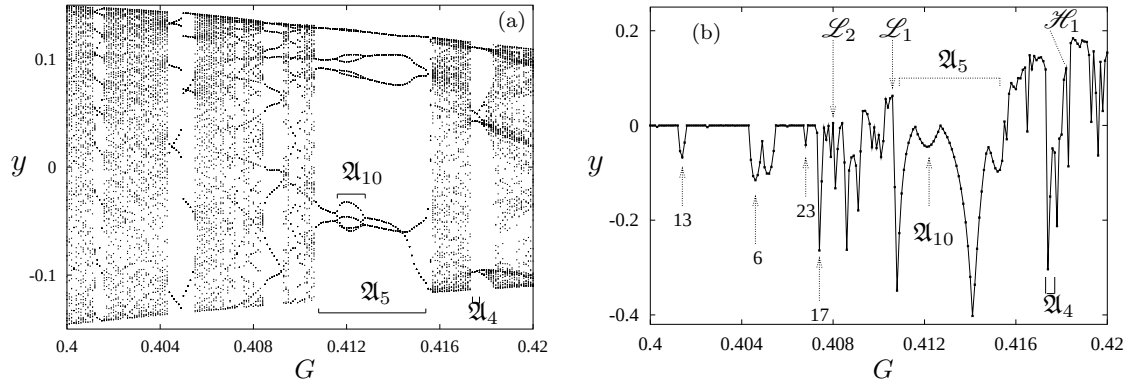

Figure 2.41: (a) Projection on y of sequences of P-attractors as a function of G, for $F = 1.25$ fixed. The last 100 points of each iteration loop are plotted, the step in G is 10^{-4}. See text for explanation. (b) Maximal Lyapunov exponent on the attractors in (a).

Inside the Arnol′d tongues, period doublings also may occur in entire cascades. The four-piece strange attractor $\mathscr{H}_1$ in Figure 2.42 (a) is created by this mechanism, which corresponds to route A in Figure 2.40. At $G = 0.4175$ the map P has a period four attractor inside the tongue $\mathfrak{A}^{1/4}$ (Figure 2.41 (a) and (b)). Then, at $G = 0.4177$ and $G = 0.4179$ period 8 respectively 16 points occur, followed by a whole period-doubling cascade, and $\mathscr{H}_1$ appears. Notice that each of its four components is obviously Hénon-like (component 1 is magnified in Figure 2.42 (b)). Component k is mapped by P to $k + 1$ for $k = 1, 2, 3$ and 4 is mapped to 1.

Another four-piece Hénon-like attractor occurs at $G = 0.4182$, but folded circles like $\mathscr{L}_1$ reappear for larger G, from the fusion of the various pieces. The fusion of the parts of a multi-piece attractor is usually due to heteroclinic tangencies, see [104].

So far, the Lyapunov dimension $\mathrm{D_L}$ of the attractors is still close to one. However, $\mathrm{D_L}$ can grow above two for parameter values further inside $\mathfrak{L}_1$. In Figure 2.43 (a) sequences of attractors are plotted for $G = 0.5$ fixed and F increasing from 1, where the fixed point $\mathscr{A}$ is detected. Notice that the maximal Lyapunov exponent λ_1 (Figure 2.43 (b)) increases linearly, until a Hopf bifurcation[20] $\mathcal{H}$ occurs at $F \simeq 1.08$ and the circle attractor $\mathscr{C}$ is created. Although $\mathscr{C}$ is not visible in Figure 2.43 (a) (because of its small size, compare Remark 2.9), its presence is revealed by the Lyapunov

[20] Belonging to the curve $\mathcal{H}_1$ in Figure 2.5 (left), Sec. 2.1.3.

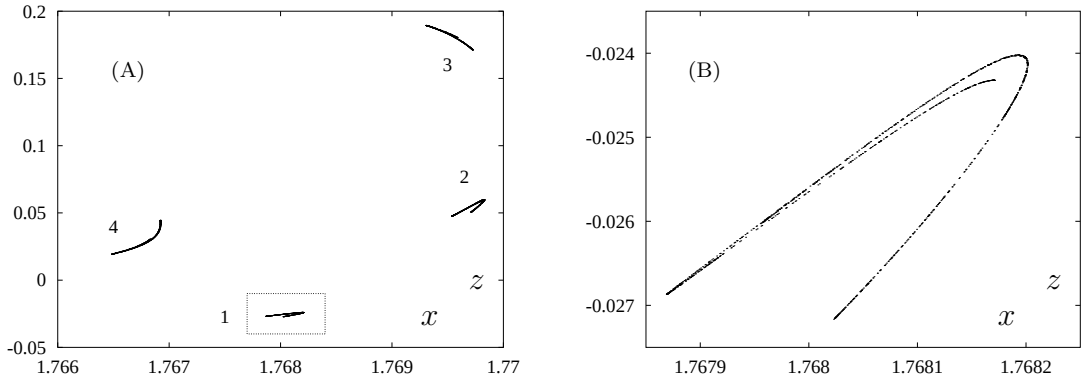

Figure 2.42: (A) Projection on (x, z) of the Hénon-like strange attractor $\mathscr{H}_1$ of P for $(F, G) = (1.25, 0.4181)$. (B) Magnification of one component.

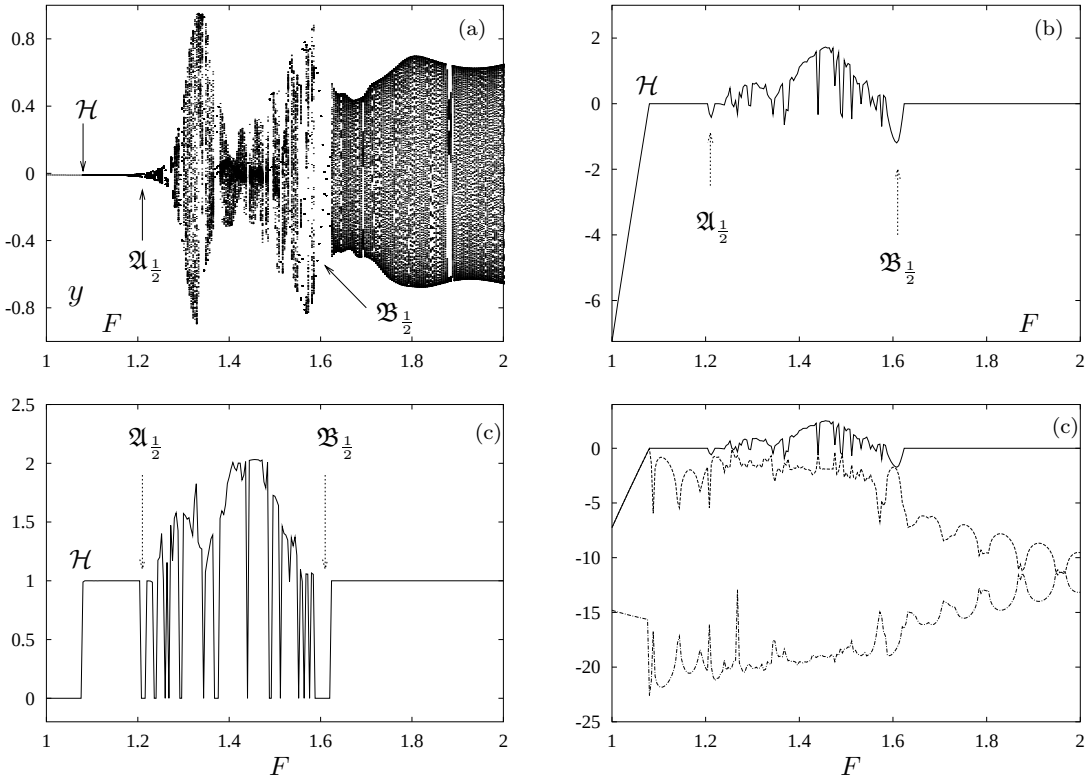

Figure 2.43: (a) Projection on y of sequences of P-attractors as a function of F for $G = 0.5$ fixed. The step in F is 0.004 and 2×10^5 iterates of DP were computed for each F. Two Arnol′d tongues $\mathfrak{A}_{\frac{1}{2}}$ and $\mathfrak{B}_{\frac{1}{2}}$ of rotation number 1/2 are pointed by an arrow. (b) Maximal Lyapunov exponent on the attractors in (a). (c) Lyapunov dimension of the attractors in (a). (d) The three Lyapunov exponents on the attractors in (a).

dimension (Figure 2.43 (c)), which jumps to one at $\mathcal{H}$. An Arnol′d tongue of rotation number 1/2 is labelled by $\mathfrak{A}_{\frac{1}{2}}$. Then $\mathscr{C}$ breaks and strange attractors occur in the interval $1.2 \lessdot F \lessdot 1.7$. Close to the extremes of the interval, the Lyapunov dimension is not much larger than one and the corresponding strange attractors are folded circles.

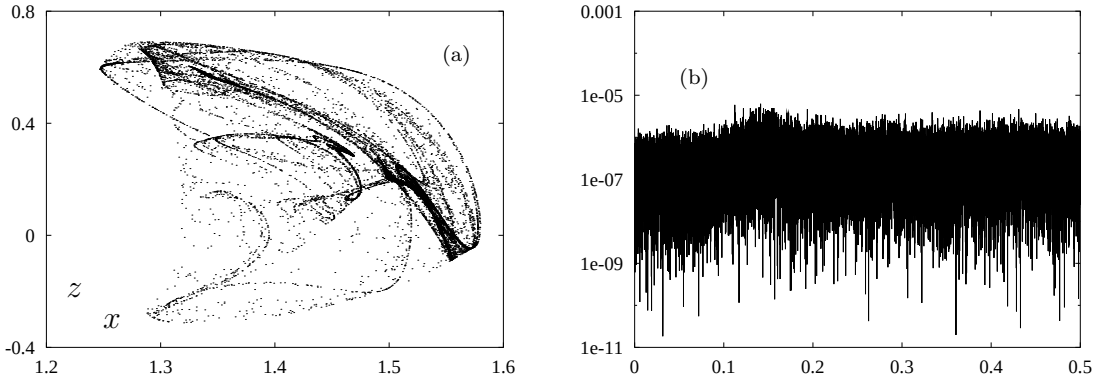

Figure 2.44: (a) Projection on (x, z) of a P-attractor, which we name $\mathscr{X}_1$, occurring in $\mathfrak{L}_1$ at $(F, G) = (1.5, 0.5)$. (b) Power spectrum of $\mathscr{X}_1$.

In the central part, the structure of the attractors is more complicated, displaying interaction with other dynamical objects. Intermittency phenomena disappear from the power spectra and the Lyapunov dimension is larger. An attractor ($\mathscr{X}_1$) occurring in this parameter range is plotted in Figure 2.44. Some one-dimensional structure is still preserved in the form of several invariant folded curves crossing $\mathscr{X}_1$. However, the power spectrum indicates uncorrelation of the iterates (Remark 2.12) and the Lyapunov dimension is ~ 1.6. At the other extreme of the chaotic interval, a tongue $\mathfrak{B}_{\frac{1}{2}}$ with rotation number $1/2$ occurs, and the circle $\mathscr{C}$ reappears for $F \geqslant 1.7$.

It is well known [104] that the evolution of strange attractors is a process of birth and death (sometimes called 'crisis' [54]). This is clearly seen in Figures 2.41 and 2.43. strange attractors are first created by homoclinic tangencies, then disappear because of the birth of a hyperbolic periodic attractor through a saddle-node bifurcation. They may reappear in multi-piece form due to doubling cascades, then the various pieces melt by heteroclinic tangencies and, eventually, the strange attractor might grow in size due to further heteroclinic tangencies. A perhaps less known scenario is described in the next section.

2.4.9 The chaotic range $\mathfrak{L}_2$

This chaotic region lies in the half-plane $F \geqslant 5$ inside $\mathfrak{M}_{0.5}$. Most strange attractors in $\mathfrak{L}_2$ originate at the breakdown of a doubled circle $2\mathscr{C}$, the latter created through one quasi-periodic period doubling of $\mathscr{C}$. For this reason, we begin by describing this bifurcation.

Quasi-periodic period doubling

The quasi-periodic period doubling of an invariant curve can occur in two different ways [32] and both have been found in the family $P_{F,G}$. The first is illustrated in Figure 2.45, for $F = 11$ fixed. At $G = 0.4972$ the circle attractor $\mathscr{C}$ is detected. Here $\mathscr{C}$ is still normally hyperbolic, with quasi-periodic dynamics, but it is close to loss of normal hyperbolicity. Indeed, the maximal Lyapunov exponent λ_1 is zero, while λ_2 is negative and close to zero (Table 2.4). The peak at the fundamental frequency

	D_L	λ_1	λ_2	λ_3	e_1	e_2	e_3
A	1	-5.e-6	-0.0066	-14.8	6.e-7	2.e-6	1.e-6
B	1	4.e-5	-0.08	-14.7	5.e-6	5.e-6	1.e-6

Table 2.4: Lyapunov exponents of the circle attractors in Figure 2.45 (A) and (B).

$f_1 = 0.377$ of $\mathscr{C}$ is labelled by 2 in Figure 2.45 (a). Peaks marked by $2k$ occur at harmonics $f_k = k\, f_1$ of the fundamental frequency.[21] When λ_2 goes through zero, $\mathscr{C}$ undergoes a quasi-periodic period-doubling. A circle attractor $2\mathscr{C}$ is created, of roughly double length and half the rotation number of $\mathscr{C}$ (Figure 2.45 (B)). In this bifurcation, only λ_2 crosses zero: the lowest Lyapunov exponent λ_3 of both $\mathscr{C}$ and $2\mathscr{C}$ is less than -14 (Table 2.4). After the doubling, $\mathscr{C}$ still coexists with $2\mathscr{C}$, but it is unstable. The power spectrum of $2\mathscr{C}$ inherits all harmonics of a frequency close to f_1. Furthermore, new peaks appear at uneven multiples $g_k = kg_1$ of the fundamental frequency $g_1 \approx f_1/2$ of $2\mathscr{C}$ (each harmonic g_k is labelled by k in Figure 2.45 (b)). Again, because of the mirroring one has $g_1 = 1/2(f_1 \ \mathrm{mir}\,\frac{1}{2}) = 0.3115$. It is also possible to identify small peaks corresponding to g_1, g_2 and g_3 in Figure 2.45 (a). This is due to intermittency of type III.

For the family $P_{F,G,0.5}$, the circle $\mathscr{C}$ often undergoes similar doublings in the interval $5 \lessapprox F < 12$. Each of these bifurcation points belongs to a frayed curve as described in Sec. 15. For some F values, $2\mathscr{C}$ may undergo a doubling as well, but a different type of bifurcation occurs. This is illustrated in Figure 2.46, again for $F = 11$ fixed. At $G = 0.4958$ the circle $2\mathscr{C}$ is detected (Figure 2.46 (A)). All peaks in the power spectrum occur on harmonics of the fundamental frequency $g_1 = 0.32579$. The first five harmonics $g_k = kg_1$ are labelled by k in Figure 2.46 (a). Between $G = 0.4958$ and 0.4959, $2\mathscr{C}$ turns into a saddle invariant curve and two curves are created, each of them attracting and invariant under P^2. The union of these two curves is the P-attractor $4\mathscr{C}$, plotted in Figure 2.46 (B) (also see Figure 2.7 in Sec. 2.1.3). The dynamics of P on $4\mathscr{C}$ is the skew product of an invariant curve and a period two point. In other words, the P-iterates jump from one curve to the other and back, so we call $4\mathscr{C}$ a period two curve. Therefore, the dynamics has two fundamental frequencies, one of which is 0.5, the other is close to the frequency of $2\mathscr{C}$ and is again called g_1. In fact, all harmonics of g_1 are found in the power spectrum of $4\mathscr{C}$, while the 'new' harmonics h_k correspond to $0.5 - g_k$ (Figure 2.46 (b)).

For other values of $F < 12$, at most two consecutive doublings were observed (just as above). A complete cascade does not take place, see next section.

We note that the centre manifold of the period doubling is a two-dimensional Möbius strip [31, 99]. As a result, the breakdown of a doubled circle is almost invariably followed by the creation of a strange attractor with a two-dimensional Möbius-like structure. Examples of this are presented in Sec. 21.

[21] In particular, f_k is obtained modulo 1 for $k = 6, 10, 12, 16, 18, 20, 22$, whereas for the remaining harmonics one gets $f_k \ \mathrm{mir}\,\frac{1}{2}$.

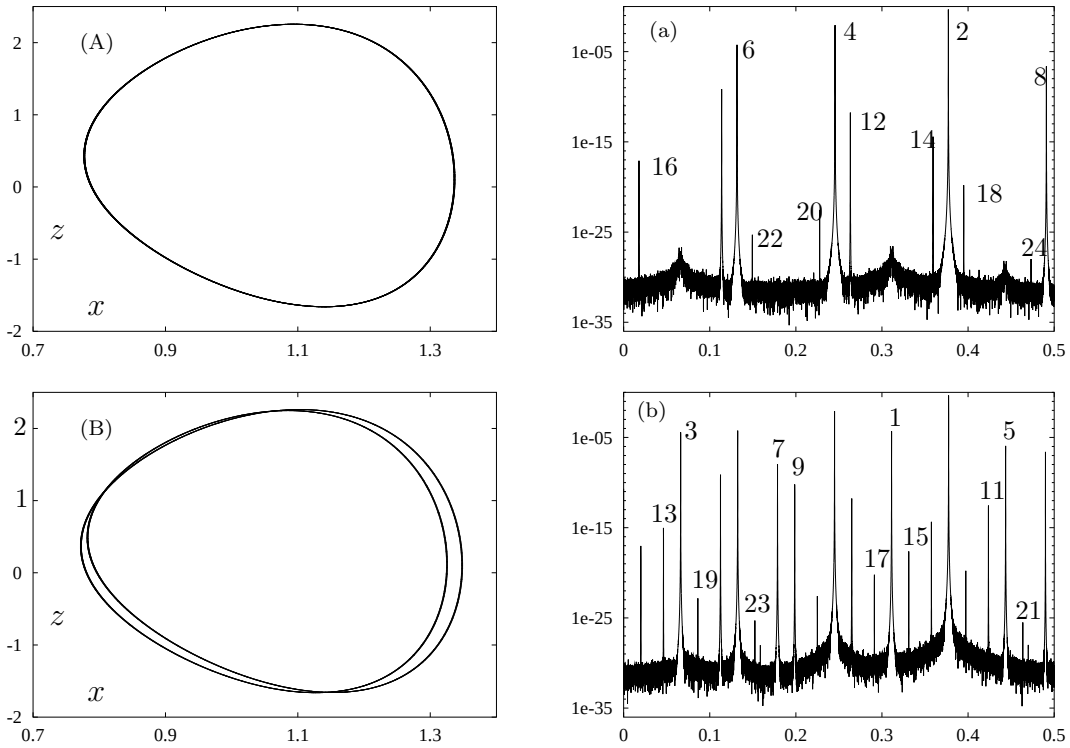

Figure 2.45: (A), (B) Projections on (x, z) of circle attractors of $P_{11,G,0.5}$ for $G = 0.4872$ and $G = 0.4874$ respectively. (a), (b) Power spectra of the attractors.

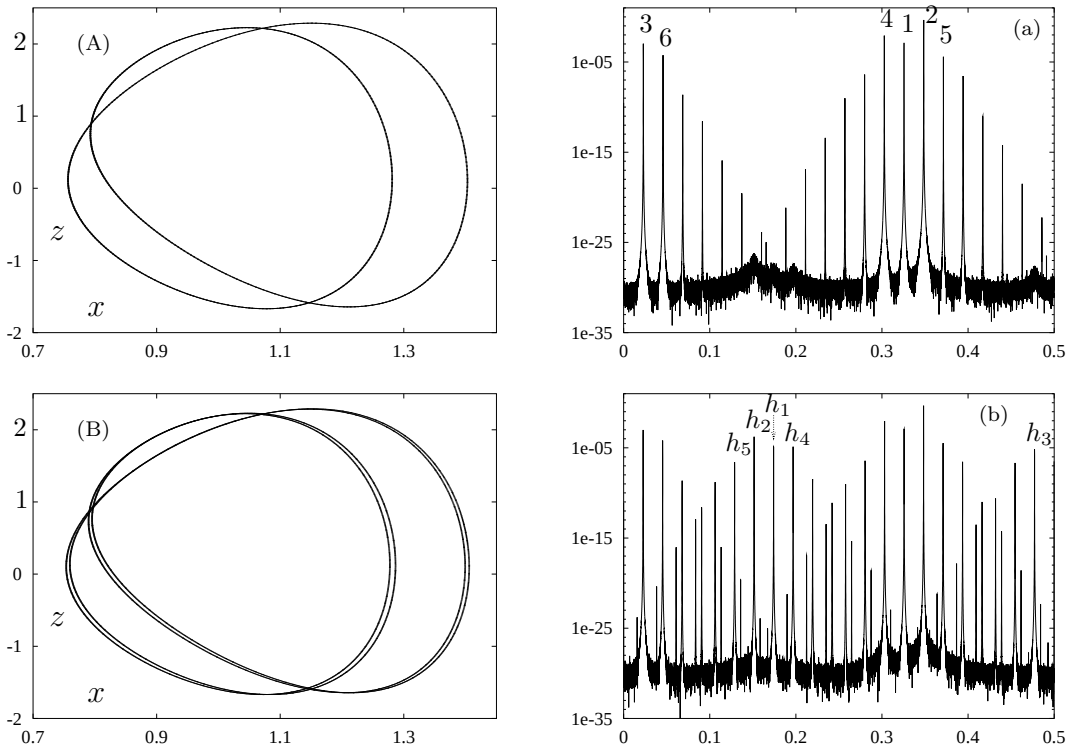

Figure 2.46: (A), (B) Projections on (x, z) of attractors of $P_{11,G,0.5}$ for $G = 0.4958$ and $G = 0.4959$ respectively. (a), (b) Power spectra of the attractors.

Arnol′d tongues and breakdown of circles in $\mathfrak{L}_2$

The structure of region $\mathfrak{L}_2$ is in fact rather similar to that of $\mathfrak{L}_1$. In both regions, fixed and periodic points are organised in intricate structures of Arnol′d tongues. This is illustrated in Figure 2.47 (left) (compare with Figure 2.5 (right)), where we plot a magnification of Figure 2.2 (b), obtained by taking a smaller window and a finer spacing of the grid. A few edges of tongues (saddle-node bifurcation curves) of low period are plotted in Figure 2.47 (right). Several cusps are found on most saddle-node curves. A Hopf bifurcation curve $\mathcal{H}$ was detected, interrupted by three 1:1 and three 1:2 resonance points. At the 1:1 resonance points, a saddle-node curve $\mathcal{S}$ is tangent to $\mathcal{H}$, whereas a period doubling curve $\mathcal{D}$ is tangent to $\mathcal{H}$ at the 1:2 points. Furthermore, $\mathcal{D}$ and $\mathcal{S}$ are tangent to each other at the codimension two saddle-node-period-doubling point $\mathcal{SPD}$. See [79] for a study of this type of bifurcation. The occurrence of the Arnol′d tongues is quite similar to that found in the fattened

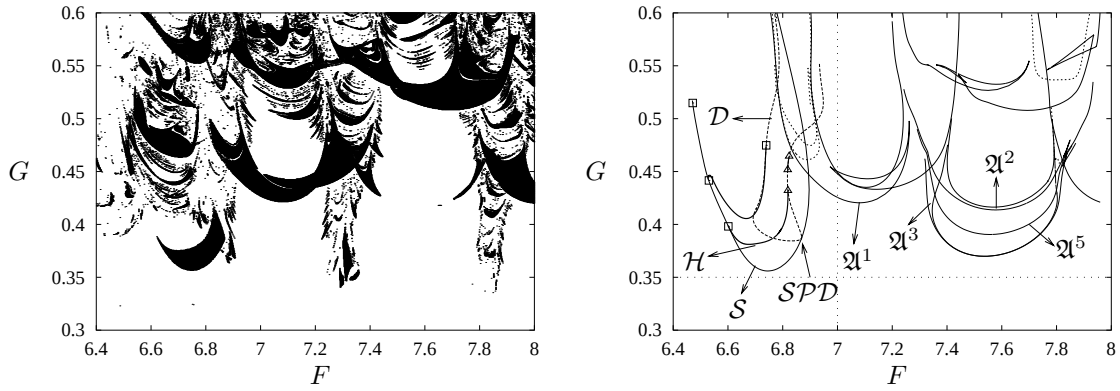

Figure 2.47: Left: Magnification of Figure 2.2 (b), obtained with a grid of spacing 2×10^{-3} in F and 5×10^{-4} in G. A maximum of 150 iterates of P were executed, starting from $(x, y, z) = (1, 2, 3)$. Right: Arnol′d tongues of period k are labelled by $\mathfrak{A}^k$ for $k = 1, 2, 3, 5$. The other solid curves are saddle-node bifurcations of fixed points. Dashed curves are period doublings of a fixed point. A Hopf curve $\mathcal{H}$ is plotted with a thick solid line. On $\mathcal{H}$, the 1:1 and 1:2 resonance points are marked by small boxes respectively triangles.

Arnol′d family [23]. One sees that the edges of the bifurcation curves accumulate on each other as G increases. This is probably due to the same mechanism as described in [23], which may possibly be a route for the creation of infinitely many sinks (the Newhouse phenomenon [87, 96]).

The resonant circle inside the tongues in Figure 2.47 is $2\mathscr{C}$. In fact $\mathscr{C}$ has undergone a doubling at lower values of G and possibly persists as a saddle circle. The breakdown of $2\mathscr{C}$ happens according to what discussed in Sec. 2.4.7. Therefore, the 'curve' of breakdown of $2\mathscr{C}$ (which we sketched by curve $\mathcal{B}$ in Figure 2.4) has a complicated fine structure (compare [23]). This is illustrated by a plot of the Lyapunov exponents λ_1 and λ_2 (Figure 2.48) along the two dashed lines in Figure 2.47 (right).

For $F = 7$ (Figure 2.48 (a)), the circle $2\mathscr{C}$ persists beyond the tongue $\mathfrak{A}^1$ in Figure 2.47 (right). The first strange attractor found increasing G is labelled by $\mathscr{L}$ and is a folded circle. However, for $G = 0.35$ (Figure 2.48 (b)) three intervals appear

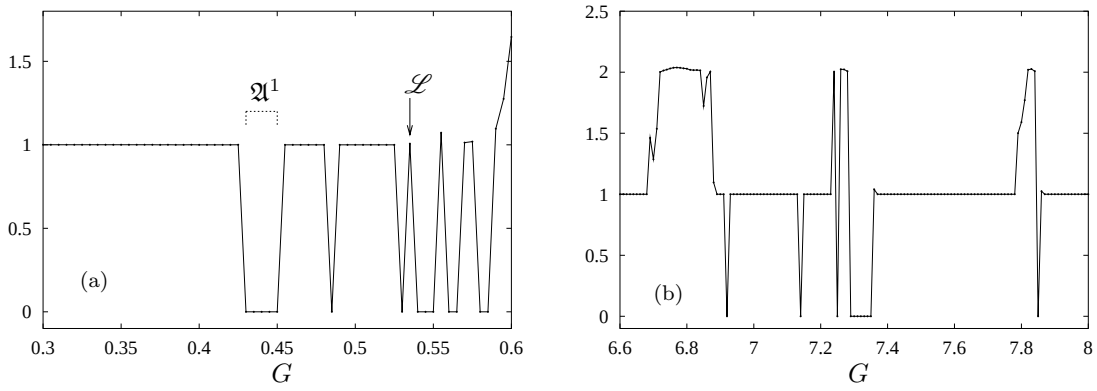

Figure 2.48: (a) Lyapunov dimension of the P attractors for parameter values on the vertical line $F = 7$ in Figure 2.47 (right). (b) Same as (a), for the horizontal line $G = 0.35$. The step is 0.01 in both plots.

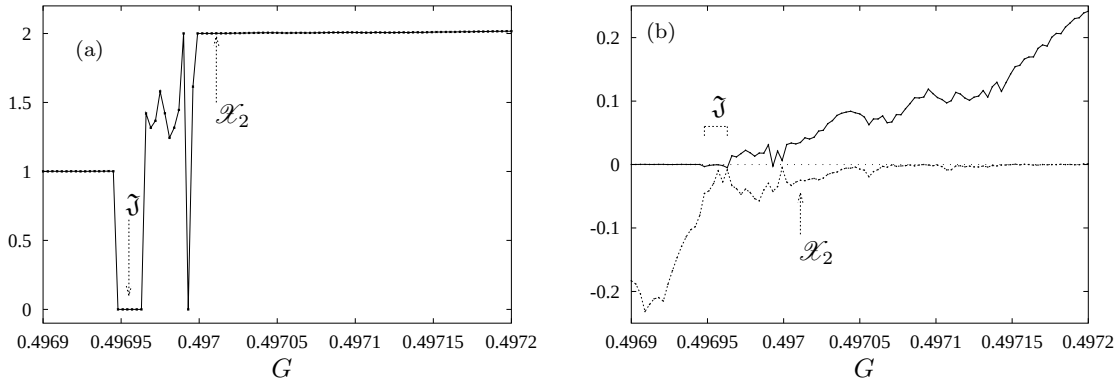

Figure 2.49: (a) Lyapunov dimension of P-attractors as a function of G for $F = 11$ fixed. The step in G is 3×10^{-6}. For these estimates 2×10^5 iterates of DP were computed. An arrow points at the G value where the attractor $\mathscr{X}_2$ occurs (Figure 2.50 (d)). (b) Lyapunov exponents λ_1 and λ_2 on the attractors in (a).

where the Lyapunov dimension is larger than one, while $2\mathscr{C}$ still exists outside them. This implies that curve $\mathcal{B}$ is in reality much more complicated than what is sketched in Figure 2.4.

Quasi-periodic Hénon-like strange attractors

In region $\mathfrak{L}_2$, at most two consecutive quasi-periodic period doublings occur as G increases, depending on the value of F. A whole cascade has not been observed, because the attractors $2\mathscr{C}$ or $4\mathscr{C}$ are eventually destroyed by a homoclinic tangency inside an Arnol′d tongue (as in Sec. 2.4.7).

We illustrate this route for the period two circle attractor $4\mathscr{C}$ (Figure 2.7 (A)) by means of a plot of the Lyapunov dimension Figure 2.49 (a). For G close to 0.4969, the period two circle $4\mathscr{C}$ persists and it is quasi-periodic since $\mathrm{D_L} \simeq 1$. At this moment, the saddle invariant circle $2\mathscr{C}$ still coexists with $4\mathscr{C}$. Moreover, the unstable manifold of $2\mathscr{C}$ is a two-dimensional Möbius strip, whose edge is $4\mathscr{C}$.

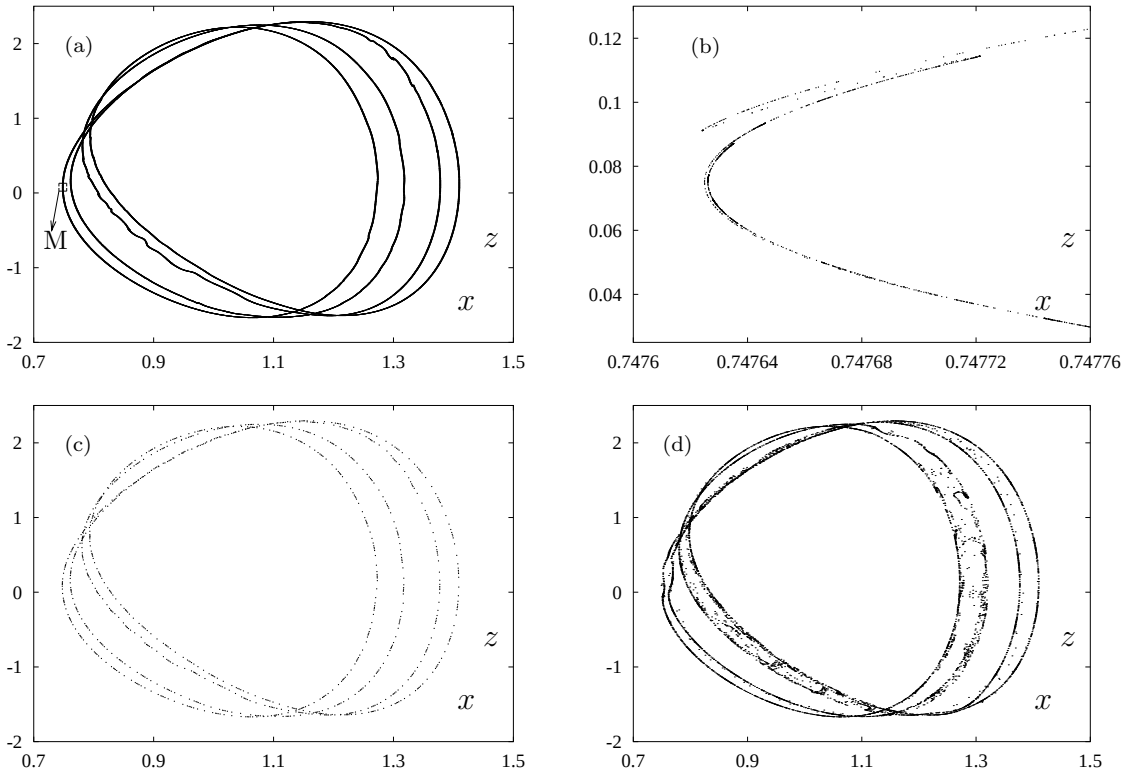

Figure 2.50: (a) Projection on (x, z) of the strange attractor $\mathscr{L}_3$ of P at $(F, G) = (11, 0.4969532)$. (b) Magnification of box M in (a). (c) Same as (a) for the period 1098 point of P at $G = 0.496951$. (d) Same as (a) for the strange P-attractor $\mathscr{X}_2$ at $G = 0.497011$.

Then $4\mathscr{C}$ enters some Arnol′d tongue, where λ_1 becomes negative. In the G-interval $\mathfrak{J} = \{G \mid 0.496948 < G < 0.496963\}$ only periodic points are detected ($\mathrm{D_L} = 0$ in Figure 2.49 (b)). In reality, strange attractors occur in $\mathfrak{J}$ as well.[22] One of these is the 'large' strange attractor $\mathscr{L}_3$ occurring at $G = 0.4969532$, Figure 2.50 (a). In Figure 2.50 (b) a small piece of $\mathscr{L}_3$ is enlarged, illustrating the folded circle structure. The maximal Lyapunov exponent on $\mathscr{L}_3$ is $\lambda_1 \simeq 0.0025$. However, attracting periodic points of high period are prevalent in the neighbourhood, like the period 1098 point in Figure 2.50 (c).

For G larger the P-iterates begin to wander in the transversal unstable manifold of the saddle circle $2\mathscr{C}$. This is reflected in the Lyapunov dimension, which grows up to two. For the attractor $\mathscr{X}_2$ in Figure 2.50 (d) the Lyapunov dimension is almost two, but λ_2 is still negative. This identifies it as an intermediate stage between a broken-circle and a quasi-periodic Hénon-like attractor. For G larger λ_2 approaches zero and the P-iterates spread even more in the transversal manifold. Notice that $\lambda_2 \simeq 0$ near $G = 0.4972$, where the attractor $\mathscr{Q}_1$ occurs (Figure 2.7 (B)). This means that quasi-periodic Hénon-like attractors seem to be persistent under perturbations.

However, for (F, G) farther inside $\mathfrak{L}_2$ more complicated types of attractors are found, with no intermittency in the power spectra. An example is the attractor in

[22] They are not revealed in Figure 2.49 because of the step size in G.

	D_L	λ_1	λ_2	λ_3	e_1	e_2	e_3
a	1.05	1.72	-33.6	-128.4	4.e-4	6.e-4	7.e-4
b	1.27	4.8	-18.1	-100.5	1.e-3	6.e-4	2.e-3

Table 2.5: Lyapunov exponents of the strange attractors $\mathscr{S}_1$ (a) and $\mathscr{S}_2$ (b) in Figures 2.9 and 2.10.

Figure 2.53 (a).

2.4.10 The chaotic range $\mathfrak{U}$

We now turn to the attractors in the chaotic region $\mathfrak{U}$. No invariant circles occur here, and periodic point attractors are prevalent. strange attractors appear suddenly where the periodic points lose stability. To describe this, consider Figure 2.12. At $G = 2$, the fixed point $\mathscr{A}$ is detected. Parameter values lie inside the narrow black strip below region $\mathfrak{Q}_2$ (Figure 2.2 (b)) where $\mathscr{A}$ is the unique attractor. As G is decreased, $\mathscr{A}$ is suddenly replaced by the Shil′nikov-like strange attractor $\mathscr{S}_1$ (Figure 2.9 left). The dynamics on $\mathscr{S}_1$ is quite sensitive with respect to initial conditions, due to the size of the maximal Lyapunov exponent (Table 2.5). Indeed, the fact that the power spectrum of $\mathscr{S}_1$ (Figure 2.9 (b)) looks like white noise confirms that the iterates of P are almost uncorrelated. However, $\mathscr{S}_1$ has a rather one-dimensional character, since $D_L(\mathscr{S}_1) \simeq 1.05$. Most Shil′nikov-like strange attractors inside $\mathfrak{U}$ have richer structure than $\mathscr{S}_1$ (compare Figure 2.10 (a)). This corresponds to a larger maximal Lyapunov exponent and larger Lyapunov dimension.

Among Shil′nikov-like, also Hénon-like attractors may occur. The strange attractor $\mathscr{H}_2$ in Figure 2.51 (A) is found at $(F, G) = (5, 1.29)$. A projection of $\mathscr{H}_2$ also can be seen as a small segment in Figure 2.35. A magnification of a portion of $\mathscr{H}_2$ suggests that $\mathscr{H}_2$ is a quite narrow Hénon-like attractor. Similar attractors also exist in $\mathfrak{U}'$ (Figure 2.38 (a)). Shil′nikov-like attractors like $\mathscr{S}_3$ (Figure 2.51 (B)) occur for nearby parameter values. The transition from $\mathscr{H}_2$ to $\mathscr{S}_3$ corresponds to a jump in the largest Lyapunov exponent, although both attractors have dimension just slightly larger than one (see Table 2.6). Notice that a portion of $\mathscr{S}_3$ (singled out by box N) approximately agrees with $\mathscr{H}_2$, while the small spiral part (magnified in Figure 2.51 (B1)) looks like the Shil′nikov attractors found in [13]. A magnification of a tiny piece of the spiral is plotted in Figure 2.51 (B2). Some parts of $\mathscr{S}_3$ are visited by a small fraction of the total number of iterates. This is not a transient effect: $\mathscr{S}_3$ has low density at such parts. For instance, the domain $(y, z) \in [0.69, 1.48] \times [-0.91, 1.39]$ contains 97.9% of the points in $\mathscr{S}_3$. Among them 99.8% are on $x \in [-0.35, 0.61]$.

	D_L	λ_1	λ_2	λ_3	e_1	e_2	e_3
A	1.046	0.58	-12.6	-77.9	1.e-5	4.e-4	4.e-4
B	1.097	1.13	-11.7	-87.1	1.e-3	2.e-4	1.e-3

Table 2.6: Lyapunov exponents of the strange attractors $\mathscr{H}_2$ (A) and $\mathscr{S}_3$ (B) in Figure 2.51.

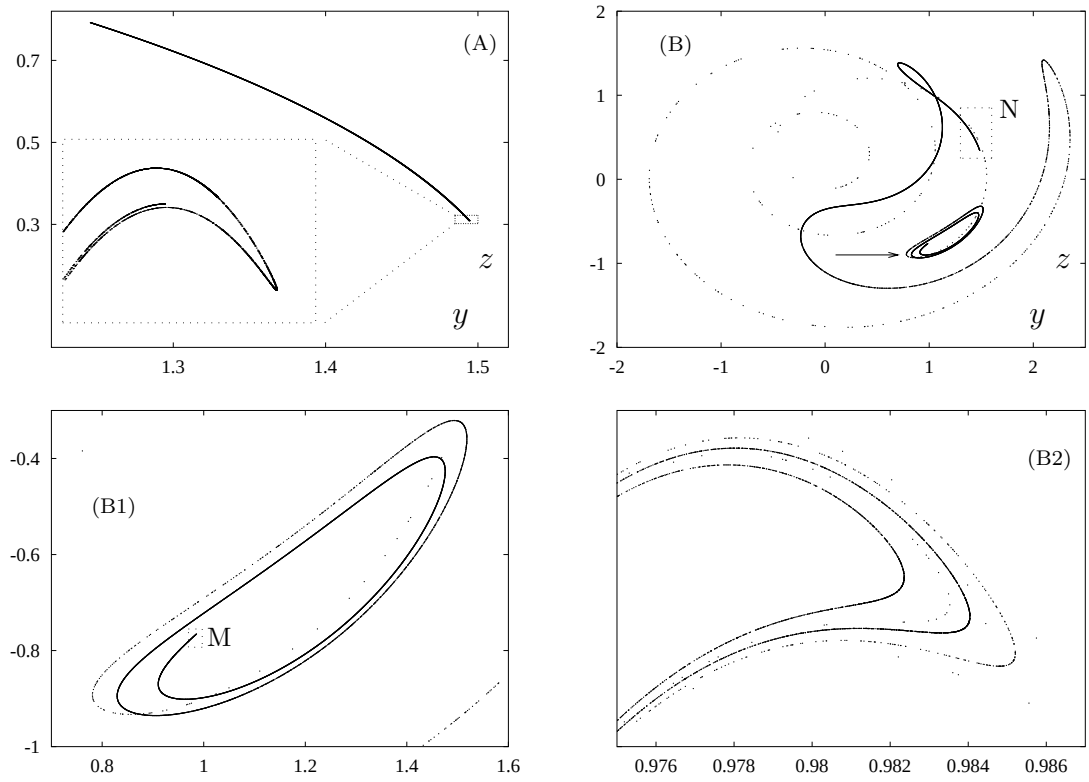

Figure 2.51: (A) Projection on (y, z) of the Hénon-like attractor $\mathscr{H}_2$ for $(F, G) = (5, 1.29)$. A small piece of $\mathscr{H}_2$ is magnified in the box. There, the graph has been affinely deformed by plotting $(y, \tilde{z})$, with $\tilde{z} = z + 3.81 \times (y - 1.49)$. (B) Same as (A) for the Shil′nikov-like attractor $\mathscr{S}_3$ at $G = 1.29005$. The portion of $\mathscr{S}_3$ inside box N approximately coincides with $\mathscr{H}_2$. (B1) Magnification of the spiral part of $\mathscr{S}_3$, box N in (B). (B2) Magnification of box M in (B1) around the tip of the spiral part. The graph has been affinely deformed by plotting $(y, \tilde{z})$, with $\tilde{z} = z - 0.965 \times (y - 0.975)$. The width of the vertical window in (B2) is 1.4×10^{-4}.

The ranges of existence of Shil′nikov–like strange attractors are interspersed by relatively large windows of fixed points, where the corresponding T-periodic limit cycles of system (2.2) are of spiral type (compare Figure 2.12). However, strange attractors become prevalent close to the value (F_0, G_0) where a Shil′nikov-like attractor occurs. To be more precise, given an open ball $\mathfrak{B}_\delta \in \mathfrak{M}_{0.5}$ of radius δ, centred at (F_0, G_0), denote by $\mathfrak{S}_\delta$ the set of parameter values in $\in \mathfrak{B}_\delta$ for which a strange attractor occurs. Our numerical results seem to suggest that

$$\frac{\text{meas}\,\mathfrak{S}_\delta}{\text{meas}\,\mathfrak{B}_\delta} \to C \quad \text{as } \delta \to 0, \quad \text{with } C > 0, \tag{2.14}$$

where "meas" denotes the Lebesgue measure in $\mathfrak{M}_{0.5}$. This is illustrated in Figure 2.52, where we plotted the Lyapunov dimension of P-attractors against the parameter G. On a larger scale (Figure 2.52 left), periodic points are prevalent, since they occur in open parameter sets of large relative measure. On the other hand, in a small neighbourhood of $G = 1.21124$ (where a strange attractor occurs), strange attractors are prevalent (Figure 2.52 right).

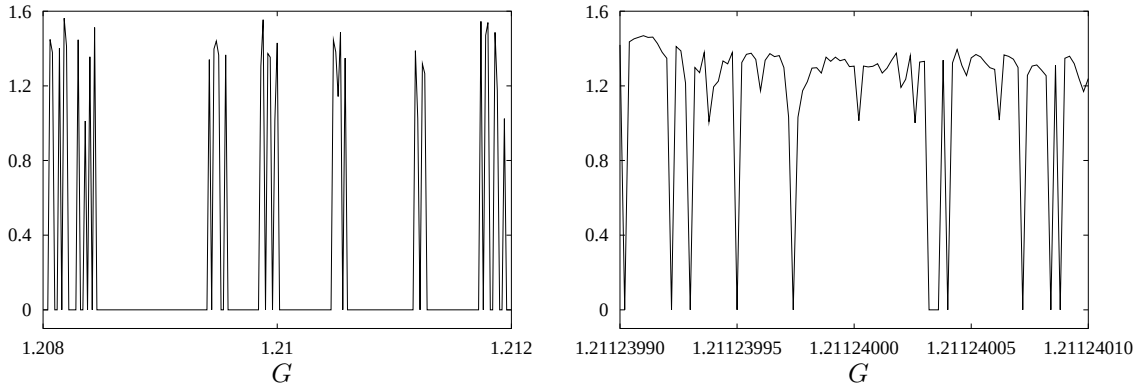

Figure 2.52: Left: Lyapunov dimension of P-attractors as a function of G for $F = 8$ fixed. The step in G is 0.01. Right: same as left part with G-step 2×10^{-9}, displaying the magnification of a small interval around $G = 1.21124$.

Abundance of strange attractors, expressed by (2.14), is typical for parameters near a homoclinic tangency, see [42, 86, 95]. The results in Figure 2.52 right give further evidence that Shil′nikov-like attractors are created by Shil′nikov tangency bifurcations of a saddle-focus fixed point, see Sec. 2.5.

2.4.11 Summary on the strange attractors of the Poincaré map

We now sketch a classification of the strange attractors found in the family $P_{F,G,\varepsilon}$.

Hénon-like attractors of two types are found in both $\mathfrak{L}_1$ and $\mathfrak{L}_2$: folded circles and 'small' attractors. Both types of attractors have a local Hénon-like structure and occur close (in the parameter space) to an invariant circle, at the boundary of $\mathfrak{L}_1$ and $\mathfrak{L}_2$. Folded circles, like $\mathscr{L}_1$ (Figure 2.6), $\mathscr{L}_2$ (Figure 2.38 (b)) and $\mathscr{L}_3$ in Figure 2.50 (a), are also called 'large' [13, 23], since they wind inside a whole annulus containing the unstable manifold of some saddle periodic point (see Sec. 2.4.7). This does not hold for 'small' Hénon-like attractors, like $\mathscr{H}_1$ in Figure 2.42. Deeper inside $\mathfrak{L}_1$ and $\mathfrak{L}_2$, strange attractors of other types are detected, like $\mathscr{X}_1$ (Figure 2.44), $\mathscr{X}_2$ (Figure 2.50 (d)) or Figure 2.53 (a).

Some narrow Hénon-like attractors occur in both $\mathfrak{U}'$ (Figure 2.38 (a)) and $\mathfrak{U}$ (Figure 2.51 (A)). Furthermore, in $\mathfrak{U}$ also Shil′nikov-like attractors exist, like in Figure 2.9, 2.10 and 2.51 (B).

2.5 Discussion and outlook

In this Chapter, we present an inventory of the dynamics in the driven Lorenz-84 system, giving, whenever possible, an explanation of the changes occurring as the (F, G) vary in the plane $\mathfrak{M}_\varepsilon$, for $\varepsilon = 0.5$, and as ε is increased from zero. Several phenomena are discussed at the level of guesses or possibilities. It was not possible, indeed, to focus on all open problems in the course of this large-scale investigation.

In the next section we first summarise our findings for $\varepsilon = 0.5$ with a rough

subdivision of $\mathfrak{M}_{0.5}$, sketched in Figure 2.4 (b). Our exploration of the parameter space raises several questions of both theoretical and applied nature. These are discussed in Sec. 2.5.2.

2.5.1 Summary of results

The parameter plane $\mathfrak{M}_\varepsilon$ for $\varepsilon = 0.5$ can be divided into several regions, each with different dynamical phenomena. Three regions inside $\mathfrak{M}_{0.5}$, denoted by $\mathfrak{Q}_1$, $\mathfrak{Q}_2$ and $\mathfrak{F}$, have a rather simple dynamics (see next section). Four regions are characterised by the occurrence of strange attractors (Sec. 2.5.1). We finally describe results obtained for other values of ε.

Regular dynamics

A fixed point attractor $\mathscr{A}$ exists in the connected component $\mathfrak{F}$ of Figure 2.4 (b) containing the upper left corner. This corresponds to small F (see Figure 2.1 (a), (b)), large G (compare the fixed points at the right of all pictures in Figure 2.1) and to a thin strip between region $\mathfrak{Q}_2$ and $\mathfrak{U}$, $\mathfrak{U}'$.

A circle attractor $\mathscr{C}_2$ occurs in region $\mathfrak{Q}_2$. Sections of $\mathfrak{Q}_2$ by a vertical line $F = F_0$ give one-parameter families $\mathscr{C}_2 = \mathscr{C}_2(F_0, G)$ of circles. The cigar-shaped sequences of attractors in Figure 2.1 (e) and (f) are projections of such families. Region $\mathfrak{Q}_2$ is bounded by the Hopf curve $\mathcal{H}_2$, see Sec. 2.4.1. Arnol′d tongues inside $\mathfrak{Q}_2$ are very thin and the prevalent behaviour seems to be quasi-periodicity. Although the dynamics in $\mathfrak{Q}_2$ is rather simple, the role played by the several strong resonance points on $\mathcal{H}_2$ is not yet completely clear, especially for $\varepsilon \geq 0.5$.

Circle dynamics characterises region $\mathfrak{Q}_1$ as well. The circle attractor $\mathscr{C}$ occurs at $G = 0$ for $F > 1$ and persists at least up to $G = 0.28$ (dotted horizontal line in Figure 2.4 (left)). In fact, for some values of F this circle persists up to a larger value of G (see Secs. 2.4.5 and 21). Curve $\mathcal{B}$ in Figure 2.4 (b) roughly indicates the G-value up to which $\mathscr{C}$ seems to persist. Some thick dots indicate the occurrence of a quasi-periodic period doubling, where $\mathscr{C}$ loses stability and a doubled circle attractor $2\mathscr{C}$ appears (see Sec. 2.4.9). The fine structure of this bifurcation, and in particular the role played by resonances and 'bubbles', is not yet fully understood. See Sec. 15 and compare with Chapter four.

Chaotic dynamics

We turn to the description of the domains in $\mathfrak{M}_{0.5}$ where strange attractors occur. We have distinguished four regions $\mathfrak{L}_1$, $\mathfrak{L}_2$, $\mathfrak{U}'$ and $\mathfrak{U}$ (Figure 2.4 (b)). In all of them, strange attractors occur in regions of seemingly positive measure, interrupted by open windows of periodicity (Arnol′d tongues). In $\mathfrak{L}_2$ there is prevalence of strange attractor, while the typical behaviour in $\mathfrak{U}$ is periodicity (compare Figure 2.12).

The creation of strange attractors in $\mathfrak{L}_2$ and $\mathfrak{L}_1$ is mostly due to homoclinic tangencies of a saddle periodic point inside an Arnol′d tongue (compare Figure 2.50). Cascades of period doublings of periodic attractors are also observed (see Figure 2.41). At the border of $\mathfrak{L}_2$ or $\mathfrak{L}_1$, the dynamics on the attractors tends to follow the unstable manifold of a saddle periodic point, which for close parameter values still forms an

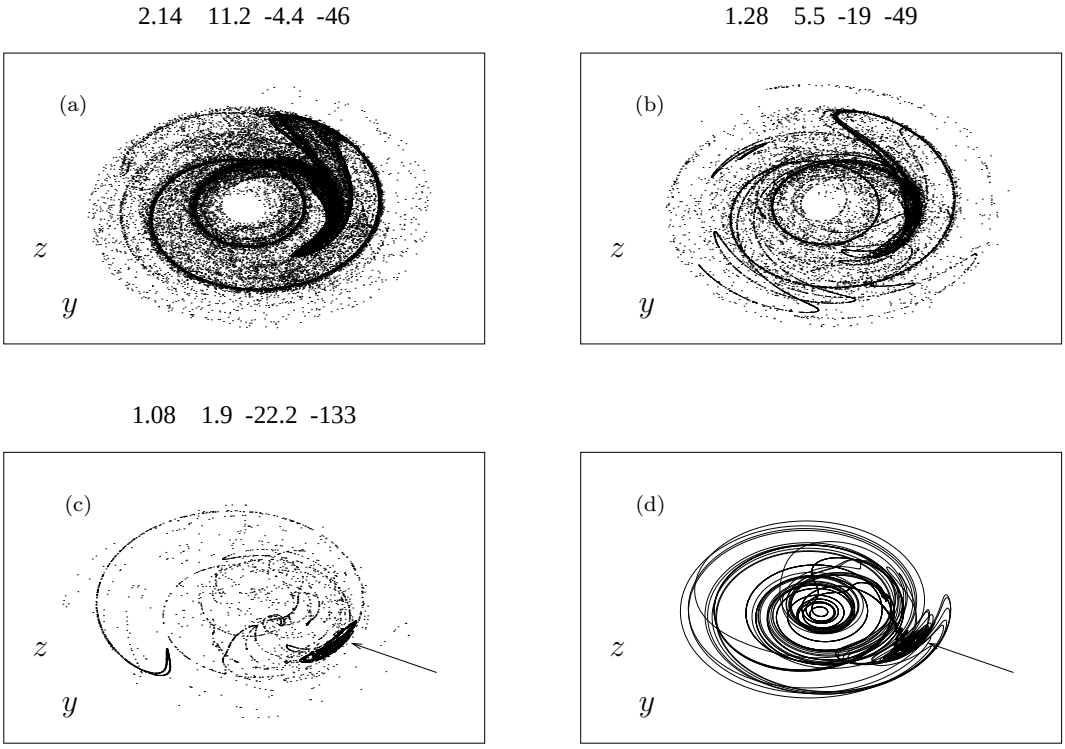

Figure 2.53: (a), (b), (c): Projection on (y, z) of strange attractors of P for $\varepsilon = 0.5$ and $F = 7$. (d) Same projection of an attracting period $5T$ limit cycle of system (2.2). G is fixed at: (a) 1, (b) 1.08, (c) 1.4, (d) 1.400000037. The (y, z) window is $[-4, 4] \times [-3, 4]$ for all pictures. A spiral structure is pointed to by an arrow in (c) and (d).

invariant circle (Figures 2.6 and 2.50). Therefore most attractors have dimension close to one (Figure 2.41). Intermittency is often observed in the power spectra. Marked peaks persist, close to the corresponding harmonics before the breakdown of the circle, and broad band has low power. As the parameters are shifted further inside $\mathfrak{L}_2$ or $\mathfrak{L}_1$, the dimension of the strange attractors grows above two (Figures 2.43 and 2.49) and a broad band component arises in the power spectra (Figure 2.44). In $\mathfrak{L}_2$, quasi-periodic Hénon-like strange attractors may appear (Sec. 21). The mechanism for the birth of strange attractor could not be so well clarified for region $\mathfrak{U}$. Most strange attractors have dimension between 1.1 and 1.4, the first case usually corresponding to narrow Hénon-like attractors. Shil′nikov like attractors (Figures 2.9 and 2.10) of different type are found (see Sec. 2.4.10). The transition between $\mathfrak{L}_2$ and $\mathfrak{U}$ is quite sudden (Figure 2.12). It seems reasonable to believe that this transition (on 'curve' $\mathcal{SH}$, Figure 2.4 (b)) and the birth of Shil′nikov–like strange attractors are due to three-dimensional homoclinic tangencies of a saddle-focus fixed point (Shil′nikov tangency bifurcation). Indeed, a spiral structure like in Figure 2.51 (B1) appears in the strange attractors when passing from $\mathfrak{L}_2$ to $\mathfrak{U}$, across 'curve' $\mathcal{SH}$. In particular, an increasing fraction of the points is contained in the spiral part (Figure 2.53). Furthermore, the Lyapunov dimension and the maximal Lyapunov exponents decrease.

A high number of saddle spiral limit cycles coexists with the Shil′nikov strange

attractors, and attracting spiral limit cycles occur for nearby parameter values. The spiral portion of the strange attractors roughly corresponds to that of the above limit cycles, see Figure 2.53 (c) and (d). Compare also Figure 2.9 (A) and Figure 2.10 (A) to Figure 2.11 (A) and (B), respectively. Attractors similar to the spiral portion were found in [13] (see Figure 2.9), their occurrence being caused by a Shil′nikov tangency.

It is known that close (in the C^1 topology) to a 3D diffeomorphism having a Shil′nikov homoclinic tangency, diffeomorphisms with strange attractors [120] or displaying the Newhouse phenomenon occur [51, 96]. However, more detailed numerical and analytical studies are needed both to establish a relation with the occurrence of attractors like in Figures 2.9 and 2.10 (A), to determine the effect on the bifurcation set of a map and to establish the relative abundance of such attractors.

Overview of the plane $\mathfrak{M}_\varepsilon$ for other values of ε

To quickly get information on the changes occurring for different values of ε, we performed other large-scale explorations of $\mathfrak{M}_\varepsilon$ like in Figure 2.2. The results, displayed in Figure 2.54, suggest the following remarks. As ε increases:

1. Arnol′d tongues inside region $\mathfrak{Q}_2$ become wider, especially close to the strong resonance gaps on the lower branch of $\mathcal{H}_2$. As ε grows these gaps become larger as well and, eventually, 'eat up' the whole lower branch of $\mathcal{H}_2$ (compare also Sec. 2.4.1). At $\varepsilon = 0.9$, $\mathfrak{Q}_2$ is also shifted to larger F, which suggests that it may completely disappear for $\varepsilon \geq 1$. This is supported by the following data: Up to $\varepsilon = 0.7$ the $\mathfrak{Q}_2$ region can be seen to appear around $F = 6$. For $\varepsilon = 0.9, 0.93, 0.95, 0.97, 0.98$ and 0.99 the first invariant curves have been detected around $F = 14, 20, 30, 58, 95$ and 250, respectively.

2. Region $\mathfrak{Q}_1$ shrinks. As ε grows, the circle $\mathscr{C}(F_0, G)$ is destroyed at smaller values of G. Consequently, the chaotic range $\mathfrak{L}_2$ increases in size.

3. The fraction of periodicity increases inside $\mathfrak{L}_2$. In particular, the structures of Arnol′d tongues, which occupy a minor fraction of $\mathfrak{L}_2$ for small ε (Figure 2.54 (a)), invade most of $\mathfrak{L}_2$ at $\varepsilon = 0.9$.

4. The chaotic range $\mathfrak{U}$, almost invisible for $\varepsilon = 0.1$ grows in size.

Several dynamical phenomena of the autonomous system persist only for ε sufficiently small. For example, the repelling invariant torus $\mathscr{T}$ occurring at $\varepsilon = 0.01$ (Sec. 15) seems to have completely disappeared for $\varepsilon = 0.5$ (see Sec. 2.4.5). One of the various ways in which $\mathscr{T}$ is destroyed is illustrated in Figure 2.55. The torus repellor $\mathscr{T}$ at $\varepsilon = 0.01$ is plotted in Figure 2.55 (A). Since the two largest Lyapunov exponents λ_1 and λ_2 are approximately zero (Table 2.7), it seems reasonable to assume that the two fundamental frequencies f_1 and g_1 of $\mathscr{T}$ satisfy a Diophantine condition.[23] At $\varepsilon = 0.066$, $\mathscr{T}$ is locked to a period 16 invariant curve. One of the frequencies of $\mathscr{T}$ is of course $f_1 = 16^{-1}$, since each of the 16 circles in Figure 2.55 (B) is invariant under P^{16}, quasi-periodic and normally hyperbolic. This is confirmed by the fact that

[23] This could be numerically checked up to some order of resonance by using refined Fourier analysis, see [50].

λ_1 is zero and λ_2 slightly negative. The other fundamental frequency $g_1 = 0.0116$ is equal to $j/16$, where j is the frequency of P^{16} of each of the 16 invariant circles. In Figure 2.55 (b) we indicated f_1 and g_1, together with their combinations $h_k = g_1 + kf_1$ with $k = 1,\ 2,\ 3$.

The same situation seems to persist for an interval of values of ε, but beyond $\varepsilon = 0.0665$ the exponent λ_1 becomes slightly positive. In this case, the circles in Figure 2.55 (B) have lost smoothness. A strange repellor $\mathscr{U}$ is created, see Figure 2.55 (C), with $\mathrm{D_L}(\mathscr{U}) \simeq 2.083$. Several properties of $\mathscr{U}$ and of the strange attractor $\mathscr{Q}_1$ (Figure 2.7) are analogous. The fact that $\lambda_2 \simeq 0$ indicates that a quasi-periodic component persists in the dynamics on $\mathscr{U}$. The power spectrum of $\mathscr{U}$ has some broad band, but several harmonics of the resonant torus still persist. In Figure 2.55 (c), $f_2 = 0.25$, $f_3 = 0.5$ and g_1 are identified, but the h_k's persist as well. This is also due to intermittency, although of an unconventional type. It seems here that the dynamics is still driven by the ghost of the quasi-periodic circles in Figure 2.55 (B). Notice that $\mathscr{U}$ is made up of eight strips, each invariant under P^8. The destruction of the 16 circles corresponds to the degeneration of frequency f_1 into broad band.

For ε even larger (Figure 2.55 (D)), the strips of Figure 2.55 (D) have melted into a global one-piece repellor. Although the Lyapunov dimension and λ_1 have increased further, the second Lyapunov exponent is still zero, and a peak around h_3 can still be distinguished. However, all harmonics of f_1 have merged into broad band in the power

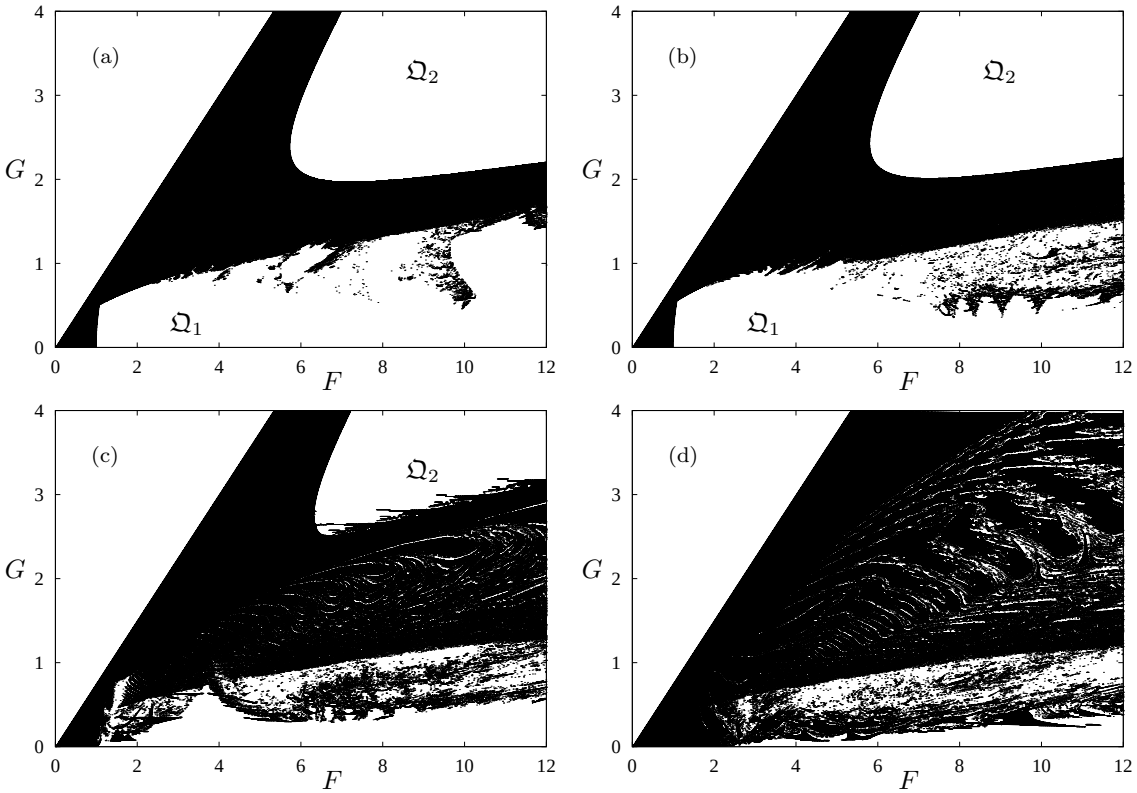

Figure 2.54: Same as Figure 2.2 (b). Parameter planes $\mathfrak{M}_\varepsilon$ were scanned looking for periodic points, for the following values of ε: (a) 0.1, (b) 0.3, (c) 0.7, (d) 0.9.

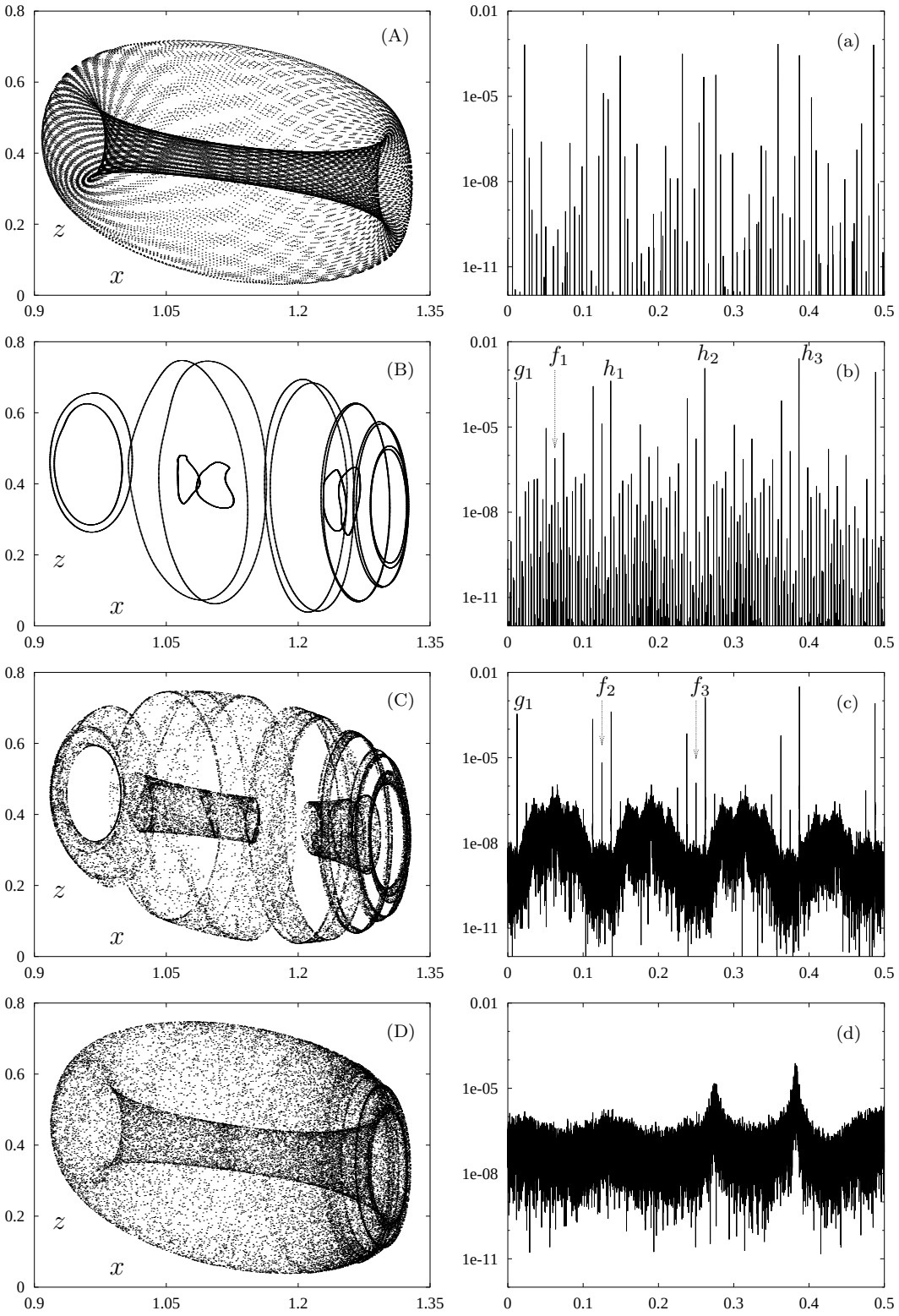

Figure 2.55: Projections on (x, z) of repellors of $P_{F,G,\varepsilon}$ for $(F, G) = (1.8, 1.65)$ and (A) $\varepsilon = 0.01$ (B) $\varepsilon = 0.066$ (C) $\varepsilon = 0.0665$ (D) $\varepsilon = 0.0685$. (a), (b), (c), (d) Power spectra of the repellors in (A), (B), (C), (D) respectively. The same initial point as for Figure 2.17 has been used.

	D_L	λ_1	λ_2	λ_3	e_1	e_2	e_3
A	2	4.5e-5	2.e-5	-0.47	6.e-6	3.e-6	4.e-6
B	1	2.e-5	-0.041	-0.35	2.e-6	2.e-5	3.e-5
C	2.083	0.035	-2.e-4	-0.42	1.e-4	2.e-6	1.e-4
D	2.37	0.2	6.7e-5	-0.56	5.e-4	1.e-6	6.e-4

Table 2.7: Lyapunov exponents (in the reversed time) and dimension of the repellors in Figure 2.55.

spectrum. A similar merging occurs in the creation of the quasi-periodic attractor $\mathscr{Q}_1$ from the period two curve $4\mathscr{C}$ (Figure 2.7). Indeed, by the analogies between $\mathscr{Q}_1$ and $\mathscr{U}$ we call the latter a quasi-periodic Hénon-like repellor.

Seemingly, for all (F, G) the torus repellor $\mathscr{T}$ is destroyed long before ε reaches 0.5. As a consequence, the frayed boundary $\mathcal{QH}_{sub}$ may possibly persist only for small values of ε. Furthermore, the torus repellor is the boundary between the basins of two different attractors, the circle $\mathscr{C}$ and the point $\mathscr{A}$. Probably, the strange repellors born at the destruction of $\mathscr{T}$ still are basin boundaries, although of fractal dimension. However, for some values of (F, G) inside $\mathfrak{M}_{0.5}$, both the circle attractor $\mathscr{C}$ and the torus have disappeared (Sec. 2.4.5), and the fixed point attractor $\mathscr{A}$ is the unique invariant object. This might be due to the fact that the basin of $\mathscr{A}$ swallows the other.

We return to the disappearance of the $\mathcal{HSN}$ between $\varepsilon = 0$ and $\varepsilon = 0.5$. It is possible to continue the codimension two point $\mathcal{HSN}$ as a function of ε. In Figure 2.56 a plot of the evolution of the (positive) argument of an eigenvalue of modulus 1 is displayed. The same figure shows also the Hopf and saddle-node bifurcation curves, tangent to each other at the $\mathcal{HSN}$ point, for $\varepsilon = 0.245$. The curves are rather close for this value of ε. Guided by these results, we see that a codimension three bifurcation takes place between $\varepsilon = 0.277$ and $\varepsilon = 0.5$. The global picture, however, is not clear.

2.5.2 Bifurcations of codimension two and higher

The disappearance of the torus repellors implies that the frayed curve of quasi-periodic Hopf bifurcations $\mathcal{QH}_{sub}$ is destroyed by some higher codimension bifurcation. Strong resonances could take place on $\mathcal{QH}_{sub}$, similarly to what occurs for the Hopf curves $\mathcal{H}_1$ and $\mathcal{H}_2$ (Sec. 2.4.3). In fact, several strong resonance points were found there at $\varepsilon = 0.5$ (Secs. 2.4.2 and 2.4.1). These points occur in couples delimiting gaps in the Hopf curves. The first open question is to determine the bifurcation diagram close to these strong resonance points and the implications for the breakdown of circles and tori. Although no strange attractors were found in the neighbourhood of the strong resonances, the theory prescribes their occurrence, perhaps confined in exponentially small regions in the parameter plane (compare [20, 21, 107]).

Secondly, the two endpoints of such resonance gaps merge into one degenerate strong resonance at $\varepsilon = 0$ (since no gaps occur on the Hopf curves). From this degenerate point, two curves of strong resonance points come out in the parameter space $\mathfrak{M} = \{F, G, \varepsilon\}$, bounding, at each ε fixed, a gap on a Hopf curve contained inside parameter plane $\mathfrak{M}_\varepsilon$. Then, how do these curves of 1:1 resonance bifurcations

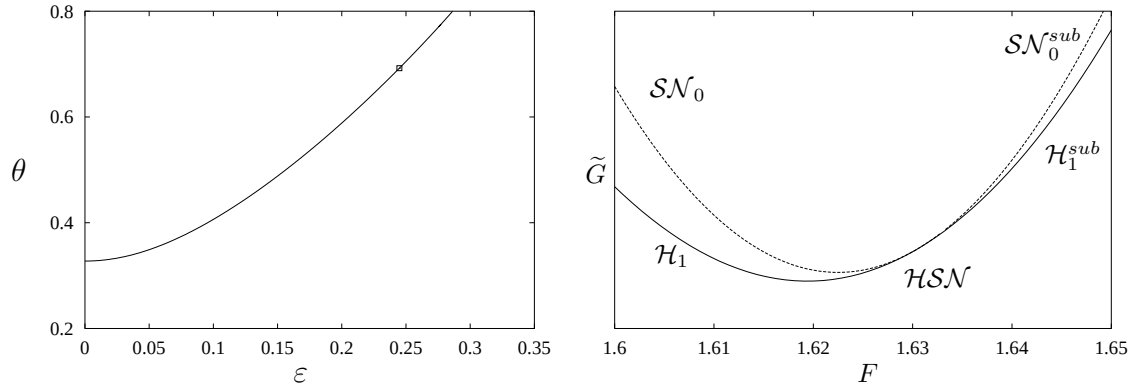

Figure 2.56: Left: argument θ of the complex conjugate eigenvalues of DP on the fixed points belonging to the curve of $\mathcal{HSN}$ points, in the parameter space $\mathfrak{M} = \{F, G, \varepsilon\}$. Right: local bifurcation diagram of P close to the point $\mathcal{HSN}$ at $\varepsilon = 0.245$ (plotted at the left with a small box), inside the plane $\mathfrak{M}_{0.245} = \{\varepsilon = 0.245\}$. The graph has been affinely transformed by plotting $\widetilde{G} = G - 1.36 \times (F - 1.5)$. The vertical width is 2×10^{-4}.

evolve inside $\mathfrak{M}$?

This discussion leads naturally to take codimension three bifurcations into account. Such phenomena can only be studied by using three control parameters in system (2.2). We have proved the occurrence of a Hopf-saddle-node bifurcation of higher codimension inside the parameter space $\mathfrak{M} = \{F, G, \varepsilon\}$ Sec. 2.4.3. This follows indeed by a continuity argument: at $\varepsilon = 0.277$ there is a Hopf saddle node point (see Figure 2.15), while at $\varepsilon = 0.5$ it has disappeared. A bifurcation causing $\mathcal{HSN}$ to disappear could be a codimension three Hopf-saddle-node strong resonance, where the three eigenvalues of P are $\mu_1 = 1$, $\mu_2 = \exp(2\pi ip/q)$ and $\mu_2 = \exp(-2\pi ip/q)$, with $q = 1, \ldots, 4$.

All the previous questions can be dealt with from an experimental point of view, namely by studying the driven Lorenz-84 model in deeper detail. This requires careful numerical tools, due to the large period and to the tiny size of the domains where some phenomena occur. Furthermore, some of the codimension two and three bifurcations found in the model, like the codimension two and the degenerate Hopf-saddle-node, have yet to be studied even from a theoretical viewpoint. For this it is of help to construct of suitable local model maps.

2.5.3 Global bifurcations and model maps

Beyond the questions discussed in the previous section, some global bifurcations taking place in the Lorenz-84 system have to be better understood, like the three-dimensional Shil′nikov homoclinic tangency of a saddle-focus fixed point. Evidence for the occurrence of such bifurcations was presented in Sec. 2.4.4, but its relationship with the creation of Shil′nikov-like attractors (Secs. 2.4.10 and 2.5.1) is not yet clear. This could be investigated by constructing appropriate model maps.

Model maps could also be used to investigate the creation of quasi-periodic Hénon-like attractors (Sec. 21) and repellors (Sec. 2.5.1). In particular, one might also

consider cascades of quasi-periodic period doublings of invariant circles. Research is in progress in these directions.

Appendix to Chapter two: on the numerical methods

2.A Integration and continuation

The numerical computation of the trajectories of system (2.2) is performed using a Taylor expansion of the solutions around time t (cf. [22]). We use the polynomial approximation

$$(x(t+h), y(t+h), z(t+h)) \simeq \sum_{k=0}^{N} (x_k(t), y_k(t), z_k(t)) h^k$$

where

$$x_k(t) = \frac{1}{k!}\frac{d^k}{dt^k}x(t) \qquad y_k(t) = \frac{1}{k!}\frac{d^k}{dt^k}y(t) \qquad z_k(t) = \frac{1}{k!}\frac{d^k}{dt^k}z(t) \tag{2.15}$$

Given an initial point (x_0, y_0, z_0), the coefficients (2.15) for $k \geq 1$ are computed recursively using the Leibnitz rule. One has for example:

$$\frac{d^k}{dt^k}y^2 = \sum_{m=0}^{k} \frac{k!}{m!(k-m)!} d^m y d^{k-m} y = k! \sum_{m=0}^{k} y_m y_{k-m}$$

For $k \geq 1$, substituting expressions like above in (2.2), one gets

$$\begin{aligned}
x_{k+1} &= \Big(-a x_k - \sum_{m=0}^{k} (y_m y_{k-m} + z_m z_{k-m}) + aF\varepsilon c_k\Big)/(k+1) \\
y_{k+1} &= \Big(-y_k + \sum_{j=0}^{k} (x_j y_{k-j} - b x_j z_{k-j}) + G\varepsilon s_k\Big)/(k+1) \\
z_{k+1} &= \Big(-z_k + \sum_{j=0}^{k} (b x_j y_{k-j} + x_j z_{k-j})\Big)/(k+1),
\end{aligned}$$

where $c_k(t) = \frac{1}{k!}\frac{d^k}{dt^k}\cos(\omega t)$ and $s_k(t) = \frac{1}{k!}\frac{d^k}{dt^k}\sin(\omega t)$. We usually fixed the order of the Taylor polynomial to $N = 24$, since this showed good convergence in the testing. Furthermore, a variable step size option is adopted. After computing all coefficients (x_k, y_k, z_k), the step size h is determined by

$$h = \min\left\{ \left(\frac{\eta}{a_N}\right)^{\frac{1}{N}}, \left(\frac{\eta}{a_{N-1}}\right)^{\frac{1}{N-1}} \right\},$$

where $a_k = \max(|x_k|, |y_k|, |z_k|)$ and $\eta = 10^{-16}$. The first variational equations of system (2.2) are handled in a similar way. For a specific treatment of the Taylor method, see [64].

We briefly describe the method used to compute curves of (bifurcations of) fixed points, based on [105]. For other strategies, see [78, 101]. For many other related problems, like continuation of cusp points or homoclinic tangencies, see [23]. Let (x_0, y_0, z_0) be a fixed point of P at parameter values F_0, G_0, ε_0 and suppose F_0 and ε_0 are kept fixed. It is convenient to consider G as a fourth variable. We look for zeroes of the function H, defined by

$$H : \mathbb{R}^4 \times I \to \mathbb{R}^3, \qquad H(q, G) \stackrel{\text{def}}{=} P(q) - q, \qquad q = (x, y, z) \tag{2.16}$$

knowing that $q_0 = (x_0, y_0, z_0)$ is a solution for $G = G_0$. Under the condition that the derivative $DH(q, G) = DP(q, G) - I$ has maximal rank, the Implicit Function Theorem guarantees the existence of a curve $\alpha(s) \in \mathbb{R}^4$ of solutions of passing through (q_0, G_0). A point $(\tilde{q}_1, \tilde{G}_1)$ on $\alpha(s)$ is predicted using interpolation and used as initial seed for a Newton corrector. The point (q_1, G_1) obtained after this refinement lies on the curve $q(s)$.

There exist procedures to do continuation of invariant circles. Some are based on the continuation of the Fourier coefficients [34], other on a derivation of the graph transform [19] and on fixed points of a synthesised return map using non-integer powers of a map [106].

2.B Estimates of Lyapunov exponents

The Lyapunov exponents are estimated according to the algorithm described by Galgani, Giorgilli, Benettin and Strelcyn [12]. The first variational equations of system (2.2) are integrated during a period T, with the identity matrix as initial condition. The canonical orthonormal basis is thereby mapped onto a new set of vectors $(\mathbf{v}_1^1, \mathbf{v}_2^1, \mathbf{v}_3^1)$. Each vector tends to align itself along the direction of maximal expansion (or of minimal compression). Thus all $\mathbf{v}_1^1$, $\mathbf{v}_2^1$, and $\mathbf{v}_3^1$ tend to collapse onto one direction. To prevent this, the Gram-Schmidt process is applied to $(\mathbf{v}_1^1, \mathbf{v}_2^1, \mathbf{v}_3^1)$ after a few steps of the numerical integrator, yielding a set $(\tilde{\mathbf{v}}_1^1, \tilde{\mathbf{v}}_2^1, \tilde{\mathbf{v}}_3^1)$ of orthogonal vectors. Define $\mathbf{w}_j^1 = \tilde{\mathbf{v}}_j^1 / \left\|\mathbf{v}_j^1\right\|$ for $j = 1, 2, 3$. Then a new frame of vectors $(\mathbf{v}_1^2, \mathbf{v}_2^2, \mathbf{v}_3^2)$ is computed by integrating the first variational equations taking as initial condition the orthonormal vectors $(\mathbf{w}_1^1, \mathbf{w}_2^1, \mathbf{w}_3^1)$ from the previous step. At iteration step k, define

$$c_j^k = \prod_{i=1}^{k} \left\|\tilde{\mathbf{v}}_j^k\right\| \quad \text{and} \quad \mathbf{w}_j^k = \frac{\tilde{\mathbf{v}}_j^k}{\left\|\tilde{\mathbf{v}}_j^k\right\|} \quad \text{for} \quad j = 1, 2, 3.$$

The orthonormalisation process does not change the direction of $\mathbf{v}_1^k$, so that $\mathbf{w}_1^k$ still points to the direction of maximal stretch. Denoting by λ_1, λ_2 and λ_3 the Lyapunov exponents, in decreasing order, the length c_1^k of $\mathbf{v}_1^k$ is approximately proportional to $e^{k\lambda_1}$. The plane spanned by $\mathbf{v}_1^k$ and $\mathbf{v}_2^k$ is not changed by the Gram-Schmidt process and tends to adjust to the subspace of maximal growth of surfaces. The rate of growth of areas is proportional to $e^{k(\lambda_1+\lambda_2)}$. In particular, since $\mathbf{v}_1^k = \mathbf{w}_1^k$ and $\mathbf{w}_2^k$ are orthonormal, the length of the projection of $\mathbf{v}_2^k$ upon $\mathbf{w}_2^k$ is proportional to $e^{k\lambda_2}$. A similar argument for growth of volumes yields that c_j^k is proportional to $e^{k\lambda_j}$. Therefore, the Lyapunov exponent λ_j is estimated by the averages

$$\lambda_j \approx \frac{1}{k} \log(c_j^k), \qquad \text{with} \quad k = 1, 2 \ldots, N. \tag{2.17}$$

For the computation of the Lyapunov spectrum of a single attractor, a total of $N = 10^5$ iterates of DP is carried out. After a transient of 10^4 iterations, only the maxima of c_j^k over consecutive blocks of 100 iterations of DP are used. This idea goes back to [22]. After computing a number of blocks, say 150, we compute the average of the c_j^k as in (2.17). Then a new set of 50 blocks is computed and the c_j^k are averaged over the last 150 blocks. The maximum of the differences between the last three averages is used as an estimation for the error in the Lyapunov exponent. Results of a test with 10^5 iterates of DP are shown in Figure 2.57 (a). The solid line joins the maxima

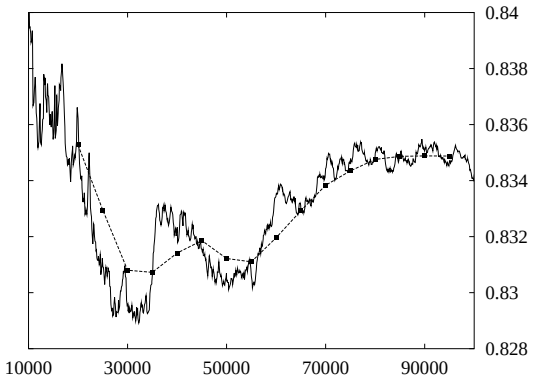

Figure 2.57: (a) Test on the computation of Lyapunov exponents, for $F = 5$ and $G = 1.29$. See text for explanation.

of c_1^k on blocks of 100 iterates. The small black boxes are the estimates obtained by averaging over 150 blocks.

Because of the high computational cost of integrating variational equations for a long period $T = 73$, when scanning for Lyapunov exponents for several parameter values (like in Figure 2.12 (b)-(d)), a quicker procedure has been adopted. For each parameter value, 10^4 iterates of DP are computed in total (sometimes 2×10^4), preceded by a transient of 500 iterates of P. The last 1000 approximations obtained by (2.17) are averaged. This provides the desired estimate.

For more precise methods of estimation of the Lyapunov exponents, see [40].

2.C Power spectrum estimation

For the technical terminology and the definitions of several concepts used in this section, we refer the reader to [15, 98]. The power spectra are estimated by using the Discrete Fourier Transform, denoted by DFT. Given an array $\mathbf{c}$ of complex values (called time series [30]) its DFT is the array:

$$\hat{\mathbf{c}} = (\hat{c}_0, \hat{c}_1, \ldots, \hat{c}_{N-1}), \quad \text{where} \quad \hat{c}_k \stackrel{\text{def}}{=} \frac{1}{N} \sum_{n=0}^{N-1} c_n \exp\left(-2\pi i \frac{nk}{N}\right). \tag{2.18}$$

In practice, the DFT of an array is computed using a Fast Fourier Transform (FFT) algorithm. The power spectrum is a plot of the square moduli of the coefficients c_k against so-called Fourier frequency $f_k = k/N$.

Given a P-invariant set $\mathscr{W}$, a (real) time series is constructed in the following way. An orbit of P with N points on $\mathscr{W}$ is first determined by iteration. We mostly fix $N = 2^{16}$ and compute N points q_k starting from $q_0 \in \mathscr{W}$, where $q_k = P(q_{k-1}) \in \mathbb{R}^3$. To produce a time series, this orbit has to be 'measured' by means of an observable $\Omega : \mathbb{R}^3 \to \mathbb{R}$, cf. [30]. In most cases, we chose Ω as the projection onto the coordinate y, yielding the time series $\mathbf{y} = (y_0, \ldots, y_{N-1})$, with $y_k = \Omega(q_k)$. Then an estimate of the power spectrum of $\mathscr{W}$ is obtained by plotting the square modulus $|\hat{y}_k|^2$ against the Fourier frequency f_k, for $k = 0, \ldots, N/2$. If the attractor $\mathscr{W}$ is an invariant curve, the fundamental frequency is the rotation number modulo $1/2$. In the case of the circle $\mathscr{C}$ (Figure 2.45 (a)-(b)) the fundamental frequency is close to the Fourier frequency with the highest peak. For $2\mathscr{C}$, one has to take a Fourier frequency corresponding to one half of that with the highest peak. Pictures such as Figure 2.36 left are produced by computing power spectra on circle attractors, usually with a low number of iterates, *e.g.* 4096 points. A few comments of technical nature have to be added.

Remarks.

1. Each power spectrum is computed from a single time series inside $\mathscr{W}$. Another possibility is to compute a number m time series' in $\mathscr{W}$—all with the same length N and with distinct initial points—and then to average the m spectra, compare [2].

2. Before computing a power spectrum, the array $\mathbf{y}$ is brought to zero average. Furthermore, a Hanning windowing of order two is applied in order to reduce frequency leakage. In particular, we first apply the translation

$$\mathbf{y} \mapsto \mathbf{u} = (u_0, \ldots, u_{N-1}), \qquad \text{with} \qquad u_j = y_j - \frac{1}{N}\sum_{k=0}^{N-1} y_k.$$

   FFT is performed on a second array $\mathbf{v}$, defined by

$$v_k = H_2^k \, u_k \qquad \text{where} \qquad H_2^k = \frac{2}{3}\cos\left(1 - 2\pi\frac{k}{N}\right)^2$$

   (Hanning windowing, see again [15, 98]). After that, the resulting coefficients, denoted again by $\hat{y}_k$ for simplicity, are normalised by dividing for the norm of the array $\mathbf{H} = (H_2^0, \ldots, H_2^{N-1})$.

3. We note that frequencies are computed modulo 1, since all frequencies lying outside the interval $[0, 1)$ are shifted inside this interval. This phenomenon, called aliasing, is unavoidable when dealing with discrete time evolutions. Indeed, since no sampling of a continuous time evolution is performed, the Nyquist frequency is always fixed at $1/2$. The frequency range is further restricted to $[0, 1/2]$, since the power spectrum of a real sequence $\mathbf{r}$ is symmetric with respect to $1/2$. One indeed has $\hat{r}_{N-k} = \overline{\hat{r}}_k$, since

$$\hat{r}_{N-k} = \frac{1}{N}\sum_{n=0}^{N-1} r_n \exp\left(-2\pi i\frac{(N-k)n}{N}\right) = \frac{1}{N}\sum_{n=0}^{N-1} r_n \exp\left(2\pi i\frac{kn}{N}\right).$$

The last remark provides motivation to introduce the following notation:

$$f \ \text{mir}\, \frac{1}{2} \stackrel{\text{def}}{=} 1 - (f \mod 1) = (-f) \mod 1.$$

For example, $0.28 \ \text{mir}\, \frac{1}{2} = 0.72$ and $1.91 \ \text{mir}\, \frac{1}{2} = 0.09$. Given the above symmetry, the power spectrum has the same value at f and at $f \ \text{mir}\, \frac{1}{2}$.

A simple test has been performed to estimate the propagation of random errors in the FFT algorithm. Given a time series $\mathbf{a}$, a 'random' perturbation $\mathbf{b}$ is prepared as follows. We generate a sequence of random numbers r_k with uniform probability distribution in $[0, 1]$ and define $b_k = m_k y_k$, where

$$m_k = \begin{cases} 1 - 10^{-14} & \text{if } r_k < 0.5, \\ 1 + 10^{-14} & \text{otherwise.} \end{cases}$$

The DFT's $\hat{\mathbf{a}}$ and $\hat{\mathbf{b}}$ are computed and the second is subtracted from the first, yielding an array $\mathbf{c}$. The square moduli of the coefficients c_k are plotted against k/N. For the two tests in Figure 2.58 (a) and (b), an orbit on the circle attractor in Figure 2.7 (B) respectively on the strange attractor in Figure 2.10 have been used. The size of the sample has been kept to $N = 2^{16}$. In the first case, the propagated error $|c_k|^2$ varies

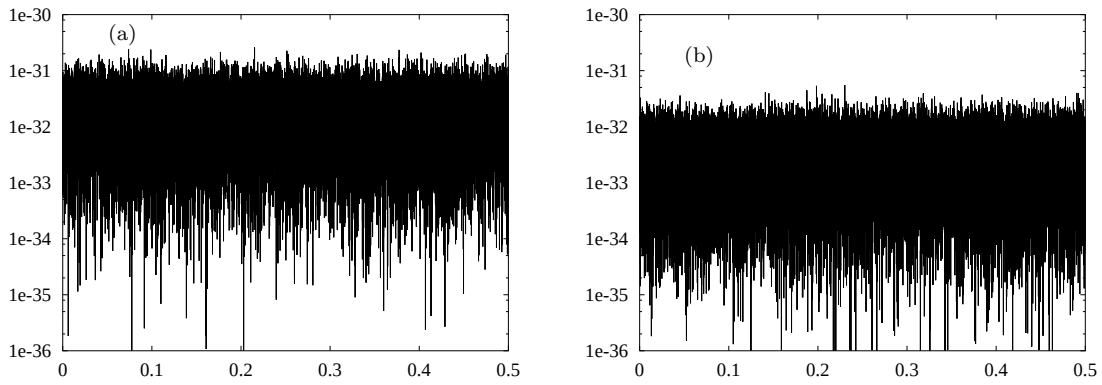

Figure 2.58: (a), (b) Tests on the propagation of errors in the DFT algorithm. See text for explanation.

between order 10^{-35} and 10^{-31}. Therefore we have that $0.001 \lessapprox |c_k| / 10^{-14} \lessapprox 0.1$, and the same holds for the second case. Since the size of the sample is of order 1, we conclude that the random error propagates to the amplitudes divided by a factor ranging between 0.1 and 0.001.

Remark 2.12. The power spectrum is often used as an estimator of the spectral density of a stationary stochastic process. Given a stationary, zero-average, discrete time stochastic process $\{X_n\}_{n \in \mathbb{Z}}$ on a probability space (Ω, ν), the autocorrelation function is defined by

$$\gamma_X : \mathbb{Z} \to \mathbb{C}, \qquad \gamma_X(n) = E[X_n X_0],$$

where E denotes the expected value with respect to ν. A white noise stochastic process is characterised by $\gamma_X(n) = 0$ except at $n = 0$, where $\gamma_X(0)$=1. Furthermore, the spectral density [30] is constant.

Consider a P-attractor $\mathscr{W} \subset \mathbb{R}^3$ and suppose that it has a unique Sinai-Ruelle-Bowen measure[24] ν. This allows us to define a process $\{X_n\}_{n\in\mathbb{Z}}$ on the probability space $(\mathscr{W}, \nu)$, where $X_n = Y \circ P^n$ is the n-th iterate of P on $\mathscr{W}$, measured by the observable $Y : \mathscr{W} \to \mathbb{R}$. Then power spectra like in Figure 2.9 (A) indicate a practically constant spectral density. This implies that the random variables X_n and X_m are uncorrelated when $m \neq n$.

[24] In fact, this is a rather strong assumption, see *e.g.* [122].

Chapter 3

Hénon-like strange attractors in a family of maps of the solid torus

3.1 Introduction

The research presented in this Chapter is motivated by the following question:

> Are there maps having quasi-periodic Hénon-like attractors?

Numerical examples of quasi-periodic Hénon-like attractors are given in Chapters one and two. We begin by giving definitions of the concepts used here, mainly following the terminology in [42, 86, 120]. Consider a C^1 diffeomorphism $F : M \to M$, where M is an m-dimensional smooth manifold. A set $\mathscr{A} \subset M$ is called an *attractor* if $\mathscr{A}$ is a topologically transitive compact F-invariant set such that the stable set (basin of attraction) $W^s(\mathscr{A})$ has nonempty interior. We recall that an F-invariant set $\mathscr{A} \subset M$ is called topologically transitive if there exists a point $z \in \mathscr{A}$ such that the orbit $\mathrm{Orb}(z) = \{F^j(z)\}_{j\geq 0}$ of z under F is dense in $\mathscr{A}$. An attractor $\mathscr{A}$ is called *strange* if there exist constants $\kappa > 0$, $\lambda > 1$, a dense orbit $\mathrm{Orb}(z) \subset \mathscr{A}$ and a vector $v \in T_zM$ such that

$$\|DF^n(z)v\| \geq \kappa\lambda^n \qquad \text{for } n \geq 0. \tag{3.1}$$

Condition (3.1) means that the attractor $\mathscr{A}$ has a positive Lyapunov exponent on the dense orbit $\mathrm{Orb}(z)$. The attractor $\mathscr{A}$ is called *Hénon-like* [42, 86, 120] if there exist a saddle periodic orbit $\mathrm{Orb}(p) = \{s, F(p), \ldots, F^n(p)\}$, a point z in the unstable manifold $W^u(\mathrm{Orb}(p))$, constants $\kappa > 0$, $\lambda > 1$, and tangent vectors $v, w \in T_zM$, with $w \neq 0$, such that

$$\mathscr{A} = \operatorname{clos} W^u(\mathrm{Orb}(p)),$$

$\mathrm{Orb}(z)$ is dense in $\mathscr{A}$, equation (3.1) holds, and furthermore

$$\|DF^n(z)w\| \to 0 \qquad \text{as } n \to \pm\infty. \tag{3.2}$$

Hénon-like attractors are strange by (3.1), and are non-uniformly hyperbolic by (3.2). In particular, Hénon-like attractors contain *critical points*, that is, points belonging to a dense orbit for which a nonzero tangent vector w exists, which is contracted both by positive and by negative iteration of the derivative DF.

We say that the attractor $\mathscr{A}$ is *quasi-periodic Hénon-like* if there exist a quasi-periodic invariant circle $\mathscr{C}$ of saddle type, a point $p \in W^u(\mathscr{C})$, constants $\kappa > 0$, $\lambda > 1$, and a vector $v \in T_pM$ such that condition (3.1) holds, while

$$\mathscr{A} = \operatorname{clos} W^u(\mathscr{C}).$$

In the last decade several mathematical results have been obtained concerning the structure of strange attractors in families of maps. A basic example is provided by the Hénon attractor [58], occurring in the family of maps

$$H_{a,b} : \mathbb{R}^2 \to \mathbb{R}^2, \quad (x, y) \mapsto (1 - ax^2 + y,\, bx), \tag{3.3}$$

where a and b are real parameters. Benedicks and Carleson [10, 11] proved that there exists a set of parameter values $\mathfrak{S}$, with positive Lebesgue measure, such that for all $(a, b) \in \mathfrak{S}$ the Hénon map $H_{a,b}$ (3.3) has an attractor coinciding with the closure $\operatorname{clos} W^u(p)$ of the unstable manifold of a saddle fixed point p. By using analogous ideas, strange attractors were proved to occur in parametrised families of maps, near homoclinic tangencies in two or higher dimensions [86, 96, 113, 120], and near tangencies in the saddle-node critical case [42]. See [127] for a general set-up to prove existence of strange attractors having one positive Lyapunov exponent. All strange attractors considered in the cited papers are Hénon-like, see the definition above. See [121] for a result concerning existence of strange attractors with two or more positive Lyapunov exponents.

In this Chapter we provide two partial answers to the question formulated at the beginning of this introduction. Our first result concerns the C^3-family of skew-product diffeomorphisms $T_{\alpha,\delta,a,\varepsilon}$, defined on the solid torus $\mathbb{R}^2 \times \mathbb{S}^1$, where $\mathbb{S}^1 = \mathbb{R}/\mathbb{Z}$, and given by

$$T_{\alpha,\delta,a,\varepsilon} : \mathbb{R}^2 \times \mathbb{S}^1 \to \mathbb{R}^2 \times \mathbb{S}^1, \qquad \begin{pmatrix} x \\ y \\ \theta \end{pmatrix} \mapsto \begin{pmatrix} 1 - ax^2 + \varepsilon f(a, x, y, \theta, \varepsilon, \alpha, \delta) \\ \varepsilon g(a, x, y, \theta, \varepsilon, \alpha, \delta) \\ \theta + \alpha + \delta \sin(2\pi\theta) \end{pmatrix}. \tag{3.4}$$

The restriction of (3.4) to $\mathbb{S}^1$ is the Arnol′d family of circle maps [4]:

$$A_{\alpha,\delta} : \mathbb{S}^1 \to \mathbb{S}^1, \quad \theta \mapsto \theta + \alpha + \delta \sin(2\pi\theta). \tag{3.5}$$

For $0 \le \delta < (1/2\pi)$ and $\alpha \in [0, 1]$, the map $A_{\alpha,\delta}$ is a diffeomorphism of the circle $\mathbb{S}^1$. There exist open subsets $\mathfrak{A}^{q/n}$ of the (α, δ) plane (Arnol′d tongues), such that the rotation number of $A_{\alpha,\delta}$ is q/n for all $(\alpha, \delta) \in \mathfrak{A}^{q/n}$.

The map (3.4) is a generalization of the planar Hénon-like families considered in [86, 120]. The latter are families of planar diffeomorphisms, which are C^3-small perturbations of the logistic family

$$Q_a : \mathbb{R} \to \mathbb{R}, \qquad x \mapsto 1 - ax^2. \tag{3.6}$$

In $T_{\alpha,\delta,a,\varepsilon}$, the planar part also depends on the circle dynamics by the perturbative terms f and g. The only requirement on f and g is that their C^3-norms are bounded on compact sets. Occurrence of Hénon-like attractors is proved in the family $T_{\alpha,\delta,a,\varepsilon}$ for all parameter values belonging to a set of of positive (Lebesgue) measure. For all

values in this set, the parameters (α, δ) are such that the dynamics of the Arnol′d family $A_{\alpha,\delta}$ (3.5) is of Morse-Smale type: there exist periodic points θ^s and θ^r in $\mathbb{S}^1$, such that θ^s is attracting and θ^r repelling for $A_{\alpha,\delta}$. The attractors $\mathscr{A}$ we obtain coincide with the closure of the one-dimensional unstable manifold

$$\mathscr{A} = \operatorname{clos} W^u\left(\operatorname{Orb}(p)\right),$$

where $p = (x_0, y_0, \theta^s) \in \mathbb{R}^2 \times \mathbb{S}^1$ belongs to a hyperbolic periodic orbit of saddle type. Occurrence of such attractors holds on a positive measure set of parameter values for all sufficiently C^3-small perturbations of f and g. This result is formulated in more detail in the next section.

A second situation is analysed subsequently. Fix $n > 0$ and let $K : \mathbb{R}^2 \to \mathbb{R}^2$ be a dissipative planar C^n-diffeomorphism having a hyperbolic saddle fixed point $p' \in \mathbb{R}^2$ with a transversal homoclinic point. Then it is well-known that the closure of the unstable manifold $\operatorname{clos} W^u(p')$ attracts an open set of points (initial states) [86, 95]. This result is here generalised to certain families of maps of the solid torus, having an invariant circle of saddle type. Let P_α be a family of diffeomorphisms of $\mathbb{R}^2 \times \mathbb{S}^1$ given by the product of a map K as above with a rigid rotation of angle α on $\mathbb{S}^1$, *i.e.*,

$$P_\alpha : \mathbb{R}^2 \times \mathbb{S}^1 \to \mathbb{R}^2 \times \mathbb{S}^1, \quad (x, y, \theta) \mapsto \big(K(x, y), \theta + \alpha\big).$$

The map P_α has the invariant saddle-like circle $\mathscr{C} = \{p'\} \times \mathbb{S}^1$. Then for any sufficiently C^2-small perturbation of P_α, the circle $\mathscr{C}$ persists as a normally hyperbolic C^1-manifold, and the invariant set $\operatorname{clos} W^u(\mathscr{C})$ attracts an open set of points, *i.e.*,

$$\operatorname{int}(W^s(\operatorname{clos} W^u(\mathscr{C}))) \neq \emptyset. \tag{3.7}$$

Notice that in general $\operatorname{clos} W^u(\mathscr{C})$ is not topologically transitive, as required in the definition of attractor we use. For example, $\operatorname{clos} W^u(\mathscr{C})$ might contain periodic attractors. Property (3.7) holds for an open set in the parameter space. However, by standard KAM arguments, the quasi-periodicity of $\mathscr{C}$ (which implies the transitivity of $\mathscr{C}$) generically is persistent only for a nowhere dense set of positive measure in the parameter space, see *e.g.* [17].

3.1.1 Hénon-like strange attractors in a family of skew product maps

We here formulate our main result about the family $T_{\alpha,\delta,a,\varepsilon}$ in (3.4). Throughout, the family $T_{\alpha,\delta,a,\varepsilon}$ is assumed to be C^3 in all variables and parameters. The parameter space is the set of all $(\alpha, \delta, a, \varepsilon) \in \mathbb{R}^4$ such that

$$\alpha \in [0, 1],\ \delta \in \big[0, 1/(2\pi)\big),\ a \in [0, 2],\ |\varepsilon| < 1. \tag{3.8}$$

Furthermore, we require the C^3-norm of f and g to be bounded on compact sets. We call such skew-product families *rotating Hénon-like*. For the statement of the result we need a few definitions and notations.

Definition 3.1. *Consider a map $M : J \to J$, where $J \subset \mathbb{R}$ is an interval.*

1. *The map M is called* topologically mixing *if for any open intervals J_1, $J_2 \subset J$ there exists n_0 such that*

$$M^n(J_1) \cap J_2 \neq \emptyset \quad \text{for all } n \geq n_0.$$

2. *A point $p \in \mathbb{R}$ is* preperiodic *for M if there exists an $m \geq 2$ such that $M^m(p)$ is a periodic point of M.*

3. *For a given integer $n > 1$, denote by $\Phi(n)$ the set of all integers q such that q and n are relatively prime, where $1 \leq q < n$. If $n = 1$ put $\Phi(n) = \{1\}$.*

4. *The interval $K_a = [Q_a^2(0), Q_a(0)]$ is called the* core *or the* restrictive interval *of the logistic family Q_a (3.6).*

It is well-known that $Q_a([0,1]) = Q_a(K_a) = K_a$ for all a, where K_a is the core of Q_a (3.6), see *e.g.* [83].

Theorem 3.1. *Choose $a^* \in (0,2)$ such that the quadratic map Q_{a^*} in (3.6) is topologically mixing on its core $K = [1 - a^*, 1]$ and its critical point $c = 0$ is preperiodic. Let $n \geq 1$ be an integer and p_0 be a (repelling) periodic point of the n-th iterate $Q_{a^*}^n$. Then there exist positive constants $\bar{\varepsilon}_n$, $\bar{a}_n$ and χ_n such that the following holds.*

1. *For all $(\alpha, \delta, a, \varepsilon)$ as in (3.8), with*

$$(\alpha, \delta) \in \cup_{q \in \Phi(n)} \operatorname{clos} \mathfrak{A}^{q/n}, \quad |a - a^*| < \bar{a}_n, \quad |\varepsilon| < \bar{\varepsilon}_n \tag{3.9}$$

the map $T_{\alpha,\delta,a,\varepsilon}$ has a saddle periodic point p such that the unstable manifold $W^u(\mathrm{Orb}(p))$ is one-dimensional.

2. *For all $(\alpha, \delta, \varepsilon)$ as in (3.9) there exists a set $\mathfrak{S}_{\alpha,\delta,\varepsilon}$ with*

$$\mathfrak{S}_{\alpha,\delta,\varepsilon} \subset [a^* - \bar{a}_n, a^* + \bar{a}_n], \qquad \operatorname{meas}(\mathfrak{S}) > \chi_n$$

such that for all $a \in \mathfrak{S}_{\alpha,\delta,\varepsilon}$ the closure $\operatorname{clos} W^u(\mathrm{Orb}(p))$ is a Hénon-like strange attractor of $T_{\alpha,\delta,a,\varepsilon}$.

Corollary 3.1. *The set of parameter values for which $T_{\alpha,\delta,a,\varepsilon}$ has a Hénon-like attractor contains the set*

$$\mathfrak{S} = \bigcup_{n \in \mathbb{N}} \left\{ (\alpha, \delta, a, \varepsilon) \;\mid\; (\alpha, \delta) \in \cup_{q \in \Phi(n)} \operatorname{clos} \mathfrak{A}^{q/n}, \quad |\varepsilon| < \bar{\varepsilon}_n, \quad a \in \mathfrak{S}_{\alpha,\delta,\varepsilon} \right\},$$

and the set $\mathfrak{S}$ has positive Lebesgue measure

$$\operatorname{meas}(\mathfrak{S}) \geq 2 \sum_{n=1}^{\infty} \bar{\varepsilon}_n \chi_n \sum_{q \in \Phi(n)} \operatorname{meas} \mathfrak{A}^{q/n}.$$

Our proof of Theorem 3.1 is given in Sec. 3.2. It is based on a result of Díaz-Rocha-Viana [42], and relies on the following facts:

1. For (α, δ) inside any tongue $\mathfrak{A}^{q/n}$, the asymptotic dynamics of $T_{\alpha,\delta,a,\varepsilon}$ is described by an $\mathcal{O}(\varepsilon)$-perturbation of the n-th iterate Q_a^n.

2. For all n the map Q_a^n is a generic n-modal family, in the sense of [42]. See the definition given in Sec. 3.2.

Two attractors occurring in the family

$$\begin{pmatrix} x \\ y \\ \theta \end{pmatrix} \mapsto \begin{pmatrix} 1 - (a + \varepsilon \sin(2\pi\theta))x^2 + y \\ bx \\ \theta + \alpha + \delta \sin(2\pi\theta) \end{pmatrix}, \tag{3.10}$$

are shown in Figure 3.1 (A) and (B), for (α, δ) in an Arnol′d tongue of period two and three, respectively. The Hénon-like character of these attractors remains conjectural for the specific parameter values considered. Notice that the family (3.10) takes the form (3.4) after a rescaling $y \mapsto \sqrt{|b|}y$ and by choosing $b = \mathcal{O}(\varepsilon)$.

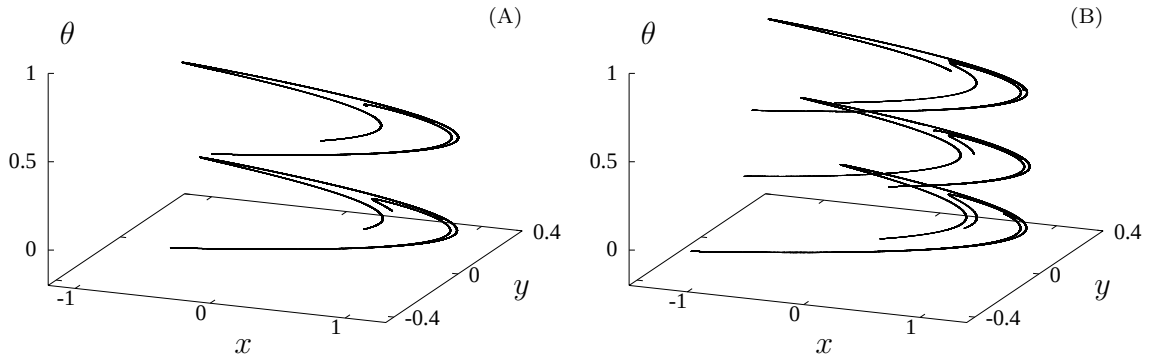

Figure 3.1: Attractors of the family in (3.10) for (α, δ) in Arnol′d tongues of periods two and three. (A) Parameters are fixed at $a = 1.3$, $b = 0.3$, $\varepsilon = 0.2$, $(\alpha, \delta) = (0.51, 0.116)$. (B) Same as (A) for $\alpha = 0.33793$.

A case which is not covered by Theorem 3.1 is when the dynamics of the forcing map $A_{\alpha,\delta}$ in (3.4) is quasi-periodic. In such a situation, by [11] it is straightforward that at $\varepsilon = 0$ Hénon-like strange attractors occur for a positive measure set of parameters (α, δ, a). To fix ideas, consider the family in (3.10). Choose a and b such that the Hénon map (3.3) has a strange attractor $\mathscr{A}'$, coinciding with the closure of the unstable manifold of a saddle fixed point p. According to [11], such (a, b) form a set of positive measure. Since at $\varepsilon = 0$ the dynamics of (3.10) on $\mathbb{R}^2$ is uncoupled from that on $\mathbb{S}^1$, map (3.10) has a strange attractor $\mathscr{A} = \mathscr{A}' \times \mathbb{S}^1$. Furthermore, $\mathscr{A}$ coincides with the closure of the unstable manifold of the quasi-periodic saddle-type invariant circle $\{p\} \times \mathbb{S}^1$. Numerical experiments (see Figure 3.2 (A)) suggest that attractors like $\mathscr{A}$ persist for small ε. Occurrence of the same kind of quasi-periodic Hénon-like strange attractors has been observed in several numerical studies. Compare [90] and the literature on strange nonchaotic attractors [49, 53, 65, 66, 68, 74, 91, 119]. In Chapter two of this thesis a diffeomorphism P of $\mathbb{R}^3 = \{x, y, z\}$ is studied (also see [24]). There we conjectured that the attractor $\mathscr{A}$ of P in Figure 3.2 (B) is contained inside the closure $\operatorname{clos} W^u(\mathscr{C})$ of the unstable manifold of a quasi-periodic invariant circle $\mathscr{C}$ of saddle type. A cross-section Σ of $\mathscr{A}$, magnified in Figure 3.3 left, suggests that the two-dimensional unstable manifold of $\mathscr{C}$ is folded onto itself, thereby creating a Hénon-like structure. To illustrate the dynamics inside $\mathscr{A}$ we computed the image $P(\Sigma)$. This yields a folded curve looking like a planar Hénon attractor.

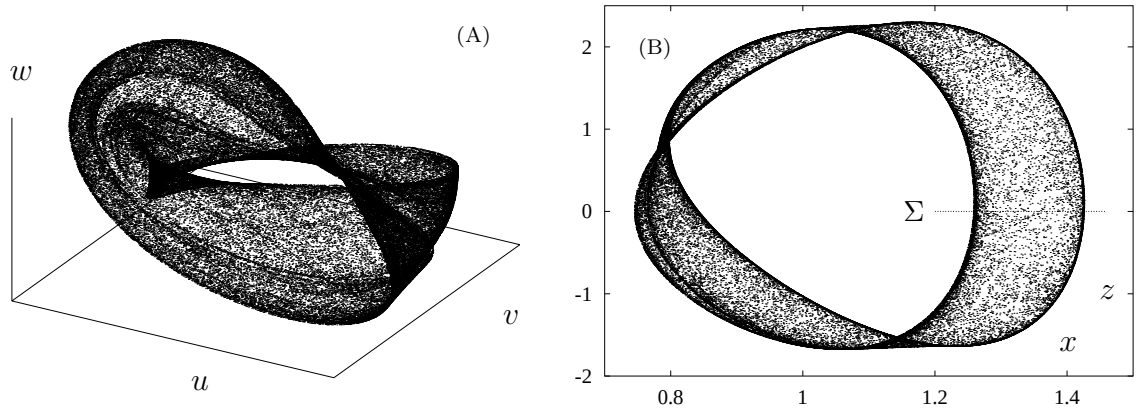

Figure 3.2: (A) Attractor of map (3.10) in the quasi-periodic case. Parameter values are fixed at $a = 1.85$, $b = -0.2$, $\delta = 0$, $\alpha = (\sqrt{5}-1)/2$, $\varepsilon = 0.1$. For a better visualisation of the folds, the plot is given in the variables (u, v, w), where $u = (r+4)\cos(\theta)$, $v = (r+4)\sin(\theta)$, with $r = x\cos(\theta) + 10y\sin(\theta)$, and $w = -x\sin(\theta) + 10y\cos(\theta)$. (B) Projection on the (x, z)-plane of a strange attractor of the three-dimensional Poincaré map $P_{F,G,\varepsilon}$ of Chapter two, also see [24].

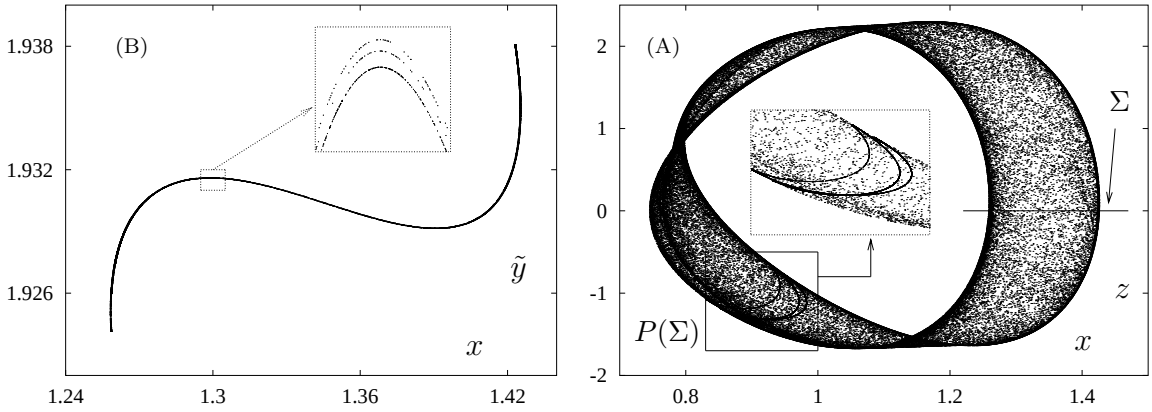

Figure 3.3: (A) Projection on $(x, \tilde{y})$, with $\tilde{y} = y - 0.133 * z$, of a slice Σ of the attractor $\mathscr{A}$ in Figure 3.2 (B). The slice Σ contains all points such that the distance from the plane $z = 0$ is less than 0.0001. (B) The attractor $\mathscr{A}$, with the slice Σ and the image $P(\Sigma)$ under the diffeomorphism P. The image $P(\Sigma)$ is magnified in the central box.

3.1.2 Homoclinic intersections of saddle invariant circles

Hénon-like attractors coincide with the closure $\operatorname{clos} W^u(\mathrm{Orb}(p))$ of the unstable manifold of a saddle periodic orbit. For the dissipative Hénon map (3.3), *i.e.*, for $|b| < 1$, under suitable hypotheses the Hénon attractor is *contained* in $\operatorname{clos} W^u(\mathrm{Orb}(p))$ [11, 86, 95]. We generalise this result to families of maps of the following type. Fix an integer $n \geq 2$ and let $K = (K_1, K_2) : \mathbb{R}^2 \to \mathbb{R}^2$ be a dissipative (area contracting) C^n-diffeomorphism. Denote by $R_\alpha : \mathbb{S}^1 \to \mathbb{S}^1$ the rigid rotation $R_\alpha(\theta) = \theta + \alpha$. Consider

the C^n-family of diffeomorphisms

$$P_{\alpha,\varepsilon} : \mathbb{R}^2 \times \mathbb{S}^1 \to \mathbb{R}^2 \times \mathbb{S}^1, \quad (x, y, \theta) \mapsto \big(K_1(x, y) + f(x, y, \theta, \alpha, \varepsilon), \\ K_2(x, y) + g(x, y, \theta, \alpha, \varepsilon), \\ \theta + \alpha + h(x, y, \theta, \alpha, \varepsilon)\big), \tag{3.11}$$

where $f = g = h = 0$ for $\varepsilon = 0$. A hyperbolic saddle fixed point p of K corresponds to an invariant circle $\mathscr{C}_{\alpha,0}$ of saddle type for the map $P_{\alpha,\varepsilon}$ at $\varepsilon = 0$. The circle $\mathscr{C}_{\alpha,0}$ is *normally hyperbolic* (see [60] for a definition), and, therefore, it is persistent under small perturbations. Notice that the perturbation in $P_{\alpha,\varepsilon}$ is of a more general type than in $T_{\alpha,\delta,a,\varepsilon}$, since no preservation of the skew-product structure is now required. A few basic results are summarised in the following proposition.

Proposition 3.2. *Suppose that K has a saddle fixed point $p = (x_0, y_0)$. Then for all $\alpha \in [0, 1]$ the map $P_{\alpha,0}$ has an invariant circle $\mathscr{C}_\alpha$ of saddle type. The manifold $\mathscr{C}_\alpha$ is r-normally hyperbolic for all integers r with $1 \le r \le n$. Moreover, for all $r < n$ there exists an $\varepsilon_r > 0$ such that for all $\varepsilon < \varepsilon_r$ and all $\alpha \in [0, 1]$, $P_{\alpha,\varepsilon}$ has a C^r-saddle invariant circle $\mathscr{C}_{\alpha,\varepsilon}$, C^r-close to $\mathscr{C}_{\alpha,0}$.*

Proof: The dynamics of $P_{\alpha,0}$ on $\mathscr{C}_{\alpha,0}$ is parallel with rotation number α. This implies that $\mathscr{C}_{\alpha,0}$ is an r-normally hyperbolic invariant manifold for all $r \le n$ and, therefore, it is C^n. So $\mathscr{C}_{\alpha,0}$, as well as its stable and unstable manifolds, is persistent under C^n-small perturbations. This directly follows from [60]. □

Proposition 3.2 allows us to construct a basin of attraction with nonempty interior for the invariant set $\operatorname{clos} W^u(\mathscr{C}_{\alpha,\varepsilon})$, provided that the one-dimensional unstable manifold $W^u(p)\mathbb{R}^2$ of the map K does not escape to infinity. For $(x, y, \theta) \in \mathbb{R}^2 \times \mathbb{S}^1$, denote by $\omega(x, y, \theta)$ the ω-limit set of (x, y, θ) under $P_{\alpha,\varepsilon}$.

Theorem 3.2. *Fix integers n and r such that $n \ge 2$ and $1 \le r < n$. Choose $\varepsilon < \varepsilon_r$ as in Proposition* 3.2 *and let $\alpha \in [0, 1]$. Suppose that $K : \mathbb{R}^2 \to \mathbb{R}^2$ is C^n and satisfies:*

1. *K has a saddle fixed point $p \in \mathbb{R}^2$ and a transversal homoclinic point $q \in W^s(p) \cap W^u(p)$.*
2. *The map K is uniformly dissipative: there exists $\kappa < 1$ such that $|\det(DK(x, y))| \le \kappa$ for all $(x, y) \in \mathbb{R}^2$.*
3. *$W^u(p)$ is contained in a bounded subset of $\mathbb{R}^2$.*

Then there exists an $\varepsilon^* < \varepsilon_r$ such that for all $\varepsilon < \varepsilon^*$ there exists an open, nonempty bounded set $U \subset \mathbb{R}^2 \times \mathbb{S}^1$ such that for all $(x, y, \theta) \in U$

$$\omega(x, y, \theta) \subset \operatorname{clos} W^u(\mathscr{C}_{\alpha,\varepsilon}). \tag{3.12}$$

Under the conditions of Theorem 3.2, the invariant set $\operatorname{clos} W^u(\mathscr{C}_{\alpha,\varepsilon})$ attracts all orbits with initial state in an open set U. This holds for an open set of ε-values. In general, however, $\operatorname{clos} W^u(\mathscr{C}_{\alpha,\varepsilon})$ is not an attractor in the sense of our definition (compare Sec. 3.1), since it might be non-topologically transitive. This occurse for example if $\operatorname{clos} W^u(\mathscr{C}_{\alpha,\varepsilon})$ contains a periodic attractor.

In the next theorem we prove that at least the circle $\mathscr{C}_{\alpha,\varepsilon}$ is quasi-periodic (and, hence, topologically transitive) for a set of parameter values of large relative measure.

Theorem 3.3. *Let $P_{\alpha,\varepsilon}$ be a C^n-family of diffeomorphisms as in* (3.11)*, where n is sufficiently large ($n \geq 5$ will do). Choose ε^* as in Theorem* 3.2*. Then for all $\varepsilon < \varepsilon^*$ sufficiently small the following holds.*

1. *There exists a set $D_\varepsilon \subset [0,1]$ with Lebesgue measure $\mathrm{meas}(D_\varepsilon) > 0$ such that for $\alpha \in D_\varepsilon$ the restriction of $P_{\alpha,\varepsilon}$ to the circle $\mathscr{C}_{\alpha,\varepsilon}$ is smoothly conjugate to an irrational rigid rotation.*

2. *$\mathrm{meas}(D_\varepsilon)$ tends to 1 for $\varepsilon \to 0$.*

Proofs of Theorems 3.2 and 3.3 are given in Sec. 3.3.

Remark 3.1. The quasi-periodicity of the dynamics inside $\mathscr{C}_{\alpha,\varepsilon}$ may have consequences for the dynamics in its stable and unstable manifolds. This is certainly the case if α is irrational and if the map $P_{\alpha,0}$ is perturbed within the class of skew-products, that is

$$P_{\alpha,\varepsilon}(x,y,\theta) = \big(K(x,y) + \varepsilon f(x,y,\theta,\alpha,\varepsilon), \theta + \alpha\big).$$

In this case, indeed, the dynamics inside $W^u(\mathscr{C}_{\alpha,\varepsilon})$ and $W^s(\mathscr{C}_{\alpha,\varepsilon})$ has a quasi-periodic component, given by a rotation over angle α, see [57]. More precisely, $W^u(\mathscr{C}_{\alpha,\varepsilon})$ can be parametrised as

$$W^u(\mathscr{C}_{\alpha,\varepsilon}) = \big\{(W(\theta,\eta),\theta) \;\mid\; \theta \in \mathbb{S}^1 \text{ and } \eta \in \mathbb{R}\big\},$$

where $W : \mathbb{S}^1 \times \mathbb{R} \to \mathbb{R}^2$. Furthermore,

$$P_{\alpha,\varepsilon}(W(\theta,\eta),\theta) = \big(W(\theta+\alpha, N(\theta,\eta)), \theta+\alpha\big),$$

where $N : \mathbb{S}^1 \times \mathbb{R} \to \mathbb{R}$. See [57] for rigorous statements and proofs.

3.2 Existence of Hénon-like attractors

Our proof of Theorem 3.1 is based on a result of Díaz-Rocha-Viana [42]. We begin by stating this result.

3.2.1 Perturbations of multimodal families

Two definitions from [42] are introduced now. For more information about the terminology, we refer to [83].

Definition 3.2. *Let $J \subset \mathbb{R}$ be a compact interval. Fix $d \geq 1$, $k \geq 3$, $a^* \in \mathbb{R}$, and an interval of parameter values $\mathfrak{U} = [a_-, a_+]$, with $a^* \in \operatorname{int}\mathfrak{U}$. A C^k-family of maps $M_a : J \to J$, with $a \in \mathfrak{U}$, is called a d-family if it satisfies the following conditions:*

1. Invariance: *$M_{a^*}(J) \subset \operatorname{int}(J)$;*

2. Nondegenerate critical points: *M_{a^*} has d critical points $\{c_1, \ldots, c_d\} \stackrel{\text{def}}{=} \operatorname{Cr} M_{a^*}$ that satisfy*

$$M''_{a^*}(c_i) \neq 0 \;\; \textit{for all } i \quad \textit{and} \quad M_{a^*}(c_i) \neq c_j \;\; \textit{for all} \;\; i,j;$$

3. Negative Schwarzian derivative: $SM_{a^*} < 0$ *for all* $x \neq c_i$, *where*
$$Sf(x) = \frac{f'''(x)}{f'(x)} - \frac{3}{2}\left(\frac{f''(x)}{f'(x)}\right)^2;$$

4. Topological mixing: *for any open intervals* J_1, J_2 *in the core of* M_{a^*} *there exists* n_0 *such that*
$$M_{a^*}^n(J_1) \cap J_2 \neq \emptyset \quad \text{for all } n \geq n_0$$
(for the definition of core of a multimodal map, see e.g. [83]*);*

5. Preperiodicity: *for each* $1 \leq i \leq d$ *there exists* m_i *such that* $p_i = M_{a^*}^{m_i}(c_i)$ *is a (repelling) periodic point of* M_{a^*}*;*

6. Genericity of unfolding: *For all* $c_i \in \operatorname{Cr} M_{a^*}$, *denote by* $c_i(a)$ *and* $p_i(a)$ *the continuations of* c_i *and* p_i, *respectively, for* a *close to* a^*. *Then*
$$\frac{\mathrm{d}}{\mathrm{d}a}\big(M_a^{m_i}(c_i(a)) - p_i(a)\big) \neq 0 \qquad \text{at } a = a^*.$$

Next we introduce the notion of η-*perturbation* of a d-family M_a, with $a \in \mathfrak{U}$ and $d \geq 1$ fixed.

Definition 3.3. *Fix* $\sigma > 0$ *and consider the family* $\overline{M}_a$ *obtained by extending* M_a *as follows:*
$$\overline{M}_a : J \times I_\sigma \to J \times I_\sigma, \quad \overline{M}_a(x,y) \stackrel{\text{def}}{=} (M_a(x), 0). \tag{3.13}$$
Also denote by M *the map*
$$M : \mathfrak{U} \times J \times I_\sigma \to J \times I_\sigma, \quad M(a,x,y) \stackrel{\text{def}}{=} \overline{M}_a(x,y) = (M_a(x), 0).$$
Given a C^k*-family of diffeomorphisms*
$$G_a : J \times I_\sigma \to J \times I_\sigma, \qquad a \in J,$$
for a $k \geq 3$, *denote by* G *its extension*
$$G : \mathfrak{U} \times J \times I_\sigma \to J \times I_\sigma, \quad G(a,x,y) \stackrel{\text{def}}{=} G_a(x,y).$$
Then G *is called a* η-perturbation *of the* d*-family* $\{M_a\}_a$ *if*
$$\|M - G\|_{C^k} \leq \eta,$$
where $\|\cdot\|_{C^k}$ *denotes the* C^k*-norm over* $\mathfrak{U} \times J \times I_\sigma$.

The following result asserts that for η sufficiently small, any η-perturbation G_a of a d-family has a non-uniformly hyperbolic strange attractor for all parameter values a in a set $\mathfrak{S}$ of positive Lebesgue measure. See [10, 11, 86, 96, 120, 127] for similar results.

Proposition 3.3. **[42, Theorem 5.2]** *Let* $\{M_a\}_a$ *be a* d*-family and* p *a periodic point of* M_{a^*}. *Then there exist* $\eta > 0$, $\bar{a}$ *and* $\chi > 0$ *such that, given any* η*-perturbation* $\{G_a\}_a$ *of* $\{M_a\}_a$ *the following holds.*

1. *For all* a *with* $|a - a^*| < \bar{a}$ *the map* G_a *has a periodic point* p_a *which is the continuation of the periodic point* $(p, 0)$ *of the map* $\overline{M}_a$ *in* (3.13).

2. *There exists a set* $\mathfrak{S}$, *contained in the interval* $[a^* - \bar{a}, a^* + \bar{a}] \subset \mathfrak{U}$, *with* $\operatorname{meas}(\mathfrak{S}) > \chi$, *such that for all* $a \in \mathfrak{S}$ *the set* $\operatorname{clos} W^u(p_a)$ *is a Hénon-like strange attractor of the map* G_a.

3.2.2 Strange attractors in rotating Hénon-like families

We here present a proof of Theorem 3.1. The argument is based on three facts. First, suppose that $a^* \in [0,2]$ is such that the quadratic family $Q_a(x) = 1 - ax^2$ in (3.6) is a d-family in the sense of Definition 3.2, with $d = 1$. Then for all $n \geq 1$ the family $M_a \stackrel{\text{def}}{=} Q_a^n$ given by the n-th iterate of Q_a is a d-family for some $d \leq 2^n$. Second, for all $\eta_1 > 0$, the composition of an η_1-perturbation of Q_a with an η_1-perturbation of Q_a^n is an η_2-perturbation of Q_a^{n+1}, where $\eta_2 = C(n)\eta_1$ and $C(n)$ is a positive constant depending on n. Third, for each $n > q \geq 1$ and for each $(\alpha, \delta) \in \mathfrak{A}^{q/n}$, the asymptotic dynamics of $T_{\alpha,\delta,a,\varepsilon}$ is described by a map that turns out to be an η-perturbation of the d-family M_a, with $\eta = \mathcal{O}(\varepsilon)$. Application of Proposition 3.3 then concludes the proof.

In the next lemma we show that M_a is a d-family. For each $\tilde{a} \in [0,2)$ there exists a $\beta > 0$ such that for all a with $a \in [0, \tilde{a}]$ the interval $J = [-1-\beta, 1+\beta] \subset \mathbb{R}$ satisfies $Q_a(J) \subset \text{int}(J)$. In the sequel, it is always assumed that the family Q_a is defined on such an interval J, and that the values of a we consider are such that $Q_a(J) \subset \text{int}(J)$.

Lemma 3.4. *Suppose $a^* \in [0,2) \stackrel{\text{def}}{=} \mathfrak{U}$ is such that the quadratic family*

$$Q_a : J \to J, \quad Q_a(x) = 1 - ax^2$$

satisfies hypotheses 4 and 5 of Definition 3.2. Then for all $n \geq 1$ there exists $d \geq 1$ such that the family

$$M_a : J \to J, \quad M_a \stackrel{\text{def}}{=} Q_a^n$$

is a d-family with $d \leq 2^n - 1$ critical points.

Proof. Take a^* as above. We first prove the case $n = 1$, that is, $Q_a : J_a \to J_a$ is a 1-family. Conditions 1, 2, 3 of Definition 3.2 are obviously satisfied by Q_a. Condition 6 will now be proved. By Conditions 4 and 5 (assumed by hypothesis), Q_{a^*} is a Misiurewicz map [84], *i.e.*, it has no periodic attractor and $c \notin \omega(c)$, where $c = 0$ is the critical point of Q_{a^*}. Moreover, by [83, Theorem 6.3] the map Q_{a^*} is Collet-Eckmann (see *e.g.* [83, Sec. V.4]), that is, there exist constants $\kappa > 0$ and $\lambda > 1$ such that

$$\left| DQ_{a^*}^j(Q_{a^*}(c)) \right| \geq \kappa \lambda^j \quad \text{for all } j \geq 0. \tag{3.14}$$

Therefore, according to [115, Theorem 3]

$$\lim_{n\to\infty} \frac{\frac{\mathrm{d}}{\mathrm{d}a} Q_a^n(c) \mid_{a=a^*}}{\frac{\mathrm{d}}{\mathrm{d}x} Q_{a^*}^{n-1}(Q_{a^*}(c))} > 0. \tag{3.15}$$

Assume $Q_{a^*}^k(c) = p$, with p periodic (and repelling) under Q_{a^*}. By $p(a)$ denote the continuation of p for a close to a^*. Then, for all n sufficiently large,

$$\begin{aligned}
\frac{\mathrm{d}}{\mathrm{d}a} Q_a^n(c) \mid_{a=a^*} &= \frac{\partial Q_a^{n-k}}{\partial a}(Q_{a^*}^k(c)) \mid_{a=a^*} + \frac{\partial Q_a^{n-k}}{\partial x}(Q_{a^*}^k(c)) \mid_{a=a^*} \frac{\mathrm{d}}{\mathrm{d}a} Q_a^k(c) \mid_{a=a^*} = \\
&= \frac{\partial}{\partial a} Q_a^{n-k}(p) \mid_{a=a^*} + \frac{\partial}{\partial x} Q_a^{n-k}(p) \mid_{a=a^*} \frac{\mathrm{d}}{\mathrm{d}a} \left[p(a) + Q_a^k(c) - p(a) \right] \mid_{a=a^*} = \\
&= \frac{\mathrm{d}}{\mathrm{d}a} \left(Q_a^{n-k}(p(a)) \right) + \frac{\partial}{\partial x} Q_{a^*}^{n-k}(p) \frac{\mathrm{d}}{\mathrm{d}a} \left[Q_a^k(c) - p(a) \right] \mid_{a=a^*} .
\end{aligned} \tag{3.16}$$

The point $Q_a^{n-k}(p(a))$ belongs to a hyperbolic periodic orbit, that varies smoothly with the parameter a. Therefore, its derivative with respect to a (which is the first term in the last equality) is uniformly bounded in n. On the other hand,

$$\frac{\mathrm{d}}{\mathrm{d}x}Q_{a^*}^{n-1}(Q_{a^*}(c)) = \frac{\partial}{\partial x}Q_{a^*}^{n-k}(p)\frac{\mathrm{d}}{\mathrm{d}x}Q_{a^*}^{k-1}(Q_{a^*}(c)).$$

Therefore, by (3.14), (3.15), and (3.16) we conclude that

$$0 < \lim_{n\to\infty} \frac{\frac{\mathrm{d}}{\mathrm{d}a}Q_a^n(c)\mid_{a=a^*}}{\frac{\mathrm{d}}{\mathrm{d}x}Q_{a^*}^{n-1}(Q_{a^*}(c))} = \frac{\frac{\mathrm{d}}{\mathrm{d}a}\left[Q_a^k(c) - p(a)\right]_{a=a^*}}{\frac{\mathrm{d}}{\mathrm{d}x}Q_{a^*}^{k-1}(Q_{a^*}(c))}. \tag{3.17}$$

This proves that Q_a satisfies Condition 6 of Definition 3.2.

We now show that the n-th iterate M_a of the quadratic map is a d-family for all $n > 1$ and for some $d \le 2^n$. For simplicity, we denote Q_{a^*} by Q for the rest of the proof. Condition 1 holds for M_{a^*} since it holds for Q_{a^*}. Condition 3 follows from the fact that the composition of maps with negative Schwarzian derivative also has negative Schwarzian derivative, see *e.g.* [83]. Condition 4 is obviously satisfied.

Condition 2 is now proved by induction on n, where the case $n = 1$ is obvious. Since Q is 2-to-1, the set $\mathrm{Cr}\, M_{a^*}$ of critical points of M_{a^*} has cardinality $d \le 2^n - 1$. Moreover,

$$\mathrm{Cr}\, M_{a^*} = Q^{-1}\left(\mathrm{Cr}\, Q^{n-1}\right) \cup \mathrm{Cr}\, Q = \bigcup_{j=0}^{n-1}(Q^{-j})(\mathrm{Cr}\, Q). \tag{3.18}$$

Suppose that Condition 2 holds for a given $n \ge 1$. We first show that

$$(Q^{n+1})''(x) \neq 0 \qquad \text{for all } \; x \in \mathrm{Cr}\, Q^{n+1}. \tag{3.19}$$

By (3.18), if $x \in \mathrm{Cr}\, Q^{n+1}$ then either $x = c$, or $Q(x) \in \mathrm{Cr}\, Q^n$. If $x = c$ then

$$(Q^{n+1})''(x) = (Q^n)'\,(Q(c)) \cdot (Q)''(c). \tag{3.20}$$

The second factor is nonzero. If the first factor is zero, then

$$0 = (Q^n)'\,(Q(c)) = Q'(Q^n(c)) \ldots Q'(Q(c)).$$

Therefore there exists j such that $Q^j(c) = c$, so that c is an attracting periodic point of Q. But this contradicts the fact that Q is Misiurewicz, so that (3.20) is nonzero. The other possibility is that $c \neq x$ and $Q(x) \in \mathrm{Cr}\, Q^n$. In this case,

$$(Q^{n+1})''(x) = (Q^n)''\,(Q(x)) \cdot Q'(x)^2,$$

which is nonzero. Indeed, $Q'(x) \neq 0$, otherwise $x = c$. Moreover $(Q^n)''\,(Q(x)) \neq 0$ by the induction hypotheses since the critical points of Q^n are nondegenerate. This proves (3.19), from which the first part of Condition 2 follows.

We now prove, again arguing by contradiction, that

$$Q^{n+1}(x) \neq y \qquad \text{for all } \; x, y \in \mathrm{Cr}\, Q^{n+1}.$$

Suppose that there exist $x, y \in \operatorname{Cr} Q^{n+1}$ such that $Q^{n+1}(x) = y$. By (3.18) there exist i and j such that $Q^i(x) = Q^j(y) = c$, where $0 \le i, j \le n$. This would imply that

$$Q^{n+1+j-i}(c) = Q^j(Q^{n+1}(x)) = Q^j(y) = c,$$

with $n + 1 + j - i \ge 1$ and, therefore, c would be an attracting periodic point of Q, which is impossible since Q is Misiurewicz. Condition 2 is proved.

To prove Condition 5, fix $y \in \operatorname{Cr} M_{a^*}$ and $j \ge 0$ such that $Q^j(y) = c$. Since c is preperiodic for Q by hypothesis, there exists $k \ge 1$ such that $Q^{j+k}(y) = p$, where p is periodic under Q with period $u \ge 1$. The orbit of y under M_{a^*} is, except for a finite number of initial iterates, a subset of the orbit of p under Q. This shows that y is preperiodic for M_{a^*}.

To prove Condition 6, take $y \in \operatorname{Cr} M_{a^*}$, j, u, k and $p \in J$ as in the proof of Condition 5. Then there exist integers l and m, with $0 \le l < u$ and $m \ge 1$, such that

$$M^m_{a^*}(y) = Q^{k+l}(c) = Q^l(p) \in \operatorname{Orb}_Q(p). \tag{3.21}$$

By Condition 5 (assumed by hypothesis) and by (3.21), the point $z = Q^l(p)$ is periodic (and repelling) under M_{a^*}. Denote by $y(a)$, $z(a)$, and $p(a)$ the continuations of y, z, and p, respectively, for a close to a^*. In particular,

$$Q^j_a(y(a)) = c \quad \text{and} \quad Q^l_a(p(a)) = z(a).$$

We have to show that

$$\frac{\mathrm{d}}{\mathrm{d}a}\left[M^m_a(y(a)) - z(a)\right]\big|_{a=a^*} \neq 0. \tag{3.22}$$

By the chain rule we get

$$\begin{aligned}
\frac{\mathrm{d}}{\mathrm{d}a}\, Q^{l+k}_a(c)\big|_{a=a^*} &= \frac{\partial Q^l_a}{\partial a}\,(Q^k_a(c))\big|_{a=a^*} + \frac{\partial Q^l_a}{\partial x}\,(Q^k_a(c))\big|_{a=a^*}\,\frac{\mathrm{d}Q^k_a}{\mathrm{d}a}\,(c)|_{a=a^*} = \\
&= \frac{\partial Q^l_{a^*}}{\partial a}(p) + \frac{\partial Q^l_{a^*}}{\partial x}(p)\,\frac{\mathrm{d}Q^k_{a^*}}{\mathrm{d}a}(c), \\
\frac{\mathrm{d}}{\mathrm{d}a}\, Q^l_a(p(a))\big|_{a=a^*} &= \frac{\partial Q^l_{a^*}}{\partial a}(p) + \frac{\partial Q^l_{a^*}}{\partial x}(p)\,\frac{\mathrm{d}}{\mathrm{d}a}p(a^*),
\end{aligned}$$

where $p = p(a^*) = Q^k_{a^*}(c)$. Therefore,

$$\begin{aligned}
\frac{\mathrm{d}}{\mathrm{d}a}\left[M^m_a(y(a)) - z(a)\right]\big|_{a=a^*} &= \frac{\mathrm{d}}{\mathrm{d}a}\left[Q^{k+l}_a(c) - Q^l_a(p(a))\right]\big|_{a=a^*} = \\
&= \frac{\partial Q^l_{a^*}}{\partial x}(p)\,\frac{\mathrm{d}}{\mathrm{d}a}\left[Q^k_a(c) - p(a)\right]\big|_{a=a^*}.
\end{aligned}$$

The factor $\frac{\mathrm{d}}{\mathrm{d}a}\left[Q^k_a(c(a)) - p(a)\right]\big|_{a=a^*}$ is nonzero by (3.17). The same holds for the other factor, otherwise p would be an attracting periodic point of Q_{a^*}. This proves inequality (3.22). □

In the next lemma we show that the composition of a small perturbation of the map $\overline{Q}_a(x, y) = (Q_a(x), 0)$ (we use here the notation of Definition 3.3) with a small perturbation of $\overline{Q^n_a}(x, y) = (Q^n_a(x), 0)$ yields a small perturbation of $\overline{Q^{n+1}_a}(x, y)$. As in Definition 3.3, denote by $Q, Q^n : [0, 2] \times J \times I \to J \times I$ the functions $Q(a, x, y) = (Q_a(x), 0)$ and $Q^n(a, x, y) = (Q^n_a(x), 0)$, respectively.

Lemma 3.5. *For each $\eta > 0$ there exists a $\zeta > 0$ such that for all $F, G : [0,2]\times J\times I \to J \times I$ such that*

$$\|G - Q\|_{C^3} < \zeta \quad \textit{and} \quad \|F - Q^n\|_{C^3} < \zeta, \tag{3.23}$$

we have

$$\left\|G \circ F - Q^{n+1}\right\|_{C^3} < \eta. \tag{3.24}$$

Proof. Write

$$G(a,x,y) = \begin{pmatrix} Q_a(x) + g_1(a,x,y) \\ g_2(a,x,y) \end{pmatrix} \quad \text{and} \quad F(a,x,y) = \begin{pmatrix} Q_a^n(x) + f_1(a,x,y) \\ f_2(a,x,y) \end{pmatrix}.$$

Then

$$G \circ F(a,x,y) - \begin{pmatrix} Q_a^{n+1}(x) \\ 0 \end{pmatrix} = \\ \begin{pmatrix} -2a(f_1(a,x,y))^2 - 2af_1(a,x,y)Q_a^n(x) + g_1\big(a, \tilde{f}_1(a,x,y), f_2(a,x,y)\big) \\ g_2\big(a, \tilde{f}_1(a,x,y), f_2(a,x,y)\big) \end{pmatrix},$$

where $\tilde{f}_1(a,x,y) = Q_a^n(x) + f_1(a,x,y)$. The C^3-norm of the terms $-2a(f_1(a,x,y))^2$ and $-2af_1(a,x,y)Q_a^n(x)$ is bounded by a constant times the C^3-norm of f_1. We now estimate the norm of $\tilde{g}_1$, defined by

$$\tilde{g}_1(x_0,x_1,x_2) = g_1(a, \tilde{f}_1(a,x,y), f_2(a,x,y)).$$

Denote $x_0 = a$, $x_1 = x$, and $x_2 = y$. Then any second order derivative of $\tilde{g}_1$ is a sum of terms of the following type:

$$\frac{\partial^2 g_1}{\partial x_j x_k}\,\frac{\partial \tilde{f}_k}{\partial x_l}, \quad \frac{\partial g_1}{\partial x_k}\,\frac{\partial^2 \tilde{f}_k}{\partial x_j x_l},$$

where we put $\tilde{f}_2 = f_2$ to simplify the notation. For the third order derivatives a similar property holds. Since the C^3-norm of $\tilde{f}_k$ is bounded, we get that each term in the third order derivative of $\tilde{g}_1$ is bounded by a constant times the C^3-norm of the g_j. This concludes the proof. □

Proof of Theorem 3.1**.** The theorem will be first proved for $a^* < 2$. The case $a^* = 2$ follows by choosing another value $\bar{a}^* < 2$ sufficiently close to 2. Fix $a^* \in [0,2)$ verifying the hypotheses of Lemma 3.4. To begin with, we consider the case $(\alpha,\delta) \in \operatorname{int}\mathfrak{A}^1$, the interior of the tongue of period one. Then the Arnol′d family $A_{\alpha,\delta}$ on $\mathbb{S}^1$ has two hyperbolic fixed points θ_1^s (attracting) and θ_1^r (repelling), see [41, Sec. 1.14]. The θ-coordinate of both points depends on the choice of $(\alpha,\delta) \in \operatorname{int}\mathfrak{A}^1$. So for all $\theta \in \mathbb{S}^1$ with $\theta \neq \theta_1^r$, the orbit of θ under $A_{\alpha,\delta}$ converges to θ_1^s. This means that the manifold

$$\Theta_1 = \left\{(x,y,\theta) \in \mathbb{R}^2 \times \mathbb{S}^1 \;\mid\; \theta = \theta_1^s\right\} \subset \mathbb{R}^2 \times \mathbb{S}^1$$

is invariant and attracting under $T_{\alpha,\delta,a,\varepsilon}$. Denote by $G_{a,1}$ the restriction of $T_{\alpha,\delta,a,\varepsilon}$ to Θ_1:

$$G_{a,1} : \Theta_1 \to \Theta_1, \qquad (x,y,\theta_1^s) \mapsto (1 - ax^2 + \varepsilon f_1,\ \varepsilon g_1,\ \theta_1^s),$$

where $f_1 = f(a, x, y, \theta_1^s, \alpha, \delta)$ and similarly for g_1. Since $Q_{a^*}(J) \subset \mathrm{int}(J)$, there exists a constant $\sigma > 0$ such that for all ε sufficiently small and all a close enough to a^*,

$$\begin{aligned} G_{a,1}(J \times I_\sigma \times \{\theta_1^s\}) &\subset \mathrm{int}(J \times I_\sigma \times \{\theta_1^s\}) \quad \text{and} \\ T_{\alpha,\delta,a,\varepsilon}\left(J \times I_\sigma \times (\mathbb{S}^1 \setminus \{\theta_1^r\})\right) &\subset \mathrm{int}\left(J \times I_\sigma \times (\mathbb{S}^1 \setminus \{\theta_1^r\})\right). \end{aligned} \tag{3.25}$$

Since Θ_1 is diffeomorphic to $\mathbb{R}^2$, we consider $G_{a,1}$ as a map of $\mathbb{R}^2$. Then $G_{a,1}$, is an η-perturbation of the quadratic family $Q_a(x)$, where $\eta = \mathcal{O}(\varepsilon)$. We now apply Proposition 3.3 to the family $G_{a,1}$. Let p_0 be a periodic point of M_{a^*}. For all ε sufficiently small there exists a constant $\bar{a} > 0$ and a set $\mathfrak{S}$ of positive Lebesgue measure, contained in the interval $[a^* - \bar{a}, a^* + \bar{a}]$, such that the following holds. For all $a \in [a^* - \bar{a}, a^* + \bar{a}]$, $G_{a,1}$ has a saddle periodic point $\bar{p}$ which is the continuation of the point p_0. Furthermore, for all $a \in \mathfrak{S}$ the closure $\widetilde{\mathscr{A}} = \mathrm{clos}\, W^u(\bar{p})$ is a Hénon-like strange attractor of $G_{a,1}$ contained inside Θ_1. The point $p = (\bar{p}, \theta_1^s)$ is a saddle periodic point of the map $T_{\alpha,\delta,a,\varepsilon}$, and $W^u(p) = W^u(\bar{p}) \times \{\theta_1^s\}$. Therefore $\mathscr{A} = \mathrm{clos}\, W^u(p) = \widetilde{\mathscr{A}} \times \{\theta_1^s\}$. Moreover, the basin of attraction of $\mathrm{clos}\, W^u(p)$ has nonempty interior in $\mathbb{R}^2 \times \mathbb{S}^1$ because of (3.25). This proves the claim for $(\alpha, \delta) \in \mathrm{int}\, \mathfrak{A}^1$.

We pass to the case of higher period tongues. Suppose that $(\alpha, \delta) \in \mathrm{int}\, \mathfrak{A}^{q/n}$, with $n > q \geq 1$. Then $A_{\alpha,\delta}$ has (at least) two hyperbolic periodic orbits

$$\begin{aligned} \mathrm{Orb}(\theta_1^s) &= \{\theta_1^s, \theta_2^s, \ldots, \theta_n^s\} \quad \text{attracting, and} \\ \mathrm{Orb}(\theta_1^r) &= \{\theta_1^r, \theta_2^r, \ldots, \theta_n^r\} \quad \text{repelling.} \end{aligned}$$

For $j = 1, \ldots, n$, denote by Θ_j the manifold

$$\Theta_j = \left\{(x, y, \theta) \in \mathbb{R}^2 \times \mathbb{S}^1) \;\mid\; \theta = \theta_j^s\right\},$$

and define maps G_j as the restriction of $T_{\alpha,\delta,a,\varepsilon}$ to Θ_j:

$$\begin{aligned} &G_j : \Theta_j \to \Theta_{j+1} \qquad \text{for } j = 1, \ldots, n-1 \\ &G_n : \Theta_n \to \Theta_1, \qquad \text{where} \\ &(x,\ y,\ \theta_1^s) \overset{G_j}{\mapsto} (Q_a(x) + \varepsilon f_j,\ \varepsilon g_j,\ \theta_{j+1}^s), \qquad \text{for } j = 1, \ldots, n-1 \\ &(x,\ y,\ \theta_n^s) \overset{G_n}{\mapsto} (Q_a(x) + \varepsilon f_n,\ \varepsilon g_n,\ \theta_1^s). \end{aligned}$$

Here, $f_j = f(a, x, y, \theta_j^s, \alpha, \delta)$. The manifold Θ_1 is invariant and attracting under the n-th iterate of the map $T_{\alpha,\delta,a,\varepsilon}$. For all (x, y, θ) in the complement of the set

$$\{(x, y, \theta) \;\mid\; \theta \in \mathrm{Orb}(\theta_1^r)\},$$

the asymptotic dynamics is given by the map

$$G_{a,1,\ldots n} \overset{\mathrm{def}}{=} G_n \circ G_{n-1} \circ \cdots \circ G_1.$$

Notice that each of the G_j's is an η_j-perturbation of the family Q_a in the sense of Definition 3.3, where $\eta_j = B\varepsilon$ and B can be chosen uniform on θ_j^s (and, therefore, on (α, δ)).

Let p_0 be a periodic point of $M_a \stackrel{\text{def}}{=} Q_a^n$. Then $(p_0, 0)$ is a saddle periodic point for the map $\overline{M}_a$ defined as in (3.13). Take η, $\bar{a}$, and χ as in Proposition 3.3. By inductive application of Lemma 3.5 there exists an $\bar{\varepsilon} > 0$ depending on η and n such that

$$\|G_{a,1,\dots n} - Q^n\|_{C^3} < \eta,$$

for all $(\alpha, \delta) \in \operatorname{int} \mathfrak{A}^{q/n}$ and all $|\varepsilon| < \bar{\varepsilon}$. That is, $G_{a,1,\dots n}$ is an η-perturbation of M_a for all q with $1 \le q < n$ and all $(\alpha, \delta, a, \varepsilon)$ with

$$(\alpha, \delta) \in \mathfrak{A}^{q/n}, \quad \varepsilon \in [-\bar{\varepsilon}, \bar{\varepsilon}].$$

By Proposition 3.3 there exist an $\bar{a} > 0$ and a set $\mathfrak{S}$ contained in the interval $[a^* - \bar{a}, a^* + \bar{a}]$ such that $\operatorname{meas}(\mathfrak{S}) \ge \chi$ and the following holds. For all $a \in [a^* - \bar{a}, a^* + \bar{a}]$ the map $G_{a,1,\dots,n}$ has a periodic point $\bar{p}_a$ which is the continuation of the periodic point $(p_0, 0)$ of $\overline{M}_a$. Moreover, for all $a \in \mathfrak{S}$ the closure $\widetilde{\mathscr{A}} = \operatorname{clos} W^u(\bar{p}_a)$ is a Hénon-like strange attractor of $G_{a,1,\dots,n}$, contained inside Θ_1.

To finish the proof, observe that $p_a = (\bar{p}_a, \theta_1^s)$ is a saddle periodic point of $T_{\alpha,\delta,a,\varepsilon}$. The set $\mathscr{A} = \operatorname{clos} W^u(p_a)$ is compact and invariant under $T_{\alpha,\delta,a,\varepsilon}$, where

$$\mathscr{A} = \big(\widetilde{\mathscr{A}} \times \{\theta_1^s\}\big) \cup T_{\alpha,\delta,a,\varepsilon}\big(\widetilde{\mathscr{A}} \times \{\theta_1^s\}\big) \cup \dots \cup T^{n-1}_{\alpha,\delta,a,\varepsilon}\big(\widetilde{\mathscr{A}} \times \{\theta_1^s\}\big).$$

To show that $\mathscr{A}$ has a dense orbit, suppose that the orbit of $z = (x_0, y_0, \theta_1^s)$ under $G_{a,1,\dots n}$ is dense in $\widetilde{\mathscr{A}}$. Then given $\eta > 0$ and a point

$$q = T^j_{\alpha,\delta,a,\varepsilon}(q') \in T^j_{\alpha,\delta,a,\varepsilon}(\widetilde{\mathscr{A}} \times \{\theta_1^s\}), \quad \text{with } 1 \le j \le n-1,$$

there exists $m > 0$ such that $\operatorname{dist}(G^m_{a,1,\dots n}(z), q') < \eta$. By continuity of $T^j_{\alpha,\delta,a,\varepsilon}$, for all $\varrho > 0$ there exists $\eta > 0$ such that

$$\operatorname{dist}(T^j_{\alpha,\delta,a,\varepsilon}(q''), T^j_{\alpha,\delta,a,\varepsilon}(q')) < \varrho \quad \text{for all } q'' \text{ with } \quad \operatorname{dist}(q'', q') < \eta.$$

We conclude that for all $\varrho > 0$ there exists $m > 0$ such that

$$\operatorname{dist}(T^j_{\alpha,\delta,a,\varepsilon}(G^m_{a,1,\dots n}(z)), T^j_{\alpha,\delta,a,\varepsilon}(q')) = \operatorname{dist}(T^{j+mn}_{\alpha,\delta,a,\varepsilon}(z), q) < \varrho.$$

This proves that the orbit of z under $T_{\alpha,\delta,a,\varepsilon}$ is dense in $\mathscr{A}$. Properties (3.1) and (3.2) will now be proved. Since $G_{a,1,\dots,n} = T^n_{\alpha,\delta,a,\varepsilon}$ on Θ_1, for any $m \in \mathbb{N}$ and any $z \in \mathscr{A}$ we have

$$DT^m_{\alpha,\delta,a,\varepsilon}(z) = DT^r_{\alpha,\delta,a,\varepsilon}(G^s_{a,1,\dots,n}(z)) DG^s_{a,1,\dots,n}(z),$$

where $s = m \mod n$ and $r = m - s$. Take $z \in \mathscr{A}$ having a dense orbit and $v = (v_x, v_y, 0) \in T_z\mathscr{A}$ such that $\left\|DG^s_{a,1,\dots,n}(z)v\right\| \ge \kappa\lambda^s$ for all s, where $\kappa > 0$ and $\lambda > 1$ are constants. Since $T^r_{\alpha,\delta,a,\varepsilon}$ is a diffeomorphism for all $r = 1, \dots, s-1$ and $G^s_{a,1,\dots,n}(z)$ belongs to the compact set $\mathscr{A}$ for all $s \in \mathbb{N}$, then there exists a constant $c > 0$ such that

$$\left\|DT^m_{\alpha,\delta,a,\varepsilon}(z)v\right\| = \left\|DT^r_{\alpha,\delta,a,\varepsilon}(G^s_{a,1,\dots,n}(z)) DG^s_{a,1,\dots,n}(z)v\right\| \ge c \left\|DG^s_{a,1,\dots,n}(z)v\right\|,$$

where c is uniform in r. This proves property (3.1). Property (3.1) is proved similarly. This shows that the closure $\operatorname{clos} W^u(p_a)$ is a Hénon-like strange attractor of $T_{\alpha,\delta,a,\varepsilon}$.

Remark 3.2. At the boundary of a tongue $\mathfrak{A}^{q/n}$ the Arnol′d family $A_{\alpha,\delta}$ has a saddle-node periodic point θ_1. However, the basin of attraction of $\operatorname{Orb}\theta_1$ still has nonempty interior, so that the above conclusions hold for all (α, δ) in the closure $\operatorname{clos} \mathfrak{A}^{q/n}$.

□

3.3 Basins of attraction and invariant circles

In this section we give proofs of Theorems Theorem 3.2 and Theorem 3.3. The setting of the problem is now briefly recalled, also see Sec. 3.1.2. Suppose $K : \mathbb{R}^2 \to \mathbb{R}^2$ is a dissipative (area contracting) C^n-diffeomorphism, where $n \geq 2$. Define the direct product map

$$P_{\alpha,0} : \mathbb{R}^2 \times \mathbb{S}^1 \to \mathbb{R}^2 \times \mathbb{S}^1, \quad (x, y, \theta) \mapsto (K(x, y), \theta + \alpha), \tag{3.26}$$

where $\mathbb{S}^1 = \mathbb{R}/\mathbb{Z}$. We consider C^n-small perturbations $P_{\alpha,\varepsilon}$ of $P_{\alpha,0}$, to be written as

$$\begin{aligned} P_{\alpha,\varepsilon} &: \mathbb{R}^2 \times \mathbb{S}^1 \to \mathbb{R}^2 \times \mathbb{S}^1, \\ &(x, y, \theta) \mapsto \big(K(x, y) + \varepsilon f_\varepsilon(x, y, \theta, \alpha), \theta + \alpha + \varepsilon g_\varepsilon(x, y, \theta, \alpha)\big), \end{aligned}$$

see (3.11). Here the dependence of $P_{\alpha,\varepsilon}$ on the parameters (α, ε) is C^n. In general $P_{\alpha,\varepsilon}$ has not a skew-product structure such as the rotating Hénon map (3.4). We assume that K has a saddle fixed point $p = (x_0, y_0)$. This corresponds to an invariant circle $\mathscr{C}_\alpha$ of saddle type of $P_{\alpha,\varepsilon}$ at $\varepsilon = 0$. Normal hyperbolicity of $\mathscr{C}_\alpha$ guarantees its persistence under small perturbations, see Proposition 3.2. Our proof of Theorem 3.3 is based on a version of the KAM Theorem holding for finite differentiability. We begin by proving Theorem 3.2

3.3.1 Basins of attraction: The Tangerman-Szewc argument generalised

Let $K : \mathbb{R}^2 \to \mathbb{R}^2$ be a dissipative diffeomorphism having a saddle fixed point $p = (x_0, y_0)$. Suppose the stable and unstable manifolds $W^s(p)$ and $W^u(p)$ intersect transversally at the homoclinic point $q \in W^s(p) \cap W^u(p)$, see Figure 3.4. Also assume that $W^u(p)$ is bounded as a subset of $\mathbb{R}^2$. The Tangerman-Szewc Theorem

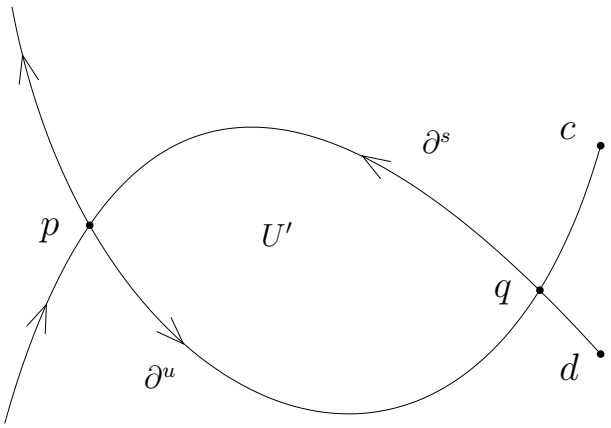

Figure 3.4: Segments ∂^s and ∂^u of the stable and unstable manifold, respectively, of a saddle fixed point p bound a region U, see text for more explanation.

states that the basin of attraction of the closure of $W^u(p)$ contains the open region

U' bounded by the two arcs $\partial^s \subset W^s(p)$ and $\partial^u \subset W^u(p)$ with extremes p and q, see Figure 3.4. This argument is by now standard, see *e.g.* [95] Appendix 3. It is also used to prove existence of strange attractors close to homoclinic tangencies of a saddle fixed point of a dissipative diffeomorphism, cf. [86, 120, 127].

We first prove Theorem 3.2 for $\varepsilon = 0$. This is a straightforward generalisation of the above Tangerman-Szewc Theorem. For small ε, the result is obtained by using persistence of normally hyperbolic invariant manifolds [60] and two transversality lemmas.

Proof of Theorem 3.2. Consider the circle $\mathscr{C}_\alpha = \mathscr{C}_{\alpha,0}$, invariant under map $P_{\alpha,0}$ in (3.26). The manifolds $W^u(\mathscr{C}_\alpha)$ and $W^s(\mathscr{C}_\alpha)$ are given by $W^u(p) \times \mathbb{S}^1$ and $W^s(p) \times \mathbb{S}^1$, respectively. They intersect transversally at a circle $\mathscr{H} = \{q\} \times \mathbb{S}^1$, consisting of points homoclinic to $\mathscr{C}_\alpha$. Consider the two arcs $\partial^s \subset W^s(p)$ and $\partial^u \subset W^u(p)$ with extremes p and q (Figure 3.4).They bound an open set $U' \subset \mathbb{R}^2$. Define D^s and D^u to be the portions of stable, and unstable manifold of $\mathscr{C}_\alpha$, respectively, given by

$$D^s = \partial^s \times \mathbb{S}^1 \subset W^s(\mathscr{C}_\alpha) \qquad \text{and} \qquad D^u = \partial^u \times \mathbb{S}^1 \subset W^u(\mathscr{C}_\alpha).$$

Both surfaces D^s and D^u are compact, and their union forms the boundary of the open region $U = U' \times \mathbb{S}^1$, which is topologically a solid torus.

The volume of U decreases under iteration of $P_{\alpha,0}$. Denoting by $\mathrm{meas}(\cdot)$ the Lebesgue measure both on $\mathbb{R}^2$ and on $\mathbb{R}^2 \times \mathbb{S}^1$, due to Condition 2 in Theorem 3.2 we have

$$\mathrm{meas}(P^n_{\alpha,0}(U)) = 2\pi \int_{K^n(U')} dxdy = 2\pi \int_{U'} |\det DK^n|\, dxdy \leq 2\pi\kappa^n \,\mathrm{meas}(U').$$

This implies that the forward evolution of every point $(x, y, \theta) \in U$ approaches the boundary of $P^n_{\alpha,0}(U)$:

$$\mathrm{dist}\big(P^n_{\alpha,0}(x, y, \theta), \partial P^n_{\alpha,0}(U)\big) \to 0 \quad \text{as } n \to +\infty.$$

Indeed, suppose that this does not hold. Then there exists a $\varrho > 0$ such that for all n there exists $N > n$ such that the ball with centre $P^N_{\alpha,0}(x, y, \theta)$ and radius $\varrho > 0$ is contained inside $P^N_{\alpha,0}(U)$. But this would contradict the fact that $\mathrm{meas}(P^n_{\alpha,0}(U)) \to 0$ as $n \to +\infty$.

The boundary of $P^n_{\alpha,0}(U)$ also consists of two portions of stable and unstable manifold of $\mathscr{C}$:

$$\partial P^n_{\alpha,0}(U) = P^n_{\alpha,0}(D^s) \cup P^n_{\alpha,0}(D^u).$$

The diameter of $P^n_{\alpha,0}(D^s)$ tends to zero as $n \to +\infty$, because all points in D^s are attracted to the circle $\mathscr{C}_\alpha$. Since $W^u(\mathscr{C}_\alpha)$ is bounded, all evolutions starting in U are bounded and approach $W^u(\mathscr{C}_\alpha)$, that is,

$$\mathrm{dist}(P^n_{\alpha,0}(x, y, \theta), P^n_{\alpha,0}(D^u)) \to 0 \quad \text{as } n \to +\infty$$

for all $(x, y, \theta) \in U$. This implies that $\omega(x, y, \theta) \subset \mathrm{clos}\, W^u(\mathscr{C}_\alpha)$ for all $(x, y, \theta) \in U$.

To extend this result to small perturbations $P_{\alpha,\varepsilon}$ of F_α, the following transversality lemmas are used.

Lemma 3.6. **[94, 103]** *Consider a map $f : V \to M$, where V and M are C^r-differentiable manifolds and f is C^r. Suppose V is compact, $W \subset M$ is a closed C^r-submanifold and f is transversal to W at V (notation: $f \pitchfork W$). Then $f^{-1}(W)$ is a C^r-submanifold of codimension $\operatorname{codim}_V(f^{-1}(W)) = \operatorname{codim}_M(W)$. Further suppose that there is a neighbourhood of $f(\partial_V) \cup \partial_W$ disjoint from $f(V) \cap W$, where ∂_V and ∂_W are the boundaries of V and W. Then any map $g : V \to M$, sufficiently C^r-close to f, is also transversal to W, and the two submanifolds $g^{-1}(W)$ and $f^{-1}(W)$ are diffeomorphic.*

Lemma 3.7. **[59]** *Let V_1, V_2, and M be C^r-differentiable manifolds and consider two diffeomorphisms $f_i : V_i \to M$, $i = 1, 2$. Then $f_1 \pitchfork f_2$ if and only if $f_1 \times f_2 \pitchfork \Delta$, where $f_1 \times f_2 : V_1 \times V_2 \to M \times M$ is the product map and $\Delta \subset M \times M$ is the diagonal: $\Delta = \{(y, y) \mid y \in M\}$.*

Fix $r \in \mathbb{N}$ and take $\varepsilon < \varepsilon_r$, where ε_r is given in Proposition 3.2. Then the map $P_{\alpha,\varepsilon}$ has an r-normally hyperbolic invariant circle $\mathscr{C}_{\alpha,\varepsilon}$ of saddle type. Furthermore, the manifolds $W^u(\mathscr{C}_{\alpha,\varepsilon})$, $W^s(\mathscr{C}_{\alpha,\varepsilon})$, and $\mathscr{C}_{\alpha,\varepsilon}$ are C^r-close to $W^u(\mathscr{C}_\alpha)$, $W^s(\mathscr{C}_\alpha)$, and $\mathscr{C}_\alpha$. We now show that the two manifolds $W^u(\mathscr{C}_{\alpha,\varepsilon})$, $W^s(\mathscr{C}_{\alpha,\varepsilon})$ still intersect transversally. To apply Lemma 3.6 we restrict to two suitable compact subsets $A^u \subset W^u(\mathscr{C}_\alpha)$ and $A^s \subset W^s(\mathscr{C}_\alpha)$ as follows. Consider the segments $\overline{pc} \subset W^u(p)$ and $\overline{pd} \subset W^s(p)$ in Figure 3.4. Define

$$A^u = \overline{pc} \times \mathbb{S}^1, \qquad A^s = \overline{pd} \times \mathbb{S}^1.$$

In this way, the circle $\mathscr{H}$ is the intersection of the manifolds A^u and A^s, bounded away from their boundaries. Consider the inclusions $i : A^u \to M$ and $j : A^s \to M$. By the closeness of $W^u(\mathscr{C}_\alpha)$ to $W^u(\mathscr{C}_{\alpha,\varepsilon})$ there exists a C^r-diffeomorphism $h : A^u \to A^u_\varepsilon \subset W^u(\mathscr{C}_{\alpha,\varepsilon})$ such that the map i is C^r-close to $i_\varepsilon \circ h$, where $i_\varepsilon : A^u_\varepsilon \to M$ is the inclusion [94]. Similarly, there exists a diffeomorphism $k : A^s \to A^s_\varepsilon \subset W^s(\mathscr{C}_{\alpha,\varepsilon})$ such that the map j is C^r-close $j_\varepsilon \circ k$, where $j_\varepsilon : A^s_\varepsilon \to M$ is the inclusion. By Lemma 3.7 the map $i \times j : A^u \times A^s \to M \times M$ is transversal to the diagonal Δ. For ε small, the map $(i_\varepsilon \circ h) \times (j_\varepsilon \circ k) : A^u \times A^s \to M \times M$ is C^r-close to $i \times j$:

$$\begin{array}{ccc} A^u \times A^s & \xrightarrow{i \times j} & M \times M \\ {\scriptstyle h \times k}\big\downarrow & & \\ A^u_\varepsilon \times A^s_\varepsilon & \xrightarrow{i_\varepsilon \times j_\varepsilon} & M \times M. \end{array}$$

Since Δ is closed and $A^u \times A^s$ is compact, Lemma 3.6 implies that there exists an ε^*, with $0 < \varepsilon^* < \varepsilon_r$, such that $(i_\varepsilon \circ h) \times (j_\varepsilon \circ k) \pitchfork \Delta$ for $\varepsilon < \varepsilon^*$. Furthermore, the submanifolds

$$(i \times j)^{-1}(\Delta) \quad \text{and} \quad \big((i_\varepsilon \circ h) \times (j_\varepsilon \circ k)\big)^{-1}(\Delta)$$

are diffeomorphic. We also have that $\big((i_\varepsilon \circ h) \times (j_\varepsilon \circ k)\big)^{-1}(\Delta)$ is diffeomorphic to $A^u_\varepsilon \cap A^s_\varepsilon$, and $(i \times j)^{-1}(\Delta) = A^u \cap A^s = \mathscr{H}$.

This shows that the intersection $\mathscr{H}_\varepsilon = A^u_\varepsilon \cap A^s_\varepsilon$ is diffeomorphic to $\mathscr{H}$. Define D^u_ε as the part of $W^u(\mathscr{C}_{\alpha,\varepsilon})$ bounded by the invariant circle $\mathscr{C}_{\alpha,\varepsilon}$ and the circle of homoclinic points $\mathscr{H}_\varepsilon$. Define $D^s_\varepsilon = k(D^s)$ similarly. Then the manifolds $D^u_\varepsilon \subset W^u(\mathscr{C}_{\alpha,\varepsilon})$ and $D^s_\varepsilon \subset W^s(\mathscr{C}_{\alpha,\varepsilon})$ form the boundary of an open region $U \subset M$ homeomorphic to a torus. By the closeness of the perturbed manifolds $W^s(\mathscr{C}_{\alpha,\varepsilon})$ and $W^u(\mathscr{C}_{\alpha,\varepsilon})$ to the

unperturbed $W^s(\mathscr{C})$ and $W^u(\mathscr{C})$, both U and $W^u(\mathscr{C}_{\alpha,\varepsilon})$ are bounded. Also notice that $P_{\alpha,\varepsilon}$ is dissipative: by taking ε^* small enough, we ensure that $|\det(DF(x,y,\theta))| < \tilde{c} < 1$ for all $\varepsilon < \varepsilon^*$ and (x,y,θ) in U. Therefore, all forward evolutions beginning at points $(x,y,\theta) \in U$ remain bounded. Like in the first part of the proof, one has

$$\omega(x,y,\theta) \subset \operatorname{clos} W^u(\mathscr{C}_{\alpha,\varepsilon})$$

for all $(x,y,\theta) \in U$, $\alpha \in [0,1]$ and $\varepsilon < \varepsilon^*$. □

3.3.2 Quasi-periodic invariant circles

So far, we did not discuss the dynamics in the saddle invariant circle $\mathscr{C}_{\alpha,\varepsilon}$ of map $P_{\alpha,\varepsilon}$ in (3.11). Generically, the dynamics on $\mathscr{C}_{\alpha,\varepsilon}$ is of Morse-Smale type. In this case, the circle consists of the union of the unstable manifold of some periodic saddle. Theorem 3.3 describes a complementary case, for which the dynamics is quasi-periodic. Fix $\tau > 2$ and define the set of Diophantine frequencies D_γ by

$$D_\gamma = \left\{ \alpha \in [0,1] \;\mid\; \left| \alpha - \frac{p}{q} \right| \geq \gamma q^{-\tau} \quad \text{for all } p,\, q \in \mathbb{N},\, q \neq 0 \right\}, \tag{3.27}$$

where $\gamma > 0$. Since we will apply a dissipative version of the KAM theorem in the case of finite differentiability (see [17, 18]), a certain amount of smoothness of the circle $\mathscr{C}_{\alpha,\varepsilon}$ is needed, depending on the Diophantine condition specified in (3.27). Therefore we require that the perturbed family of maps $P_{\alpha,\varepsilon}$ is C^n, for n large enough.

Proof of Theorem 3.3. Consider map F_α in (3.26), and let $p = (x_0, y_0)$ be a saddle fixed point of the dissipative diffeomorphism K. The invariant circle $\mathscr{C}_{\alpha,0}$ of F_α can be seen as a graph over $\mathbb{S}^1$:

$$\mathscr{C}_{\alpha,0} = \left\{ (\theta, x_0, y_0) \in \mathbb{R}^2 \times \mathbb{S}^1 \;\mid\; \theta \in \mathbb{S}^1 \right\}.$$

Fix $r \in \mathbb{N}$ large enough and $\varepsilon < \varepsilon_r$, where ε_r is taken as in Proposition 3.2. By the C^r-closeness of $\mathscr{C}_{\alpha,0}$ and $\mathscr{C}_{\alpha,\varepsilon}$ (Proposition 3.2), the circle $\mathscr{C}_{\alpha,\varepsilon}$ of $P_{\alpha,\varepsilon}$ can be written as a C^r-graph over $\mathbb{S}^1$:

$$\mathscr{C}_{\alpha,\varepsilon} = \left\{ (\theta, x_\varepsilon(\theta), y_\varepsilon(\theta)) \in \mathbb{R}^2 \times \mathbb{S}^1 \;\mid\; \theta \in \mathbb{S}^1 \right\}, \tag{3.28}$$

where $x_\varepsilon : \mathbb{S}^1 \to \mathbb{R}$, $x_\varepsilon(\theta) = x_0 + \mathcal{O}(\varepsilon)$, and similarly for $y_\varepsilon(\theta)$. So the restriction of $P_{\alpha,\varepsilon}$ to $\mathscr{C}_{\alpha,\varepsilon}$ has the following form

$$P_{\alpha,\varepsilon}\big|_{\mathscr{C}_{\alpha,\varepsilon}} : \mathscr{C}_{\alpha,\varepsilon} \to \mathscr{C}_{\alpha,\varepsilon}, \qquad P_{\alpha,\varepsilon}(\theta) = \theta + \alpha + \varepsilon g_\varepsilon(x_0, y_0, \theta, \alpha) + \mathcal{O}(\varepsilon^2).$$

By (3.28), we may consider $P_{\alpha,\varepsilon}$ as a map on $\mathbb{S}^1$. Fix $\gamma > 0$, $\tau > 3$ and take D_γ as in (3.27). For $\alpha \in D_\gamma$, the map $P_{\alpha,\varepsilon}$ can be averaged repeatedly over the circle, putting the θ-dependency into terms of higher order in ε, compare [23, Proposition 2.7] and [29, Sec. 4]. After such changes of variables, $P_{\alpha,\varepsilon}$ is brought into the normal form

$$P_{\alpha,\varepsilon}(\theta) = \theta + \alpha + c(\alpha,\varepsilon) + \mathcal{O}(\varepsilon^{r+1}).$$

In fact, it is convenient to consider α as a variable, and to define the cylinder maps

$$\begin{aligned} P_\varepsilon &: \mathbb{S}^1 \times [0,1] \to \mathbb{S}^1 \times [0,1], \qquad P_\varepsilon(\theta,\alpha) = (P_{\alpha,\varepsilon}(\theta),\alpha) \\ R &: \mathbb{S}^1 \times [0,1] \to \mathbb{S}^1 \times [0,1], \qquad R(\theta,\alpha) = (R_\alpha(\theta),\alpha), \end{aligned}$$

where $R_\alpha : \mathbb{S}^1 \to \mathbb{S}^1$ is the rigid rotation of an angle α. We now apply a finite differentiability version of the KAM Theorem to the family of diffeomorphisms P_ε, see *e.g.* [17, 18]. There exists an integer m with $1 \leq m < r$ and a C^m-map

$$\Phi_\varepsilon : \mathbb{S}^1 \times [0,1] \to \mathbb{S}^1 \times [0,1], \quad \Phi_\varepsilon(\theta,\alpha) = (\theta + \varepsilon A(\theta,\alpha,\varepsilon), \alpha + \varepsilon B(\alpha,\varepsilon)), \qquad (3.29)$$

such that the restriction of Φ_ε to $\mathbb{S}^1 \times D_\gamma$ makes the following diagram commute:

$$\begin{array}{ccc} \mathbb{S}^1 \times D_\gamma & \xrightarrow{R} & \mathbb{S}^1 \times D_\gamma \\ {\scriptstyle \Phi_\varepsilon}\uparrow & & {\scriptstyle \Phi_\varepsilon}\uparrow \\ \mathbb{S}^1 \times D_\gamma & \xrightarrow{P_\varepsilon} & \mathbb{S}^1 \times D_\gamma. \end{array}$$

The differentiability of Φ_ε restricted to $\mathbb{S}^1 \times D_\gamma$ is of Whitney type. Since $P_{\alpha,\varepsilon}\big|_{\mathscr{C}_{\alpha,\varepsilon}}$ is C^m-conjugate to a rigid rotation on $\mathbb{S}^1$, the circle $\mathscr{C}_{\alpha,\varepsilon}$ is in fact C^m. This proves parts 1 and 2 of the Theorem.

Furthermore, the constant γ in (3.27) can be taken equal to ε^r. This gives that the measure of the complement of D_γ in $[0,1]$ is of order ε^r as $\varepsilon \to 0$. □

3.4 Overview and future research

In this Chapter we prove that Hénon-like strange attractors occur in a family $T_{\alpha,\delta,a,\varepsilon}$ of diffeomorphisms of the solid torus $\mathbb{R}^2 \times \mathbb{S}^1$. The family $T_{\alpha,\delta,a,\varepsilon}$ is a perturbation of the quadratic family $Q_a(x) = 1 - ax^2$, and has a skew-product structure over $\mathbb{S}^1$. The strange attractors we obtain coincide with the closure of the one-dimensional unstable manifold $W^u(\mathrm{Orb}(p))$, where $\mathrm{Orb}(p)$ is a hyperbolic periodic orbit of saddle type which is a sink for the restriction of $T_{\alpha,\delta,a,\varepsilon}$ to $\mathbb{S}^1$.

In a slightly different context, we show that the invariant set $\operatorname{clos} W^u(\mathscr{C})$ attracts an open set of points, where $\mathscr{C}$ is an invariant circle of saddle type. This is proved for a family $P_{\alpha,\varepsilon}$ of diffeomorphisms of $\mathbb{R}^2 \times \mathbb{S}^1$, obtained as follows. We first consider the direct product of a rigid rotation on $\mathbb{S}^1$ with a diffeomorphism of $\mathbb{R}^2$ with a saddle fixed point having a point of transversal homoclinic intersection. Then $P_{\alpha,\varepsilon}$ is a perturbation of this product map.

Future research will focus on scenario's in which $\mathscr{A} = \operatorname{clos} W^u(\mathscr{C})$ is a strange attractor, *i.e.*, it is topologically transitive and has a dense orbit with a positive Lyapunov exponent, where $\mathscr{C}$ is a quasi-periodic invariant circle of saddle type. Attractors having these properties are called quasi-periodic Hénon-like attractors, see Chapter two and compare the numerical examples in Figures 3.3 and 3.5. Similar types of attractors have been found in several numerical studies [65, 66, 74, 91, 119].

We like to mention three other points of interest related to the above problem.

1. Consider first the strange attractors we obtain for the map $T_{\alpha,\delta,a,\varepsilon}$ (3.4), see Theorem 3.1 and compare Figure 3.1. An open problem is to characterize the bifurcations occurring when approaching the boundary of a resonance region for the dynamics in $\mathbb{S}^1$ (Arnol′d tongue). This corresponds to the transition from Hénon-like to quasi-periodic Hénon-like attractors.

2. Secondly, the transition between the strange attractors obtained in Theorem 3.1 for the map $T_{\alpha,\delta,a,\varepsilon}$ (3.4), and the attractors for maps which are perturbations of $T_{\alpha,\delta,a,\varepsilon}$ where the skew-product structure is slightly perturbed, *e.g.*, by adding terms depending on (x, y) to the angular dynamics.

3. Finally, the transition from attractors of $T_{\alpha,\delta,a,\varepsilon}$ (3.4), for which $\delta = 0$ and α irrational to attractors of maps which are perturbations of $T_{\alpha,\delta,a,\varepsilon}$ as in the previous item.

In all cases homoclinic bifurcations [95] are likely to play a fundamental role.

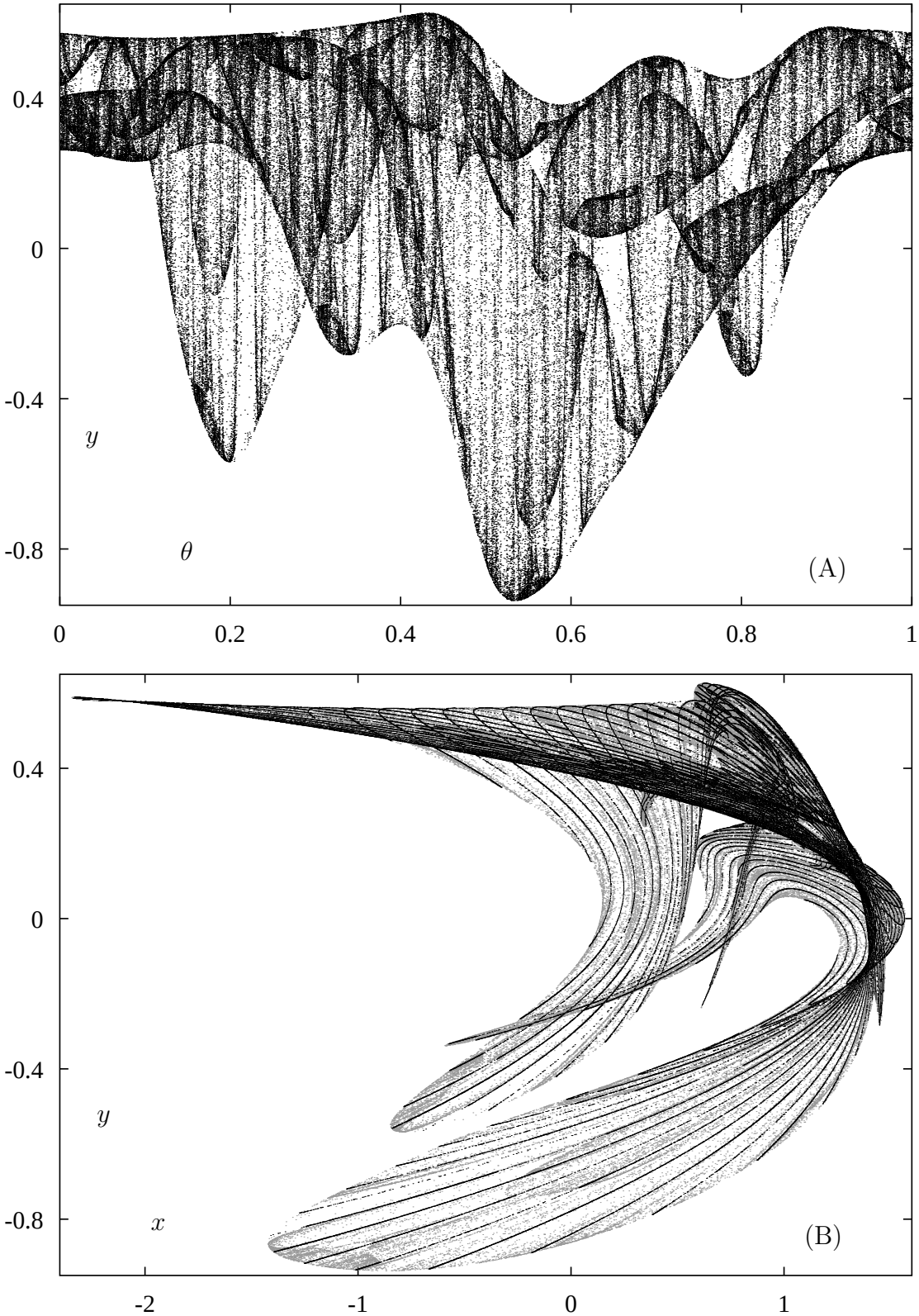

Figure 3.5: (A) Attractor of map (3.10) in the quasi-periodic case. Parameter values are fixed at $a = 0.8$, $b = 0.4$, $\delta = 0$, $\alpha = (\sqrt{5} - 1)/2$, $\varepsilon = 0.7$, initial conditions $x_0 = 1.5$, $y_0 = 0$, $\theta_0 = 0$. Projection on the (θ, y)-plane. (B) Same as (A), with projection on the (x, y)-plane in the background (in grey) with 'slices' of the attractor $2\pi\theta \in [0.1 \times j, 0.1 \times j + 0.001]$, for $j = 0, 1, \ldots, 62$ (in black).

Chapter 4

Hopf-saddle-node bifurcation for fixed points of diffeomorphisms

4.1 Introduction

In this Chapter we examine two model maps for the Hopf-saddle-node (HSN) bifurcation of fixed points of diffeomorphisms. The purpose is to understand the typical bifurcation patterns by means of a case study, where the two model maps are constructed 'as generic as possible'.

The HSN bifurcation for equilibria of vector fields has been investigated by several authors [16, 28, 31, 39, 48, 56, 69, 75, 78, 111]. We show that in the model maps phenomena occur which are qualitatively different from the previously considered vector field situations. The differences can be roughly divided into three groups:

1. Resonances along a curve of Hopf bifurcations of invariant circles [78, 112].
2. Resonant dynamics on a normally hyperbolic invariant 2-torus.
3. Breakdown of an invariant 2-torus and occurrence of strange attractors near heteroclinic intersections of the invariant manifolds of two fixed points of saddle-focus type with different stability indices.

The two models are introduced in the next section, and their construction is described in Sec. 4.1.2. The dynamics of the two model maps is briefly presented by means of numerical simulations in Sec. 4.1.3, where we also give an outline of the rest of this Chapter.

4.1.1 Setting of the problem

The purpose of this Chapter is to describe the dynamics of the local 3D model maps G and Q:

$$G : \begin{pmatrix} w \\ z \end{pmatrix} \mapsto \begin{pmatrix} e^{i\omega} w[1-\gamma(\gamma\mu + az + \gamma z^2)] \\ z + \gamma(1 - |w|^2 - z^2) \end{pmatrix} + \begin{pmatrix} \gamma^3(\varepsilon_1 \overline{w}^4 + \varepsilon_2 z^4) \\ 0 \end{pmatrix}, \tag{4.1}$$

$$Q : \begin{pmatrix} x \\ y \\ z \end{pmatrix} \mapsto \begin{pmatrix} \mathrm{Re}\,(e^{i\omega} w[1-\gamma(\gamma\mu + az + \gamma z^2)]) \\ \mathrm{Im}\,(e^{i\omega} w[1-\gamma(\gamma\mu + az + \gamma z^2)]) \\ z + \gamma(1 - |w|^2 - z^2) \end{pmatrix} + \begin{pmatrix} \gamma^3\varepsilon_1(y^4 + z^4) \\ \gamma^3\varepsilon_2(x^4 + z^4) \\ \gamma^3\varepsilon_3(x^4 + y^4) \end{pmatrix}. \tag{4.2}$$

Both families depend on the three real parameters (γ, μ, ω). The family G is given in the coordinates (w, z), where $w = x + iy \in \mathbb{C}$ and $z \in \mathbb{R}$, while Q is given in real coordinates (x, y, z). Moreover, $a = a_1 + ia_2$ is a complex constant while ε_j is real for $j = 1, 2, 3$.

Before explaining the construction and the purpose of the model maps G (4.1) and Q (4.2), we give two definitions. Let $\alpha \in \mathbb{R}^p$ be a multi-parameter, and denote by $\mathbb{S}^1 = \mathbb{R}/2\pi \subset \mathbb{C}$ the unit circle. Let $F_\alpha : \mathbb{R}^3 \to \mathbb{R}^3$ be a C^∞-family of diffeomorphisms. We say that F_α is an *HSN-family of diffeomorphisms* if

$$F_0(0) = 0, \quad \text{and} \quad \operatorname{spec} DF_0(0) = \{e^{i\omega_0}, e^{-i\omega_0}, 1\} \subset \mathbb{S}^1, \tag{4.3}$$

where the complex conjugate eigenvalues satisfy the non-resonance conditions

$$e^{in\omega_0} \neq 1 \qquad \text{for} \quad n = 1, 2, 3, 4. \tag{4.4}$$

Let X_α be a C^∞-family of vector fields on $\mathbb{R}^3$. We call X_α a *HSN-family of vector fields* if

$$X_0(0) = 0 \quad \text{and} \quad \operatorname{spec} DX_0(0) = \{\pm i\omega_0, 0\}, \quad \omega_0 \neq 0. \tag{4.5}$$

To have a generic HSN bifurcation of equilibria, the 3-jet of X_α at the origin has to satisfy appropriate open and dense conditions, for example those given in Lemma 4.3, Appendix 4.B, also see [56, 75, 78].

Remark 4.1. The values $n = 1, 2, 3, 4$ in (4.4) are the so-called strong resonances [112, 78, 71]. They are excluded since they correspond to HSN bifurcations of higher codimension.

A standard approach for the study of a bifurcation of fixed points for a family of diffeomorphisms F_α consists in the derivation of the Takens approximating vector field [112]. Let $DF_0(0) = S + N$ be the decomposition in semisimple and nilpotent part of $DF_0(0)$. By Takens's theorem there exists a change of coordinates, defined in a neighbourhood of the origin of $\mathbb{R}^3 \times \mathbb{R}^k$ and preserving the parameters, such that in the new coordinates the diffeomorphism F_α takes the form

$$F_\alpha = S \circ X_\alpha^1 + M.$$

Here the Taylor expansion of the remainder M near the origin is identically zero. Moreover, X_α^1 denotes the time-1 map of the flow of a family of vector fields X_α, defined on $\mathbb{R}^3$ and such that

$$X_0(0) = 0 \quad \text{and} \quad \operatorname{spec} DX_0(0) = \{0\}.$$

However, if F is an HSN-family of diffeomorphisms, one can apply a slightly different version of this theorem, given in Lemma 4.5, Appendix 4.D. Indeed, there exists a coordinate transformation such that in the new coordinates the diffeomorphism takes the form

$$F_\alpha = X_\alpha^1 + M, \tag{4.6}$$

where the 3-jet of the remainder M is zero. In this case X_α is an HSN-family of vector fields, *i.e.*, equation (4.5) holds. This approach has the advantage that a fair amount

of information is available on HSN-families of vector fields [56, 75, 78]. In particular, given a two-parameter HSN-family of vector fields X_α, satisfying the generic conditions given in Lemma 4.3 (Appendix 4.B), there exist a coordinate transformation and a reparametrisation $\beta = \beta(\alpha)$ which brings X_α to the form

$$Y_\beta(w, z) + \mathcal{O}(\|w, z\|^4),$$

where Y_β is the third degree polynomial family of vector fields on $\mathbb{R}^3$ given by

$$Y_\beta(w, z) = \begin{pmatrix} (-\beta_2 + i\omega)w - awz - wz^2 \\ -\beta_1 - s\,|w|^2 - z^2 \end{pmatrix}, \tag{4.7}$$

with $a = a(\beta) \in \mathbb{C}$ and $s = \pm 1$, see [78].

Our approach for the study of an HSN bifurcation of diffeomorphisms is the converse of the standard one. We start from the time-1 map Y_β^1 of the vector field in (4.7) and construct the two models G (4.1) and Q (4.2) by adding perturbative terms of order strictly higher than three (see the next section for details). By the combination of Lemma 4.5 and Lemma 4.3, this yields models which are representative for a large class of HSN-families of diffeomorphisms. However, the choice of the higher order perturbative terms depends on the value of ω, and this motivates the use of different models. Two situations are considered here.

1. For G (4.1), the parameter ω is confined to a neighbourhood of $\omega_0 = 2\pi/5$. In particular, G is constructed to study a 1:5 resonance along a curve of Hopf bifurcations. This is a special case of item 1 at the beginning of this introduction.

2. On the other hand, the investigation specified in item 2 at the beginning of this introduction is carried out by means of Q (4.2). Correspondingly, for Q the parameter ω is allowed to vary in the interval $[0, 2\pi]$.

The dynamics of the polynomial vector field Y_β (4.7) is the starting point for the construction of G and Q, which is described in the next section.

4.1.2 Preliminaries

This section is divided in three parts. First the dynamics of generic HSN-families of vector fields is discussed, then we present the construction of the model maps G (4.1) and Q (4.2). In the third subsection, we outline our theoretical expectations for the dynamics of G and Q, given our knowledge on the vector field case.

The Hopf-saddle-node bifurcation for vector fields

We start the discussion by analysing the third degree polynomial family of vector fields Y_β (4.7), closely following [78]. The two-parameter family Y_β is *axially symmetric*: for all $\theta \in \mathbb{R}$, Y_β commutes with the rotation R_θ of angle $\theta \in \mathbb{R}$ around the z-axis, given by

$$R_\theta : \mathbb{R}^3 \to \mathbb{R}^3, \quad R_\theta(w, z) = (e^{i\theta}w, z).$$

In cylindrical coordinates (r, φ, z), where $w = re^{i\varphi}$, the vector field Y_β takes the form

$$\begin{aligned} \dot{r} &= r(-\beta_2 - a_1 z - z^2), \\ \dot{\varphi} &= \omega - a_2 z, \\ \dot{z} &= -\beta_1 - z^2 - sr^2. \end{aligned} \tag{4.8}$$

The equations for $(\dot{r}, \dot{z})$ in (4.8) are independent on ϕ, and yield the planar reduction

$$\begin{aligned} \dot{r} &= r(-\beta_2 - a_1 z - z^2), \\ \dot{z} &= -\beta_1 - z^2 - sr^2. \end{aligned} \tag{4.9}$$

Notice that the planar reduction (4.9) is $\mathbb{Z}_2$-equivariant, namely, it is symmetric under the transformation $(r, z) \mapsto (-r, z)$.

According to the signs of s and a_1, the topological structure of the phase portrait of the reduced system (4.9) belongs to one of four classes (if a time-reversal is allowed [78]). We only describe the case $s = 1$, $a_1 < 0$, for which both Hopf and heteroclinic bifurcations occur. The bifurcation diagram of the planar system (4.9) consists of the curves $\mathcal{SN}$, $\mathcal{P}$, $\mathcal{H}$ and $\mathcal{HET}$:

$$\begin{aligned} \mathcal{S} &= \{(\beta_1, \beta_2) \ \mid \ \beta_1 = 0\} \\ \mathcal{P} &= \left\{(\beta_1, \beta_2) \ \mid \ \beta_1 = -\frac{\beta_2^2}{a_1^2} + o(\beta_2^2)\right\} \\ \mathcal{H} &= \{(\beta_1, \beta_2) \ \mid \ \beta_1 < 0, \beta_2 = 0\} \\ \mathcal{HET} &= \left\{(\beta_1, \beta_2) \ \mid \ \beta_1 < 0, \beta_2 = \frac{a_1}{3a_1 - 2}\beta_1 + o(\beta_1)\right\}. \end{aligned}$$

Compare Figure 4.1, where we also indicate the phase portraits of the planar system system (4.9). Saddle-node, pitchfork, and (Andronov-)Hopf bifurcations of equilibria take place for parameters on the curves $\mathcal{SN}$, $\mathcal{P}$, and $\mathcal{H}$ respectively, while $\mathcal{HET}$ is a curve of heteroclinic bifurcations of equilibria. Two equilibria $\mathscr{O}_\pm = (\pm\sqrt{-\beta_1}, 0)$ exist in regions 2 up to 6. In regions 3, 4, and 5 the equilibria $\mathscr{O}_\pm$ are of saddle type and have a one-dimensional heteroclinic connection along the z-axis. This connection is persistent in (4.9) due to the $\mathbb{Z}^2$-symmetry. Furthermore, a third equilibrium $\mathscr{C}$ coexist with $\mathscr{O}_\pm$ in regions 3, 4, 5. The equilibrium $\mathscr{C}$ is attracting in region 3 and repelling in regions 4 and 5. Entering region 4 from region 3 across curve $\mathcal{H}$, the equilibrium $\mathscr{C}$ loses stability through a Hopf bifurcation, whereby an attracting limit cycle $\mathscr{T}$ is created. As (β_1, β_2) approach the curve $\mathcal{HET}$, the limit cycle $\mathscr{T}$ grows in size and in period. For $(\beta_1, \beta_2) \in \mathcal{HET}$, the limit cycle $\mathscr{T}$ turns into a heteroclinic connection formed by the z-axis and by the unstable manifold of $\mathscr{O}_+$, which has merged with the stable manifold of $\mathscr{O}_-$.

The dynamics of the three-dimensional polynomial family Y_β (4.8) is easily reconstructed from the dynamics of (4.9). The equilibria $\mathscr{O}_\pm$ of (4.9) correspond to equilibria of Y_β belonging to the z-axis. For simplicity, we keep the same names for the bifurcations and the invariant manifolds of Y_β and of the planar reduction (4.9). On the curve $\mathcal{P}$ the equilibrium $\mathscr{O}_+$ loses stability through a Hopf bifurcation, and a limit cycle $\mathscr{C}$ is created. Across curve $\mathcal{H}$, the limit cycle $\mathscr{C}$ loses stability through a

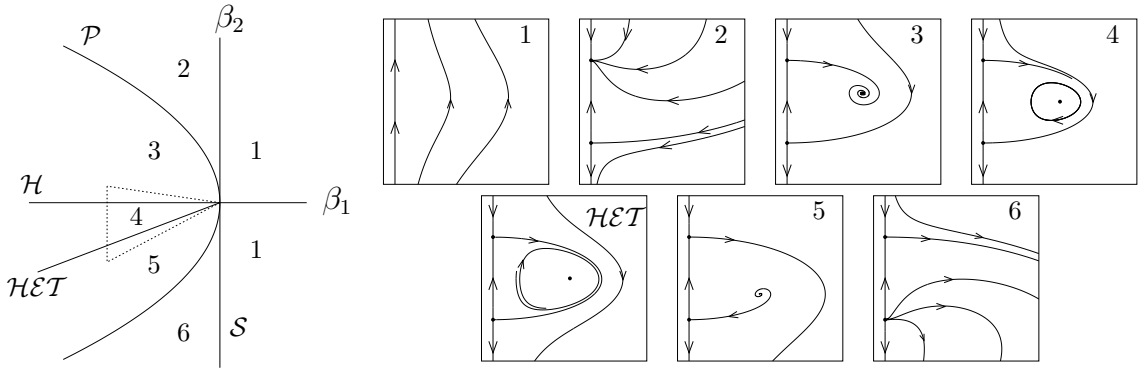

Figure 4.1: Left: bifurcation diagram of the polynomial reduced planar system (4.9) in the unfolding case determined by $s = 1$, $a_1 < 0$, from [78]. Phase portraits in the (r, z)-plane are given on the right.

Hopf (also called Neĭmark-Sacker, see footnote 6 in Sec. 2.1.3) bifurcation, where an attracting torus $\mathscr{T}$ is created. Then $\mathscr{T}$ merges into a heteroclinic sphere-like structure on the curve $\mathcal{HET}$.

We now discuss the dynamics of a generic HSN-family X_α of vector fields, *i.e.*, an HSN-family satisfying the hypotheses of Lemma 4.3. Denote by X_β the vector field X_α expressed in the coordinates and parameters provided by Lemma 4.3:

$$X_\beta(w, z) = Y_\beta(w, z) + \mathcal{O}(\|w, z\|^4), \tag{4.10}$$

where Y_β is the vector field in (4.7). Only the unfolding case determined by $\operatorname{Re} a = a_1 < 0$, $s = 1$ is considered here. A large part of the bifurcation diagram of Y_β (Figure 4.1) persists in the family X_β. In particular, X_β has the same *local* bifurcations as Y_β: there are curves $\mathcal{S}$, $\mathcal{P}$, and $\mathcal{H}$ of saddle-node, Hopf, and Neĭmark-Sacker bifurcations of X_β, near the corresponding curves of Y_β.

The main differences between the vector fields X_β and Y_β occur in the parameter region close to the curve $\mathcal{HET}$. The heteroclinic sphere of Y_β is destroyed by a generic ∞-flat perturbation [29]. For a generic vector field X_β, the two-dimensional manifolds of the saddle foci $\mathscr{O}_\pm$ intersect transversally along an even number of heteroclinic orbits [16, 31, 69]. In the parameter plane, the region of existence of such a heteroclinic structure is a narrow horn. The boundary of this horn is formed by two bifurcation curves, on which 'inner' and 'outer' tangencies of the manifolds occur, compare [20, 21]. Moreover, the heteroclinic connection along the z-axis does not take place in the generic case, and this allows the occurrence of Shil′nikov homoclinic bifurcations [16, 31, 48, 56, 78]. The possible occurrence of heteroclinic and Shil′nikov bifurcations implies that the germ of the vector field Y_β (4.7) is not topologically stable [28, 110]. The torus $\mathscr{T}$ of X_β breaks down when approaching the heteroclinic structure. This phenomenon is only partially understood from the theoretical viewpoint [1, 7, 8, 23, 42, 56, 78, 93]. For parameters inside a resonance tongue, homoclinic tangency bifurcations of periodic orbits lying inside $\mathscr{T}$ are often related to the breakdown of the torus and to the creation of strange attractors [2, 61, 69, 70, 76, 77, 117, 123].

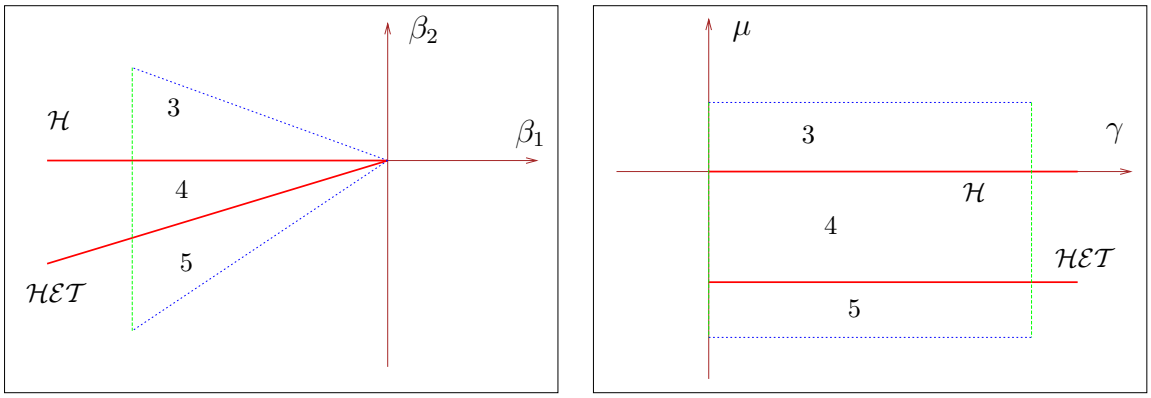

Figure 4.2: Left: magnification of Figure 4.1 near the sector of interest in the (β_1, β_2)-parameter plane. Right: in the (γ, μ)-parameter plane, where (γ, μ) are given by the scaling (4.11), the sector of interest (left picture) is blown up near the origin.

Construction of the model maps

The models G and Q are obtained by perturbing an approximate time-1 map of the flow of Y_β (4.7), in the case $a_1 < 0$, $s = 1$. We restrict to a subset of the (β_1, β_2)-parameter plane given by a sector containing region 4 and parts of regions 3 and 5. The relevant sector is bounded by dashed lines in Figure 4.1, whereby only negative values of β_1 are considered. New parameters (γ, μ) are introduced by

$$\beta_1 = -\gamma^2, \quad \beta_2 = \gamma^2 \mu, \tag{4.11}$$

where $\gamma > 0$ and $\mu \in \mathbb{R}$. The effect of this reparametrisation is sketched in Figure 4.2. The dashed sector in Figure 4.1 (magnified in Figure 4.2 left) is blown up near the origin and mapped onto a horizontal strip in the (γ, μ)-plane (Figure 4.2 right). Thereby, the bifurcation curves $\mathcal{H}$ and $\mathcal{HET}$ both turn into horizontal lines in the (γ, μ)-parameter plane.

Remark 4.2. Notice that, for the model maps, ω must be taken as parameter together with (γ, μ). Indeed, the HSN bifurcation has codimension at least three for a diffeomorphism, while it has codimension two in the generic vector field case. In particular, for a HSN-family of vector fields, ω can be set to one by a time-scaling.

Beyond the reparametrisation (4.11), the variables and the time of (4.7) are rescaled as follows:

$$w = \gamma \widehat{w}, \quad z = \gamma \widehat{z}, \quad t = \widehat{t}/\gamma. \tag{4.12}$$

In the rescaled variables $(\widehat{w}, \widehat{z})$, the sizes of the limit cycle $\mathscr{C}$ and of the torus $\mathscr{T}$ are $\mathcal{O}(1)$ as $\gamma \to 0$. Denote by $Y_{\gamma,\mu,\omega}$ the vector field Y_β (4.7) written in the new variables and parameters given by (4.12) and (4.11). By dropping all hats, $Y_{\gamma,\mu,\omega}$ reads

$$Y_{\gamma,\mu,\omega} = Y_1 + Y_2, \quad \text{with} \quad Y_1 = \begin{pmatrix} -\gamma\mu w - awz - \gamma w z^2 \\ 1 - z^2 - |w|^2 \end{pmatrix}, \quad Y_2 = \begin{pmatrix} i\omega w/\gamma \\ 0 \end{pmatrix}. \tag{4.13}$$

The vector field $Y_{\gamma,\mu,\omega}$ is integrated with a time step $\gamma > 0$. Since Y_1 commutes with Y_2, the time-γ map of $Y_{\gamma,\mu,\omega}$ is given by the composition of the time-γ maps Y_1^γ and

Y_2^γ (this is a corollary of the Baker-Campbell-Hausdorff formula [116]). So we first compute an *approximated* time-γ map of Y_1 by performing one step of length γ of the Euler integration formula:

$$\begin{pmatrix} w \\ z \end{pmatrix} \mapsto \begin{pmatrix} w \\ z \end{pmatrix} + \gamma \begin{pmatrix} -\gamma\mu w - awz - \gamma w z^2 \\ 1 - z^2 - |w|^2 \end{pmatrix}. \tag{4.14}$$

Then the map (4.14) is composed with the time-γ map Y_2^γ, yielding the axially symmetric map S:

$$S : \begin{pmatrix} w \\ z \end{pmatrix} \mapsto \begin{pmatrix} e^{i\omega} w[1 - \gamma(\gamma\mu + az + \gamma z^2)] \\ z - \gamma(-1 + |w|^2 + z^2) \end{pmatrix}. \tag{4.15}$$

To construct the model maps G (4.1) and Q (4.2), resonant terms of order strictly larger than three are added to S (4.2), compare Lemma 4.5. In particular, non-axisymmetric resonant terms of order four are added to S, in order to break the axial symmetry. The choice of these order four terms depends on the value of ω we wish to focus on.

Model G – 1:5 resonance To study the dynamics in the vicinity of a resonant frequency ω_0, with $\omega_0/(2\pi) = p/q \in \mathbb{Q}$, the model map G (4.1) is used. However, instead of using ω as control parameter, we introduce a scaled detuning parameter δ by $\omega = \omega_0 + \gamma\delta$. In this Chapter we only consider the resonant value $\omega_0/(2\pi) = 1/5$, which is the lowest-order resonance compatible with the assumptions in (4.4). For $\omega_0/(2\pi) = 1/5$ the lowest-order non-axisymmetric resonant terms in the $\partial/\partial w$ and in the $\partial/\partial z$-direction are $\overline{w}^4$ and $\operatorname{Re} w^5$, respectively. Since even by adding these terms to S (4.15) the z-axis remains invariant, a (non-resonant) term in z^4 is added to the w-component. This yields the map

$$\begin{pmatrix} w \\ z \end{pmatrix} \mapsto \begin{pmatrix} e^{i(\omega_0+\gamma\delta)} w[1 - \gamma(\gamma\mu + az + \gamma z^2)] \\ z - \gamma(-1 + |w|^2 + z^2) \end{pmatrix} + \begin{pmatrix} \gamma^3(\varepsilon_1 \overline{w}^4 + \varepsilon_2 z^4) \\ \gamma^4 \varepsilon_3 \operatorname{Re} w^5 \end{pmatrix}, \tag{4.16}$$

where ε_1 and ε_2 are complex while ε_3 is real. A few simplifications are applied to (4.16), in order to obtain the model G (4.1), see Appendix 4.E for details.

Model Q – all frequencies To study the dynamics in the frequency interval $\omega \in [0, 2\pi]$ we use the model map Q (4.2). This map is obtained by writing S (4.15) in Cartesian coordinates (x, y, z), where $w = x + iy$, and by adding to S the fourth order polynomial

$$\gamma^3\varepsilon_1(y^4 + z^4)\frac{\partial}{\partial x} + \gamma^3\varepsilon_2(x^4 + z^4)\frac{\partial}{\partial y} + \gamma^3\varepsilon_3(x^4 + y^4)\frac{\partial}{\partial z},$$

where ε_j is real for $j = 1, 2, 3$. The purpose of adding this perturbation term is to have 'generic' higher order terms in Q.

The coefficients ε_j, $j = 1, 2, 3$, and γ are perturbation parameters. However, in the sequel we treat ε_j as constants varying in a fixed compact set, while only γ is used as perturbation parameter, varying in a neighbourhood of 0. Moreover, the constant a is assumed to vary in a fixed compact set such that a_1 is negative and bounded away from zero.

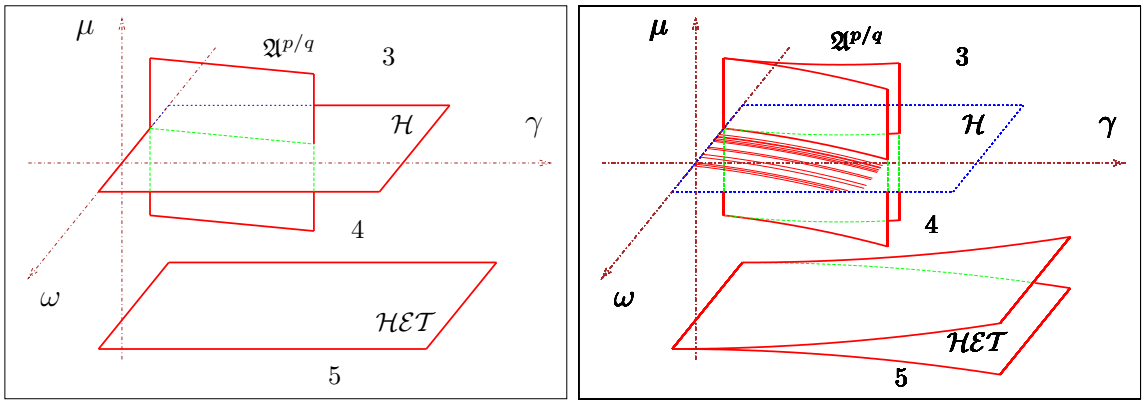

Figure 4.3: Left: bifurcation set of the time-γ map $Y^{\gamma}_{\gamma,\mu,\omega}$ of the vector field (4.13) in the parameter region of interest. $\mathfrak{A}^{p/q}$ is the set of all parameter values for which the rotation number on the invariant circle $\mathscr{C}$ is $p/q \in \mathbb{Q}$. See text for the meaning of $\mathcal{H}$ and $\mathcal{HET}$. Right: expected bifurcation set of the model maps G (4.1) and Q (4.2) in the generic case. $\mathfrak{A}^{p/q}$ is an Arnol'd tongue of rotation number p/q, $\mathcal{HET}$ is an exponentially narrow horn where transversal heteroclinic intersections occur. Of the surface $\mathcal{H}$, only a Cantor-like foliation by curves survives.

The expected dynamics of the model maps

To introduce the dynamical phenomena we are interested in, and the related (γ, μ, δ)-parameter regions, our expectations for the model maps G (4.1) and Q (4.1) are now discussed.

The models G and Q are perturbations of an approximate time-γ map of the axisymmetric vector field $Y_{\gamma,\mu,\omega}$ (4.13), where γ is the perturbation parameter. By general theory [5, 6, 17, 18, 35, 36, 38, 46, 56, 60, 78, 88, 94, 95, 99, 103], normally hyperbolic invariant manifolds and nondegenerate (quasi-periodic) bifurcations of the time-one map $Y^{\gamma}_{\gamma,\mu,\omega}$ persist in the model maps G and Q (assuming genericity of the model maps). Compare the discussion in Chapter two, on the relation between the periodically driven and the autonomous Lorenz-84 system. On the one hand, due to axisymmetry, the dynamics of the map $Y^{\gamma}_{\gamma,\mu,\omega}$ is highly degenerate (below we are more specific about this). However, the bifurcation set of $Y^{\gamma}_{\gamma,\mu,\omega}$ provides a 'geometrical skeleton' for the structure of the parameter space of G and Q, which we now sketch.

The dashed rectangle in Figure 4.2 right corresponds to a horizontal layer in the (γ, μ, ω)-parameter space for the diffeomorphism $Y^{\gamma}_{\gamma,\mu,\omega}$. See the sketch in Figure 4.3 left. Hopf bifurcations take place in the halfplane

$$\mathcal{H} = \{\gamma > 0,\ \mu = 0,\ \omega \in \mathbb{R}\},$$

while heteroclinic bifurcations on the half-surface

$$\{\gamma > 0,\ \mu = \frac{-a_1}{3a_1 - 2} + o(1) \text{ as } \gamma \to 0,\ \omega \in \mathbb{R}\}.$$

The parameter region of interest in is a horizontal layer containing the surfaces $\mathcal{H}$ and $\mathcal{HET}$ in its interior. For parameters in this layer (*i.e.*, for $|\mu|$ sufficiently small) the time-γ map $Y^{\gamma}_{\gamma,\mu,\omega}$ has an invariant circle $\mathscr{C}$. For μ negative, between the surfaces

$\mathcal{H}$ and $\mathcal{HET}$, the circle $\mathscr{C}$ is repelling and it coexists with an attracting invariant torus $\mathscr{T}$. For later reference, a set $\mathfrak{A}^\rho$ is sketched in Figure 4.3 left, given by all parameter values for which the rotation number on $\mathscr{C}$ is a fixed constant ρ. The set $\mathfrak{A}^\rho$ is a codimension one submanifold for all $\rho \in \mathbb{R}$. This is one of the two main degeneracies of the diffeomorphism $Y^\gamma_{\gamma,\mu,\omega}$. The other degeneracy, due to axisymmetry, is the occurrence of a sphere-like invariant set for parameters on $\mathcal{HET}$.

We now describe the implications for the model maps G (4.1) and Q (4.2), which are perturbations of the axially symmetric map S (4.15). Since S is an *approximate* time-γ map of the flow of $Y_{\gamma,\mu,\omega}$ (see the previous subsection), the parameter region of interest for S is shifted with respect to the sketch in Figure 4.3 left. The exact amount of this shift is computed later on (Sec. 4.2), for the moment we keep the discussion at a conceptual level. The hyperbolic invariant manifolds of the diffeomorphism $Y^\gamma_{\gamma,\mu,\omega}$ are expected to persist in the maps G and Q. Therefore, the equilibria $\mathscr{O}_\pm$ occurring in regions 3,4,5 (compare Figure 4.1) turn into fixed points of saddle-focus type for the models G and Q. As usual, we keep the same names for invariant manifolds and bifurcations of S, G, Q, and of $Y^\gamma_{\gamma,\mu,\omega}$. So the invariant circle $\mathscr{C}$ and the invariant torus $\mathscr{T}$ of $Y^\gamma_{\gamma,\mu,\omega}$ correspond to an invariant circle and an invariant torus for the model maps S, G, Q.

We first consider a parameter region lying above and sufficiently far from $\mathcal{H}$, labelled by 3 in Figure 4.3 left. In this region, for the maps G and Q the set $\mathfrak{A}^\rho$ persists as a surface only for those rotation numbers ρ satisfying a Diophantine condition, see [17, 18]. The set of all such surfaces forms a Cantor-like foliation in the parameter space. For rational $\rho = p/q$, the sets $\mathfrak{A}^{p/q}$ turn into tongue-shaped regions (Arnol′d tongues [6, 4]) in the parameter space of the maps G and Q, see the sketch in Figure 4.3 right. In the interior of a tongue $\mathfrak{A}^{p/q}$, the circle $\mathscr{C}$ is phase-locked to a periodic attractor with period q. Saddle-node bifurcations of periodic orbits take place at the boundaries of the tongues. Apart from this well-known alternation of periodicity and quasi-periodicity on $\mathscr{C}$, no complicated dynamics is expected to occur for G and Q, for parameter values sufficiently far from $\mathcal{H}$.

On the other hand, complicated dynamics is expected near $\mathcal{H}$. A theory of bifurcations of an invariant circle exists only for the case when the rotation number is Diophantine [17, 18, 35]. Much less is known in the resonant case, see [9, 36, 37]. According to [17, 18, 35], $\mathcal{H}$ is expected to turn into a frayed bifurcation boundary for G and Q, roughly given by the intersection of $\mathcal{H}$ with the Cantor foliation formed by the union of the surfaces $\mathfrak{A}^\rho$ for which the rotation number ρ on $\mathscr{C}$ is Diophantine (compare the sketch in Figure 4.3 right). Near $\mathcal{H}$ the complement of this frayed bifurcation boundary is the union of the so-called 'bubbles' [9, 35, 36, 37], where the theory does not prescribe what is happening to the bifurcating circle. Bubbles occur near parameter values for which:

1. The rotation number on the circle is rational. Generically this corresponds to a phase-locked circle, with periodic points of saddle and node type [5, 6].

2. The rotation number on the circle has a resonance with the normal frequency.

One of the main points of interest is the interplay between Hopf bifurcations and resonances, *i.e.*, the bifurcation structure in the bubbles of the first type. As mentioned in Sec. 4.1.2, the model G is used for this part of the investigation. Slightly abusing

notation, we again denote the frayed Hopf bifurcation boundary of G and Q by the symbol $\mathcal{H}$.

We now turn to a different part of the parameter space. The surface $\mathcal{HET}$ in Figure 4.3 left is expected to turn into a narrow horn for the models G and Q, compare Figure 4.3 right. This horn is denoted $\mathcal{HET}$ as well in the sequel. For parameters in the interior of the horn, the two-dimensional manifolds of the fixed points $\mathscr{O}_+$ and $\mathscr{O}_-$ intersect transversally or have tangencies. For parameters near the horn, the torus $\mathscr{T}$ is expected to break down, and occurrence of strange attractors is likely [1, 3, 9]. There are only partial theoretical explanations for this breakdown. One of these involves the occurrence of homoclinic tangencies inside some resonance tongues where the torus $\mathscr{T}$ is phase-locked to an invariant circle, see Chapter two for examples.

4.1.3 Sketch of the results

In this Chapter we investigate three groups of dynamical phenomena

1. The interaction between resonances on the circle $\mathscr{C}$ and Hopf bifurcations of $\mathscr{C}$, and the induced bifurcations of invariant circles and tori. The model used for this purpose is G. In particular, we analyse the bifurcation set of G near a 1:5 resonance bubble on the Hopf bifurcation boundary $\mathcal{H}$, compare Figure 4.3 right.

2. Resonant dynamics on the invariant torus $\mathscr{T}$. This study is performed by means of the model map Q. The relevant parameter region lies between the Hopf boundary $\mathcal{H}$ and the $\mathcal{HET}$-horn, see Figure 4.3 right. Here the global organisation of the tongues (the *Arnol'd web*) is quite complicated, due to the interaction between the two internal frequencies of the torus $\mathscr{T}$.

3. Phenomena occurring in the map G near the heteroclinic horn $\mathcal{HET}$: bifurcations of the torus $\mathscr{T}$, occurrence of strange attractors and of heteroclinic tangencies. The parameter region is a neighbourhood of the $\mathcal{HET}$-horn, which we call the *heteroclinic region*.

The rest of this Chapter is organised as follows. In the next three subsections we briefly illustrate the dynamics of the model maps in each of the three parameter regions outlined above. This part of the investigation is performed by means of numerical simulations. The study is presented in more detail in sections 4.3, 4.4, and 4.5. Results obtained by analytical means are reported in Sec. 4.2 and in the second part of Sec. 4.3. In Sec. 4.2 the axially symmetric model map S (4.15) is examined. Quantitative asymptotic information is obtained, about the location of the Hopf bifurcation boundary and of the heteroclinic region. In the second part of Sec. 4.3 we present analytical results concerning the bifurcation diagram of the map G (4.1) near the 1:5 bubble.

All proofs are contained in Appendix 4.A. A derivation of the normal form (4.10) is given in Appendix 4.B. A similar normal form lemma holds for HSN-families of diffeomorphisms, see Appendix 4.C. Two versions of Takens's theorem [112] are given in Appendix 4.D. The construction of the model maps is justified by the version given in Lemma 4.5, which establishes the connection between HSN-diffeomorphisms

and HSN-vector fields. On the other hand, in Secs. 4.2 and 4.3 the model maps are analysed by looking at approximating vector fields provided by the 'classical' version of Takens's theorem [112].

The Hopf bifurcation boundary

We here present a sketch of the bifurcation diagram of the model G (4.1), obtained by numerically computing the Lyapunov exponents of the attractors, see Figure 4.4. To produce Figure 4.4, the attractors of G are classified on the basis of the Lyapunov exponents (l_1, l_2, l_3), with $l_1 \geq l_2 \geq l_3$, according to the rules in Table 4.1. The coefficients of G are $\varepsilon_1 = \varepsilon_2 = 1$, $a_1 = -1$, $a_2 = 1/\sqrt{2}$. Only the 1:5 resonance $\omega_0/(2\pi) = 1/5$ is considered here. Moreover the parameter γ is fixed at 0.1. Therefore the results are presented in the parameter plane (μ, δ), where $\omega = \omega_0 + \gamma\delta$.

Remark 4.3. For clarity, when giving numerical values of the parameters δ and ω, we always use $\delta/(2\pi)$ and $\omega/(2\pi)$ in the sequel. This is also indicated in the labelling and the captions of all figures.

Figure 4.4 is produced by scanning the (μ, δ)-parameter plane on horizontal lines $\delta = const$, from right to left. First δ is fixed at, say, -0.1. Then μ is set to $\mu = 1.5$, and a fixed number of iterates of the map G is computed. If the orbit has converged to an attractor, *i.e.*, if it has not left a neighbourhood of the origin, the three Lyapunov exponents are computed. Then μ is decreased by a small step and the procedure is restarted, until μ reaches 0. The same is repeated for many values of δ.

Remark 4.4. Notice that by this method we cannot detect

1. The existence of saddle-type or repelling invariant manifolds;
2. Coexistence of several attractors.

On the one hand, several features of Figure 4.4 are in accordance with the expectations discussed in the previous section. An attracting invariant circle $\mathscr{C}$ occurs for large μ. The grey strip pointed by an arrow at the right of Figure 4.4 is a resonance gap where two period five points occur, an attractor and a saddle. This period five gap is a section of a three-dimensional Arnol′d tongue by means of a vertical plane $\gamma = const$, compare Figure 4.3 right. The boundaries $\mathcal{SN}^5_\pm$ of the period five gap are two curves of saddle-node bifurcations of a period five point, which take place on the circle $\mathscr{C}$. See the magnification in Figure 4.5 left and compare with the bifurcation diagram in Figure 4.5 right. Near $\mathcal{SN}^5_\pm$, the circle $\mathscr{C}$ still exists and it is phase-locked, but for parameters inside the gap, the circle $\mathscr{C}$ may lose its normal hyperbolicity. Apart from this kind of resonance phenomena, for sufficiently large μ no dramatic differences appear between the model G and the time-γ map of the vector field $Y_{\gamma,\mu,\omega}$ (4.7).

On the other hand, the situation is much more complicated near the intersection of the Hopf bifurcation boundary $\mathcal{H}$ with the period five gap. The curves $\mathcal{SN}^5_\pm$ intersect the Hopf boundary at two points $\mathcal{HSN}^5_\pm$ where the circle $\mathscr{C}$ is phase-locked to one period five orbit undergoing an HSN bifurcation. At the points $\mathcal{HSN}^5_\pm$, the curves $\mathcal{SN}^5_\pm$ are tangent to two curves $\mathcal{H}^5_\pm$ of Hopf bifurcations of a period five orbit. Two degenerate Hopf bifurcations $\mathcal{DH}^5_\pm$ take place along the curve $\mathcal{H}^5_+$. Moreover, several

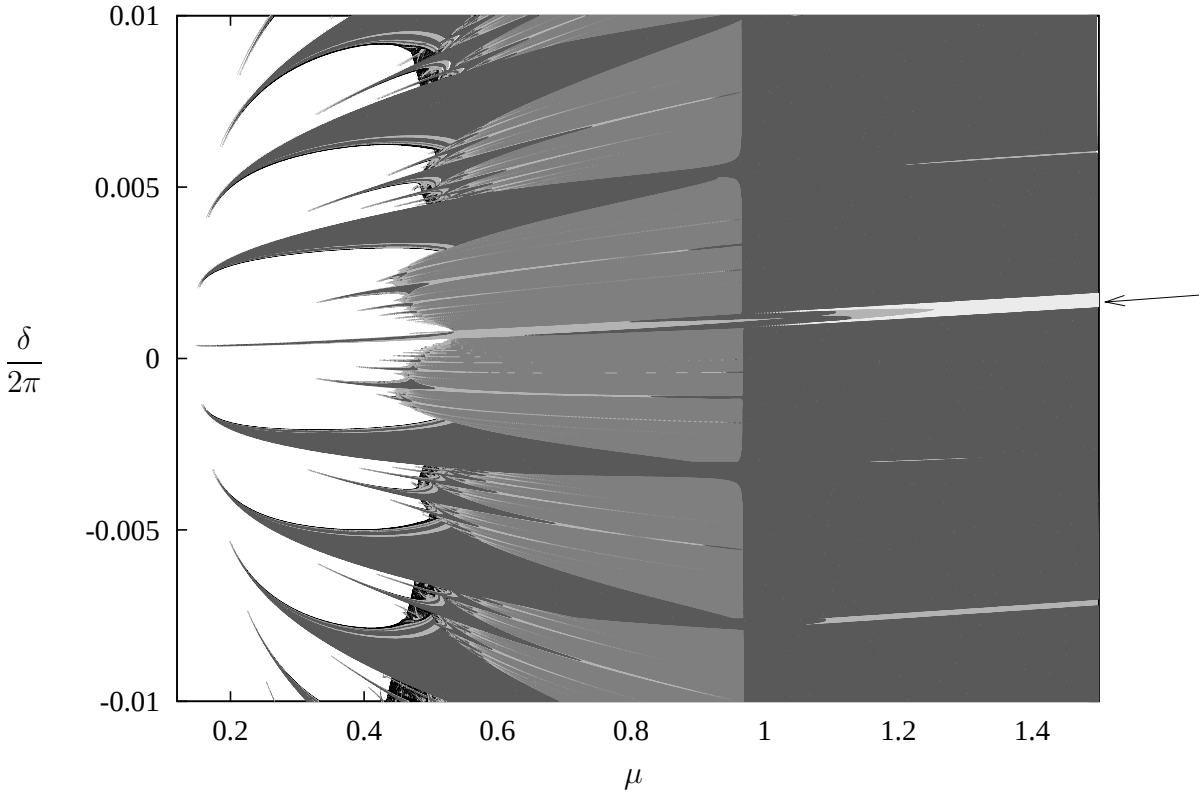

Figure 4.4: Numerical scan of the attractors of G in the $(\mu, \delta/(2\pi))$-parameter plane. The five tones of grey correspond to distinct classes of attractors of G. See Table 4.1 for the the greyscale coding.

colour	Lyapunov exponents	attractor type
black	$l_1 > 0 = l_2 > l_3$	strange attractor
black	$l_1 > 0 > l_2 > l_3$	strange attractor
grey 3	$l_1 = 0 > l_2 = l_3$	invariant circle of focus type
grey 2	$l_1 = l_2 = 0 > l_3$	invariant 2-torus
grey 1	$l_1 = 0 > l_2 > l_3$	invariant circle of node type
grey 0	$0 > l_1 > l_2 = l_3$	fixed point of focus type
grey 0	$0 > l_1 = l_2 >= l_3$	fixed point of focus type
grey 0	$0 > l_1 > l_2 > l_3$	fixed point of node type
white		no attractor is detected

Table 4.1: Legend of the grey scales for Figure 4.4, 4.5 left, 4.6, and 4.15. The attractors are classified by means of the Lyapunov exponents (l_1, l_2, l_3). Grey 0 indicates the palest tone, as in the strip pointed by an arrow in Figure 4.4 (a magnification is given in Figure 4.5 left). Grey 3 indicates the darkest tone, as in the tongues at the left of Figure 4.4. Grey 2 (darker) and 1 (paler) are intermediate tones.

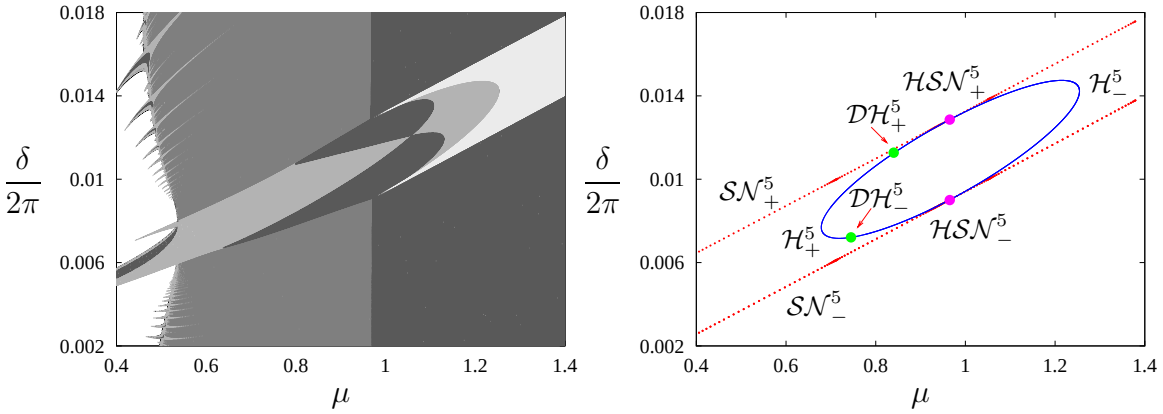

Figure 4.5: Left: magnification of Figure 4.4 around the period five tongue and the 1:5 bubble on the Hopf boundary. Right: numerically computed bifurcation diagram of period five points of the map G near the Hopf bifurcation boundary. The notation is explained in the text. Same $(\mu, \delta/(2\pi))$-window as the left picture.

additional bifurcation curves of invariant circles and invariant tori are detected near the 1:5 bubble. We refer to Sec. 4.3.1 for details.

In Sec. 4.3.2 we analytically prove the existence of all the bifurcations of period five points of G as mentioned above. This is achieved by studying a vector field approximation for the map G, obtained by the Takens theorem [112].

Torus dynamics and the Arnol′d resonance web

In this subsection we present the resonance phenomena which characterise the dynamics on the invariant torus $\mathscr{T}$. The results are obtained by numerical simulations with the model map Q (4.2), and the relevant region in the parameter space is labelled by 4 in Figure 4.3 right. Since γ is kept fixed, the results are illustrated in the (μ, ω)-parameter plane. A numerical overview of the (μ, ω)-plane is given in Figure 4.6 top, obtained by interpreting the Lyapunov exponents of the attractors of Q in the same way as for Figure 4.4. Notice that the positions of the Hopf boundary $\mathcal{H}$ ($\mu \approx 0.97$) and of the heteroclinic region ($0.3 \lesssim \mu \lesssim 0.5$) are approximately the same for G and Q, compare with Figure 4.4.

Two types of resonances may occur on the torus $\mathscr{T}$: one related to the fast 'longitudinal' rotation, and the other one related to the relatively slow 'latitudinal' rotation. Either type occurs in tongue-shaped regions in the (γ, μ, ω) space, but unlike the tongues of the circle $\mathscr{C}$, those of $\mathscr{T}$ have all possible orientations. The intersection of these tongues with a plane $\gamma = const$ yields a pattern of resonance gaps and gap intersections in the (μ, ω)-parameter plane, called the Arnol′d web. An illustration of this web is given in Figure 4.6 bottom, which is a magnification of Figure 4.6 top.

Remark 4.5. The visualisation of the Arnol′d web as in Figure 4.6 bottom is the main reason for the use of the model Q besides the model G (4.1).

Quasi-periodic saddle-node bifurcations of an invariant circle [17, 18], taking place inside the torus $\mathscr{T}$, bound each resonance gap. Again, near such bifurcations we expect the whole range of phenomena described by Chenciner [35, 36, 37]. Moreover, since the

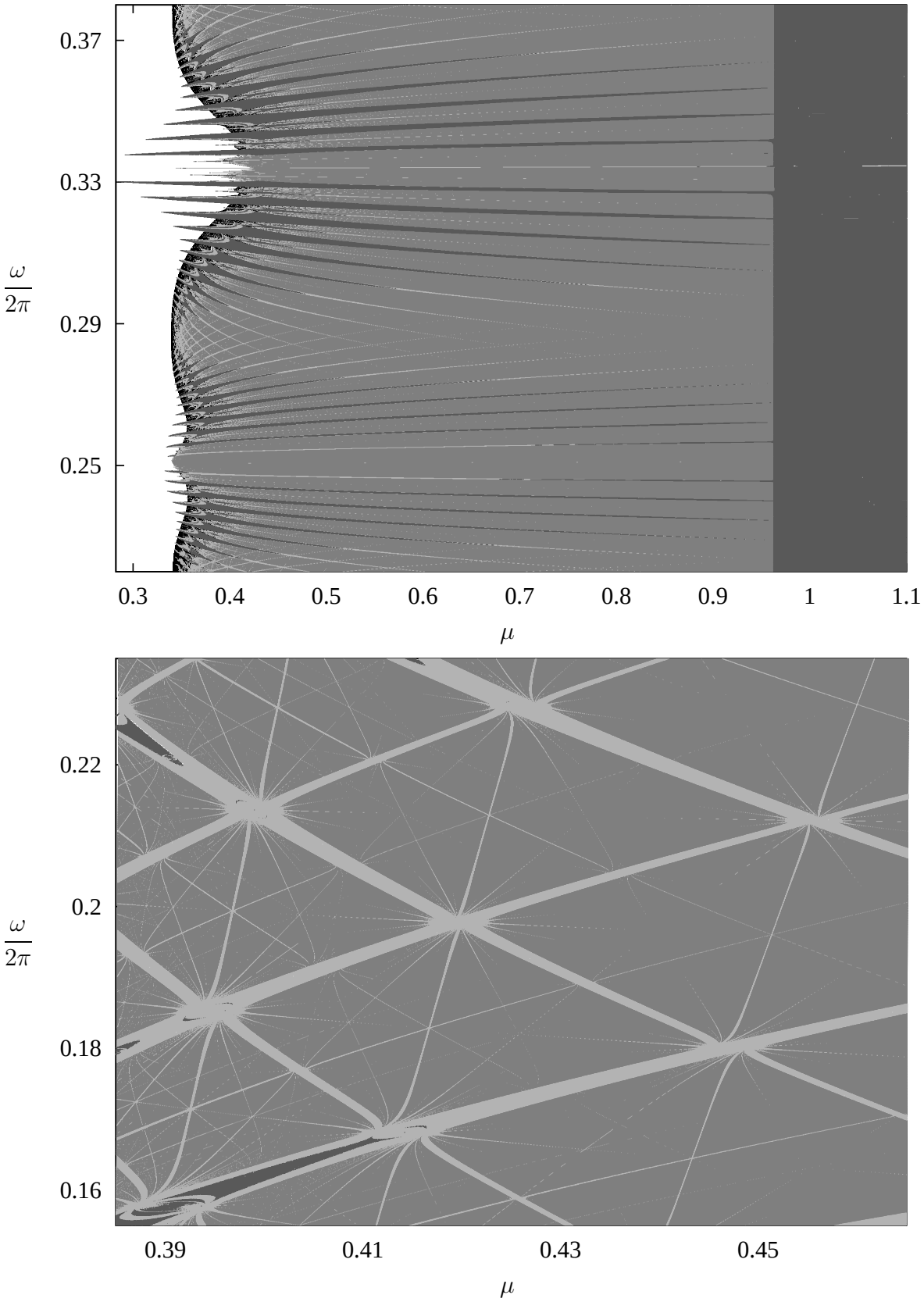

Figure 4.6: Top: numerical scan of the attractors of the map Q in the $(\mu, \omega/(2\pi))$-parameter plane. The greyscale code is given in Table 4.1. Bottom: magnification of top picture near a region characterised by several resonance gap crossings.

invariant circle undergo other bifurcations inside the gaps (*e.g.*, quasi-periodic Hopf bifurcations) phenomena like in [9] are also expected to occur. Finally, a a concrete route for the Newhouse-Ruelle-Takens scenario [89, 100] is possible near the crossings (intersections) of several resonance gaps. Indeed, for parameters inside a gap crossing, the two internal frequencies of the torus $\mathscr{T}$ satisfy two rational relations. This means that a lattice of attracting periodic points occurs inside $\mathscr{T}$. If these points become of saddle type, this situation preludes to the creation of a two-dimensional strange attractor contained in $\mathscr{T}$. We refer to Sec. 4.4 for numerical examples of the dynamics near such gap crossings.

Quasi-periodic strange attractors near the heteroclinic region

Numerical evidence like in Figures 4.4 and 4.6 top suggests that strange attractors of G and Q occur more often (in the sense of relative measure in parameter space) near the heteroclinic region $\mathcal{HET}$ than in the other regions. Two types of strange attractors may be distinguished on the basis of the Lyapunov exponents (l_1, l_2, l_3): those for which the $l_1 > 0$ and $l_2 < 0$, and those with $l_1 > 0$ and $l_2 \approx 0$. We conjecture that the former attractors are of *Hénon-like* type [11, 86, 95, 113, 120], *i.e.*, that these coincide with the closure of the unstable manifold of a periodic orbit of saddle type. On the other hand, strange attractors for which $l_1 > 0$ and $l_2 \approx 0$ are conjectured to be *quasi-periodic Hénon-like* strange attractors [24, 25, 27], meaning that these coincide with the unstable manifold of a quasi-periodic invariant circle of saddle type. Compare Remark 1.1 and see the discussion in Chapters two and three. Numerical evidence suggests that the large majority of the strange attractors of the maps G and Q is of quasi-periodic Hénon-like type. Hénon-like attractors of G and Q occur with much less frequency in the parameters.

We now sketch one of the typical scenarios for the creation of strange attractors in the heteroclinic region. A sequence of quasi-periodic period doublings [17, 18] is involved in this route. At first an attracting invariant circle $\mathscr{L}$ occurs (Figure 4.7 A). When decreasing μ, three consecutive quasi-periodic period doublings take place, and an attracting circle $\mathscr{L}_8$ is created (Figure 4.7 B). These three quasi-periodic bifurcations are of 'length doubling' type, in the sense that the attractor created at the bifurcation point is one connected closed curve such that its length is roughly twice the length of the circle which is losing stability [31]. A slight variation in μ yields loss of normal hyperbolicity of $\mathscr{L}_8$, and a strange attractor appears (Figure 4.7 C). This strange attractor is formed by one narrow 'belt', closely winding around the region where $\mathscr{L}_8$ formerly occurred. By further decreasing μ, various parts of the 'belt' melt with each other (Figure 4.7 D). Notice that the second Lyapunov exponent of the strange attractors in Figure 4.7 (C) and (D) is zero (within the numerical precision). Therefore these strange attractors appear to be of quasi-periodic Hénon-like type.

In the above route, the strange attractor is formed by a gradual process, involving several period doublings of an attracting invariant circle. We refer to Sec. 4.5 for other routes. Similar scenarios have been described for the Poincaré map P analysed in Chapter two of this thesis. One of the organising centres of the bifurcation diagram of P is an HSN bifurcation of fixed points of diffeomorphisms.

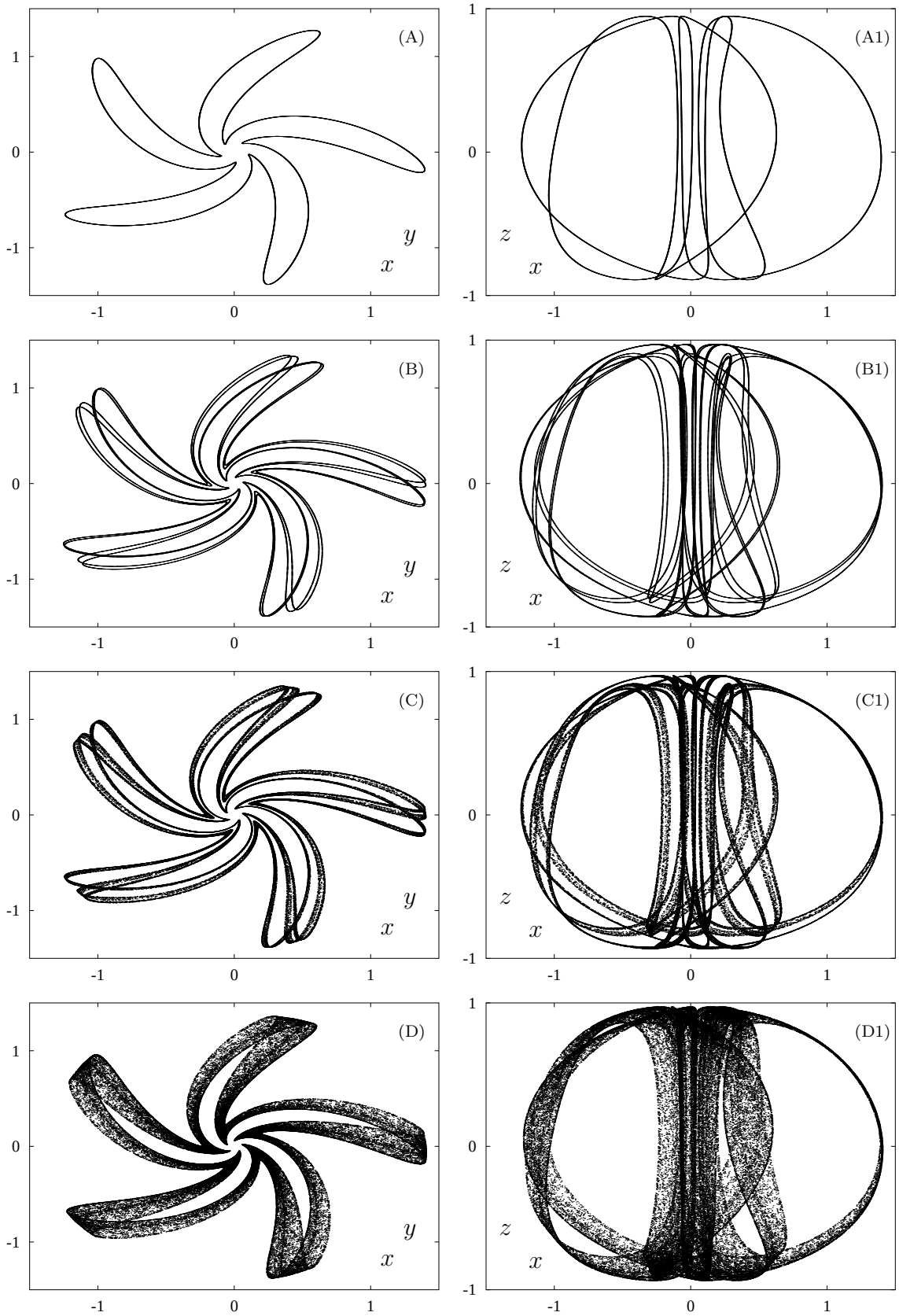

Figure 4.7: Attractors of the model map G (4.1) for $\delta/(2\pi) = 0.0247$ fixed, and at four values of μ. Left column: projections on (x, y), where $w = x + iy$. Right column: projections on (x, z). (A) $\mu = 0.53$, (B) 0.49, (C) 0.48, (D) 0.46.

4.2 The axially symmetric model map

Both models G (4.1) and Q (4.2) are perturbations of the axially symmetric family S (4.15). In cylindrical coordinates (r, ϕ, z), where $w = r\exp(i\phi)$, S reads

$$S : \begin{pmatrix} r \\ \phi \\ z \end{pmatrix} \mapsto \begin{pmatrix} r\,|1-\gamma(\gamma\mu + az + \gamma z^2)| \\ \phi + \omega + \arg(1-\gamma(\gamma\mu + az + \gamma z^2)) \\ z - \gamma(-1 + r^2 + z^2) \end{pmatrix}. \tag{4.17}$$

Since the dynamics in the (r, z)-components is independent on ϕ, we consider the reduced planar map $\widetilde{S}$

$$\widetilde{S} : \begin{pmatrix} r \\ z \end{pmatrix} \mapsto \begin{pmatrix} r\,|1-\gamma(\gamma\mu + az + \gamma z^2)| \\ z - \gamma(-1 + r^2 + z^2) \end{pmatrix}, \tag{4.18}$$

which is tangent to the identity at the origin and only depends on the parameters (γ, μ). Since S is an approximate time-γ map of the vector field $Y_{\gamma,\mu,\omega}$ (4.13), the locations of the Hopf and heteroclinic bifurcations of S are shifted with respect to the locations of the corresponding bifurcations of $Y_{\gamma,\mu,\omega}$. These shifts are computed in the next proposition up to order $\mathcal{O}(\gamma)$. We recall that γ is a perturbation parameter, varying in a neighbourhood of 0, while a is a constant belonging to a fixed compact set, see Sec. 4.1.2. A fundamental tool for the proof (see Appendix 4.A) is the Takens approximating vector field of the planar map $\widetilde{S}$ (4.18).

Lemma 4.1. *1. For all values of μ and of the constant $a \in \mathbb{C}$, and for γ sufficiently small, the map $\widetilde{S}$ (4.18) has a unique fixed point $(r_0, z_0)(\gamma, \mu)$, of the form*

$$z_0 = -\frac{\mu}{a_1}\gamma + \mathcal{O}(\gamma^2), \quad r_0 = 1 + \mathcal{O}(\gamma^2). \tag{4.19}$$

This fixed point undergoes a Hopf bifurcation at $\mu^{\mathcal{H}}(\gamma) = a_1^2 + \mathcal{O}(\gamma)$, is attracting for $\mu > \mu^{\mathcal{H}}(\gamma)$, and repelling for $\mu < \mu^{\mathcal{H}}(\gamma)$. The estimates in (4.19) on the order of γ are uniform on compact sets in the constant a and in the parameters (μ, ω).

2. In a neighbourhood of the origin $(r, z, \gamma) = (0, 0, 0)$, we have

$$\widetilde{S} = T^{\gamma}_{\widetilde{S}} + \mathcal{O}(\gamma^3) \tag{4.20}$$

where $T^{\gamma}_{\widetilde{S}}$ is the time-γ map of the planar vector field $T_{\widetilde{S}}$

$$T_{\widetilde{S}} \begin{pmatrix} r \\ z \end{pmatrix} = \begin{pmatrix} -a_1 rz \\ 1 - r^2 - z^2 \end{pmatrix} + \gamma \begin{pmatrix} r\left(-\mu + \frac{a_1}{2} - \frac{a_1}{2}r^2 - (1 + \frac{\mathrm{Re}(a^2+a)}{2})z^2\right) \\ z - (1+a_1)r^2 z - z^3 \end{pmatrix}. \tag{4.21}$$

3. The vector field (4.21) has a Hopf bifurcation of equilibria for parameters on the curve $\mu^{\mathcal{H}}(\gamma) = a_1^2 + \mathcal{O}(\gamma)$, and it has a heteroclinic connection for

$$\mu^{\mathcal{HET}} = \frac{a_1}{2} - \frac{b}{3} - \frac{2a_1(1-a_1) - \frac{bc}{3} - 1}{c+3} + \mathcal{O}(\gamma), \tag{4.22}$$

where $b = 1 + \mathrm{Re}(a^2 + a)/2$ and $c = -2/a_1$.

4. *The fixed point* $(r_0, z_0)(\gamma, \mu)$ *of* $\widetilde{S}$ *in* (4.19) *corresponds to an invariant circle*

$$\mathscr{C} = \left\{(r_0, z_0, \phi) \;\mid\; \phi \in \mathbb{S}^1\right\}$$

of the map S (4.17)*, having radius* r_0 *and contained in a horizontal plane* $\{z = z_0\}$*, where* (r_0, z_0) *do not depend on* ω*. The circle* $\mathscr{C}$ *has the same stability properties as the fixed point* (r_0, z_0) *of* $\widetilde{S}$*. The rotation number on* $\mathscr{C}$ *also depends on* ω *but the dynamics on* $\mathscr{C}$ *is always a rigid rotation. Denote* $\omega = \omega_0 + \gamma\delta$*, where* $\omega_0/(2\pi) = 1/5$*. For parameter values* $(\gamma, \mu, \delta_5(\gamma, \mu))$*, where*

$$\delta_5(\gamma, \mu) = -\frac{a_2\mu}{a_1}\gamma + \mathcal{O}(\gamma^2), \tag{4.23}$$

all points on $\mathscr{C}$ *have period five for the map* S*.*

5. *For* μ *bounded away from* $\mu^{\mathcal{H}}(\gamma)$*, and for* γ *sufficiently small, the circle* $\mathscr{C}$ *persists as a normally hyperbolic invariant manifold for the maps* G (4.1) *and* Q (4.2)*. The bounds on* μ *and* γ *are uniform on compact sets in all other parameters and coefficients of* G *and* Q*.*

Remark 4.6.

1. As mentioned in item 1 of Lemma 4.1, all estimates on the order of γ are uniform on compact sets in the constant a and in the parameters (μ, ω). Moreover, in the case of (4.20) the estimates hold in a sufficiently small neighbourhood of the origin in the variables (w, z).

2. The map S is degenerate, due to the fact that the dynamics on $\mathscr{C}$ is a rigid rotation also for rational rotation numbers. However, description of S provides the 'skeleton' dynamics of the models G and Q. Indeed, the position of the Hopf boundary and of the heteroclinic strip in the two models agrees up to order $\mathcal{O}(\gamma)$ with the values $\mu^{\mathcal{H}}$ and $\mu^{\mathcal{HET}}$given in Lemma 4.1. In particular, for $a_1 = -1$ and $\gamma = 0.01$ we have $\mu^{\mathcal{H}} = 1$ and $\mu^{\mathcal{HET}} = 0.35$. Comparison with Figures 4.4 and 4.6 top suggests that these approximate values are accurate within the error bound, which is of order $\mathcal{O}(\gamma)$.

3. We will show later that the period five tongue of G splits linearly in the parameter ε_1 and quadratically in γ around the 1:5 resonant surface $(\gamma, \mu, \delta_5(\gamma, \mu))$, where $\delta_5(\gamma, \mu)$ is given in (4.23). Moreover, the 1:5 bubble splits linearly in ε_1 and quadratically in γ around the curve

$$(\mu^{\mathcal{H}}(\gamma), \delta_5(\gamma, \mu^{\mathcal{H}}(\gamma))) = \left(a_1^2 + \mathcal{O}(\gamma), -a_1a_2\gamma + \mathcal{O}(\gamma^2)\right)$$

in the parameter space (γ, μ, δ). For these parameter values, the circle $\mathscr{C}$ of S consists of period five points and undergoes a Hopf bifurcation.

4.3 Hopf bifurcation boundary near the 1:5 resonance bubble

This section is divided in two parts. We first present in more detail the numerical bifurcation diagram of the map G (4.1) near the 1:5 bubble, introduced in Sec. 4.1.3. The analysis of the bifurcations of period five points is carried out in Sec. 4.3.2, by means of a Takens approximating vector field for the map G.

4.3.1 Dynamics near the 1:5 bubble

In this section we describe the dynamics of the model G (4.1) near the 1:5 bubble, by means of numerical simulations. The coefficients of G are set to the values: $\varepsilon_1 = \varepsilon_2 = 1$, $a_1 = -1$, $a_2 = 1/\sqrt{2}$, as in Sec. 4.1.3. In particular, since γ is fixed at 0.01, the results are presented in the (μ, δ)-parameter plane.

The bifurcation diagram of period five points of G near the 1:5 bubble is given in Figure 4.5 right (Sec. 4.1.3). Several bifurcations of invariant circles and invariant tori, not displayed in Figure 4.5 right, occur at the left of the Hopf boundary near the $\mathcal{HSN}^5_-$ point. A partial bifurcation diagram of invariant curves and invariant tori is given Figure 4.8. The curve $\mathcal{H}^5_+$ is the same as in Figure 4.5 right. On the other curves we have

$\mathcal{SNC}^5_-$**:** quasi-periodic saddle-node bifurcations of a period five invariant circle.

$\mathcal{HC}^5_-$**:** quasi-periodic Hopf bifurcations of a period five invariant circle.

$\mathcal{SNT}_-$**:** quasi-periodic saddle-node bifurcations of an invariant torus.

In fact, these are frayed bifurcation boundaries and not continuous curves, compare the discussion in Sec. 4.1.3. The curve $\mathcal{SNC}^5_-$ is tangent to $\mathcal{H}^5_+$ at a degenerate Hopf bifurcation $\mathcal{DH}^5_-$ of period five points. Furthermore, there exists a narrow parameter region $\mathcal{HET}^5_-$, lying very close to $\mathcal{SNT}_-$, where both transversal heteroclinic intersections and heteroclinic tangencies of two period five orbits of saddle-focus type occur.

To further clarify Figure 4.8 we describe a small 'movie' of the attractors and repellors of G. Four parameter values, labelled 1 to 4, are selected on the vertical line $\mu = 0.72$ in Figure 4.8, where δ is decreased each time. At point 1, the period five attracting circle $\mathscr{C}^5_-$ coexists with two period five orbits $\mathscr{P}^5_\pm$, which are of saddle-focus type and have different stability indices (see Figure 4.9 (A)). When crossing the line $\mathcal{SNT}_-$, an attracting torus $\mathscr{T}$ and a repelling torus $\mathscr{T}_r$ are born, and the period five circle $\mathscr{C}^5_-$ coexists with both $\mathscr{T}$ and $\mathscr{T}_r$. See Figure 4.9 (B), computed for parameters on the point 2 in the box of Figure 4.8. The period five circle $\mathscr{C}^5_-$ is contained in the solid torus bounded by $\mathscr{T}_r$, and the latter is contained in the solid torus bounded by $\mathscr{T}$. Therefore the repellor $\mathscr{T}_r$ forms the basin boundary between the attractors $\mathscr{T}$ and $\mathscr{C}^5_-$.

Near the region $\mathcal{HET}^5_-$, the torus $\mathscr{T}_r$ approaches a heteroclinic structure formed by the intersection of the two-dimensional manifolds of the period five orbits $\mathscr{P}^5_\pm$. Eventually it is destroyed and replaced by strange repellor (Figure 4.9 (C), parameters lie on point 3 in the box of Figure 4.8). By decreasing δ past region $\mathcal{HET}^5_-$, a period five torus repellor $\mathscr{T}^5$ appears, which surrounds the circle $\mathscr{C}^5_-$. See Figure 4.9 (D), computed for parameters on point 4 in the box of Figure 4.8. The period five torus $\mathscr{T}^5$ collapses with the circle attractor $\mathscr{C}^5_-$ at the bifurcation curve $\mathcal{H}$, whereby $\mathscr{C}^5_-$ turns into a repellor. By further decreasing δ through the curve $\mathcal{H}^5_+$, one of the two period five orbits in Figure 4.9 (A) undergoes a Hopf bifurcation and turns into a repellor. At that moment, a period five invariant circle $\mathscr{C}^5_+$ of saddle type is created. Across the curve $\mathcal{SNC}^5_-$, the two period five circles $\mathscr{C}^5_\pm$ melt with each other and disappear through a quasi-periodic saddle-node bifurcation.

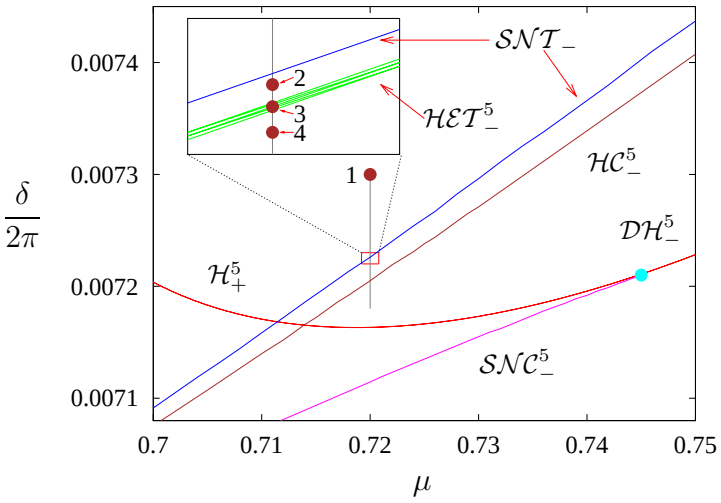

Figure 4.8: Numerically computed bifurcation diagram of the map G (4.1) near the point $H\mathcal{SN}^5_-$, in the $(\mu, \delta/(2\pi))$-plane. The curve $\mathcal{H}^5_+$ and the point $\mathcal{DH}^5_-$ are also plotted in Figure 4.5 right, the remaining curves are not. Invariant manifolds occurring at the parameter values labelled by 1 to 4 are plotted in Figure 4.9 (A) to (D), respectively.

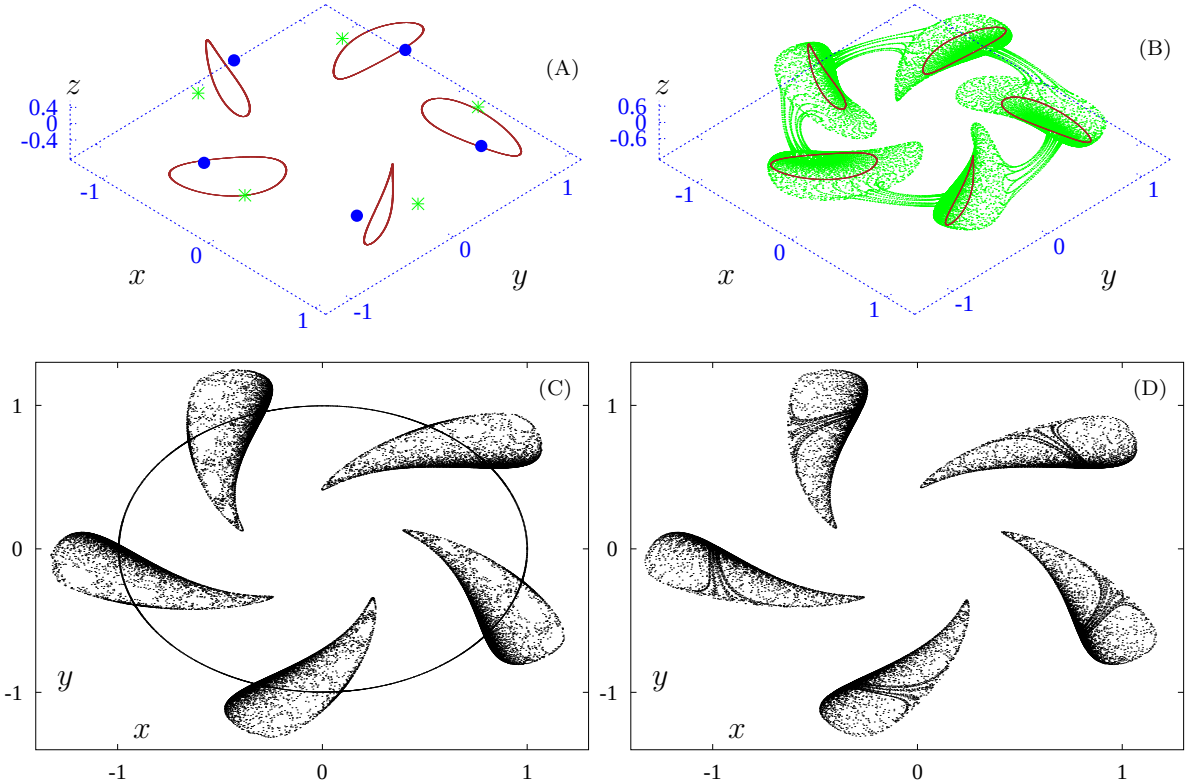

Figure 4.9: Invariant manifolds of G (4.1), for $\mu = 0.72$ and δ fixed in each picture. (A) Attracting period five invariant circle $\mathscr{C}^5_-$, coexisting with two period five orbits of saddle-focus type, $\delta/(2\pi) = 0.0073$. (B) Repelling torus $\mathscr{T}_r$, coexisting with the circle $\mathscr{C}^5_-$ at $\delta/(2\pi) = 0.00722673$. (C) Strange repellor at $\delta/(2\pi) = 0.0072266005$. (D) Period five torus repellor $\mathscr{T}^5$ at $\delta/(2\pi) = 0.0072265$.

The bifurcation diagram in Figure 4.8, obtained by looking at the attractors and repellors of G, is incomplete. Finer methods (based on Fourier analysis [34, 50, 63, 85]) could be used to pursue the study of the quasi-periodic bifurcations near the 1:5 bubble. In particular, more codimension two bifurcations seem to occur in the neighbourhood.

4.3.2 Mathematical analysis of a vector field approximation

In this section we perform a bifurcation analysis for a vector field approximation of the model G (4.1). For ease of reading, the equation of G (4.1) is given here again:

$$G : \begin{pmatrix} w \\ z \end{pmatrix} \mapsto \begin{pmatrix} e^{i(\omega_0+\gamma\delta)}w[1-\gamma(\gamma\mu + az + \gamma z^2)] \\ z + \gamma(1 - |w|^2 - z^2) \end{pmatrix} + \begin{pmatrix} \gamma^3(\varepsilon_1\overline{w}^4 + \varepsilon_2 z^4) \\ 0 \end{pmatrix}.$$

Throughout the section we assume that ω_0 is fixed at $2\pi/5$. The role of perturbation parameter is played by γ. The parameters (μ, δ) and the remaining coefficients of G are assumed to vary in a fixed compact set. For $\gamma = 0$, the linear part DG at the origin of $\mathbb{R}^3 = \{w, z\}$ is the axial rotation $R_{\omega_0}(w, z) = (e^{i\omega_0}w, z)$. Notice that G is not in Poincaré normal form, due to the presence of the non-resonant term $\varepsilon_2 z^4$. By normal form theory [39, 112], there is a transformation such that this term is removed in the new coordinates. We write G in the new coordinates, and restrict to terms of order four in (w, z). This amounts to setting $\varepsilon_2 = 0$ in G, which will be assumed throughout the rest of the section.

Notice that the fifth iterate G^5 is tangent to the identity map at the origin of $\mathbb{R}^3 \times \mathbb{R} = \{w, z, \gamma\}$, while G self is not. This makes G^5 suitable for application of Takens's theorem [112], also see Appendix 4.D. In fact we apply Takens's theorem to a sort of 'fifth root' H of G^5, where H is defined by

$$H(w, z) = \begin{pmatrix} e^{i\gamma\delta}w[1-\gamma(\gamma\mu + az + \gamma z^2)] + \gamma^3 e^{-i\omega_0}\varepsilon_1\overline{w}^4, \\ z + \gamma(1 - |w|^2 - z^2). \end{pmatrix} \tag{4.24}$$

The relation between G and H is made precise in the next lemma.

Lemma 4.2. *For the maps G (4.1) and H (4.24) we have*

$$G^5 = H^5 + \mathcal{O}(\gamma^4), \tag{4.25}$$

where the estimate on the order of γ is uniform on compact sets in the other coefficients and parameters of G and H, and hold in a sufficiently small neighbourhood of the origin in the variables (w, z).

For the map H (4.24) we compute a vector field approximation T_H such that the time-γ map T_H^γ approximates H up to order four in γ. As in Lemma 4.2, the estimates on the order of γ given in the next theorem are uniform on compact sets in the remaining coefficients and parameters of the map G and hold in a sufficiently small neighbourhood of the origin in the variables (w, z). Also see Sec. 4.2.

Theorem 4.1 (Takens approximation). *Consider the vector field T_H given by*

$$T_H = T_{H,0} + \gamma T_{H,1} + \gamma^2 T_{H,2}, \tag{4.26}$$

where

$$T_{H,0} = \begin{pmatrix} w(i\delta - az) \\ 1 - |w|^2 - z^2 \end{pmatrix}, \tag{4.27}$$

$$T_{H,1} = \begin{pmatrix} w\left(-\mu + \frac{a}{2} - \frac{a}{2}|w|^2 - z^2\left(1 + \frac{a^2+a}{2}\right)\right) \\ z - (1+a_1)|w|^2 z - z^3 \end{pmatrix} \tag{4.28}$$

$$T_{H,2} = \begin{pmatrix} \varepsilon_1 e^{-i\omega_0}\overline{w}^4 + U_w \\ U_z \end{pmatrix}, \tag{4.29}$$

and

$$U_w = w\Big\{(z + ia\frac{\delta}{2})(1 - |w|^2 - z^2) - az(\mu + z^2 + \frac{\delta^2}{2} + iaz\delta) + i\frac{\delta^3}{3} + \\ + \frac{1}{12}\Big[\big((i\delta - az) - a(1 - |w|^2 - z^2)\big)^2 + 2a\big(2(i\delta - az - 2z)(z - (1+a_1)|w|^2 z - z^3) + \\ + |w|^2 \operatorname{Re}\left[(i\delta - az)^2 - a(1 - |w|^2 - z^2)\right]\big)\Big]\Big\}, \tag{4.30}$$

$$U_z = -|w|^2(\mu + z^2 + \frac{\delta^2}{2} - a_2 z\delta) + \frac{1}{3}z\Big\{(1 - (1+a_1)|w|^2 - 3z^2)(1 - (1+a_1)|w|^2 - z^2) + \\ + (1+a_1)|w|^2 \operatorname{Re}\left[(i\delta - az)^2 - a(1 - |w|^2 - z^2)\right]\Big\}. \tag{4.31}$$

Then:

1. *The time-γ map T_H^γ approximates the map H (4.24) up to order four in γ,* i.e., *$T_H^\gamma = H + \mathcal{O}(\gamma^4)$.*
2. *The time-5γ map $T_H^{5\gamma}$ approximates the fifth iterate G^5 of (4.1) up to order four in γ,* i.e., *$T_H^{5\gamma} = G^5 + \mathcal{O}(\gamma^4)$.*
3. *The vector field T_H is $\mathbb{Z}_5$-equivariant, meaning that it commutes with the axial rotation R_{ω_0}, where $\omega_0/(2\pi) = 1/5$.*
4. *The vector field $T_{H,0} + \gamma T_{H,1}$, given by the terms up to order $\mathcal{O}(\gamma^2)$ of T_H, is axially symmetric, and its planar reduction coincides with the vector field $T_{\widetilde{S}}$ (4.21).*

By the last part of Theorem 4.1 and by Lemma 4.1, for γ sufficiently small the vector field $T_{H,0} + \gamma T_{H,1}$ has a limit cycle $\mathscr{C}$ contained in a horizontal plane $z = z_0$. For $\mu > \mu^{\mathcal{H}}(\gamma) = a_1^2 + \mathcal{O}(\gamma)$, $\mathscr{C}$ is an attractor, and it is a repellor for $\mu < \mu^{\mathcal{H}}(\gamma)$, where $\mu^{\mathcal{H}}(\gamma)$ is the position of the Hopf bifurcation boundary for T_H, up to order $\mathcal{O}(\gamma^2)$. Moreover, for γ sufficiently small and for μ bounded away from $\mu^{\mathcal{H}}(\gamma)$, $\mathscr{C}$ persists as a normally hyperbolic invariant manifold for the vector field T_H. We are especially interested in the bifurcations taking place near the Hopf bifurcation boundary. The location of the bifurcations of equilibria of T_H near the Hopf boundary is computed in the next theorem, see Figures 4.10 and 4.11 for illustrations.

Theorem 4.2 (Tongue and cone). *Consider the vector field T_H (4.26).*

1. *For γ sufficiently small, T_H has ten families $\mathscr{P}^5_{k,\pm}$ of equilibria, $k = 0, \dots, 4$, depending on the parameters (γ, μ, δ''), where*

$$\delta = -\frac{a_2\mu}{a_1}\gamma + \delta''\gamma^2, \quad \delta'' \in \left(-\frac{|a|}{|a_1|}\varepsilon_1, \frac{|a|}{|a_1|}\varepsilon_1\right). \tag{4.32}$$

The cylindrical coordinates $(r_\pm, \phi_{k,\pm}, z_\pm)$ of $\mathscr{P}^5_{k,\pm}$ have the form

$$\begin{aligned} z_\pm &= -\frac{\mu}{a_1}\gamma + z''_\pm\gamma^2 + \mathcal{O}(\gamma^3), \qquad r_\pm = 1 - \frac{\mu^2}{2a_1^2}\gamma^2 + \mathcal{O}(\gamma^3), \\ \phi_{k,\pm} &= \frac{1}{5}\left(2\pi k - \omega_0 + \arctan\frac{\delta'' - a_2 z''_\pm}{a_1 z''_\pm}\right) + \mathcal{O}(\gamma), \quad k = 0, \dots, 4, \end{aligned} \tag{4.33}$$

where $\phi_{k+1,\pm} - \phi_{k,\pm} = \omega_0$ and

$$z''_\pm = \frac{a_2\delta'' \pm \sqrt{\Delta}}{|a|^2}, \quad \Delta = |a|^2\varepsilon_1^2 - a_1^2(\delta'')^2. \tag{4.34}$$

2. *The five equilibria simultaneously undergo saddle-node bifurcations at the surfaces $\mathcal{SN}^5_\pm$ parametrised by $(\gamma, \mu, \delta(\gamma, \mu))$, where*

$$\delta(\gamma, \mu) = -\frac{a_2\mu}{a_1}\gamma \pm \frac{|a|}{|a_1|}\varepsilon_1\gamma^2 + \mathcal{O}(\gamma^3). \tag{4.35}$$

3. *$\mathscr{P}^5_{k,+}$ simultaneously undergo Hopf bifurcations at the surface $\mathcal{H}^5_+$ parametrised by (γ, μ', δ''), where*

$$\mu = a_1^2 + \mu'\gamma + \mathcal{O}(\gamma^2), \quad \delta = -a_1a_2\gamma + \delta''\gamma^2 + \mathcal{O}(\gamma^3), \tag{4.36}$$

and the parameters δ'' and μ' depend on each other by the relations

$$\begin{aligned} \left((2a_1 - 5a_2^2)\mu' - 5a_1a_2\delta''\right)^2 + \left(3a_1a_2\mu' + (3a_1^2 - 2a_1)\delta''\right)^2 \\ = (2a_1 + 2a_1^2 - 5\,|a|^2)^2\varepsilon_1^2, \end{aligned} \tag{4.37}$$

$$-\delta''a_2(1 + a_1) + (a_1 - a_2^2)\mu' > 0. \tag{4.38}$$

The cylindrical coordinates of $\mathscr{P}^5_{k,-}$ at the Hopf bifurcations are

$$\begin{aligned} z_\pm &= -a_1\gamma + z''_\pm\gamma^2 + \mathcal{O}(\gamma^3), \qquad r_\pm = 1 - \frac{a_1^2}{2}\gamma^2 + \mathcal{O}(\gamma^3), \\ \phi_{k,\pm} &= \frac{1}{5}\left(2\pi k - \omega_0 + \arctan\frac{\delta'' - a_2 z''_\pm}{\mu' + a_1 z''_\pm}\right) + \mathcal{O}(\gamma), \quad k = 0, \dots, 4, \end{aligned}$$

where $\phi_{k+1,\pm} - \phi_{k,\pm} = \omega_0$ and

$$z''_\pm = \frac{a_2\delta'' - a_1\mu' \pm \sqrt{\Delta'}}{|a|^2}, \quad \Delta' = |a|^2\varepsilon_1^2 - (a_1\delta'' + a_2\mu')^2. \tag{4.39}$$

4. *$\mathscr{P}^5_{k,-}$ undergo Hopf bifurcations at the curve $\mathcal{H}^5_-$, defined by* (4.37)*, where the inequality sign in* (4.38) *is reversed.*

5. *For parameters on the curves $\mathcal{HSN}^5_\pm$ given by $(\gamma, \mu_\pm(\gamma), \delta_\pm(\gamma))$, where*

$$\mu_\pm(\gamma) = a_1^2 \pm \frac{a_2(1+a_1)}{|a|}\varepsilon_1\gamma + \mathcal{O}(\gamma^2), \quad \delta_\pm(\gamma) = -a_1a_2\gamma \pm \frac{a_1 - a_2^2}{|a|}\varepsilon_1\gamma^2 + \mathcal{O}(\gamma^3), \tag{4.40}$$

the equilibria $\mathscr{P}^5_{k,\pm}$ simultaneously undergo five HSN bifurcations. The coordinates of the bifurcating equilibria are

$$z_\pm = -a_1\gamma \pm \frac{a_2}{|a|}\gamma^2 + \mathcal{O}(\gamma^3), \qquad r_\pm = 1 - \frac{a_1^2}{2}\gamma^2 + \mathcal{O}(\gamma^3),$$
$$\phi_{k,\pm} = \frac{1}{5}\left(2\pi k - \omega_0 + \arctan\frac{a_1}{a_2}\right) + \mathcal{O}(\gamma), \quad k = 0, \dots, 4,$$

i.e., *$e^{i\phi_{k,\pm}}$ are the fifth roots of $\frac{i\overline{a}}{|a|}e^{-i\omega_0}$.*

6. *Suppose the coefficients of H are fixed at $\varepsilon_1 = 1$, $a_1 = -1$ and $a_2 = 1/\sqrt{2}$ (as in Sec.* 4.3.1*). Then $\mathcal{HSN}^5_\pm$ belong to the same unfolding class of Hopf-saddle-node bifurcations. To be precise, for $k = 0, \dots, 4$ denote by*

$$Y_{\beta,k,\pm}(w,z) = \begin{pmatrix} (-\beta_{2,k,\pm} + i\omega_{5,\pm})w - a_{5,\pm}wz - wz^2 \\ -\beta_{1,k,\pm} - s_{5,\pm}|w|^2 - z^2 \end{pmatrix} \tag{4.41}$$

the truncated normal form of T_H provided by Lemma 4.3*, after translation of T_H into the singularity $\mathscr{P}^5_{k,\pm}$. Then the coefficients* $\mathrm{Re}(a_{5,\pm})$ *and $s_{5,\pm}$ in* (4.41) *are*

$$\mathrm{Re}(a_{5,\pm}) = -1 + \mathcal{O}(\gamma), \quad s_{5,\pm} = \mathrm{sign}(\gamma),$$

and a reversal of time is introduced by the transformation bringing T_H into (4.41)*.*

Near the 1:5 bubble, the bifurcation diagram of T_H is organised by the two Hopf-saddle-node bifurcations of equilibria $\mathcal{HSN}^5_\pm$, proved to occur in Theorem 4.2. At such points, there are five degenerate equilibria on $\mathscr{C}$ which undergo a Hopf and a saddle-node bifurcation simultaneously. The intersection of the bifurcation surfaces $\mathcal{SN}^5_\pm$ (4.35) and $\mathcal{H}^5_\pm$ (4.36) with the plane $\gamma = 0.01$ is plotted in Figure 4.10 left, which is in good agreement with the numerical picture obtained for the map G in Figure 4.5 right. The coefficients of H used to plot Figure 4.10 left have the same values used at point 6 of Theorem 4.2 and in Sec. 4.3.1 for the map G.

Remark 4.7. The dynamical analogies between the vector field T_H (4.26) and the map G (4.1) are in fact a corollary of Theorem 4.2. Indeed, the fifth iterate G^5 is a perturbation of the time-5γ map $T_H^{5\gamma}$. Therefore, by application of perturbation theory the bifurcations $\mathcal{SN}^5_\pm$, $\mathcal{H}^5_\pm$, and $\mathcal{HSN}^5_\pm$ in Theorem 4.2 persist for the map G^5. By perturbation theory we mean the implicit function theorem, the theory of persistence of normally hyperbolic invariant manifolds [46, 60], the theory of persistence of non-degenerate bifurcations [6, 38, 56, 78, 88, 94, 95, 99, 103], quasi-periodic bifurcation theory [17, 18, 35, 36], and KAM theory [5, 6, 17, 18]. See the discussion in the last subsection of Sec. 4.1.2.

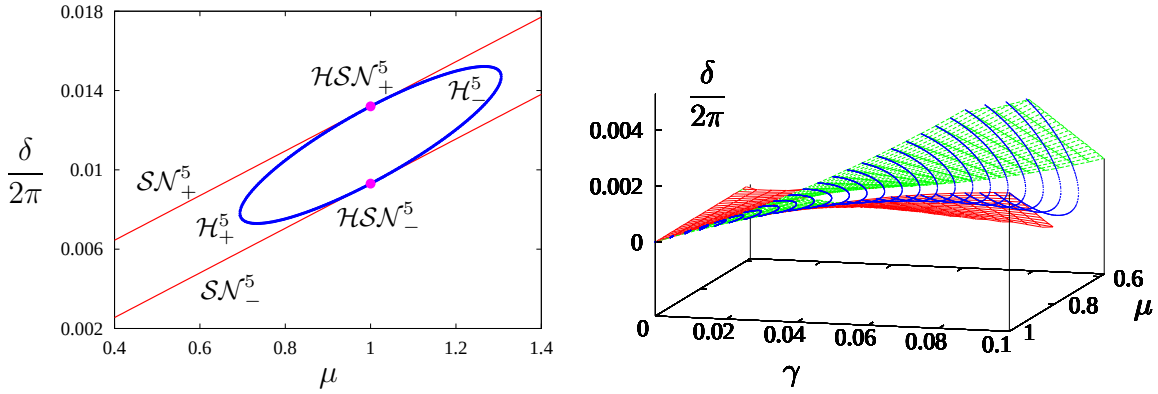

Figure 4.10: Left: the bifurcation curves $\mathcal{H}^5_\pm$ and $\mathcal{SN}^5_\pm$ of the map G, according to Theorem 4.2. Compare the numerical results in Figure 4.5 right. Right: the tongue bounded by $\mathcal{SN}^5_\pm$ and the cone-like bifurcation set bounded by $\mathcal{H}^5_\pm$, as in Theorem 4.2. Only a part of the surfaces is displayed, and the graph has been deformed for better visibility.

In the parameter space (γ, μ, δ), the surfaces $\mathcal{SN}^5_\pm$ delimit a tongue whose width is quadratic in γ, and shrinks to a line for $\gamma \to 0$. The Hopf bifurcations $\mathcal{H}^5_\pm$ form a cone-like surface contained in the interior of the three-dimensional tongue, see the illustration in Figure 4.10 right. The vertex of the cone is the point $(\gamma, \mu, \delta) = (0, 1, 0)$, where the derivative DT_H at the equilibrium $(w, z) = (1, 0)$ is equal to zero. This is a special case of the three-dimensional nilpotent singularity studied in [43].

We conjecture that the bifurcations $\mathcal{SN}^5_\pm$ (4.35) take place *on the horizontal invariant circle* $\mathscr{C}$. In the terminology of [78], and modulo the 1:5 symmetry, these are called saddle-node homoclinic bifurcation. Near these bifurcations, the circle $\mathscr{C}$ is normally hyperbolic and it is formed by the unstable manifolds of one of the two families of equilibria $\mathscr{P}^5_{k,\pm}$. However, this structure does not persist near the curves $\mathcal{H}^5_\pm$, since there the equilibria undergo Hopf bifurcations in the direction normal to $\mathscr{C}$. This implies loss of normal hyperbolicity of $\mathscr{C}$.

A qualitative sketch of the bifurcation diagram near the 1:5 bubble is given in Figure 4.11. The existence of the solid curves in Figure 4.11, as well as of the points $\mathcal{HSN}^5_\pm$, is analytically proved in Theorem 4.2. The remaining dashed curves, as well as the degenerate Hopf bifurcations $\mathcal{DH}^5_\pm$, are conjectured to occur on the basis of the numerical results for the map G described in the previous subsection.

We also conjecture that the bifurcations $\mathcal{HSN}^5_\pm$ of T_H take place on the circle $\mathscr{C}$, yielding a Hopf-saddle-node homoclinic bifurcation (in the terminology of [78]) or Hopf-saddle-node with global reinjection in the terminology of [73]. This type of bifurcation has not yet been studied in detail. A planar model vector field V is considered in [73]. There are many analogies between the bifurcation diagrams of T_H (Figure 4.10) and of V. In fact, several bifurcations of V correspond to the bifurcations of invariant circles and invariant tori of the model G (4.1) described in the previous section. The relation between the vector fields T_H (4.26) and V [73], as well as the completion of the bifurcation diagram of T_H in Figure 4.10, are subjects of future research, see Sec. 4.6.

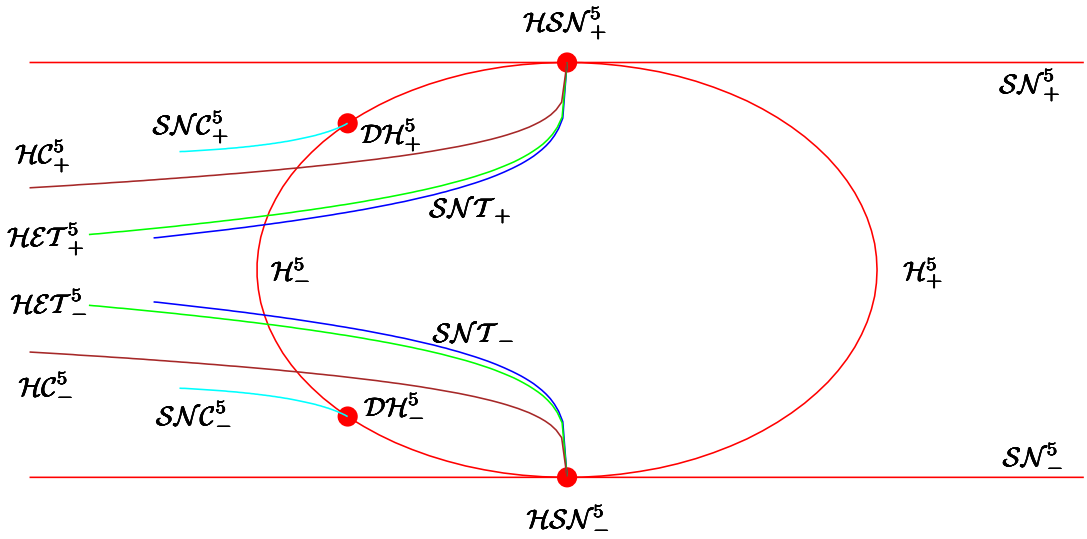

Figure 4.11: Qualitative sketch of the bifurcation diagram of the vector field T_H (4.26) near the 1:5 bubble (in a 'rotated' (μ, δ)-plane). The curves $\mathcal{SN}^5_\pm$ and $\mathcal{H}^5_\pm$ have been proved to exist in Theorem 4.2. Occurrence of the remaining curves, as well as of the points $\mathcal{DH}^5_\pm$, remains at this moment conjectural.

4.4 The Arnol′d resonance web

In this section we briefly describe the parameter space organisation related to the dynamics on the invariant torus $\mathscr{T}$. The results are obtained for the model map Q (4.2) by means of numerical simulations. The region in the (γ, μ, δ)-space we focus on is labelled by 4 in Figure 4.3 right, see Sec. 4.1.3 for a preliminary discussion. Throughout the section, the coefficients of Q are fixed at the values given in Sec. 4.1.3. In particular, since $\gamma = 0.01$, the results are presented in the (μ, δ)-parameter plane.

The resonances between the two internal frequencies of the torus $\mathscr{T}$ are organised in gaps having a countable number of orientations in the parameter plane. Quasi-periodic saddle-node bifurcations occur at the boundary of all gaps. These bifurcations take place on the torus $\mathscr{T}$, in the sense that for nearby parameter values the torus still persists and it is 'phase-locked' to a pair of (possibly periodic) invariant circles, an attractor $\mathscr{A}$ and a circle $\mathscr{B}$ of saddle type. In other words the torus consists of the union $\mathscr{T} = \mathscr{A} \cup W^u(\mathscr{B})$. In the interior of a gap the torus $\mathscr{T}$ possibly ceases to exist, for example being destroyed in a homoclinic tangency of the stable and unstable manifolds of $\mathscr{B}$. However, in this situation the circles $\mathscr{A}$ and $\mathscr{B}$ still exist.

A particularly rich structure exists near the locations where various resonance gaps 'cross'. In Figure 4.12 left several resonance gaps are plotted near one of the crossings. We stress that infinitely many gaps and gap crossings occur near the boundary of any given gap. Therefore the transition between two neighbouring gaps generically passes through an infinite number of quasi-periodic saddle-node bifurcations of an invariant circle. Another possibility, sketched in Figure 4.13, involves a sequence of heteroclinic tangency bifurcations of two periodic points of saddle type. Two attracting invariant circles $\mathscr{A}$ and $\mathscr{B}$, occurring at different (but nearby) parameter values, are plotted in Figure 4.13 (A) and (B) respectively. The circle $\mathscr{A}$ occurs near the right boundary of the gap labelled by I in Figure 4.12 right, whereas $\mathscr{B}$ occurs near the left boundary of gap II. Both parameter values are marked by a dot in Figure 4.12 right.

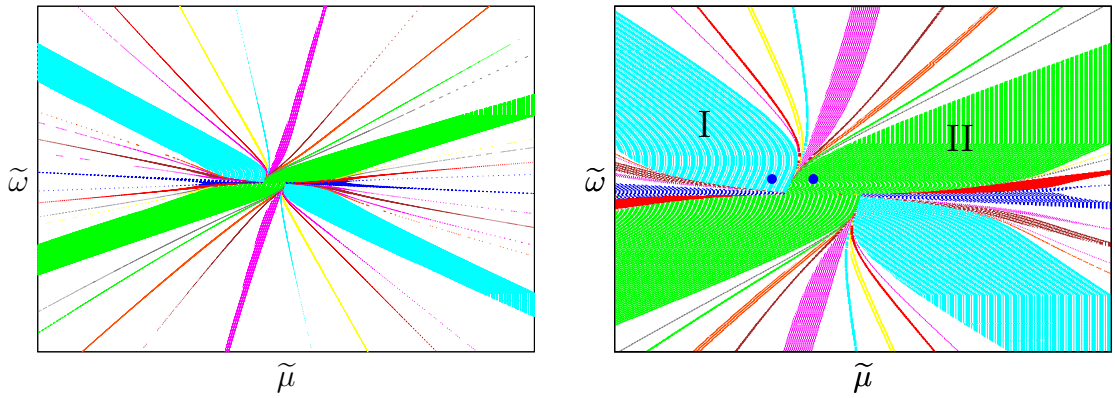

Figure 4.12: Left: parameter plane near a resonance gap crossing. To have a symmetric picture with respect to the axes, the variables $(\widetilde{\mu}, \widetilde{\omega})$ are plotted, obtained by a transformation $(\widetilde{\mu}, \widetilde{\omega}) = C(\mu, \omega)$. Parameter gaps with resonances of different orders (inside $\mathscr{T}$) are displayed with different tones of grey. Right: magnification of left. The dots in region I and region II mark the parameter values at which the attractors $\mathscr{A}$ and $\mathscr{B}$ in Figure 4.13 respectively occur.

A possible theoretical scenario for the transition from $\mathscr{A}$ to $\mathscr{B}$ is the following. The invariant torus $\mathscr{T}$ exists for all parameter values in a connected neighbourhood $\mathcal{N}$ of the two values for which $\mathscr{A}$ and $\mathscr{B}$ occur. Depending on the parameters, the torus $\mathscr{T}$ is phase-locked either to $\mathscr{A}$, or to $\mathscr{B}$, or to none of the two. Consider the dynamics restricted to the two-dimensional surface given by the invariant torus $\mathscr{T}$. Two periodic orbits $\mathscr{P}^{\pm}$ of saddle type occur inside $\mathscr{T}$. In a narrow parameter subset of $\mathcal{N}$, the unstable manifold $W^u(\mathscr{P}^+)$ and the stable manifold $W^s(\mathscr{P}^-)$ have transversal heteroclinic intersections or heteroclinic tangencies. When approaching the heteroclinic structure formed by $W^u(\mathscr{P}^+) \cup W^s(\mathscr{P}^-)$, the invariant circle $\mathscr{A}$ is destroyed. Then the circle $\mathscr{B}$ 'reappears' at the other side of the region of heteroclinic intersections, see the qualitative sketch in Figure 4.14 (A) and (B). Both situations in Figure 4.14 (A) and (B) are obtained by perturbing the time-one map of an integrable vector field defined on the torus $\mathbb{S}^1 \times \mathbb{S}^1$, the dynamics of which is sketched in Figure 4.14 (C).

The above scenario is suggested by the 'swapping' between the 'vertical straight segments' of $\mathscr{A}$ and of $\mathscr{B}$, as illustrated in Figure 4.13 (C) and (D). Notice that the 'horizontal straight segments' of $\mathscr{A}$ and $\mathscr{B}$ are quite close. According to the above scenario, this is due to the fact that the invariant circles pass in a narrow 'corridor' bounded by the manifolds $W^u(\mathscr{P}^+)$ and $W^s(\mathscr{P}^-)$, compare Figure 4.14 (A) and (B). The validity of the above description will be subject of future research, see Sec. 4.6.

4.5 Dynamics in the heteroclinic region

We begin this section by a few comments on a magnification of Figure 4.4, given in Figure 4.15. See Table 4.1 for the meaning of the greyscales. Many resonance tongues occupy the (μ, δ)-parameter plane. Most of them become wider as they approach the heteroclinic region, and eventually overlap. This corresponds to coexistence of

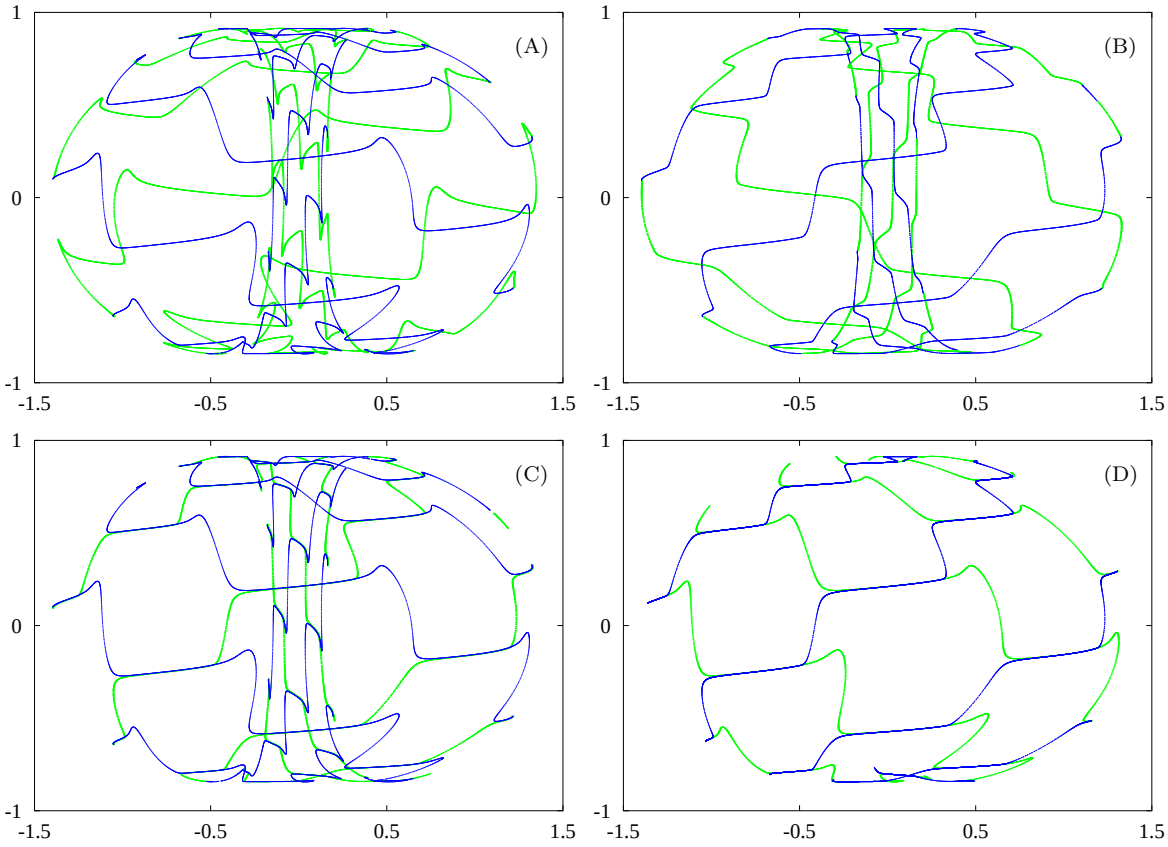

Figure 4.13: (A) Attracting invariant curve $\mathscr{A}$, occurring for (μ, ω) near the left boundary of region I in Figure 4.12 left. Projection on (x, z). The 'front half' of $\mathscr{A}$ (*i.e.*, all points (x, y, z) for which $y > 0$) is plotted with thicker dots. (B) Same as (A) for attracting invariant curve $\mathscr{B}$, occurring for (μ, ω) near the right boundary of region II in Figure 4.12 left. Parameter values of (A) and (B) are marked by two dots in Figure 4.12 right. (C) Simultaneous projection on (x, z) of (A) (thicker dots) and of (B), where only the 'front half' of both is plotted, by displaying points (x, y, z) for which $y > 0$. (D) Same as (C) for $y > 0.3$, where $\mathscr{B}$ is plotted with thicker dots.

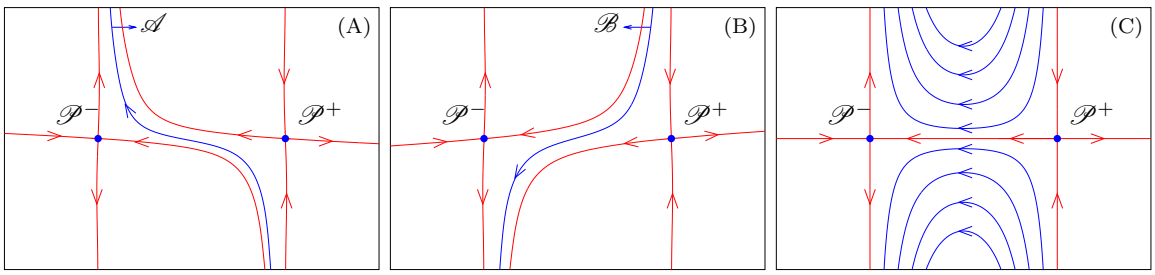

Figure 4.14: (A) Qualitative sketch of the positions of the attracting invariant circle $\mathscr{A}$ and of the stable and unstable manifolds of the periodic points $\mathscr{P}^{\pm}$ inside the torus $\mathscr{T}$. (B) Same as (A) for attracting invariant curve $\mathscr{B}$. (C) Sketch of dynamics for the time-one map of a Hamiltonian vector field on the torus $\mathbb{S}^1 \times \mathbb{S}^1$, of which (A) and (B) are perturbations, see text for details.

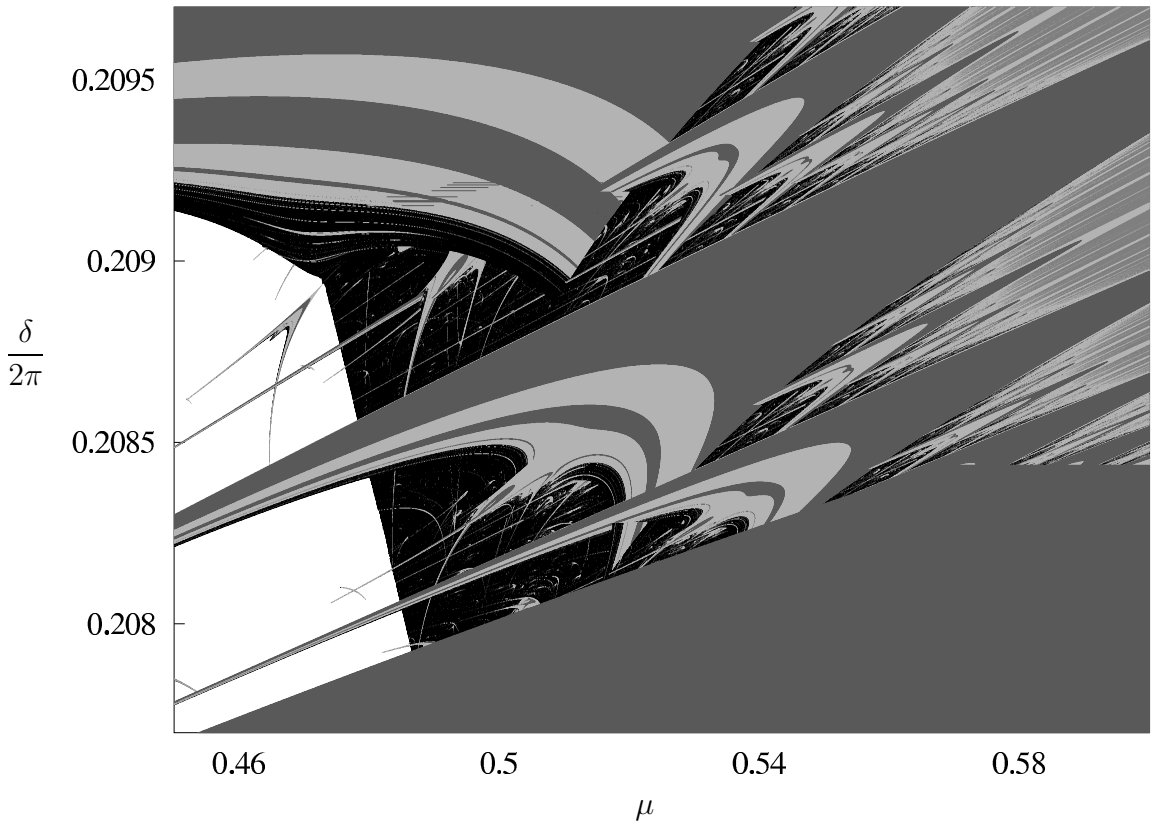

Figure 4.15: Numerical scan of the attractors of G in the $(\mu, \delta/(2\pi))$-parameter plane. The attractors are classified by means of the Lyapunov exponents, according to Table 4.1.

different attracting invariant circles at the same parameter values. The black spots in Figure 4.15 are regions where strange attractors occur. In these regions it is also possible to have coexistence of a strange attractor and an attracting invariant circle.

For parameters inside a tongue, where an invariant circle occurs, this invariant circle can be either of focus type (darker grey), or of node type (paler grey). Notice that at the left-end of many tongues, before the black spots, there are alternating regions with an invariant circle of either stability type. This is due to the occurrence of several curves of quasi-periodic period doublings of an invariant circle, usually occurring in finite number. Compare the scenario described in Sec. 4.1.3. It is also possible that a strange attractor is created at once when leaving a tongue through its boundaries, across a quasi-periodic saddle-node bifurcation of invariant circles. This is illustrated in Figure 4.16. At first the torus $\mathscr{T}$ occurs (Figure 4.16 A). By decreasing μ, the torus $\mathscr{T}$ approaches a saddle-node bifurcation of invariant circles taking place on $\mathscr{T}$ self. We like to point out the intermittency on $\mathscr{T}$ right before the saddle-node (Figure 4.16 B). Just after the saddle-node, the torus $\mathscr{T}$ is phase-locked to an attracting invariant circle $\mathscr{L}$ (Figure 4.16 C). For parameters near the saddle-node bifurcation, an invariant circle $\mathscr{L}'$ of saddle type coexists with $\mathscr{L}$, and the invariant torus $\mathscr{T}$ consists of the union $\mathscr{T} = \mathscr{L} \cup W^u(\mathscr{L}')$. However, when decreasing μ this resonant torus is destroyed, probably by a homoclinic tangency of the manifolds $W^s(\mathscr{L}')$ and $W^u(\mathscr{L}')$. Indeed, when $\mathscr{L}$ disappears through a saddle-

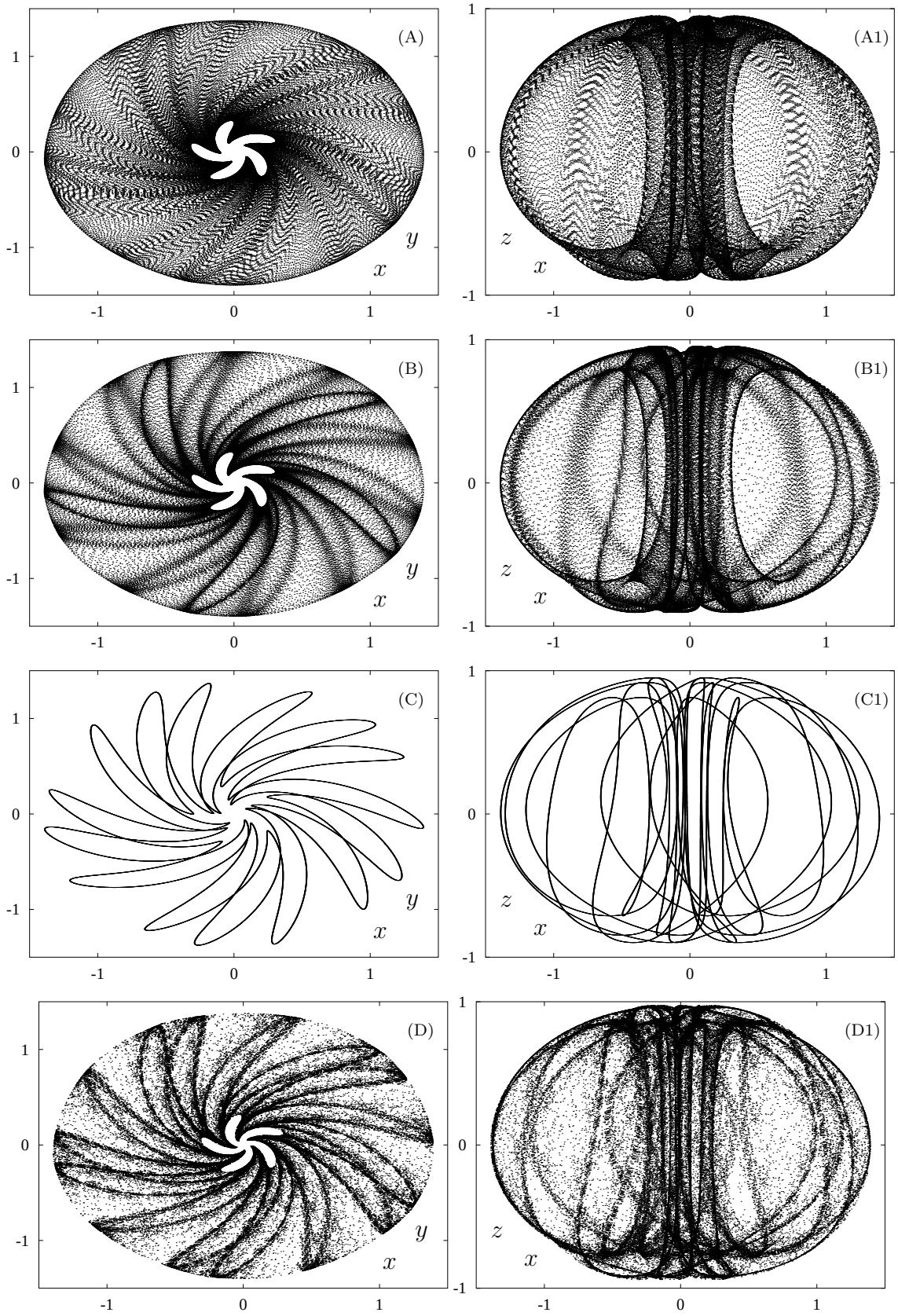

Figure 4.16: Attractors of the model map G (4.1) for $\delta/(2\pi) = 0.0247$ fixed, and at four values of μ. Left column: projections on (x, y), where $w = x + iy$. Right column: projections on (x, z). (A) $\mu = 0.47$, (B) 0.466, (C) 0.46, (D) 0.4555.

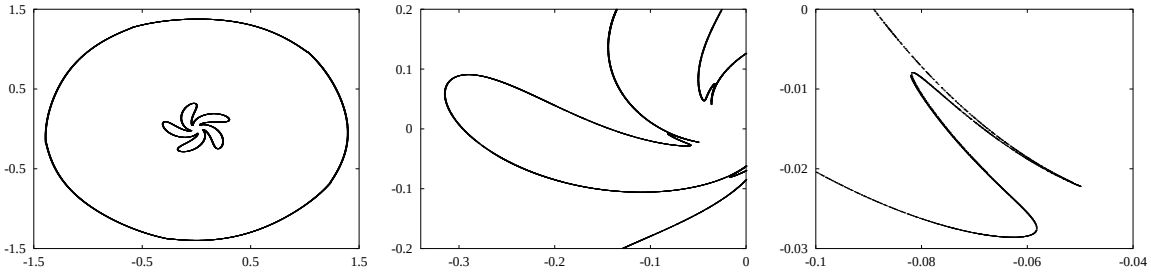

Figure 4.17: Left: section of the attractor in Figure 4.16 (D) by a layer of width $2.e-5$ around the plane $z=0$, projection on the (x,y)-plane. Center: magnification of a portion of the section. Right: further magnification.

node together with $\mathscr{L}'$ (at the other side of the tongue), a strange attractor appears, on which intermittency can be seen (Figure 4.16 D). By further decreasing of μ, the intermittency disappears.

There are strong indications for the fact that the strange attractor in Figure 4.16 D is quasi-periodic Hénon-like [24, 25, 27]. First of all, the second Lyapunov exponent is zero within the achieved numerical precision. Furthermore, a slice by a thin layer near the 'equator', followed by two magnifications, displays a Hénon-like structure in the transversal direction, see Figure 4.17. Compare the discussion in Chapters two and three, and see Remark 1.1.

There are striking analogies in the tongue-like structure displayed in Figure 4.15 and that described in [23] for a map M of the cylinder $\mathbb{R}\times\mathbb{S}^1$. The 'fattened Arnol′d map' M is constructed as an approximated return map near a homoclinic tangency of a fixed point of saddle type. Intuitively the map G can be seen as a perturbation of the fattened Arnol′d map M, where the role of the homoclinic tangency is played by a heteroclinic tangency of the two fixed points $\mathscr{O}_{\pm}$ of saddle-focus type. A study of the relation between the maps G and M is in preparation [26].

4.6 Conclusions

The dynamics of the model maps G and Q shows a variety of phenomena, including breakdown of tori due to interaction with heteroclinic bifurcations, quasi-periodic bifurcations of invariant circles and tori, and resonance bubbles along such bifurcation curves. In this Chapter we have given an overview of the dynamics of the models G and Q. In particular we focused on the study of a 1:5 resonance bubble, for which an important theoretical tool is the Takens approximation theorem [112]. We show the occurrence of two 'secondary' HSN bifurcations of period five points at the edges of the 1:5 bubble, along a frayed boundary of quasi-periodic Hopf bifurcations. Near the 1:5 bubble the bifurcation diagram is further enriched by several bifurcations of invariant circles and tori, see Sec. 4.3.

Remaining open issues (*e.g.*, see [26]) include:

1. The completion of the bifurcation diagram of the map G (4.1) near the 1:5 bubble, see Sec. 4.3.1. In particular, numerical continuation of (bifurcations of) invariant circles is required, and can be performed by one of the methods in [34, 50, 63, 85, 105].

2. The study of the dynamical effect of the global reinjection in the map G and in the vector field approximation T_H, see Sec. 4.3.2.

3. Proving the occurrence of the degenerate Hopf bifurcations $\mathcal{DH}^5_\pm$ in the vector field T_H, see Figure 4.11. An algebraic manipulator is used for this purpose, as for the proof of last item in Theorem 4.2.

4. The analysis of the bifurcation structure of the map Q (4.1) near the multiple resonance crossings, see Sec. 4.1.3. The construction of an explicit model map on the torus $\mathbb{S}^1 \times \mathbb{S}^1$, for a better mathematical understanding of the Arnol′d web.

5. The construction of a return map near the heteroclinic tangencies of the fixed points $\mathscr{O}_\pm$. The study of the relation between the tongue-like organisation of the parameter plane for the map G and for the fattened Arnol′d map [23].

Appendix to Chapter four

4.A Proofs

Proof of Lemma 4.1**.**
Part 1. Denote for simplicity $K(z) = \gamma\mu + az + \gamma z^2$ in the equations of $\widetilde{S}$ (4.18) and of S (4.15). A fixed point of the planar map $\widetilde{S}$ is given by a solution (r_0, z_0) of the equations

$$|1 - \gamma K(z_0)| = 1, \quad r_0^2 = 1 - z_0^2.$$

Define $u = \gamma z$ and

$$M(u,\gamma) = |1 - \gamma K(u/\gamma)|^2 - 1 = (1 - \gamma^2\mu - a_1 u - u^2)^2 + a_2^2 u^2 - 1.$$

By the implicit function theorem, there exists a unique function $u(\gamma)$ defined for small γ and such that $M(u(\gamma),\gamma) = 0$, with $u(\gamma) = \mathcal{O}(\gamma^2)$. Indeed,

$$M(0,0) = 0, \quad \frac{\partial}{\partial u}M(0,0) = -2a_1 \neq 0, \quad \frac{\partial}{\partial \gamma}M(0,0) = 0.$$

An explicit computation yields $u(\gamma) = -\gamma^2\mu/a_1 + \mathcal{O}(\gamma^3)$. Putting $z_0 = u(\gamma)/\gamma$ and $r_0^2 = 1 - z_0^2$ yields a fixed point (r_0, z_0) of $\widetilde{S}$.

The determinant of the derivative $D\widetilde{S}$ at (r_0, z_0), given by $1 + 2\gamma^2(\mu/a_1 - a_1) + \mathcal{O}(\gamma^3)$, is equal to 1 at $\mu = \mu^{\mathcal{H}}(\gamma) = a_1^2 + \mathcal{O}(\gamma)$, where the trace of $D\widetilde{S}$ at the fixed point is $2 + 2a_1\gamma^2 + \mathcal{O}(\gamma^3)$. There the derivative $D\widetilde{S}$ has two complex conjugate eigenvalues of modulus one. Moreover, $\det D\widetilde{S}$ is larger than 1 for $\mu < \mu^{\mathcal{H}}(\gamma)$ and smaller than 1 for $\mu > \mu^{\mathcal{H}}(\gamma)$. To check that the fixed point (r_0, z_0) undergoes a Hopf bifurcation at $\mu = \mu^{\mathcal{H}}$, the nondegeneracy conditions stated in *e.g.* [78] can be verified.

Part 2. The planar map $\widetilde{S}$ (4.18) up to terms of order $\mathcal{O}(\gamma^3)$ is

$$\begin{pmatrix} r \\ z \end{pmatrix} \overset{\widetilde{S}}{\mapsto} \begin{pmatrix} r \\ z \end{pmatrix} + \gamma \begin{pmatrix} -a_1 rz \\ 1 - r^2 - z^2 \end{pmatrix} + \gamma^2 \begin{pmatrix} r\left(-\mu + z^2\left(-1 + \frac{|a|^2}{2} - \frac{a_1^2}{2}\right)\right) \\ 0 \end{pmatrix} + \mathcal{O}(\gamma^3). \quad (4.42)$$

We look for a vector field $T_{\widetilde{S}}$ such that the time-γ map $T_{\widetilde{S}}$ satisfies

$$T_{\widetilde{S}}^{\gamma} = \widetilde{S} + \mathcal{O}(\gamma^3). \tag{4.43}$$

The time-γ map of $T_{\widetilde{S}}$ is given by

$$T_{\widetilde{S}}^{\gamma} = id + \gamma T_{\widetilde{S}} + \frac{\gamma^2}{2}\dot{T}_{\widetilde{S}} + \mathcal{O}(\gamma^3). \tag{4.44}$$

Write $T_{\widetilde{S}} = V_1 + \gamma V_2$, where the vector fields V_j, $j = 1, 2$, are to be determined and may depend on γ. By combining (4.44) and (4.43) we have

$$T_{\widetilde{S}}^{\gamma} - id = \gamma V_1 + \gamma^2 V_2 + \frac{\gamma^2}{2}\dot{V}_1 = \widetilde{S} - id + \mathcal{O}(\gamma^3),$$

which yields

$$V_1 = \frac{1}{\gamma}(\widetilde{S} - id), \quad V_2 = -\frac{1}{2}\dot{V}_1.$$

Then V_1 is easily derived from (4.42), while

$$\dot{V}_1 = \begin{pmatrix} -a_1(\dot{r}z + r\dot{z}) \\ -2(r\dot{r} + z\dot{z}) \end{pmatrix} + \mathcal{O}(\gamma) = \begin{pmatrix} -a_1(-a_1 r z^2 + r(1 - r^2 - z^2)) \\ -2(-a_1 r^2 z + z(1 - r^2 - z^2)) \end{pmatrix} + \mathcal{O}(\gamma).$$

By rearranging the terms of $V_1 + \gamma V_2$ having the same order in γ and by disregarding $\mathcal{O}(\gamma^2)$, we obtain (4.21). This proves point 2.

Part 3. For $\gamma = 0$ the vector field $T_{\widetilde{S}}$ (4.21) has an equilibrium $(r, z) = (1, 0)$. Since the derivative $DT_{\widetilde{S}}$ is invertible at $(r, z, \gamma) = (1, 0, 0)$, by the implicit function theorem there exist an equilibrium $(r, z)(\gamma) = (1, 0) + \mathcal{O}(\gamma)$ of (4.21) for all γ sufficiently small. Substitution of $(r, z)(\gamma)$ in (4.21) yields $(r, z)(\gamma) = (1, -\gamma\mu/a_1) + \mathcal{O}(\gamma^2)$.

For the stability of this equilibrium, observe that the derivative $DT_{\widetilde{S}}$ at $(r, z)(\gamma)$ is such that

$$\mathrm{Tr}(DT_{\widetilde{S}}) = \mathcal{O}(\gamma), \quad \det(DT_{\widetilde{S}}) = -2a_1 + \mathcal{O}(\gamma).$$

So for γ small the eigenvalues of $DT_{\widetilde{S}}$ at $(r, z)(\gamma)$ are complex conjugate, and their real part is

$$\frac{1}{2}\mathrm{Tr}(DT_{\widetilde{S}}) = -z - \gamma a_1 + \mathcal{O}(\gamma^2) = \gamma(\mu/a_1 - a_1) + \mathcal{O}(\gamma^2).$$

Therefore the equilibrium $(r, z)(\gamma)$ undergoes a Hopf bifurcation at $\mu^{\mathcal{H}}(\gamma) = a_1^2 + \mathcal{O}(\gamma)$.

To find the heteroclinic connection, denote the terms of $T_{\widetilde{S}}$ (4.21) of order zero and one in γ by $T_{\widetilde{S},0}$ and $T_{\widetilde{S},1}$ respectively, *i.e.*, write $T_{\widetilde{S}} = T_{\widetilde{S},0} + \gamma T_{\widetilde{S},1}$, where

$$T_{\widetilde{S},0} = \begin{pmatrix} -a_1 r z \\ 1 - r^2 - z^2 \end{pmatrix}, \quad T_{\widetilde{S},1} = \begin{pmatrix} r(-\mu + \frac{a_1}{2} - \frac{a_1}{2}r^2 - bz^2) \\ z - (1 + a_1)r^2 z - z^3 \end{pmatrix}, \tag{4.45}$$

with $b = 1 + \mathrm{Re}(a^2 + a)/2$. The vector field $T_{\widetilde{S},0}$ is integrable, with first integral

$$F(r, z) = \frac{a_1}{2} r^c \left(1 - \frac{r^2}{1 - a_1} - z^2\right), \quad c = -\frac{2}{a_1},$$

and with integrating factor r^{c-1}. Moreover, $T_{\widetilde{S},0}$ has a heteroclinic connection given by the zero level set $F^{-1}(0)$. Multiplying $T_{\widetilde{S},0}$ by the integrating factor r^{c-1} gives a Hamiltonian vector field X_0. So the vector field

$$r^{c-1}T_{\widetilde{S}} = r^{c-1}T_{\widetilde{S},0} + \gamma r^{c-1}T_{\widetilde{S},1} = X_0 + \gamma X_1$$

is a perturbation of the Hamiltonian vector field X_0. The value of the parameter μ for which the heteroclinic connection of X_0 survives for $r^{c-1}T_{\widetilde{S}}$ is given by the zeroes of the integral

$$\int\int_{\mathrm{int}(F^{-1}(0)} \mathrm{Tr}(DX_1)drdz. \tag{4.46}$$

This integral is written as a linear combination of three integrals I_{c-1}, I_{c+1}, I_{c+3}, where

$$I_\beta = \int_0^{\pi/2} \sin^\beta \theta d\theta.$$

By using the recurrence relation $I_{\beta+1} = \frac{\beta}{\beta+1}I_\beta$, the integrals can be reduced to $I_{\beta-1}$, which is factored out. Therefore, up to a multiplicative constant the integral (4.46) is equal to

$$c\left(\mu - \frac{a_1}{2} + \frac{b}{3}\right) + \frac{c(2a_1(1-a_1) - \frac{bc}{3} - 1)}{c+3}.$$

From this we arrive at point 3.

Part 4. The rotation number on the invariant circle $\mathscr{C}$ of S (4.17) is determined by the dynamics in the ϕ-component, which only depends on all parameters and on z_0. Also notice that z_0 does not depend on ω, since the map $\widetilde{S}$ (4.18) does not. Moreover, the dynamics on $\mathscr{C}$ is always a rigid rotation, since all coefficients in the ϕ-component of S are constant along all orbits on $\mathscr{C}$.

We now determine parameter values for which the rotation number on $\mathscr{C}$ is exactly $2\pi/5$. Put $\omega = \omega_0 + \gamma\delta$, where $\omega_0/(2\pi) = 1/5$. Since the map S commutes with the axial rotation $R_\theta(w,z) = (\exp(i\theta)w, z)$ for all θ (and, in particular, for $\theta = \omega_0$), a point of period five on $\mathscr{C}$ is given by (r_0, ϕ_0, z_0), where ϕ_0 is a fixed point of

$$\phi \mapsto \phi + \gamma\delta + \arg(1 - \gamma K(z_0)) = \phi + \gamma\delta + \arctan\frac{-\gamma a_2 z_0}{\mathrm{Re}(1-\gamma K(z_0))}. \tag{4.47}$$

By the implicit function theorem there exists a function $\delta_5(\gamma,\mu)$, with

$$\delta_5(\gamma,\mu) = -\frac{a_2\mu}{a_1}\gamma + \mathcal{O}(\gamma^2),$$

such that the map in (4.47) is the identity. Therefore, for parameter values $(\gamma, \mu, \delta_5(\gamma,\mu))$ *all* points of $\mathscr{C}$ have period five.

Part 5. This is a trivial consequence of the persistence of normally hyperbolic invariant manifolds, see [46, 60]. □

Proof of Lemma 4.2**.** Define the auxiliary map $\widetilde{G} = (\widetilde{G}_w, \widetilde{G}_z)$, where the two components of $\widetilde{G}$ are

$$\widetilde{G}_w(w,z) = w[1-\gamma(\gamma\mu + az + \gamma z^2)] + \gamma^3 e^{-i(\omega_0+\gamma\delta)}\varepsilon_1 \overline{w}^4$$
$$\widetilde{G}_z(w,z) = z + \gamma(1-|w|^2 - z^2).$$

Then we can write $G = R_{(\omega_0+\gamma\delta)} \circ \widetilde{G}$ and $H = R_{\gamma\delta} \circ \widetilde{G}$. For any $c \in \mathbb{C}$ of modulus one we have

$$\widetilde{G}_w(cw,z) - c\widetilde{G}_w(w,z) = \gamma^3 e^{-i(\omega_0+\gamma\delta)}(\overline{c}^4 - c)\varepsilon_1\overline{w}^4 \quad \text{and} \quad \widetilde{G}_z(w,z) = \widetilde{G}_z(cw,z).$$

For either $c = e^{-i(\omega_0+\gamma\delta)}$ or $c = e^{-i\gamma\delta}$ the term $\overline{c}^4 - c$ is of order $\mathcal{O}(\gamma)$. This implies

$$\begin{aligned} G(w,z) &= R_{(\omega_0+\gamma\delta)} \circ \widetilde{G} = \widetilde{G} \circ R_{(\omega_0+\gamma\delta)} \quad \mod \mathcal{O}(\gamma^4), \\ H(w,z) &= R_{\gamma\delta} \circ \widetilde{G} = \widetilde{G} \circ R_{\gamma\delta} \quad \mod \mathcal{O}(\gamma^4), \quad \text{and, therefore,} \\ G^5(w,z) &= \widetilde{G}^5 \circ R^5_{(\omega_0+\gamma\delta)} = \widetilde{G}^5 \circ R^5_{\gamma\delta} = R^5_{\gamma\delta} \circ \widetilde{G}^5 = H^5 \quad \mod \mathcal{O}(\gamma^4). \end{aligned}$$

This concludes the proof of Lemma 4.2. □

Proof of Theorem 4.1**.** The procedure is similar to the proof of Lemma 4.1, point 4. We search for a vector field T_H such that $T_H^\gamma = H + \mathcal{O}(\gamma^4)$. Write $T_H = V_1 + \gamma V_2 + \gamma^2 V_3$, where V_j, $j = 1,2,3$, may depend on γ. Then

$$T_H^\gamma - id = \gamma(V_1 + \gamma V_2 + \gamma^2 V_3) + \frac{\gamma^2}{2}(\dot{V}_1 + \gamma \dot{V}_2) + \frac{\gamma^3}{3!}\ddot{V}_1 + \mathcal{O}(\gamma^4). \tag{4.48}$$

Therefore the condition $T_H^\gamma - id = H - id + \mathcal{O}(\gamma^4)$ yields

$$V_1 = (H - id)/\gamma, \quad V_2 = -\frac{1}{2}\dot{V}_1, \quad V_3 = -\frac{1}{2}\dot{V}_2 - \frac{1}{6}\ddot{V}_1 = \frac{1}{12}\ddot{V}_1.$$

Denoting for simplicity $K(z) = \gamma\mu + az + \gamma z^2$ in the equation of H (4.24), we have

$$V_1 = \begin{pmatrix} w(\xi - e^{i\gamma\delta}K(z)) + \gamma^2 e^{-i\omega_0}\varepsilon_1\overline{w}^4 \\ 1 - |w|^2 - z^2 \end{pmatrix}, \qquad \xi = \frac{e^{i\gamma\delta}-1}{\gamma}$$
$$V_2 = -\frac{1}{2}\begin{pmatrix} w\left[(\xi - e^{i\gamma\delta}K(z))^2 - e^{i\gamma\delta}(a+2\gamma z)(1-|w|^2-z^2)\right] \\ 2\left[|w|^2 \operatorname{Re}(\xi - e^{i\gamma\delta}K(z)) + z(1-|w|^2-z^2)\right] \end{pmatrix},$$
$$V_3 = \frac{1}{12}\begin{pmatrix} \ddot{w}\{[i\delta - az]^2 - a\dot{z}\} - 2aw\{\ddot{z}[i\delta - az] + \operatorname{Re}(\ddot{w}\overline{w}) + z\ddot{z}\} \\ 2\{2\operatorname{Re}(\ddot{w}\overline{w})(-a_1 z) - |w|^2 a_1 \ddot{z} + \ddot{z}\dot{z} - 2z(\operatorname{Re}(\ddot{w}\overline{w}) + z\ddot{z})\} \end{pmatrix},$$

where $(\dot{w}, \dot{z})$ and $(\ddot{w}, \ddot{z})$ denote the components of V_1 and $\dot{V}_1$, respectively. Notice that terms of order $\mathcal{O}(\gamma)$ have already been discarded in V_3, since they give a contribution of order $\mathcal{O}(\gamma^3)$ in the vector field T_H and of order $\mathcal{O}(\gamma^4)$ in the time-γ map T_H^γ. By regrouping terms of the same order in γ in $T_H = V_1 + \gamma V_2 + \gamma V_3$, and by disregarding $\mathcal{O}(\gamma^3)$, we obtain (4.27)–(4.29). Part 1 of Theorem 4.1 is now proved. The proof of the remaining parts is straightforward. □

Proof of Theorem 4.2**.**
Part 1. We search for equilibria of the vector field T_H (4.26) having cylindrical coordinates (r, ϕ, z) and occurring at parameter values (γ, μ, δ) such that

$$z = \mathcal{O}(\gamma), \quad r = 1 + \mathcal{O}(\gamma^2), \quad \delta = \mathcal{O}(\gamma), \tag{4.49}$$

compare with part two of Lemma 4.1. By (4.49), the terms U_w and U_z in (4.26) are of order $\mathcal{O}(\gamma)$. By disregarding all terms of order $\mathcal{O}(\gamma^3)$, the equilibrium condition $T_H = 0$ reads

$$-i\delta + \gamma\mu + az = \gamma^2 \varepsilon_1 e^{-i(\omega_0 + 5\phi)} + \mathcal{O}(\gamma^3), \quad r = 1 + \mathcal{O}(\gamma^2). \tag{4.50}$$

An additional variable z'' and a parameter δ'' are introduced:

$$z = \gamma z' + z''\gamma^2, \quad \delta = \delta'\gamma + \delta''\gamma^2, \tag{4.51}$$

where z' and δ' are coefficients to be determined, which depend on μ but not on γ. The existence of the equilibria is proved by applying the implicit function theorem to an equation of the form $M(r, \phi, z'', \gamma, \mu, \delta'') = 0$, where the solutions (r, ϕ, z'') are functions of the parameters (γ, μ, δ''). The first equation of (4.50) is split in two, one equation for the terms in γ and another for terms of order $\mathcal{O}(\gamma^2)$. The equation for the terms in γ is divided in real and imaginary part, yielding

$$\mu + a_1 z' = 0, \quad -\delta' + a_2 z' = 0, \tag{4.52}$$

which is directly solved for z' and δ'. The terms of order $\mathcal{O}(\gamma^2)$ give

$$-i\delta'' + az'' = \varepsilon_1 e^{-i(\omega_0 + 5\phi)} + \mathcal{O}(\gamma). \tag{4.53}$$

This is split in an equation for the modulus and another for the argument, which, together with the second of (4.50), yield the system

$$M(r, \phi, z'', \delta'', \gamma) = \begin{pmatrix} (-\delta'' + a_2 z'')^2 + (a_1 z'')^2 - \varepsilon_1^2 + \mathcal{O}(\gamma) \\ \omega_0 + 5\phi - 2k\pi + \arctan \frac{-\delta'' + a_2 z''}{a_1 z''} + \mathcal{O}(\gamma) \\ r - 1 + \mathcal{O}(\gamma^2) \end{pmatrix} = 0, \tag{4.54}$$

where $k = 0, \ldots, 4$. For $\gamma = 0$, this system has the solutions $(r_\pm, \phi_{k,\pm}, z''_\pm)$ where $r_\pm = 1$, $\phi_{k,\pm}$ has the expression in (4.33), and $z''_\pm$ is given in (4.34). For small γ the result holds since the derivative DM with respect to (r, ϕ, z'') is invertible, except when $-a_2\delta'' + |a|^2 z'' = 0$. This happens if and only if $\Delta = 0$ in (4.34), *i.e.*, if the equilibria undergo saddle-node bifurcations, see the next part.

Part 2. To look for saddle-node bifurcations, the equation $\det(DT_H) = 0$ has to be added to the three deriving from the equilibrium condition $T_H = 0$. Moreover, δ'' has to be included as unknown together with (r, ϕ, z''). Up to and including terms of order two in γ we have

$$DT_H = \begin{pmatrix} i\delta - \gamma\mu - az - \frac{a}{2}\gamma & 4\varepsilon_1 e^{-i\omega_0}\gamma^2\overline{w}^3 - \frac{a}{2}\gamma w^2 & -w(a + 2\gamma z + a\gamma z) \\ -\overline{w}(1 + \gamma z) & -w(1 + \gamma z) & -2z - a_1\gamma \end{pmatrix} + \mathcal{O}(\gamma^3),$$

where we used that U_w (4.30) and U_z (4.31) are such that $DU_w = DU_z = \mathcal{O}(\gamma)$ for z and δ as in (4.51). Therefore, the saddle-node bifurcation condition reads

$$\det(DT_H) = 10(-a_2\delta + a_1\gamma\mu + |a|^2 z) + \mathcal{O}(\gamma^3) = 0, \tag{4.55}$$

which has to be solved together with (4.50). As in part 2, this system is first solved for the terms of order one in γ. In particular, equation (4.50) at order γ gives (4.52), which trivially satisfies (4.55) at order γ. The terms of order $\mathcal{O}(\gamma^2)$ give the system

$$M(r,\phi,z'',\delta'',\gamma) = \begin{pmatrix} -a_2\delta'' + |a|^2 z'' + \mathcal{O}(\gamma) \\ (-\delta'' + a_2 z'')^2 + (a_1 z'')^2 - \varepsilon_1^2 + \mathcal{O}(\gamma) \\ \omega_0 + 5\phi + \arctan\frac{-\delta''+a_2 z''}{a_1 z''} - 2k\pi + \mathcal{O}(\gamma) \\ r - 1 + \mathcal{O}(\gamma^2) \end{pmatrix} = 0,$$

where $k = 0,\dots,4$. Notice that the first equation is the derivative of the second with respect to z''. This, of course, amounts to require that the second equation has a double solution, *i.e.*, $\Delta = 0$ in (4.34). For $\gamma = 0$ this yields

$$\delta'' = \pm\frac{|a|}{|a_1|}\varepsilon_1, \quad z'' = \pm\frac{a_2}{|a|\,|a_1|}\varepsilon_1.$$

Moreover, the derivative of M with respect to (r,ϕ,z'',δ'') is invertible at $\gamma = 0$, which allows application of the implicit function theorem. In particular (4.55) and the modulus of the first of (4.50) yield

$$a_2\gamma\mu + a_1\delta = \pm\,|a|\,\varepsilon_1,$$

which are the two lines $\mathcal{SN}^5_\pm$ (4.35).

Part 3 and 4. As in part 2, an equation has to be added to (4.54). Denote by (ν_1,ν_2,ν_3) the eigenvalues of DT_H. Then the characteristic polynomial of DT_H is

$$-\nu^3 + \mathrm{Tr}(DT_H)\nu^2 - \mathrm{Sim}(DT_H)\nu + \det(DT_H),$$

where $\mathrm{Sim}(DT_H) = \nu_1\nu_2 + \nu_1\nu_3 + \nu_2\nu_3$. The condition for a Hopf bifurcation is

$$\mathrm{Sim}(DT_H)\,\mathrm{Tr}(DT_H) = \det(DT_H) \neq 0. \tag{4.56}$$

In particular, we have (4.55) for $\det(DT_H)$ and

$$\mathrm{Tr}(DT_H) = -2(\gamma\mu + a_1 z + z + a_1\gamma) + \mathcal{O}(\gamma^3), \quad \mathrm{Sim}(DT_H) = -2a_1 + \mathcal{O}(\gamma^2).$$

Thereby, (4.56) reads

$$-3a_1\mu\gamma + z(2a_1^2 + 2a_1 - 5\,|a|^2) + a_1^2\gamma + 5a_2\delta = 0. \tag{4.57}$$

To determine the coordinates of the bifurcating equilibria, it is convenient to introduce the variable z'' and the parameters (μ',δ'') by

$$z = \gamma z' + z''\gamma^2, \quad \delta = \delta'\gamma + \delta''\gamma^2, \quad \mu = \mu^0 + \gamma\mu', \tag{4.58}$$

where (z', μ^0, δ') are constants to be determined, compare with (4.51). The system given by the equilibrium condition $T_H = 0$ together with (4.57) is split in two equations, one for the terms in γ and another for the terms of order $\mathcal{O}(\gamma^2)$. The terms in γ yield the system

$$\mu^0 + a_1 z' = 0, \quad \delta' + a_2 z' = 0, \quad -3a_1\mu^0 + z'(2a_1^2 + 2a_1 - 5\,|a|^2) + a_1^2 + 5a_2\delta' = 0,$$

which has the solution

$$z' = -a_1, \quad \mu^0 = a_1^2, \quad \delta' = -a_1 a_2.$$

The terms of order $\mathcal{O}(\gamma^2)$ yield

$$M\begin{pmatrix} r, \phi, z'' \\ \gamma, \mu', \delta'' \end{pmatrix} = \begin{pmatrix} -3a_1\mu' + z''(2a_1^2 + 2a_1 - 5\,|a|^2) + 5a_2\delta'' + \mathcal{O}(\gamma) \\ (-\delta'' + a_2 z'')^2 + (\mu' + a_1 z'')^2 - \varepsilon_1^2 + \mathcal{O}(\gamma) \\ \omega_0 + 5\phi + \arctan\frac{-\delta'' + a_2 z''}{\mu' + a_1 z''} - 2k\pi + \mathcal{O}(\gamma) \\ r - 1 + \mathcal{O}(\gamma^2) \end{pmatrix} = 0,$$

where $k = 0, \ldots, 4$. For $\gamma = 0$, the first equation yields

$$z'' = \frac{1}{c}(3a_1\mu' - 5a_2\delta''), \quad c = 2a_1 + 2a_1^2 - 5\,|a|^2\,. \tag{4.59}$$

Substitution of (4.59) into the second component of M gives (4.37). Conversely, from the second component of M we have (4.39). Substitution of (4.39) into (4.59) gives

$$\pm c\sqrt{\Delta'} = -2a_1 a_2(1 + a_1)\delta'' + 2a_1(a_1 - a_2^2)\mu'. \tag{4.60}$$

Since $c < 0$, this implies that the equilibrium with $\mathscr{P}^5_{k,+}$, corresponding to the "+" sign in the left hand side of (4.60), only can have a Hopf bifurcation when the right hand side of (4.60) is negative. This gives inequality (4.38).

Part 5. The location of the $\mathcal{HSN}^5_{\pm}$ points is obtained as the solution of the system given by the equilibrium condition $T_H = 0$ (4.50), together with the saddle-node equation (4.55) and the Hopf condition (4.56). According to what has been said in part 3, (4.55) is equivalent to require $\Delta' = 0$ in (4.60). Therefore the solutions are obtained obtained by setting (4.38) equal to zero and substituting in (4.37) and (4.36).

Part 6. The proof is carried out by means of an algebraic manipulator, *i.e.*, a computer program that calculates the transformations in Lemma 4.3 up to a finite order in the variables and parameters. The algebraic manipulator used in this proof is based on [62]. □

4.B Normal forms for HSN-families of vector fields

We here sketch the normalisation steps which bring a generic HSN-family of vector field to the form (4.7), closely following [78].

Consider a C^∞-smooth family of vector fields X_α on $\mathbb{R}^3$, where $\alpha \in \mathbb{R}^k$ is a parameter. We call X_α an HSN-family of vector fields if $X_\alpha(0) = 0$ at $\alpha = 0$ and

$$\operatorname{spec} DX_0(0) = \{\pm i\nu_0,\ 0\}, \quad \nu_0 > 0. \tag{4.61}$$

Remarks 4.8. 1. To have a nondegenerate Hopf-saddle-node bifurcation, generic conditions (formulated later in this section) are required on the 3-jet of X_α around the origin of $\mathbb{R}^3$.

2. The number k of parameters should be at least sufficient to have a miniversal unfolding [5] of the linear part $DX_0(0)$. However, since we work here modulo equivalence, time scalings are allowed and the parameter unfolding the imaginary part of the eigenvalues of $DX_0(0)$ can be considered a constant. We stress that the case of a diffeomorphism is quite different in this respect, compare Remark 4.2.

In suitable coordinates (w, z) in $\mathbb{R}^3$, X_α reads

$$X_\alpha(w,z) = \begin{pmatrix} f_{000}(\alpha) + (\eta(\alpha) + i\nu(\alpha))w + \sum_{j+k+h\geq 2} f_{jkh}(\alpha)\, w^j \overline{w}^k z^h \\ g_{000}(\alpha) + \zeta(\alpha) z + \sum_{j+k+h\geq 2} g_{jkh}(\alpha)\, w^j \overline{w}^k z^h \end{pmatrix}, \tag{4.62}$$

where $f_{000}(0) = g_{000}(0) = \eta(0) = \zeta(0) = 0$, and $\nu(0) = \nu_0$.

Lemma 4.3. **[78]** *Let X_α be an HSN-family of vector fields like in* (4.62)*. Suppose X_α satisfies the open and dense conditions*

$$g_{002}(0) \neq 0, \quad g_{110}(0) \neq 0, \quad \hat{\hat{f}}_{102}(0) \neq 0,$$

where $\hat{\hat{f}}_{102}(0)$ is given by

$$\hat{\hat{f}}_{102}(0) = \operatorname{Re}\left[\hat{f}_{102} + f_{101}\left(\frac{\operatorname{Re}\hat{f}_{210}}{g_{110}} - \frac{3\hat{g}_{003}}{2g_{002}} + \frac{\hat{g}_{111}}{2g_{110}}\right) - \frac{\hat{f}_{210} g_{002}}{g_{110}}\right], \quad \alpha = 0, \tag{4.63}$$

and the coefficients $\hat{f}_{102}$, $\hat{f}_{210}$, $\hat{g}_{003}$, and $\hat{g}_{111}$ at $\alpha = 0$ are

$$\begin{aligned} \hat{f}_{102} &= f_{102} + \frac{i}{\nu_0}\left[2f_{002}(f_{200} - g_{101}) - \frac{1}{2}|f_{011}|^2 - f_{110}\overline{f}_{002}\right], \\ \hat{f}_{210} &= f_{210} + \frac{i}{\nu_0}\left[f_{110}f_{200} - \frac{1}{2}g_{200}f_{011} - |f_{110}|^2 - \frac{2}{3}|f_{020}|^2\right], \\ \hat{g}_{003} &= g_{003} - \frac{2}{\nu_0} g_{101} \operatorname{Im} f_{002}, \\ \hat{g}_{111} &= g_{111} - \frac{2}{\nu_0}\left[g_{101} \operatorname{Im} f_{110} + g_{200} \operatorname{Im} f_{011}\right]. \end{aligned} \tag{4.64}$$

Also assume that the derivative of the map

$$\alpha \mapsto (g_{000}(\alpha), \eta(\alpha)) \tag{4.65}$$

is surjective at $\alpha = 0$. Then, by smooth transformations and by introducing new parameters $(\beta_1, \beta_2) = \beta(\alpha_1, \alpha_2)$, system (4.62) *can be brought to the form*

$$\begin{pmatrix} \dot{w} \\ \dot{z} \end{pmatrix} = Y_\beta(w,z) + \mathcal{O}(\|w,z\|^4), \tag{4.66}$$

where Y_β is the third degree polynomial vector field

$$Y_\beta(w,z) = \begin{pmatrix} (-\beta_2 + i\omega)w - awz - wz^2 \\ -\beta_1 - sw\overline{w} - z^2 \end{pmatrix}. \tag{4.67}$$

For $\beta = 0$, the coefficients $a = a(\beta) \in \mathbb{C}$, $s = \pm 1$, and $\omega = \omega(\beta)$ in (4.67) *are*

$$a = \frac{f_{101}}{g_{002}}, \qquad s = \operatorname{sign}\left(\frac{g_{002}}{g_{110}}\right), \qquad \omega = -\frac{\hat{\hat{f}}_{102}}{g_{002}^2}\nu \qquad (\alpha = 0). \tag{4.68}$$

Moreover, if the coefficient $\hat{\hat{f}}_{102}(0)$ (4.63) *is positive, then the transformation from* (4.62) *to* (4.66) *includes a reversal of time.*

The proof of Lemma 4.3 consists of four transformations, which we briefly describe given their relevance in the construction of our model maps. See [78] for details.

Step 1 Poincaré-Dulac normal form.
By the general theory of normal forms of vector fields [5] there exists a parameter-preserving change of coordinates $(w,z) = C(\hat{w},\hat{z},\alpha)$ which brings X_α (4.62) into the form

$$\begin{pmatrix} \hat{f}_{100}\hat{w} + \hat{f}_{101}\hat{w}\hat{z} + \hat{f}_{210}\hat{w}^2\overline{\hat{w}} + \hat{f}_{102}\hat{w}\hat{z}^2 \\ \hat{g}_{000} + \hat{g}_{100}\hat{z} + \hat{g}_{110}\hat{w}\overline{\hat{w}} + \hat{g}_{002}\hat{z}^2 + \hat{g}_{111}\hat{w}\overline{\hat{w}}\hat{z} + \hat{g}_{003}\hat{z}^2 \end{pmatrix} + \mathcal{O}\big(\|\hat{w},\hat{z}\|^4\big). \tag{4.69}$$

Up to order three the family in (4.69) is axially symmetric. Furthermore, by a translation of the $\hat{z}$-coordinate, the coefficient $\hat{g}_{100}$ in (4.69) can be set to zero. To do this the condition $g_{002}(0) \neq 0$ is required on the 3-jet of (4.62).

The above transformation is computed in two steps. The first is done for $\alpha = 0$, then the implicit function theorem is used for α small. At $\alpha = 0$, the coefficients of (4.69) and of (4.62) are related to each other by (4.64) and by

$$\hat{f}_{100} = i\nu_0, \quad \hat{f}_{101} = f_{101}, \quad \hat{g}_{000} = 0, \quad \hat{g}_{110} = g_{110}, \quad \hat{g}_{002} = g_{002} \quad (\alpha = 0).$$

Step 2 Gavrilov normal form.
The Poincaré-Dulac normal form is further simplified by the simultaneous application of a reparametrisation of time and a change of coordinates, which for $\alpha = 0$ have the form

$$dt = (1 + b_1\hat{z} + b_2\hat{w}\overline{\hat{w}})\,d\tau, \qquad \hat{w} = \hat{\hat{w}} + b_3\hat{\hat{w}}\hat{\hat{z}}, \qquad \hat{z} = \hat{\hat{z}} + b_4\hat{\hat{z}}^2,$$

where $b_1, b_2, b_4 \in \mathbb{R}$, while $b_3 \in \mathbb{C}$. Such transformation aims at eliminating some of the cubic terms in (4.69). In particular, suitable b_j's exist such that in the new time and coordinates X_α takes the form

$$\begin{pmatrix} \hat{\hat{f}}_{100}\hat{\hat{w}} + \hat{\hat{f}}_{101}\hat{\hat{w}}\hat{\hat{z}} + \hat{\hat{f}}_{102}\hat{\hat{w}}\hat{\hat{z}}^2 \\ \hat{\hat{g}}_{000} + \hat{\hat{g}}_{110}\hat{\hat{w}}\overline{\hat{\hat{w}}} + \hat{\hat{g}}_{002}\hat{\hat{z}}^2 \end{pmatrix} + \mathcal{O}\Big(\Big\|\hat{\hat{w}},\hat{\hat{z}}\Big\|^4\Big), \tag{4.70}$$

where $\operatorname{Im}(\hat{\hat{f}}_{102}) = 0$. For the existence of this transformation, one has to assume that both $g_{110}(0)$ and $g_{002}(0)$ are nonzero in (4.62). Again, for α small one uses the

implicit function theorem. At $\alpha = 0$, the coefficients of (4.70) are related to those of the starting vector field X_α (4.62) by (4.63) and by

$$\hat{\hat{f}}_{100} = i\nu_0, \quad \hat{\hat{f}}_{101} = f_{101} - i\nu_0 \frac{\hat{g}_{003}}{g_{002}}, \quad \hat{\hat{g}}_{000} = 0, \quad \hat{\hat{g}}_{110} = g_{110}, \quad \hat{\hat{g}}_{002} = g_{002} \quad (\alpha = 0),$$

where $\hat{g}_{003}$ is given in (4.64).

Remark 4.9. 1. The time scaling used in this step depend both on the phase variables and on the parameters.

2. An equivalent normal form, due to Guckenheimer, contains the cubic term $w^2\overline{w}$ instead of wz^2, see [78]. This choice is not relevant since the resulting third degree polynomial vector fields have the same bifurcation diagram. A similar property holds for HSN-families of diffeomorphisms.

Step 3 Final scalings.
By applying a parameter-dependent rescaling of time and variables of the form

$$\tau = \frac{\hat{\hat{f}}_{102}}{\hat{\hat{g}}_{002}^2} t, \quad \hat{\hat{w}} = \sqrt{s \frac{\hat{\hat{g}}_{002}^3}{\hat{\hat{g}}_{110} \hat{\hat{f}}_{102}^2}}\, w, \quad \hat{\hat{z}} = \frac{\hat{\hat{g}}_{002}}{\hat{\hat{f}}_{102}} z, \tag{4.71}$$

(where for simplicity we re-use the starting variable names), the real coefficients $\hat{\hat{f}}_{102}$, $\hat{\hat{g}}_{110}$, and $\hat{\hat{g}}_{002}$ in (4.70) can be scaled to one, yielding

$$\begin{pmatrix} (\beta_2(\alpha) - i\omega(\alpha))w + awz + wz^2 \\ \beta_1(\alpha) + sw\overline{w} + z^2 \end{pmatrix} + \mathcal{O}(\|w, z\|^4), \tag{4.72}$$

where (a, s) are as in (4.68) and

$$\beta_1 = \frac{\hat{\hat{f}}_{102}^2}{\hat{\hat{g}}_{002}^3} \hat{\hat{g}}_{000}, \quad \beta_2 = \frac{\hat{\hat{f}}_{102}}{\hat{\hat{g}}_{002}^2} \operatorname{Re}(\hat{\hat{f}}_{100}), \quad \omega = -\frac{\hat{\hat{f}}_{102}}{\hat{\hat{g}}_{002}^2} \operatorname{Im}(\hat{\hat{f}}_{100}).$$

For the scaling (4.71) to be possible, the coefficient $\hat{\hat{f}}_{102}(0)$ (4.63) must be nonzero.

Remark 4.10. If $\hat{\hat{f}}_{102}(0) < 0$, one is introducing a reversal of time, and another reversal of time is applied in the next step. Both have to be taken into account when determining the stability type of the invariant manifolds of the final system (4.67) with respect to the starting system (4.62).

Step 4 Introduction of new parameters and reversal of time.
The regularity of the map (4.65) is equivalent to that of the map

$$\alpha \mapsto \beta = (\beta_1(\alpha), \beta_2(\alpha)).$$

This implies that the reparametrisation $\beta = \beta(\alpha)$ is locally invertible, and, therefore, β can be used as parameter instead of α. A reversal of time brings (4.72) to the form (4.67).

4.C Normal forms for HSN-families of maps

The purpose of this section is to present an analogue to Lemma 4.3 for a given HSN-family of diffeomorphisms F, depending on the multi-parameter $\alpha = (\alpha_1, \dots, \alpha_k)$. Notice that fewer simplifications are possible for a diffeomorphism than for vector fields, since we cannot scale time. Moreover in this case three parameters are needed for the Linear Centraliser Unfolding of $DF(0,0)$, hence we set $k = 3$. Assume the linear part of F is in Jordan normal form:

$$F_\alpha(w,z) = \begin{pmatrix} f_{000} + \lambda(\alpha)w + \sum_{j+k+h\geq 2} f_{jkh}(\alpha)\, w^j \overline{w}^k z^h \\ g_{000} + \nu(\alpha)z + \sum_{j+k+h\geq 2} g_{jkh}(\alpha)\, w^j \overline{w}^k z^h \end{pmatrix}, \tag{4.73}$$

where $\nu(0) = 1$ and $\lambda(0) = \lambda_0$, while $f_{000}(0) = g_{000}(0) = 0$.

Lemma 4.4. *Let F be an HSN-family of diffeomorphisms as in* (4.73)*, depending on the multi-parameter $\alpha \in \mathbb{R}^3$, with* $\operatorname{spec} DF_0(0) = \{\lambda_0, \overline{\lambda}_0, 1\} \subset \mathbb{S}^1$*. Suppose F satisfies the open and dense condition*

$$g_{002}(0) \neq 0, \quad g_{110}(0) \neq 0. \tag{4.74}$$

Also assume that the derivative of the map

$$\alpha \mapsto (g_{000}(\alpha), \lambda(\alpha)) \tag{4.75}$$

is surjective at $\alpha = 0$. Then there exist a smooth parameter-dependent transformation and a reparametrisation $\beta = (\beta_1, \beta_2, \beta_3)(\alpha)$, with $\beta_j \in \mathbb{R}$, such that in the new coordinates and parameters the diffeomorphism (4.73) *reads*

$$\begin{pmatrix} w \\ z \end{pmatrix} \mapsto \begin{pmatrix} (1+\beta_2)e^{i\beta_3}\lambda_0 w + awz + bwz^2 \\ \beta_1 + z + sw\overline{w} + z^2 + cz^3 \end{pmatrix} + \mathcal{O}(\|w,z\|^4). \tag{4.76}$$

Here the coefficients $a(\beta)$ and $b(\beta)$ are complex, while $c(\beta)$ is real and $s = \pm 1$. Furthermore, at $\beta = 0$ we have

$$a = \frac{f_{101}}{g_{002}}, \qquad b = \frac{f_{102}}{g_{002}^2}, \qquad c = \frac{g_{003}}{g_{002}^2}, \qquad s = \operatorname{sign}\left(\frac{g_{002}}{g_{110}}\right). \tag{4.77}$$

The proof is divided in two parts. First we consider the normalising procedure for $\alpha = 0$. This is achieved by two transformations performed independently. For small α the conclusion follows from the implicit function theorem, but the two transformations have to be performed simultaneously. Finally, a parameter-dependent rescaling of the variables is applied. We begin by setting $\alpha = 0$.

Step 1 Poincaré normal form.
By general theory [39, 112], for $\alpha = 0$ there exists a change of coordinates in $\mathbb{R}^3$ which is tangent to the identity at the origin, and such that in the new coordinates only resonant monomial appear in the expansion of F. For $n \geq 2$ integer, a monomial P of the form

$$P(w,z) = w^{n_1}\overline{w}^{n_2} z^{n_3}$$

is called *resonant* if it commutes with the semisimple part S of $DF_0(0)$. Because of (4.4), in suitable coordinates $(\hat{w}, \hat{z})$ the 3-jet of any HSN-family at $\alpha = 0$ is axially symmetric:

$$\begin{pmatrix} \lambda_0\hat{w} + \hat{f}_{101}\hat{w}\hat{z} + \hat{f}_{210}\hat{w}^2\overline{\hat{w}} + f_{102}\hat{w}\hat{z}^2 \\ \hat{z} + \hat{g}_{110}\hat{w}\overline{\hat{w}} + \hat{g}_{002}\hat{z}^2 + \hat{g}_{111}\hat{w}\overline{\hat{w}}\hat{z} + \hat{g}_{003}\hat{z}^3 \end{pmatrix} + \mathcal{O}\big(\|\hat{w}, \hat{z}\|^4\big). \tag{4.78}$$

Step 2 Second order Poincaré normalisation (hypernormalisation) [78].
By a transformation of the form

$$(\hat{w}, \hat{z}) = C(\hat{\hat{w}}, \hat{\hat{z}}) = (\hat{\hat{w}} + b_1\hat{\hat{w}}\hat{\hat{z}},\ \hat{\hat{z}} + b_2\hat{\hat{z}}^2).$$

the cubic terms $\hat{w}^2\overline{\hat{w}}$ and $\hat{w}\overline{\hat{w}}\hat{z}$ in (4.78) can be eliminated, yielding the map $\widehat{F}$:

$$\widehat{F}(\hat{\hat{w}}, \hat{\hat{z}}) = \begin{pmatrix} \lambda_0\hat{\hat{w}} + \hat{\hat{f}}_{101}\hat{\hat{w}}\hat{\hat{z}} + \hat{\hat{f}}_{102}\hat{\hat{w}}\hat{\hat{z}}^2 \\ \hat{\hat{z}} + \hat{\hat{g}}_{110}\hat{\hat{w}}\overline{\hat{\hat{w}}} + \hat{\hat{g}}_{002}\hat{\hat{z}}^2 + \hat{\hat{g}}_{003}\hat{\hat{z}}^3 \end{pmatrix} + \mathcal{O}\Big(\Big\|\hat{\hat{w}}, \hat{\hat{z}}\Big\|^4\Big),$$

where $\hat{\hat{f}}_{101} = \hat{f}_{101}$, $\hat{\hat{g}}_{110} = \hat{g}_{110}$, and $\hat{\hat{g}}_{002} = \hat{g}_{002}$. Indeed, by imposing the condition $\widehat{F} \circ C(\hat{\hat{w}}, \hat{\hat{z}}) = C \circ \widehat{F}(\hat{\hat{w}}, \hat{\hat{z}})$ up to terms of order three, we get the linear system

$$\begin{aligned} -\hat{g}_{002}\lambda_0 b_1 &= \hat{f}_{210} \\ -\hat{g}_{110}\lambda_0 b_1 + \hat{f}_{101}b_2 + \hat{\hat{f}}_{102} &= \hat{f}_{102} \\ \hat{g}_{002}(b_1 + \overline{b_1}) - 2\hat{g}_{002}b_2 &= \hat{g}_{111} \end{aligned} \tag{4.79}$$

in the variables $(b_1, b_2, \hat{\hat{f}}_{102})$, which is solvable due to the assumption in (4.74). This finishes the proof for $\alpha = 0$.

Step 3 Application of the implicit function theorem.
For α sufficiently small, by the implicit function theorem there exists a parameter-dependent transformation for which (4.73) takes the form

$$\begin{pmatrix} \hat{\hat{\lambda}}\hat{\hat{w}} + \hat{\hat{f}}_{101}\hat{\hat{w}}\hat{\hat{z}} + \hat{\hat{f}}_{102}\hat{\hat{w}}\hat{\hat{z}}^2 \\ \hat{\hat{g}}_{000}\hat{\hat{z}} + \hat{\hat{g}}_{110}\hat{\hat{w}}\overline{\hat{\hat{w}}} + \hat{\hat{g}}_{002}\hat{\hat{z}}^2 + \hat{\hat{g}}_{003}\hat{\hat{z}}^3 \end{pmatrix} + \mathcal{O}\Big(\Big\|\hat{\hat{w}}, \hat{\hat{z}}\Big\|^4\Big), \tag{4.80}$$

where $\hat{\hat{\lambda}}(0) = \lambda_0$. To show that the implicit function theorem can be applied, the computations are elementary, but long and tedious.

Step 4 Final scalings and reparametrisation.
A parameter-dependent scaling of the type

$$\hat{\hat{w}} = \sqrt{s\frac{\hat{\hat{g}}_{002}}{\hat{\hat{g}}_{110}}}w, \quad \hat{\hat{z}} = \frac{1}{\hat{\hat{g}}_{002}}z,$$

where s is given in (4.77), is applied to (4.80). For simplicity we re-use the names of the starting variables. This yields

$$\begin{pmatrix} w \\ z \end{pmatrix} \mapsto \begin{pmatrix} (1 + \beta_2(\alpha))e^{i\beta_3(\alpha)}\lambda_0 w + a(\alpha)wz + b(\alpha)wz^2 \\ \beta_1(\alpha) + z + sw\overline{w} + z^2 + c(\alpha)z^3 \end{pmatrix} + \mathcal{O}(\|w, z\|^4).$$

The regularity of (4.75) is equivalent to that of the map $\alpha \mapsto \beta(\alpha)$. This means that β can be taken as new parameter.

4.D The Takens vector field normal form for diffeomorphisms

In this section we present the two versions of the Takens theorem that are used in this Chapter. The first is the 'classical' Takens theorem [112], also see [39]. We refer to [112] for terminology.

Let $F : \mathbb{R}^m \times \mathbb{R}^p \to \mathbb{R}^m \times \mathbb{R}^p$ be a diffeomorphism such that $F(0,0) = (0,0)$ and $\pi_p \circ F = \pi_p$, where $\pi_p : \mathbb{R}^m \times \mathbb{R}^p \to \mathbb{R}^p$ is the projection on the p-dimensional parameter space. Let S be the semisimple part of $DF(0,0)$. By $\mathcal{V}^n$ denote the space of all homogeneous polynomial vector fields V_n of degree n on $\mathbb{R}^m \times \mathbb{R}^p$ such that

1. $S_* V_n = V_n$, *i.e.*, V_n commutes with S.

2. $\pi_p \circ V_n = 0$, *i.e.*, V_n vanishes in the parameter direction.

Given a vector field $V_1 \in \mathcal{V}^1$, denote by $\mathcal{I}^n_{V_1}$ the image of $\mathcal{V}^n$ under the adjoint operator $\mathrm{ad}_{V_1} = [V_1, -]$, where $[-,-]$ are the Lie brackets. Let $\mathcal{G}^n_{V_1}$ be a subspace of $\mathcal{V}^n$ which is complementary to $\mathcal{I}^n_{V_1}$, *i.e.*, $\mathcal{V}^n = \mathcal{I}^n_{V_1} + \mathcal{G}^n_{V_1}$.

Theorem 4.3. [112] *Let F and S be as above. Then there exist a vector field T_F on $\mathbb{R}^m \times \mathbb{R}^p$ and a diffeomorphism $C : \mathbb{R}^m \times \mathbb{R}^p \to \mathbb{R}^m \times \mathbb{R}^p$ such that*

1. *$S_* T_F = T_F$, $\pi_p \circ T_F = 0$, and $\pi_p \circ C = \pi_p$.*

2. *In the new coordinates the infinite jet of F in $(0,0)$ has the form*

$$j^\infty\big(C^{-1} \circ F \circ C\big) = S \circ T^1_F, \tag{4.81}$$

where T^1_F is the time-1 map of T_F.

3. *The infinite jet of T_F can be written as*

$$j^\infty T_F = \sum_{n=1}^{\infty} G_n, \tag{4.82}$$

where $G_1 \in \mathcal{V}^1$ has the same 1-jet as T_F in the origin and $G_n \in \mathcal{G}^n_{G_1}$ for $n \geq 2$.

Theorem 4.3 is used in Sec. 4.3.2 to construct a vector field approximation for the fifth iterate of the model map G (4.1). In fact, the vector field is computed only up to order two in γ, and not up to ∞-flat terms as in (4.81).

Notice that the vector field T_F provided by Theorem 4.3 is such that all eigenvalues are zero: $\operatorname{spec} DT_F(0,0) = \{0\}$, since the semisimple part S is factored out in (4.81). On the other hand, to construct the model maps G (4.1) and Q (4.2) we find it more convenient to start by a two-parameter HSN-family X of vector fields on $\mathbb{R}^3 \times \mathbb{R}^2$, that is, a family X for which $\operatorname{spec} DX(0,0) = \{\pm i\omega_0, 0\}$, $\omega_0 \neq 0$. Compare (4.5) and the discussion at the end of Sec. 4.1.1. Therefore, we resort to the following version of the Takens theorem.

Lemma 4.5. *Let F be a family of diffeomorphisms of $\mathbb{R}^3 \times \mathbb{R}^p$, with $\pi_p \circ F = \pi_p$ such that*

$$F(0,0) = 0 \quad \textit{and} \quad \operatorname{spec} DF(0,0) = \{e^{i\omega_0}, e^{-i\omega_0}, 1\} \subset \mathbb{S}^1.$$

Suppose that the eigenvalue $\lambda_0 = e^{i\omega_0}$ satisfies the nonresonance conditions

$$\lambda_0^r \neq 1 \qquad r = 1, \ldots, k \tag{4.83}$$

for some integer $k \geq 3$. Then there exists a degree $k-1$ polynomial vector field T_F on $\mathbb{R}^3 \times \mathbb{R}^p$, with $p \circ T_F = 0$, such that

$$F = T_F^1 + M, \tag{4.84}$$

where the remainder M is such that $\pi_p \circ M = \pi_p$ and $j^{k-1}M = 0$.

By (4.84), T_F^1 is an HSN-family of vector fields. In particular, if F is an HSN-family of diffeomorphisms, *i.e*, if $k \geq 4$ (compare (4.3)), then Lemma 4.5 implies that F can be written as a perturbation of the time-1 map T_F^1 of an HSN-family of vector fields. Moreover, the 3-jet of the perturbing term M in (4.84) is zero, which means that the Taylor expansion of M around $(0,0)$ only contains terms of order at least four. This justifies our construction of the model maps G (4.1) and Q (4.2), as described in Sec. 4.1.2. The rest of this section is devoted to sketching the proof of Lemma 4.5.

Let $\mathcal{M}^n$ be the space of all homogeneous polynomial maps

$$P : \mathbb{R}^3 \times \mathbb{R}^p \to \mathbb{R}^3 \times \mathbb{R}^p$$

of degree n, with $\pi_p \circ P = 0$. We assume that the coordinates $x = (w, z, \alpha_1, \ldots, \alpha_p)$ on $\mathbb{R}^3 \times \mathbb{R}^p$ are such that the semisimple part S of $DF(0,0)$ is diagonal. A basis of $\mathcal{M}^n$ is given by all monomial maps

$$h(x)\frac{\partial}{\partial w}, \quad h(x)\frac{\partial}{\partial z}, \quad h(x) = w^{n_1}\overline{w}^{n_2} z^{n_3} \alpha_1^{n_4} \ldots \alpha_p^{n_{p+3}}, \tag{4.85}$$

lexicographically ordered [39] and such that $n_1 + n_2 + n_3 + n_4 + \cdots + n_{p+3} = n$. Let X be a vector field on $\mathbb{R}^3 \times \mathbb{R}^p$ such that $\pi_p \circ X = 0$. Denote by $\phi(t,x)$ the flow of X at time t, starting at point x. For $r \geq 2$ write

$$\begin{aligned} X(x) &= X_1(x) + X_2(x) + \cdots + X_r(x) + \mathcal{O}(\|x\|^{r+1}), \\ \phi(t,x) &= \phi_1(t)x + \phi_2(t,x) + \cdots + \phi_r(t,x) + \mathcal{O}(\|x\|^{r+1}), \\ F(x) &= F_1 x + F_2(x) + \cdots + F_r(x) + \mathcal{O}(\|x\|^{r+1}) \end{aligned}$$

where X_n, $\phi_n(t,-)$, and F_n belong to $\mathcal{M}^n$ for all $n = 1, \ldots, r$. The linear vector field X_1 is identified with its matrix representation in the given coordinates. The equation

$$j^r F = j^r \phi(1,-), \tag{4.86}$$

where the unknown is the vector field X, can be solved by induction on r. Indeed, system (4.86) is rewritten as

$$\begin{aligned} &e^{X_1} = F_1, \\ &\int_0^1 e^{-sX_1} X_n(e^{sX_1}x)ds = e^{-X_1}F_n(x) - \int_0^1 e^{-sX_1} Z^n(s,x)ds, \quad n = 2, \ldots, r, \end{aligned} \tag{4.87}$$

where $Z^n(s,x) = \sum_{i=2}^{n-1} Z^{i,n}(s,x)$ and $Z^{i,n}(s,x)$ is given by

$$X_n(\phi(t,x)) = X_n(\phi_1(t)x) + \sum_{i=n+1}^{n} Z^{n,i}(t,x) + \mathcal{O}(\|x\|^{r+1}).$$

The key point is that system (4.87) is solvable. Indeed, let (S,N) be the semisimple-nilpotent decomposition of $DF(0,0)$. Then in the given coordinates we have

$$S = \begin{pmatrix} S_1 & 0 \\ 0 & I_p \end{pmatrix}, \quad N = \begin{pmatrix} 0 & N_1 \\ 0 & 0 \end{pmatrix}, \tag{4.88}$$

where $S_1 = \mathrm{diag}\{\lambda_0, 1, \}$, I_p is the identity matrix of order p, and N_1 is the matrix of a linear operator $N_1 : \mathbb{R}^p \to \mathbb{R}^3$. Observe that we can write $S + N = S(I + S^{-1}N)$, and that both S and $I + S^{-1}N$ have a logarithm:

$$\log(S) = \mathrm{diag}(i\omega_0, 0, 0, \ldots, 0) \stackrel{\text{def}}{=} B, \quad \log(I + S^{-1}N) = S^{-1}N, \tag{4.89}$$

the second equality since $N^2 = 0$. Therefore, the first equation of system (4.87) has the solution $X_1 = B + S^{-1}N$, since

$$F_1 = DF(0,0) = S + N = S(I + S^{-1}N) = \exp(B)\exp(S^{-1}N) = \exp(B + S^{-1}N).$$

To complete the sketch of proof for Lemma 4.5, it is enough to observe that by the next lemma the higher-order equations in system (4.87) are solvable for $n = 2, \ldots, k-1$, given the assumptions in (4.83). This is the content of the next lemma.

Lemma 4.6. *Let $X_1 = B + S^{-1}N$, where B and N are defined in* (4.89) *and* (4.88)*, respectively. Suppose that* (4.83) *holds. Then the linear operator*

$$L^n : \mathcal{M}^n \to \mathcal{M}^n, \quad L^n(P)(x) = \int_0^1 e^{-sX_1} P(e^{sX_1}x) ds \tag{4.90}$$

is invertible for all $n = 1, \ldots, k-1$.

Proof. Let P be one of the monomials in the basis of $\mathcal{M}^n$ given in (4.85) and, to begin, suppose that

$$P(x) = h(x)\frac{\partial}{\partial w}, \quad \text{where} \quad h(x) = w^{n_1}\overline{w}^{n_2} z^{n_3} \alpha_1^{n_4} \ldots \alpha_p^{n_{p+3}}.$$

In this setting, an important property is that the nilpotent part N (4.88) has no nonzero entries in the upper right block, which corresponds to phase-space variables (w,z). Therefore, by denoting $sS^{-1}N(x) = (f, \overline{f}, g, 0, \ldots, 0)$, the coefficients f and g only depend on the parameters $\alpha = (\alpha_1, \ldots, \alpha_p)$, on ω_0 and on s, but not on (w,z). Therefore we have

$$\begin{aligned} e^{sX_1}x &= e^{sB}(I + sS^{-1}N)x = \left(\lambda_0^s(w+f), \overline{\lambda}_0^s(\overline{w} + \overline{f}), z + g, \alpha\right) \\ h(e^{sX_1}x) &= \lambda_0^{s(n_1-n_2)}(w+f)^{n_1}(\overline{w} + \overline{f})^{n_2}(z+g)^{n_3}\alpha_1^{n_4}\ldots\alpha_p^{n_{p+3}}. \end{aligned}$$

The expression for $h(e^{sX_1}x)$ is a sum of terms in which the monomial $h(x)$ self appears only once, since f and g do not depend on (w,z). In particular, this implies that

the matrix of the operator L^n with respect to the basis in (4.85) (which is ordered lexicographically), is lower triangular. Therefore the eigenvalues of L^n have the form

$$\nu_w = \int_0^1 e^{i\omega_0(n_1-n_2-1)s}ds \qquad \text{for} \quad P(x) = h(x)\frac{\partial}{\partial w} \quad \text{or}$$
$$\nu_z = \int_0^1 e^{i\omega_0(n_1-n_2)s}ds \qquad \text{for} \quad P(x) = h(x)\frac{\partial}{\partial z}.$$

To check that the operator L^n is invertible, we have to show that all eigenvalues are nonzero. If $n_1 - n_2 = 1$ or $n_1 - n_2 = 0$, then $\nu_w = 1$ or $\nu_z = 1$, respectively. So there may be a zero eigenvalue only for $n_1 - n_2 \neq 0, 1$. In this case we have

$$\nu_w = \frac{\lambda_0^{n_1-n_2-1} - 1}{i\omega_0(n_1 - n_2 - 1)}, \qquad \nu_z = \frac{n_1 - n_2}{i\omega_0(n_1 - n_2)}.$$

Therefore L^n has a zero eigenvalue if and only if

$$\text{either} \quad \lambda^{n_1-n_2-1} = 1, \quad \text{with } n_1 - n_2 - 1 \neq 0 \tag{4.91}$$
$$\text{or} \quad \lambda^{n_1-n_2} = 1, \quad \text{with } n_1 - n_2 \neq 0. \tag{4.92}$$

However, given the nonresonance condition in the hypotheses, (4.91) can only happen if either $n_1 - n_2 \geq k + 2$ or $n_1 - n_2 \leq -k$, while (4.92) may be satisfied only if $|n_1 - n_2| \geq k + 1$. Since $|n_1 - n_2| \leq n$, there are no zero eigenvalues for all $n \leq k - 1$. This concludes the proof of Lemma 4.6. □

4.E Choice of numerical constants for the model maps

Numerical results suggest that variations of γ essentially result in a rescaling of the bifurcation diagram in the parameters (μ, ω) for G (4.1) and Q (4.1). To be more precise, apart from a change of scale in the other parameters, no significant alterations occur in the bifurcation diagrams. The same behaviour has been checked for ε_1 and ε_2. Therefore only the parameter plane (μ, ω) is examined in most of the numerical simulations, while the other parameters and coefficients are kept fixed:

1. The parameter γ is kept fixed at 0.1 or 0.02.

2. The coefficients ε_1 and ε_2 are fixed at 1.

3. The term with coefficient a_2 induces a change of order γz in the fast rotation number, compare (4.47). Therefore we fix $a_2 = 1/\sqrt{2}$ in the simulations.

4. The constant a_1 controls the hyperbolicity of the limit cycle branching off from the Hopf bifurcation, see Sec. 4.1.2; we fix $a_1 = -1$.

Notice that for the model G (4.1) the coefficient ε_1 can be taken real, since a transformation of the form $(w, z) = R_\theta(w', z') = (\exp(i\theta)w', z')$ for suitable θ yields a system of coordinates where $\mathrm{Im}(\varepsilon_1) = 0$. Moreover, the parameter ε_3 is fixed at zero in G.

This is reasonable, since the term in ε_3 is of order γ^4, while the $\partial/\partial z$ component of G already contains a term in γz^2. Also observe that the term in ε_1 induces an effect in the *second* iterate of (4.1), which is similar to the effect of the term in ε_3. If (w_1, z_1) denote the components of the map (4.1), then

$$w_1\overline{w}_1 = |w|^2 \left(1-2\gamma(\gamma\mu+a_1 z+\gamma z^2)+\gamma^2 \left|\gamma\mu + az + \gamma z^2\right|^2\right) + 2\gamma^3\varepsilon_1 \operatorname{Re}\left(e^{i\omega}w^5\right) + \mathcal{O}(\gamma^4).$$

Due to the term $-\gamma |w|^2$ in the $\frac{\partial}{\partial z}$-component of G, in the second iterate the above term will give a contribution to the of the form $\gamma^4\varepsilon_1 \operatorname{Re}\left(e^{-i\omega}w^5\right)$ to the $\frac{\partial}{\partial z}$-component.

Notice that some terms are missing in the 3-jet of (4.1) when compared to the generic normal form (4.76). The coefficient of (4.1) corresponding to $c(\beta)$ in (4.76) is zero, while the coefficient corresponding to $b(\beta)$ in (4.76) only depends on γ and ω in (4.1). Since no such restrictions hold in (4.76), strictly speaking, G is representative only of a subset of all possible HSN-families. However, the following heuristic arguments suggest that the missing monomials in G have a marginal influence on the dynamics of the model, which justifies their suppression. Firstly, the effect of the term in γz^2 in the $\partial/\partial z$-component dominates that of the missing term in $\gamma^2 z^3$. Secondly, inclusion of the coefficient $\operatorname{Im} f_{102}$ yields a contribution of the form $-\gamma^2 z^2 \operatorname{Im} f_{102}$ in the ϕ-component, which is one order of magnitude smaller than the term $\gamma a_2 z$ (compare (4.47)). To conclude, observe that the coefficient $\operatorname{Re} f_{102}$ influences the slow rotation number, *i.e.*, the rotation number of the invariant circle of $\widetilde{S}$ (equation (4.18)) born at the Hopf bifurcation. Its value is of no relevance for the dynamics, as long as it is sufficiently far from zero.

Bibliography

[1] V.S. Afrajmovich, L.P. Shil′nikov: On invariant two-dimensional tori, their disintegration and stochasticity, in *Methods of the qualitative theory of differential equations*, Gor′kov. Gos. University, Gor′kij (1983), 3–26.

[2] V.S. Anishchenko: *Dynamical Chaos—Models and Experiments*, World Scientific (1995).

[3] V.S. Anishchenko, M.A. Safonova, U. Feudel, J. Kurths: Bifurcations and transition to chaos through three-dimensional tori, *IJBC* **3(4)** (1994), 595–607.

[4] V.I. Arnol′d: Small denominators, I: Mappings of the circumference into itself, *AMS Transl. (Ser. 2)* **46** (1965), 213–284.

[5] V.I. Arnol′d: *Mathematical Methods of Classical Mechanics*, Springer GTM **60** (1980).

[6] V.I. Arnol′d: *Geometrical Methods in the Theory of Ordinary Differential Equations (2nd ed.)*, Springer–Verlag (1988).

[7] V.I. Arnol′d, V.S. Afrajmovich, Yu.S.Il′yashenko, L.P. Shil′nikov: I. Bifurcation Theory in *Dynamical Systems* **V** (V.I. Arnol′d Ed.), Encyclopaedia of Mathematical Sciences, Springer–Verlag (1982).

[8] D.G. Aronson, M.A. Chory, G.R. Hall, R.P. McGehee: Bifurcations from an invariant circle for two-parameter families of maps of the plane: a computer-assisted study, *Comm. Math. Phys.* **83(3)** (1982), 303–354.

[9] C. Baesens, J. Guckenheimer, S. Kim, R.S. McKay: Three coupled oscillators: mode-locking, global bifurcations and toroidal chaos, *Phys. D* **49(3)** (1991), 387–475.

[10] M. Benedicks, L. Carleson: On iterations of $1 - ax^2$ on $(-1, 1)$, *Ann. of Math. (2)* **122(1)** (1985), 1–25.

[11] M. Benedicks, L. Carleson: The dynamics of the Hénon map, *Ann. of Math. (2)* **133(1)** (1991), 73–169.

[12] G. Benettin, L. Galgani, A. Giorgilli, J.-M. Strelcyn: Lyapunov characteristic Exponents for Smooth Dynamical Systems: A Method for Computing All of Them, *Meccanica* **15** (1980), 9–30.

[13] M. Bosch, C. Simó: Attractors in a Shil′nikov–Hopf scenario and a related one-dimensional map, *Phys. D* **62** (1993), 217–229.

[14] B.L.J. Braaksma, H.W. Broer: On a quasi-periodic Hopf bifurcation, *Ann. Inst. H. Poincaré Anal. Non Linéaire* **4(2)** (1987), 115–168.

[15] W.L. Briggs, V.E. Henson: *The DFT: An Owner's Manual for the Discrete Fourier Transform*, SIAM, Philadelphia (1995).

[16] H.W. Broer: Formal normal forms for vector fields and some consequences for bifurcations in the volume preserving case, in *Dynamical Systems and turbulence, Warwick 1980* (A. Dold and B. Eckmann Eds.), Springer LNM **898** (1980), 54–74.

[17] H.W. Broer, G.B. Huitema, M.B. Sevryuk: *Quasi-periodic Motions in Families of Dynamical Systems, Order amidst Chaos*, Springer LNM **1645** (1996).

[18] H.W. Broer, G.B. Huitema, F. Takens, B.L.J. Braaksma: Unfoldings and bifurcations of quasi-periodic tori, *Mem. AMS* **83(421)** (1990), 1–175.

[19] H.W. Broer, H.M. Osinga, G. Vegter: Algorithms for computing normally hyperbolic invariant manifolds, *Z. angew. Math. Phys.* **48** (1997), 480–524.

[20] H.W. Broer, R. Roussarie: Exponential confinement of chaos in the bifurcation sets of real analytic diffeomorphisms, in *Global Analysis of Dynamical Systems, Festschrift dedicated to Floris Takens for his 60th birthday* (H.W. Broer, B. Krauskopf, and G. Vegter Eds.), IOP Publish., Bristol (2001).

[21] H.W. Broer, R. Roussarie, C. Simó: Invariant circles in the Bogdanov–Takens bifurcation for diffeomorphisms, *ETDS* **16** (1996), 1147–1172.

[22] H.W. Broer, C. Simó: Hill's equation with quasi-periodic forcing: resonance tongues, instability pockets and global phenomena, *Bol. Soc. Bras. Mat* **29** (1998), 253–293.

[23] H.W. Broer, C. Simó, J.C. Tatjer: Towards global models near homoclinic tangencies of dissipative diffeomorphisms, *Nonlinearity* **11** (1998), 667–770.

[24] H.W. Broer, C. Simó, R. Vitolo: Bifurcations and strange attractors in the Lorenz-84 climate model with seasonal forcing, *Nonlinearity* **15(4)** (2002), 1205–1267.

[25] H.W. Broer, C. Simó, R. Vitolo: Hénon-like strange attractors in a family of maps of the solid torus, *preprint University of Groningen*, submitted (2002).

[26] H.W. Broer, C. Simó, R. Vitolo: The Hopf-saddle-node bifurcation for fixed points of diffeomorphisms, in preparation.

[27] H.W. Broer, C. Simó, R. Vitolo: Quasi-periodic Hénon-like attractors in the Lorenz-84 climate model with seasonal forcing, to appear in *Proceedings Equadiff 2003*.

[28] H.W. Broer, S.J. van Strien: Infinitely many moduli of strong stability in divergence free unfoldings of singularities of vector fields, in *Geometric Dynamics, Proceedings, Rio de Janeiro 1981* (J. Palis Ed.), Springer LNM **1007** (1983), 39–59.

[29] H.W. Broer, F. Takens: Formally symmetric normal forms and genericity, *Dynamics Reported* **2** (1989), 36–60.

[30] H.W. Broer, F. Takens: Mixed spectrum and rotational symmetry, *Archive Rat. Mech. An.* **124** (1993), 13–42.

[31] H.W. Broer, G. Vegter: Subordinate Shil′nikov bifurcations near some singularities of vector fields having low codimension, *ETDS* **4** (1984), 509–525.

[32] H.W. Broer, G. Vegter: Bifurcational Aspects of Parametric Resonance, *Dynamics Reported* **1** (1992), 1–53.

[33] J.P Carcassès, C. Mira, M. Bosch, C. Simó, J.C. Tatjer: 'Crossroad area–spring area' transition (II). Parameter plane representation, *IJBC* **1** (1991), 183–196.

[34] E. Castellà, À. Jorba: On the vertical families of two-dimensional tori near the triangular points of the Bicircular problem, *Celestial Mechanics* **76** (2000), 35–54.

[35] A. Chenciner: Bifurcations de points fixes elliptiques. I. Courbes invariantes, *Publ. Math. IHES* **61** (1985), 67–127.

[36] A. Chenciner: Bifurcations de points fixes elliptiques. II. Orbites périodiques et ensembles de Cantor invariants, *Invent. Math.* **80** (1985), 81–106.

[37] A. Chenciner: Bifurcations de points fixes elliptiques. III. Orbites périodiques de "petites" périodes et élimination résonnante des couples de courbes invariantes, *Publ. Math. IHES* **66** (1988), 5–91.

[38] S.N. Chow, J.K. Hale: *Methods of bifurcation theory*, Springer–Verlag (1982).

[39] S-N. Chow, C. Li, D. Wang: *Normal Forms and Bifurcation of Planar Vector Fields*, Cambridge University Press, New York (1994).

[40] P.M. Cincotta, C. Simó: Simple tools to study global dynamics in non-axisymmetric galactic potentials – I, *Astronomy & Astrophysics Supp.* **147** (2000), 205–228.

[41] R.L. Devaney: *An Introduction to Chaotic Dynamical Systems* (2nd edition), Addison–Wesley (1989).

[42] L. Díaz, J. Rocha, M. Viana: Strange attractors in saddle cycles: prevalence and globality, *Inv. Math.* **125** (1996), 37–74.

[43] F. Dumortier, R. Roussarie, J. Sotomayor: Generic 3-parameter families of vector fields on the plane, unfolding a singularity with nilpotent linear part. The cusp case of codimension 3, *ETDS* **7(3)** (1987), 375–413.

[44] J.-P. Eckmann, D. Ruelle: Ergodic theory of chaos and strange attractors, *Rev. Mod. Phys.* **57** (1985), 617–655.

[45] M. Feigenbaum: Qualitative universality for a class of nonlinear transformations, *J. Stat. Phys.* **21** (1978), 25–52.

[46] N. Fenichel: Persistence and smoothness of invariant manifolds for flows, *Indiana Univ. Math. J.* **21** (1971/72), 193–226.

[47] M. Flatto, N. Levinson: Periodic Solutions of Singularly Perturbed Systems, *J. Rat. Mech. Anal.* **4** (1955), 943–950.

[48] P. Gaspard: Local birth of homoclinic chaos, *Phys. D* **62(1–4)** (1993), 94–122.

[49] P. Glendinning: Intermittency and strange nonchaotic attractors in quasi-periodically forced circle maps, *Phys. Lett. A* **244** (1998), 545–550.

[50] G. Gomez, J.M. Mondelo, C. Simó: Refined Fourier Analysis Procedures, *preprint Universitat de Barcelona* (2001).

[51] S.V. Gonchenko, L.P. Shil′nikov, D.V Turaev: Dynamical phenomena in systems with structurally unstable Poincaré homoclinic orbits, *Chaos* **6(1)** (1996), 15–31.

[52] P. Grassberger, I. Procaccia: Measuring the strangeness of strange attractors, *Phys. D* **9** (1983), 189–208.

[53] C. Grebogi, E. Ott, S. Pelikan, J. Yorke: Strange attractors that are not chaotic, *Phys. D* **13(1-2)** (1984), 261–268.

[54] C. Grebogi, E. Ott, J. Yorke: Chaotic attractors in crisis, *Phys. Rev. Lett.* **48(22)** (1982), 1507–1510.

[55] J. Guckenheimer: Sensitive dependence to initial conditions for one-dimensional maps. *Comm. Math. Phys.* **70(2)** (1979), 133–160.

[56] J. Guckenheimer, P. Holmes: *Nonlinear Oscillations, Dynamical Systems, and Bifurcations of Vector Fields*, Springer–Verlag (1983).

[57] A. Haro, R. de la Llave: A parametrization method for the computation of whiskers in quasi-periodic maps: rigorous results, *preprint* (2001).

[58] M. Hénon: A two dimensional mapping with a strange attractor, *Comm. Math. Phys.* **50** (1976), 69–77.

[59] M.W. Hirsch: *Differential Topology*, Springer GTM **33** (1976).

[60] M.W. Hirsch, C.C. Pugh, M. Shub: *Invariant Manifolds*, Springer LNM **583** (1977).

[61] K. Homan: *Routes to chaos in the Lorenz-84 atmospheric model*, master thesis, University of Groningen (1998).

[62] À. Jorba: A Methodology for the Numerical Computation of Normal Forms, Centre Manifolds and First Integrals of Hamiltonian Systems, *Experimental Mathematics* **8** (1999), 155–195.

[63] À. Jorba: Numerical computation of the normal behaviour of invariant curves of n-dimensional maps, *Nonlinearity* **14** (2001), 943–976.

[64] À. Jorba, M. Zou: On the numerical integration of ODE by means of high-order Taylor methods, *preprint Universitat de Barcelona* (2001).

[65] T. Nishikawa, K. Kaneko: Fractalization of a torus as a strange nochaotic attractor, *Phys. Rev. E* **56(6)** (1996), 6114–6124.

[66] T. Kapitaniak, L.O. Chua: Strange nochaotic trajectories on torus, *IJBC* **7** (1997), 423–429.

[67] J. Kaplan, J. Yorke: Chaotic behaviour of multidimensional difference equations, in *Functional Differential Equations and Approximations of Fixed Points* (H.O. Peitgen and H.O. Walther Eds.), Springer LNM **730** (1979), 204–227.

[68] G. Keller: A note on strange nonchaotic attractors, *Fund. Math.* **151(2)** (1996), 139–148.

[69] V. Kirk: Breaking of symmetry in the saddle-node Hopf bifurcation, *Phys. Lett. A* **154** (1991), 243–248.

[70] R. Kock: *Routes to chaos in the periodically driven Lorenz-84 system*, master thesis, University of Groningen (1998).

[71] B. Krauskopf: Bifurcation sequences at 1:4 resonance: an inventory, *Nonlinearity* **7(3)** (1994), 1073–1091.

[72] B. Krauskopf: *On the 1:4 resonance problem: Analysis of the bifurcation set*, PhD thesis, University of Groningen (1995).

[73] B. Krauskopf, B. Oldeman: The saddle-node Hopf bifurcation with global reinjection, *preprint*, submitted (2003).

[74] B. Krauskopf, H. Osinga: Growing 1D and quasi 2D unstable manifolds of maps, *J. Comput. Phys.* **146(1)** (1998), 404–419.

[75] B. Krauskopf, C. Rousseau: Codimension-three unfoldings of reflectionally symmetric planar vector fields, *Nonlinearity* **10** (1997), 1115–1150.

[76] B. Krauskopf, N. Tollenaar, D. Lenstra: Tori and their bifurcations in an optically injected semiconductor laser, *Optics Communications* **156(1-3)** (1998), 158–169.

[77] B. Krauskopf, S. Wieczorek: Accumulating regions of winding periodic orbits in optically driven lasers, *Phys. D* **173(1–2)** (2002), 97–113.

[78] Yu. Kuznetsov: *Elements of Applied Bifurcation Theory* (2nd ed.), Springer–Verlag (1998).

[79] Yu. Kuznetsov, H.G.E Meijer, L. van Veen: The Fold-Flip bifurcation, *preprint 1270 University of Utrecht* (2003). To appear in *IJBC*.

[80] E.N. Lorenz: Irregularity: a fundamental property of the atmosphere, *Tellus* **36A** (1984), 98–110.

[81] E.N. Lorenz: Can chaos and intransitivity lead to interannual variability?, *Tellus* **42A** (1990), 378–389.

[82] C. Masoller, A.C. Sicardi Schifino, L. Romanelli: Regular and chaotic behaviour in the new Lorenz system, *Phys. Lett. A* **167** (1992), 185–190.

[83] W. de Melo, S. van Strien: *One dimensional dynamics*, Springer–Verlag (1993).

[84] M. Misiurewicz: Absolutely continuous measures for certain maps of an interval, *Publ. Math. IHES* **53** (1981), 17–51.

[85] J.M. Mondelo: *Contribution to the Study of Fourier Methods for Quasi-Periodic Functions and the Vicintiy of the Collinear Libration Points*, PhD thesis, Universitat de Barcelona (2001).

[86] L. Mora, M. Viana: Abundance of strange attractors, *Acta Math* **171** (1993), 1–71.

[87] S. Newhouse: Diffeomorphisms with infinitely many sinks, *Topology* **13** (1974), 9–18.

[88] S. Newhouse, J. Palis, F. Takens: Bifurcations and stability of families of diffeomorphisms, *Publ. Math. IHES* **57** (1983), 5–71.

[89] S. Newhouse, D. Ruelle, F. Takens: Occurrence of strange Axiom A attractors near quasiperiodic flows on $\mathbb{T}^m$, $m \geq 3$, *Comm. Math. Phys.* **64** (1978), 35–40.

[90] H. Osinga, U. Feudel: Boundary crisis in quasiperiodically forced systems, *Physica D* **141(1-2)** (2000), 54–64.

[91] H. Osinga, J. Wiersig, P. Glendinning, U. Feudel: Multistability in the quasiperiodically forced circle map, *IJBC* **11** (2001), 3085–3105.

[92] B.B. Peckham, I.G. Kevrekidis: Lighting Arnold flames: resonance in doubly forced periodic oscillators, *Nonlinearity* **15(2)** (2002), 405–428.

[93] S. Östlund, D. Rand, J. Sethna, E. Siggia: Universal properties of the transition from quasiperiodicity to chaos in dissipative systems, *Phys. D* **8(3)** (1983), 303–342.

[94] J. Palis, W. de Melo: *Geometric Theory of Dynamical Systems, An Introduction* Springer–Verlag (1982).

[95] J. Palis, F. Takens: *Hyperbolicity & Sensitive Chaotic Dynamics at Homoclinic Bifurcations*, Cambridge Studies in Advanced Mathematics **35**, Cambridge University Press (1993).

[96] J. Palis, M. Viana: High dimension diffeomorphisms displaying infinitely many periodic attractors, *Ann. of Math. (2)* **140(1)** (1994), 91–136.

[97] Y. Pomeau, P. Manneville: Intermittent transition to turbulence in dissipative dynamical systems, *Comm. Math. Phys.* **74** (1980), 189–197.

[98] W. Press, S. Teukolsky, W. Vetterling, B. Flannery: *Numerical Recipies in C: the Art of Scientific Computing* (2nd ed.), Cambridge University Press, New York (1992).

[99] D. Ruelle: *Elements of Differentiable Dynamics and Bifurcation Theory*, Academic Press (1988).

[100] D. Ruelle, F. Takens: On the nature of turbulence, *Comm. Math. Phys.* **20** (1971), 167–192.

[101] R. Seydel: *Practical Bifurcation and Stability Analysis*, Springer–Verlag (1994).

[102] A. Shil′nikov, G. Nicolis, C. Nicolis: Bifurcation and predictability analysis of a low-order atmospheric circulation model, *IJBC* **5(6)** (1995), 1701–1711.

[103] M. Shub: *Global stability of dynamical systems*, Springer–Verlag (1986).

[104] C. Simó: On the Hénon–Pomeau attractor, *J.Stat.Phys.* **21** (1979), 465–494.

[105] C. Simó: On the analytical and numerical computation of invariant manifolds, in *Modern Methods in Celestial Mechanics* (D. Benest and C. Froeschlé Eds.), ed. Frontières, Paris (1990), 285–330.

[106] C. Simó: Effective Computations in Hamiltonian Dynamics, in *Cent ans après les Méthodes Nouvelles de H. Poincaré*, Société Mathématique de France (1996), 1–23.

[107] C. Simó, H.W. Broer, R. Roussarie: A numerical exploration of the Takens–Bogdanov bifurcation for diffeomorphisms, in *European Conference on Iteration Theory (ECIT 89), Batschuns (Austria)* (C. Mira, N. Netzer, C. Simó, and G. Targonski Eds.), World Scientific, Singapore (1991), 320–334.

[108] C. Simó, J.C. Tatjer: Basins of attraction near homoclinic tangencies, *ETDS* **14** (1994), 351–390.

[109] H.L. Swinney, J.P. Gollub: Characterization of hydrodynamic strange attractors, *Phys. D* **18** (1986), 448–454.

[110] F. Takens: A nonstabilizable jet of a singularity of a vector field, *Dynamical systems (Proc. Sympos., Univ. Bahia, Salvador, 1971)*, Academic Press, New York (1973), 583–597.

[111] F. Takens: Singularities of vector fields, *Publ. Math. IHES* **43** (1974), 47–100.

[112] F. Takens: Forced oscillations and bifurcations, in *Applications of Global Analysis* **1** (1974), Communications of the Mathematical Institute Rijksuniversiteit Utrecht **3**. Reprinted in *Global analysis of dynamical systems: Festschrift dedicated to Floris Takens for his 60th birthday* (H.W. Broer, B. Krauskopf, and G. Vegter Eds.), IOP Publish., Bristol (2001).

[113] J.C. Tatjer: Three dimensional dissipative diffeomorphisms with homoclinic tangencies, *ETDS* **21(1)** (2001), 249–302.

[114] Ph. Thieullen, C. Tresser, L.-S. Young: Positive Lyapunov exponent for generic one-parameter families of unimodal maps, *J. Anal. Math.* **64** (1994), 121–172.

[115] M. Tsujii: A simple proof for monotonicity of entropy in the quadratic family, *ETDS* **20** (2000), 925–933.

[116] V.S. Varadarajan: *Lie Groups, Lie Algebras, and Their Representations*, Springer GTM **102** (1984).

[117] L. van Veen: *Time scale interaction in low-order climate models*, PhD thesis, University of Utrecht (2002).

[118] L. van Veen, T. Opsteegh, F. Verhulst: Active and passive ocean regimes in a low-order climate model, *Tellus* **53A** (2001), 616–627.

[119] A. Venkatesan, M. Lakshmanan: Interruption of torus doubling bifurcation and genesis of strange nonchaotic attractors in a quasiperiodically forced map: Mechanisms and their characterizations, *Phys. Rev. E* **63** (2001).

[120] M. Viana: Strange attractors in higher dimensions, *Bol. Soc. Bras. Mat* **24** (1993), 13–62.

[121] M. Viana: Multidimensional nonhyperbolic attractors, *Publ. Math. IHES* **85** (1997), 63–96.

[122] M. Viana: Stochastic dynamics of deterministic systems, *Braz. Math. Colloquium* IMPA (1997), preprint at `http://www.impa.br/~viana/`.

[123] S. Wieczorek: *The dynamical complexity of optically injected semiconductor lasers*, PhD thesis, University of Amsterdam VUA (2002).

[124] S. Wieczorek, B. Krauskopf, D. Lenstra: A unifying view of bifurcations in a semiconductor laser subject to optical injection, *Optics Communications* **172** (1999), 279–295.

[125] J. Yorke, K. Alligood: Cascades of period-doubling bifurcations: a prerequisite for horseshoes, *Bull. AMS* **9** (1983), 319–322.

[126] F.O.O. Wagener: Semi-local analysis of the $k:1$ and $k:2$ resonances in quasiperiodically forced systems, in *Global Analysis of Dynamical Systems, Festschrift dedicated to Floris Takens for his 60th birthday* (H.W. Broer, B. Krauskopf, and G. Vegter Eds.), IOP Publish., Bristol (2001), 113–129.

[127] Q. Wang, L.-S. Young: Strange Attractors with One Direction of Instability, *Comm. Math. Phys.* **218** (2001), 1–97.

Summary

The research presented in this PhD thesis fits within the framework of nonlinear deterministic dynamical systems depending on parameters. The work is divided into four Chapters, where the first is a general introduction to the other three.

Chapter two deals with the investigation of a time-periodic three-dimensional system of ordinary differential equations depending on three parameters, the Lorenz-84 model with seasonal forcing. The model is a variation on an autonomous system proposed in 1984 by the meteorologist E. Lorenz to describe general atmospheric circulation at mid latitude of the northern hemisphere. In the present version of the model, two parameters are subject to periodic forcing, where the period is one year. A third parameter is the relative amplitude of the forcing, denoted by ε. In Chapter two we provide a coherent inventory of the dynamics of the forced model in the three-dimensional parameter space. The model is studied in terms of its Poincaré map (also called period- or stroboscopic map), which is a three-dimensional diffeomorphism. The study is carried out by both numerical and analytical means. Numerical computation of the Lyapunov exponents and of power spectra is used to describe the dynamics of the Poincaré map.

For small values of the parameter ε the bifurcation diagram is quite similar to that of the autonomous, unperturbed system, *i.e.*, the system at $\varepsilon = 0$. However, for positive ε new dynamical phenomena are found by numerical means in the Poincaré map of the forced system. We conjecture that at least two types of strange attractors occur: *Hénon-like* and *quasi-periodic Hénon-like*. Hénon-like attractors are quite well understood from the theoretical viewpoint. In particular, a Hénon-like attractor coincides with the closure of the unstable manifold of a periodic orbit of saddle type. Quasi-periodic Hénon-like attractors are formed by the closure of the unstable manifold of a quasi-periodic invariant circle of saddle type. The quasi-periodic Hénon-like attractors as numerically detected in the Poincaré map have dimension close to two, the second Lyapunov exponent being approximately zero. Furthermore, the power spectrum has both sharp peaks, which is typical for quasi-periodicity, and broad band, which is typical for chaos.

Rigorous mathematical characterisations of Hénon-like attractors so far have only been achieved for model systems which are much simpler than the Lorenz-84 system. Therefore in Chapter three we consider a simplified model on the solid 2-torus (*i.e.*, the product of the plane and the circle). For this model, given by the skew-coupling of the planar Hénon-map and the Arnol′d map of the circle, we establish a new result regarding Hénon-like attractors. For a related class of models we show the existence of an invariant circle of saddle type such that the closure of its unstable manifold attracts an open set of initial states. Despite this, the mathematical characterisation

of the quasi-periodic Hénon-like attractors remains, also in these cases, largely open.

In Chapter four I turn to the study of the Hopf-saddle-node bifurcation for fixed points of diffeomorphisms, by examining two model maps. This bifurcation is one of the organising centres in the family of Poincaré maps of the Lorenz-84 model. The corresponding bifurcation for equilibria of vector fields has been intensively studied (see *e.g.* the textbooks of Guckenheimer-Holmes and Kuznetsov). By a theorem of Takens, the results for the vector field provide a 'skeleton'-description of what we can expect for maps. The situation for maps is more complicated than that for vector fields, due to the occurrence of resonances and chaos. In particular, we show that near a 1:5 resonance several additional bifurcations occur. Correspondingly, a few invariant circles and tori of different stability types may coexist in certain parameter regions. Moreover, Hénon-like and quasi-periodic Hénon-like attractors are numerically detected.

Samenvatting

Het onderzoek van dit proefschrift valt in het kader van de niet-lineaire, deterministische dynamische systemen die van parameters afhangen. Het werk is onderverdeeld in vier hoofdstukken, waarbij het eerste een algemene introductie is van de resterende drie.

Hoofdstuk twee bevat een onderzoek van de dynamica van een tijd-periodiek drie-dimensionaal stelsel gewone differentiaalvergelijkingen dat van drie parameters afhangt, het Lorenz-84 model met seizoensaandrijving. Het model is een variatie op een autonoom systeem dat door de meteoroloog E. Lorenz is voorgesteld om de algemene atmosferische circulatie op gemiddelde noorderbreedte te beschrijven. In de huidige versie van het model worden twee parameters periodiek aangedreven, waarbij de periode één jaar is. Een derde parameter wordt gegeven door de relatieve amplitude van de aandrijving, aangegeven met ε. In Hoofdstuk twee geven we een coherente beschrijving van de dynamica van het aangedreven model in de drie-dimensionale parameter ruimte. Het model wordt bestudeerd door middel van zijn Poincaré afbeelding (ook periode- of stroboscopische afbeelding genoemd), die een drie-dimensionaal diffeomorfisme is. De analyse wordt uitgevoerd met numerieke en analytische methoden. Numeriek berekende Lyapunov exponenten en vermogenspectra worden gebruikt om de dynamica van de Poincaré afbeelding te beschrijven.

Voor kleine waarden van de parameter ε lijkt het bifurcatie diagram sterk op dat van het autonome, ongestoorde systeem, dat wil zeggen het systeem voor $\varepsilon = 0$. Voor positieve ε worden er echter ook nieuwe dynamische verschijnselen gevonden met numerieke middelen. We veronderstellen dat er minstens twee typen vreemde aantrekkers optreden: *Hénon-achtig* en *quasi-periodiek Hénon-achtig*. Hénon-achtige aantrekkers zijn vrij goed begrepen vanuit een theoretisch oogpunt. Een Hénon-achtige aantrekker bestaat namelijk uit de afsluiting van de onstabiele varieteit van een periodieke baan van zadel type. Quasi-periodieke Hénon-achtige aantrekkers worden gevormd door de afsluiting van de onstabiele varieteit van een quasi-periodieke invariante cirkel van zadel type. De numeriek berekende quasi-periodieke Hénon-achtige aantrekkers hebben dimensie die dichtbij twee ligt, omdat de tweede Lyapunov exponent bijna nul is. Verder vertoont het vermogenspectrum zowel scherpe pieken, wat typisch is voor quasi-periodiciteit, als broad band spectrum, wat typisch is voor chaos.

Rigoureuze wiskundige karakterisering van Hénon-achtige aantrekkers werd tot dusver uitsluitend verkregen voor modellen die veel eenvoudiger zijn dan het Lorenz-84 systeem. Daarom beschouwen we in Hoofdstuk drie een vereenvoudigd model op de gevulde 2-torus (dat wil zeggen het produkt van het vlak en de cirkel). Voor dit model, dat gegeven wordt door het scheef-koppelen van de Hénon afbeelding in het vlak met de Arnol′d afbeelding van de cirkel, krijgen we een nieuw resultaat betreffende Hénon-

achtige aantrekkers. Voor een gerelateerde klasse van modellen tonen we aan dat er een invariante cirkel van zadel type bestaat, zodanig dat de afsluiting van zijn onstabiele varieteit een open verzameling van begintoestanden aantrekt. Desondanks blijft de wiskundige karakterisering van de quasi-periodieke Hénon-achtige aantrekkers, ook voor deze gevallen, nog grotendeels open.

In Hoofdstuk vier bestudeer ik de Hopf-zadel-knoop bifurcatie voor dekpunten van diffeomorfismen, door twee model-afbeeldingen te bekijken. Deze bifurcatie is een van de organiserende knooppunten in de familie van Poincaré afbeeldingen van het Lorenz-84 model. De corresponderende bifurcatie voor vectorvelden is al intensief bestudeerd (zie bijvoorbeeld de tekstboeken van Guckenheimer-Holmes en Kuznetsov). Volgens een stelling van Takens vormen de resultaten voor het vectorveld een 'skelet'-beschrijving van wat we voor afbeeldingen kunnen verwachten. De situatie voor afbeeldingen is gecompliceerder dan die voor vectorvelden, wegens het optreden van resonanties en chaos. In het bijzonder tonen we aan dat er dichtbij een 1:5 resonantie meerdere bifurcaties optreden. Daarbij is er ook sprake van coëxistentie van enkele invariante cirkels en tori van verschillende stabiliteitstypen in bepaalde parametergebieden. Verder worden Hénon-achtige en quasi-periodieke Hénon-achtige aantrekkers numeriek gevonden.